THE LASER INDUCED DEPOSITION OF ZINC SELENIDE

A thesis submitted to the University of Manchester for the degree of Doctor of Philosophy in the Faculty of Technology

by John Simpson

Department of Chemistry

U.M.I.S.T.

1990

To Mum and Dad

No portion of the work referred to in this thesis has been submitted in support of an application for another degree or qualification of this or any other university or institution of learning.

Signed .....

Certified .....

Date January 11/90

Acknowledgements

I would like to express my sincere thanks to my supervisor, Professor J.O. Williams, for his guidance and encouragement over the period of this study. I would also like to be able to thank the Science and Engineering Research Council for their financial support.

I would also like to thank the technical staff of the Chemistry Department, particularly Mr. J. Holden and and Mr. S. Vaudrey for assistance during the construction of apparatus. I also thank Mr. Ian Brough and Dr. Andy Wright for assistance with microscopy, and Mr. Steve Hibbert for providing SIMS spectra.

I have benefitted on countless occasions from the assistance and support of Dr. Max Parrott, whose aid has proved invaluable during the preparation of this thesis. Finally, my gratitude is expressed to the hard drinking boys and girls of N floor for providing moral support whilst I served my debt to society.

Abstract

Thin films of Zinc Selenide have been deposited on (100) Gallium Arsenide by two laser-based techniques, laser photochemical deposition and laser ablation deposition.

Laser photochemical deposition was carried out by the photolytic decomposition of dimethylzinc and diethylselenide by the 193 nm ArF excimer laser radiation. A novel means of light admittance to the reactor was developed. The laser light was loosely focused on the window surface and any material removed by the laser was caught in an electrostatic ion trap to avoid the gas phase formation of heterogeneously nucleated particulates.

Films deposited by this method were of inferior crystalline quality compared with equivalent MOCVD-grown material, exhibiting (400) FWHM values of ~5 degrees at standard MOCVD epitaxial deposition temperatures. This was attributed to excessive carbon levels in the layer due to the incorporation of photolysis byproducts. Films grown under UV irradiation on amorphous substrates exhibited a marked (111) preferred orientation, with greatly superior crystallinity to (100) oriented layers. A mechanism involving the anisotropic creation of energetic photocarriers which stimulate surface reactions is proposed. The low resistance of ZnSe to thermal shock resulting from pulsed laser irradiation is identified as a serious constraint to the laser processing of this material.

Zinc Selenide films have also been deposited by the laser ablation of solid ZnSe targets to produce a highly directional plasma jet. Time of flight studies and electrical measurements were made on the laser plasmas and as a result at least two different ablation mechanisms were distinguished. A mechanism operating at low laser powers produced species with thermal energies that appeared to reflect high surface temperatures reached during ablation. At a threshold laser energy density of 210 mJ cm^{-2} a jump in ion yield was observed. The plasmas formed above this threshold energy exhibit low translational velocities and effective temperatures. Maxwell-Boltzmann distributions were fitted to the positive ion ToF profiles and are consistent with a very low initial plasma temperature (1-2 x 10^3 K).

A mechanism is proposed for the ablation of ZnSe by 193 nm laser radiation. The high absorption at this wavelength due to interband transitions results in a depopulation of bonding orbitals at the target surface. The lattice becomes decohesive and disintegrates at low temperatures. Energetic photoelectrons diffuse into the target ahead of the plasma/solid interface resulting in an overall positive charged plasma and a negatively charged plasma.

Films grown by laser plasma deposition of the vapour on (100) GaAs were of high crystalline quality and exhibited highly specular surfaces. Congruent evaporation of the ZnSe target resulted in the original target composition being maintained after repeated (3000 pulses) irradiation and a 1:1 transfer of composition from the target to the deposited film. In common with other reported laser ablation studies, the films contained sub-micron size particulates ejected from the target. Methods of reducing particulate incorporation have been identified.

CONTENTS

Chapter 1

Introduction

1.1 Compound Semiconductors

The fundamental limitations of Si as a device material have led to the investigation and development of alternative semiconductor materials which can offer specific advantages. III-V compound materials such as GaAs and InP have much greater electron mobilities at room temperature (7800 and 4600 $cm^2v^{-1}s^{-1}$ respectively) than Si (μ_e = 1300$cm^2v^{-1}s^{-1}$) and therefore electronic devices operating at much higher rates can be fabricated from these materials.

The electronic structure of several III-V and II-VI compounds also makes them potentially suitable as materials for devices which can emit visible radiation.

1.11 Electronic Structure of Semiconductors.

The E-K representations of the electronic structures of Si and representative III-V and II-VI compound semiconductors GaAs and ZnS are shown in figure 1.1. GaAs and ZnS both share the sphalerite crystal structure and as a consequence their band structures within the unit cell are very similar. The minimum in the conduction band has the same value as the valence band maximum at the zone centre. These compounds are therefore referred to as direct band gap

materials. A transition from the valence band to the conduction band in response to an external field can take place without any change in the wave vector k. However for a similar transition to take place in an indirect gap material such as Si, where the conduction band minimum is not situated at the same point in k-space as the valence band maximum, a change in momentum is also required which must come from a simultaneous lattice displacement (phonon). Absorption and emission of radiation is therefore inherently much more efficient for the direct band gap materials.

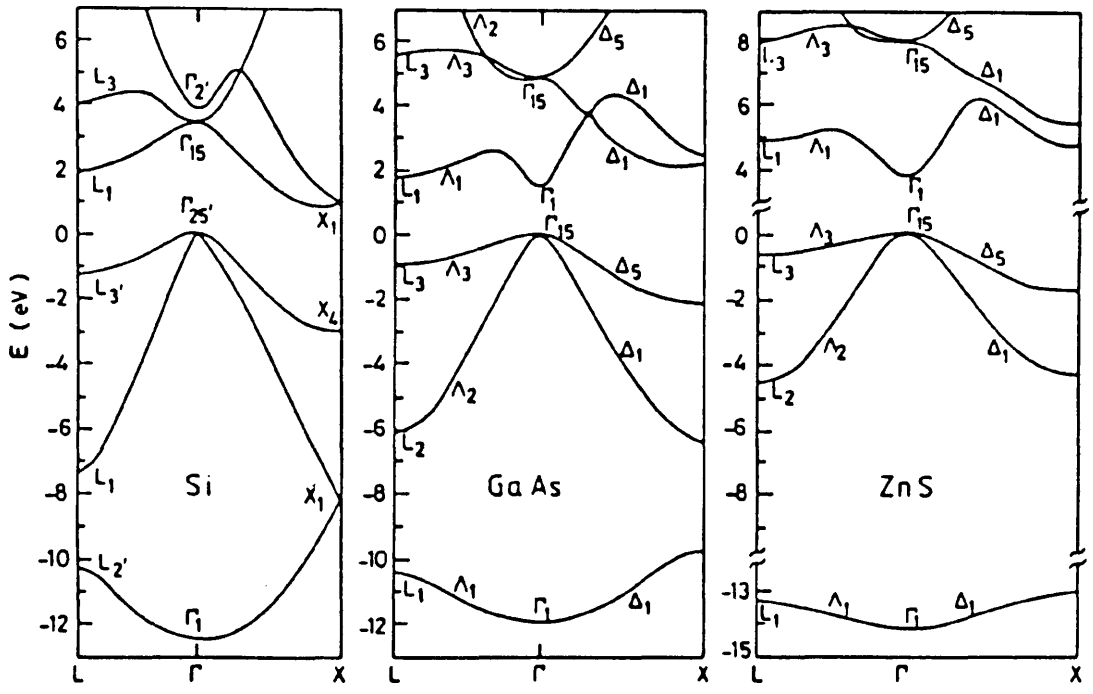

Figure 1.1 E-k reduced zone representations of the band structures of Si, GaAs and ZnS (after reference 1)

The transition at the Brillouin zone centre between the valence band maximum and the conduction band minimum is referred to as the energy or band gap E_g. The value of E_g (and the wavelength of radiation

corresponding to this transition) can range from 0.02 eV to 4.0 eV for II-VI compounds. ZnSe, another Zn chalcogenide with a very similar band structure to ZnS, has a room temperature band gap of 2.7 eV and is therefore a potential material for blue light emitting devices.

The transition at E_g marks the fundamental absorption edge at which point the material absorption coefficient begins to rise steeply. Although E_g is referred to as the band gap, there is in fact a complex variation in the energy of the forbidden gap along different axes in the Brillouin zone, resulting in a number of band gaps with energies > E_g. Direct transitions from the valence band to the conduction band can occur at almost all points in momentum space[2] and will involve energies corresponding to the local band gap. Transitions are particularly efficient where the valence and conduction levels have the same energy over a large range of positions in momentum space, i.e. the valence and conduction bands have parallel branches in the E-k diagram. For regions in the zone where this is true the resulting high density of initial and final states results in a correspondingly high absorption coefficient, many times greater than α at E_g, at which level the band edges are only parallel at the zone centre where $d^2E/dK^2 = 0$ for conduction and valence levels.

1.2 Epitaxial Deposition of Compound Semiconductors

Epitaxy is the name given to the growth of thin films, the crystallographic orientation reproduces that of the substrate on

which they are grown. Homoepitaxial growth is the deposition of a particular material on to an oriented substrate of the same material. (e.g. GaAs on GaAs). Heteroepitaxial growth involves deposition of a film of material B onto a substrate of material A (e.g. ZnSe on GaAs or GaAs on Si).

Epitaxial growth is desirable in the manufacture of thin film devices because an epitaxial film is by definition a single crystal, and the number of lattice defects which could degrade electrical and optical properties is, therefore, minimised by epitaxial growth.

Research effort into high quality epitaxial growth from the vapour is presently concentrated into two main techniques, MOCVD (metalorganic chemical vapour deposition) and MBE (molecular beam epitaxy).

1.21 Molecular Beam Epitaxy (MBE)

MBE is a relatively sophisticated form of vacuum deposition, in which neutral thermal atomic or molecular beams impinge on a substrate under UHV conditions[3]. Elemental sources are generally used and are contained in pyrolytic boron nitride crucibles heated by resistance windings. The vapour species exit from Knudsen effusion cells and the beam intensities are controlled by the cell temperature and the cell orifice area.

Although high purity electronic grade elemental sources are generally used[4] there are no fundamental reasons why compound sources could not be used for the II-VI compounds such as ZnSe which evaporate

congruently[5]. The major constraint is the lower overall purities of compound sources.

MBE has been successful in the growth of ZnSe on GaAs and the best quality (in terms of nature and quality of luminescence and the high electrical transport properties) material grown to date has been produced by this technique[6].

1.22 Metalorganic Chemical Vapour Deposition (MOCVD)

MOCVD has been used to successfully grow high quality III-V and II-VI epitaxial material, and has superseded earlier growth techniques such as vapour phase epitaxy (VPE) because of the several advantages it offers. The process was originally developed for the growth of many III-V, II-VI and IV-VI compounds by Manasevit and coworkers (see review article [7]).

In the case of compound semiconductors the group II or group III metal is delivered to the substrate in the form of a metal alkyl, transported in hydrogen (usually) as a carrier gas. The group V or VI element is usually transported as a hydride, i.e. AsH_3 or H_2Se. In the case of ZnSe, a common combination is dimethylzinc and H_2Se, the overall reaction being given by:

$$(CH_3)_2Zn + H_2Se \rightarrow ZnSe + 2CH_4$$

although the specific details of the reaction mechanisms are not fully understood. The formation of the desired compound is often

described as the pyrolysis of the metalorganics and hydrides followed by the subsequent recombination of the atomic and molecular species at or near the heated substrate, but a number of mechanistic pathways are probably involved.

There are three main reasons why MOCVD has progressed to become an established growth technology:

1. As all the constituents are in the vapour phase, their partial pressures can be accurately controlled, giving precise control over composition, thickness and stoichiometry.

2. It is the most flexible of all the epitaxial techniques in that virtually all III-V and II-VI compounds and alloys can be grown. Using computer controlled gas exchange systems, very thin, complex multilayer heterostructures comparable in quality to those produced by MBE can be fabricated.

3. The process appears to be the easiest of the available epitaxial technologies to scale up to production volumes and is currently in use as a production technology[8].

The MOCVD technique operated at reduced pressure has been shown to result in improved interface abruptness, more uniform growth over large substrates, and the reduction of gas phase parasitic reactions which adversely affect the thickness and compositional uniformity of layers.

MOCVD was first applied to the growth of sulphides, selenides and tellurides of zinc and cadmium by Manasevit and Simpson in 1971[9]. This early work was performed using sapphire and alumina substrates, and the resulting layers were therefore not epitaxial. Further interest was prompted in the late 1970s by the work of Stutius[10] and Blanconnier[11] on the heteroepitaxial growth of ZnSe. A review by Mullin et al[12] describes advances in the field prior to 1981. The developments since then have been reviewed by Wright and Cockayne[13] and most recently by Mullin et al[14].

1.3 Laser Radiation and Materials Processing

All applications of the laser make use of one or more unique features of a laser beam, whether coherence, high intensity, minimal divergence or very narrow bandwidth. When quantifying forms of energy in terms of degree of order or coherence, heat in the form of random atomic or molecular motion ranks low, whereas the coherent, spatially defined single wavelength output of a laser ranks very highly. For any physical process which needs to be driven by an activation energy or enthalpy change ΔH, heating is the most inefficient way of achieving this because all the lower energy modes of a system have to be driven until $\Delta H \sim kT$ is reached, as a consequence of the establishment of thermal equilibrium in the system[15]. Directed energy processing, whether electron, ion, or laser beam can be much more efficient at triggering physical processes when the enthalpy is much greater than kT, depending on the particular mechanism of interaction of the beam and system. Electromagnetic radiation, and laser radiation in particular, can be highly efficient and selective in activating a process requiring an energy $\Delta H \approx h\upsilon$. This could, for example, be a transition to an electronic excited state resulting in photolytic decomposition of a molecule, or generation of an electron-hole pair in a semiconductor. Radiation enhancement of the process rate will continue as long as the system retains its high energy, non-thermal character, i.e before the energy is scattered into the low-energy modes of the thermal distribution.

1.31 Thin Film Photoprocessing

In the field of semiconductor processing, lasers can be used to initiate thin film growth by providing a flux of depositing species. This can be realised either by cracking precursor molecules or the ablation of solid target material to generate an energetic vapour.

Precursor cracking may be achieved either by photochemical processes whereby radiation initiated electronic transitions lead to molecular dissociation, or by pyrolytic cracking where the laser radiation acts as an alternative heat source.

The field of photon stimulated or assisted MOCVD can, therefore, be broadly divided into two main areas depending on the role the photon source plays in the reaction scheme:

1. Photothermal processes

The photon source (IR or visible laser) acts as an alternative heat source, illuminating the substrate surface. The resulting localised heating leads to the pyrolytic decomposition of precursor molecules, either in the gas phase or when forming an adlayer. This process is analogous to conventional CVD, with the significant advantage that heating is highly localised as a result of the highly spatially defined and intense laser beam, resulting in an appropriately localised deposit. Much research in this category has been directed towards one-step processing of metal deposits, allowing electrical contacts to be drawn directly on to integrated circuits, without the need for conventional several-step lithographic processes.

2. Photochemical processes

Photochemical CVD has received attention because the metalorganic precursors used in conventional MOCVD have strong absorption bands in the 200 nm wavelength region. Absorption of a photon in this region can lead to the severing of a metal-alkyl bond, and depending on the particular molecule the sequential rupture of remaining metal-alkyl bonds. Photo-dissociation of the precursors using radiation where $h\upsilon >> kT$ allows the realisation of a growth process where the substrate temperature can be separated from pyrolytic temperature requirements of a conventional process. The availability of intense light sources in this range, initially UV lamps followed by

commercially available excimer lasers (193, 248 nm outputs), has allowed the experimental study of UV-photon stimulated deposition of several important semiconductor, metal and insulator materials to be conducted. As well as the potential for reducing deposition temperatures, precursor decomposition only takes place in the illuminated region, and as for photothermal processes, spatially defined growth is also a motivation for exploring photo CVD systems.

Within the broad areas of these definitions, there are processes such as UV induced surface heating effects and IR multiphoton molecular dissociation which could come under either category. As well as generating a flux of depositing species, radiation can modify surface kinetics by promoting effects such as molecular desorption and enhanced surface diffusion rates.

1.32 Laser Photothermal Deposition

Laser pyrolysis or photothermal deposition has mainly been applied to direct writing of metal lines for integrated circuit microconnections. Minimum dimensions for deposited structures are defined by the focussed beam dimension. Focussed laser beam dimensions are of the order of 1 μm, although process non-linearities can reduce the deposit linewidths as low as ~0.3-0.4 μm[16]. However, in most cases the linewidth is greater than the beam dimensions and is a function of laser power and the thermal properties of the deposit and substrate. At an argon ion laser power of 100mW and a laser spot width of 2.5 μm the deposit width for Ni from $Ni(CO)_4$ is 50 μm, reducing to 1 μm at 50mW[17]. Very high deposition rates are a feature of focussed laser pyrolysis, in general being a factor of 10^2-10^3 greater than deposition rates obtained in conventional large area CVD systems. The rate increase is attributed to enhanced three

dimensional reagent diffusion to the microscopic reaction zone, as opposed to 2-D diffusion to a semi-infinite growth surface[18]. Metals deposited by thermal routes include W from WF_6, Ni and Fe from $Ni(CO)_4$ and $Fe(CO)_4$[19] and Au from $AuMe(Et_3P)$[20].

1.33 Laser Photochemical Deposition of Semiconductors

Laser and UV lamp photochemical deposition has been used to deposit both elemental and compound semiconductors such as Si, Ge, GaAs, InP, CdTe, CdHgTe and ZnSe. Specific problems which have been encountered by various groups using this technique include vapour phase nucleation and layer contamination by reaction byproducts. These points are mentioned here and also in further detail in the experimental and discussion sections, where the literature is examined in more detail where relevant.

The first reported photo-epitaxial growth of compound semiconductors was by Irvine et al[21] who deposited HgTe on CdTe and InSb substrates. A high pressure Hg lamp was used to photoexcite Hg atoms which were thought to have sufficient energy to dissociate DETe molecules.

CdHgTe was deposited as low as 250° C by Irvine et al[22] using DMCd, DETe and elemental Hg, again using an Hg lamp. Use of hydrogen as carrier gas was found to result in a highly porous polycrystalline deposit whereas epitaxial growth was achieved when helium was the carrier. The proposed pathway was that Hg^* decomposed diatomic hydrogen and the monatomic H was then free to react with alkyls to liberate free Cd and Te atoms, thus increasing vapour supersaturation

and resulting in homogeneous nucleation in the gas phase. No significant difference in carbon contamination levels was found with the change in carrier gas. Epitaxial CdHgTe was deposited by Morris at 150° C using an ArF excimer laser operating at 193 nm, the beam passing parallel to the substrate to avoid heating effects. A high power density was used to photolyse all reactants over a wide area and dust contamination was avoided by using an inverted substrate, such that gas phase nucleated particles fell away from the surface.

The first completely light induced (i.e. no deposition in absence of radiation) epitaxial III-V compound growth was reported by Donnelly et al who deposited InP on (100) InP by photolysis of $(CH_3)_3In$ and $P(CH_3)_3$ at 193 nm at an ambient temperature of 350°C[23]. Material crystallinity and carbon levels were highly dependent on the laser pulse energy density. At about 20 mJ cm^{-2}, amorphous layers were obtained. At levels greater than this polycrystalline layers were obtained up to energy densities of ~100 mJ cm^{-2}, when epitaxial material was obtained. Pulsed laser induced heating of the surface was clearly playing an important role in promoting surface reactions and carbon desorption as temperatures close to the InP melting point were reached during the laser pulses. Outside of the illuminated area carbon incorporation exceeded 40% atomic concentration. At higher pulse energies (~200 mJ cm^{-2}) damage occurred and the deposit became P deficient.

GaAs has been deposited using a variety of photon sources in photothermal and photochemical systems. Roth and co-workers pyrolysed trimethylgallium (TMGa) and AsH_3 using a frequency doubled pulsed Nd-YAG laser (530 nm) to heat the GaAs substrate surface[24].

Epitaxial layers were grown in the irradiated region in the ambient temperature range 360-540° C. Below 480° C the growth rate decreased rapidly in the non-irradiated region. Deposition was thought to occur via adlayer pyrolysis in the 1μs after the 3 ns pulse during which the surface temperature fell from 1000 to 500° C. The optimum energy density was found to be 120 mJ cm^{-2}. At 70 mJ cm^{-2} the deposit was coarse and polycrystalline, and at 150 mJ cm^{-2} and above damage occurred to the substrate.

Putz et al used a low pressure Hg lamp to deposit GaAs by photolysis of AsH_3 and both triethylgallium (TEGa) and TMGa[25]. Radiation induced contributions to the growth rate were greater for the methyl compound than the ethyl, possibly a direct consequence of the lower Ga-C bond strength for the latter molecule. Morphological improvements under irradiation were noted.

Donnelly et al used an ArF excimer laser to deposit GaAs by photochemical dissociation of TMGa and AsH_3 at 193 nm[26]. Unlike InP, epitaxial growth was not achieved even at 400°C ambient temperature and 70 mJ cm^{-2} beam energy densities. There was no deposition in the absence of radiation. Carbon was found in the film at levels of 1-3 at. % and was thought to suppress epitaxial growth. The higher Ga-C over the In-C bond strength was blamed for the high C incorporation.

A number of workers have used Ar ion lasers to achieve large enhancements of GaAs MOCVD growth rates[27,28] by surface illumination of the substrate. It was not believed that pyrolytic effects were responsible for the growth rate enhancement and the 514.5 nm Ar ion

laser line does not overlap the gas phase absorption regions of TMGa, TEGa and AsH_3 spectra[29]. Further discussion of these results and their relevance to this study is presented in section 3.72.

1.34 Photochemical Deposition of Zinc Selenide

Photodeposition of zinc selenide was first reported by Johnson and Schlie[30], who deposited poor quality polycrystalline material of irregular morphology using a low power Hg lamp to dissociate DEZn and DMSe. Again using an Hg lamp to photodissociate DEZn and DMSe, Ando et al deposited ZnSe, with epitaxial material produced at ambient temperatures above 450° C. At these temperatures the photon source was enhancing the growth rate of the thermal process. Recently Shinn et al have reported deposition of ZnSe on (100) GaAs by dissociation of DMZn and DESe with 193 nm radiation from an ArF excimer laser[31]. The substrate surface was not directly irradiated. Using this configuration epitaxial growth at 200° C was claimed although no evidence was produced to support this. Growth rates stayed constant at ~1 μm $hour^{-1}$ over the range 200-400° C, above which a pyrolytic contribution increased the deposition rate.

Fujita and coworkers have deposited ZnSe and ZnS by photolysis of DMZn, DMSe and DMS using a Xe arc lamp[32]. The wavelength dependence of the growth rate was studied and was found to increase sharply at wavelengths corresponding to the band gap energies of both compounds. This result, which suggests that surface electronic processes were contributing to film growth is described in more detail in sections 3.7 and 3.8.

1.4 Plasma Deposition

A primary motivation for exploring thin film growth from a plasma is the potential for enhancement of film properties owing to the depositing species being energetic ions rather than thermal atoms. Some of the ways by which energetic species can do this have been known for some time[33]. These include :

1. reduced epitaxial growth temperature
2. increased dopant incorporation
3. crystalline phase selection through preferential bond formation
4. enhanced interdiffusion of ions
5. metastable compound formation

Depending on the energy range of the ions involved, different ion-surface interaction processes can be activated. Ions with energies < 1 eV can only activate the surface migration of adatoms. Ions in the 1-20 eV range can activate the desorption of impurity atoms and also produce activated growth centres. Increasing energies can increase interaction effects between ions arriving at the surface and the substrate (trapping or sticking), the displacement of adjacent atoms on the substrate, sputtering, and implantation at the highest energies. These effects are summarised in figure 1.2 .

The majority of plasma deposition investigations have used noble gas plasmas to generate source ions from a target (sputtering) and stimulate film growth. Marinov[34] investigated effects of 1-10 KeV ion bombardment on the vacuum deposition of Ag on glass. He found an increase in nucleation rate due to enhanced adatom mobility, and an enhanced preferential crystallographic orientation, suggesting

potential for epitaxial growth. It was also found that an ion bombardment pretreatment of an NaCl surface increased subsequent nucleation rate of Ag by the creation of active sites.

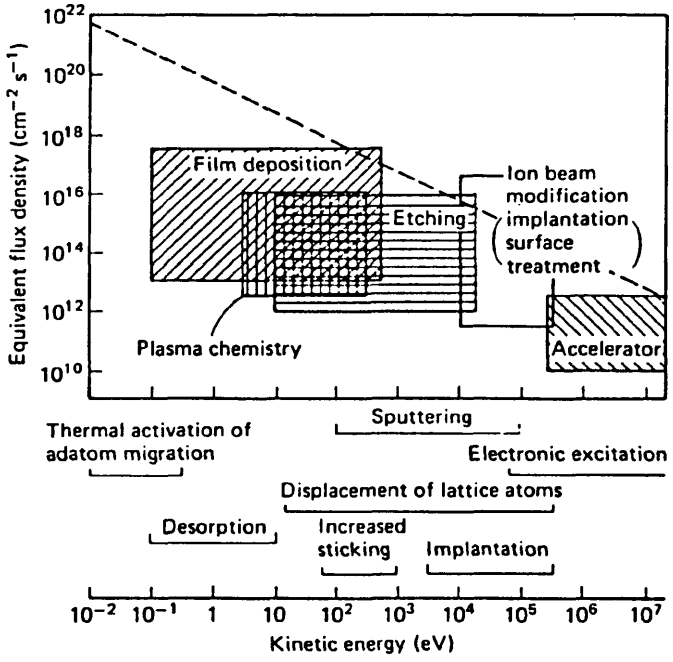

Figure 1.2 Ranges of kinetic energy of incident atoms and physical processes that can be activated (after reference 35)

Bombardment by 150 eV Ar ions has been used to enhance the thermal desorption of carbon and oxygen from GaAs at low (300°C) temperatures[36]. Epitaxial films of α-Sn have also been grown on Ar ion cleaned CdTe and InSb substrates at temperatures well above the ß-Sn transition point[37]. The study of accelerated ions of Zn, Sb, As or Ga in MBE has shown that an increase in sticking coefficients results in an increased incorporation of these elements into epilayers of GaAs or Si, allowing superior control over doping[38,39,40]

The enhanced sticking coefficients of sputtered ions allowed Cadien and coworkers[41] to deposit metastable $(GaSb)_{1-x}Ge_x$ at all points of the pseudobinary phase diagram by co-sputtering of multi-targets.

Post ionisation of thermally generated molecular and atomic beams has also been used to provide a flux of ionised source atoms. Krikorian and Sneed[42] investigated the deposition of Ge via ion beam sputtering and thermal evaporation on to a variety of substrate materials. They found that the nucleation rates increased markedly with particle energy, again indicating enhanced surface diffusion rates.

It is known that during film growth from rapidly depositing atoms, the slower the incorporation of adatoms into the lattice, the less perfect the resulting film. The time required for incorporation of atoms increases with a decrease in substrate temperature according to the relation exp(-W/kT) where W is an activation energy[43]. Thus for every deposition condition there is a temperature below which epitaxial deposition cannot be obtained at any growth rate. The use of energetic ions changes this condition because the temperature of the depositing species is now separated from substrate temperature.

Shimiza and Komiya[44] demonstrated the potential of ion assisted deposition for reduced temperature epitaxy by depositing epitaxial Si on Si(100) at 300°C, a reduction of 100°C over the usual growth temperature. The temperature needed for epitaxy was found to decrease linearly with an increase in the fraction of source atoms ionised. A maximum of 7% ionisation was possible with post ionisation of thermally generated Si.

Mechanisms of growth can also be altered with increasing ion energy. It has been shown when growing Ge homoepitaxial films that three dimensional growth islands can be eroded by 500-1000 eV ion bombardment and deposition constrained to 2D growth, resulting in epitaxial films of smoother morphology[43].

In terms of film growth the most useful energy range lies in the 10 -100 eV range, above which the risk of undesirable effects, such as induced surface damage and interdiffusion via generated defects, increases. Physically adsorbed atoms are bound to surfaces at less than 1 eV and chemically adsorbed species at the 1-10 eV range, so kinetic energies in the 10 eV range are suitable for removing impurities or weakly bound atoms from the growth surface.

Less obvious effects of ion assisted deposition have also been considered. Namba and Mori[45] found that in the case of ion deposition of ZnTe on NaCl and ZnTe, the ion flux was only of minor importance in homoepitaxy but played a major role in deposition on NaCl. A mechanism involving reduction of entropy from ionised atoms depositing on an ionic crystal was suggested.

A negative aspect of sputtering via noble gas ions is the presence of an unwanted species that may incorporate in the growing film. It is therefore preferable to use ionised source material. Post ionisation of thermally generated atomic or molecular beams has the disadvantage that complex guns are required and repulsive effects between generated ions result in practical difficulties in forming high intensity ion beams.

1.5 Pulsed Laser Ablation

Pulsed laser evaporation or ablation of solid targets at laser powers of ~ 10^7 W cm^{-2} or above has been shown to result in the generation of highly ionised vapours at high current densities. The irradiated volume is transformed into a plasma expanding away from the target at velocities corresponding to elemental ion energies in the 10^1 - 10^2 eV range. The laser induced vapours are characterised by constituent species consisting of single atoms and ions and low mericity species. The vapour jet is highly directional.

Until recently the number of reported investigations of pulsed laser ablation film deposition have been limited. This is surprising in view of the potential advantages and relative simplicity of the method.

1.51 Si and Ge Deposition

Epitaxial Ge films have been deposited by Sankur and coworkers who used a high power (10^9 W cm^{-2}) pulsed CO_2 laser[46], and Lubben et al, who ablated Ge with a KrF excimer laser (248 nm)[47]. Ion energies in the latter case were 40-100 eV (corresponding to velocities of 1.0-1.6 x 10^6 cm s^{-1}), whereas the CO_2 generated plasma produced ions in the 150-1000 eV (5-6 x 10^6 cm s^{-1}) range. Epitaxial films were produced by both groups at 300°C; the films due to the high energy CO_2 laser plasma were of particularly high quality. Films grown by Sankur and coworkers using a laser plasma nucleation stage

followed by a subsequent thermal evaporation bulk growth were of a higher quality than a completely thermal based deposition, confirming that energetic species can play an important role in film nucleation. Si films have also been deposited by Lubben et al and Hanabusa et al[48].

The deposition of diamond-like carbon films has also recently been demonstrated by Krishnaswamy and coworkers by the laser ablation of graphite[49]. Film material properties (hardness and refractive index) were improved by the novel method of discharging a capacitor into the graphite target synchronously with the laser pulse, to produce a more energetic plasma.

1.52 Compound Deposition

Compound semiconductors deposited by pulsed laser ablation include CdTe[50], CdMnTe[51] and InSb[52] which have been investigated by Bhat and Dubowski. (100) CdTe was deposited on (100) GaAs by vapourisation of a CdTe target with a Q-switched Nd:YAG laser (1.06 μm). CdTe is transparent at this wavelength, but efficient ablation can still take place for nominally transparent materials at high laser powers as non-linear absorption processes can be stimulated, greatly increasing absorption coefficients.

Electrical measurements made on the CdTe laser plasmas exhibited an ion current-laser power dependence of $I \sim P^{2-3}$ suggesting that a multiphoton absorption process was responsible for ablation, as CdTe is transparent at low powers at 1.06 μm.

The CdTe targets exhibited congruent vapourisation, unlike the InSb surfaces which became In rich after repeated striking. Lack of congruent vapourisation necessitates a more complex experimental method. Fresh material must be struck by successive pulses so the plasma and film composition is equivalent to that of the bulk target. This can be achieved by target rotation or scanning of the laser beam across the target surface.

The recent interest in high T_c superconductors has provoked a spate of publications on the laser evaporation of $Y_1Ba_2Cu_3O_x$[53-58] and later compounds such as $Bi_1Sr_1Ca_2Cu_2O_x$[53] and $Ho_1Ba_2Cu_3O_{7-x}$[54]. The recent popularity of pulsed laser ablation for preparing thin films of these ceramic compounds has undoubtedly been helped by the congruent vapourisation properties of the materials, which has allowed uncomplicated experimental procedures to be successful.

1.6 Application of Photochemical CVD and Plasma CVD to ZnSe Deposition

The fabrication of optoelectronic devices such as light-emitting diodes and injection lasers from ZnSe has been hampered by the inability to grow high conductivity p-type material necessary for high quality p-n junctions. The difficulty in obtaining p-type material has traditionally been attributed to self-compensation. When donors or acceptors are deliberately added to ZnSe, electrically active defects of the opposite type are also formed. This is believed to occur because the energy gained by the recombination of

carriers across the band gap exceeds the sum of the enthalpy of formation and ionisation energy of the defect.

The use of MBE and MOCVD has allowed high quality ZnSe to be grown, primarily due to controllability of material stoichiometry with these techniques, improvements in source material purity and also particularly a reduction in growth temperature.

The DMZn-H_2Se prereaction has been advantageous for MOCVD growth in that high pyrolysis temperatures are not necessary for precursor cracking, allowing high quality material to be grown at 280° C, which has also been reported as the temperature for optimum quality MBE grown material (best electrical properties). Native defects become more thermodynamically stable with increasing temperature, and so from this respect the growth temperature should be as low as possible. The GaAs substrates commonly used for heteroepitaxial growth are believed to be a major source of impurity, providing gallium which outdiffuses into the epilayers during growth and acts as a donor (substitutionally on the zinc site). Provided crystallinity could be maintained, a further reduction in growth temperature would reduce Ga diffusion rates.

1.7 Thesis Objective

The aim of this project was to examine the potential of laser photochemical deposition and pulsed laser ablation as a means of preparing ZnSe films on GaAs substrates at low temperatures.

References

1. M. Jaros, Physics and Applications of Semiconductor Microstructures, Oxford Science Publications, (1988).

2. J.I. Pankove, Optical Properties of Semiconductors, chapter 3, p. 35 (Dover Press, New York 1975)

3. K. Ploog, Ann. Rev. Mater. Sci. (11), 171-245 (1981)

4. T. Yao, in The Technology and Physics of Molecular Beam Epitaxy',ed. E.H.C. Parker, 313-345, Plenum Publishing Corporation (1985)

5. Landolt-Bornstein, N.S., Vol. 17b, Springer, Berlin (1982)

6. J.M. Depuyt, H. Cheng, J.E. Potts, T.L. Smith, S.K. Mohapatra, J. Appl. Phys. 62 (12), 4756 (1987)

7. H.M. Manasevit, J. Cryst. Growth, 55 (1), (1981)

8. S.W. Gersten, G.J. Vendura Jr., Y.C.M. Yeh, J. Cryst. Growth, 77, 2861, (1986)

9. H.M. Manasevit, W.I. Simpson, J. Electrochem. Soc., 118, 644 (1971)

10. W. Stutius, Appl. Phys. Lett., 33 (7), 657 (1978)

11. P. Blanconnier, M. Cerclet, P. Henoc, A.M. Jean-Louis, Thin Solid Films,55, 375 (1978)

12. J.B. Mullin, S.J.C. Irvine, D.J. Ashen, J. Cryst. Growth,55, 92 (1981)

13. B. Cockayne, P.J. Wright, J. Crystal Growth, 68, 223 (1984)

14. J.B. Mullin, S.J.C. Irvine, J. Giess, A. Royle, J. Crystal Growth, 72, 1 (1985)

15. J.A. Van Vechten, in Coherent Properties of Semiconductors Under Laser Radiation, NATO ASI conference series vol. 18, p. 430.

16. D.J. Ehrlich, R.M. Osgood Jr., T.F. Deutsch, Appl. Phys. Lett. 39, 957 (1981)

17. D. Bauerle, Chemical Physics, Springer Verlag 39, 166 (1984)

18. D.J. Ehrlich, J.Y. Tsao, in Laser Diagnostics and Photochemical Processing for Semiconductor Devices, p.3 (Elsevier, Amsterdam, 1983)

19. S.D. Allen, A.B. Trigubo, R.Y. Jan, in Laser Diagnostics and Photochemical Processing for Semiconductor Devices, p. 207

20. M. Jubber, J.I.B. Wison, J.L. Davidson, P.A. Fernie, P.John, presented at 4 th BACG Photochemical Workshop, 1989.

21. S.J.C. Irvine, J.B. Mullin, J. Tunnicliffe, J. Crystal Growth **68**, 188 (1984)

22. S.J.C. Irvine, J. Giess, J.B. Mullin, G.W. Blackmore, O.D. Dosser, J. Vac. Sci. Technol. **B3** (5), (1985)

23. V.M. Donnelly, D. Brasen, A. Appelbaum, M. Geva, J. Appl. Phys. **58** (5) (1985)

24. W. Roth, H. Krautle, A. Krings, H. Beneking in Laser Diagnostics and Photochemical Processing for semiconductor Devices, ed. R.M. Osgood, S.R.J. Brueck, H.R. Sclossberg, MRS Symposia Proceedings Vol. 17, 193 (1983)

25. P. Balk, H. Heinecke, N. Putz, C. Plass, H. Luth, J. Vac. Sci. Technol. **A4** (3), 711 (1986)

26. V.M. Donnelly, V.R. McCrary, A. Appelbaum, D. Brasen. W.P. Lowe, J. Appl. Phys. **61** (4), 1410 (1987)

27. N.H. Karam, H.Liu, I. Yoshida, S.M. Bedair, Appl. Phys. Lett. **53** (9), 767 (1988)

28. A. Doi, S. Iwai, T. Meguro, S. Namba, Jap. J. App. Phys. **27** (5), 795 (1988)

29. V.R. McRary, V.M. Donnelly, J. Crystal Growth **84**, 253 (1987)

30. W.E. Johnson, L.A. Schlie, Appl. Phys. Lett. **40** (9), 798 (1982)

31. G.B. Shinn, P.M. Gillespie, W.L. Wilson, W.M. Duncan, Appl. Phys. Lett. **54** (24), 2440 (1989).

32. S. Fujita, A. Tanabe, T. Sakamoto, M. Isemura, S. Fujita, J. Crystal Growth, **93**, 259 (1988)

33. For a review of the range of effects of energetic species in thin film deposition see J.B. Webb, Chemtronics **2** (2), 3 (1987)

34. M. Marinov, Thin Solid Films **46**, 267 (1977)

35. T.J. Takagi, J. Vac. Sci. Technol. **A2**, 384 (1984)

36. P. Oelhafen, J.L. Freeouf, G.D. Petit, J.M. Woodall, J. Vac. Sci. Technol. **B1**, 787 (1983)

37. F.C. Farrow, Thin Solid Films **106**, 3 (1983)

38. F.C. Farrow, Thin Solid Films **80**, 197 (1981)

39. M. Naganuma, K. Takahashi, Appl. Phys. Lett. **27**, 342 (1975)

40. Y. Ota, Thin Solid Films **106**, 3 (1983)

41. K.C. Cadien, A.H. Eltoukhy, J.E. Greene, J. Vac. Dev. **31**, 253 (1984)

42. E. Krikorian, R.J. Sneed, Astrophys. Space Sci. **65**, 129 (1979)

43. L. Aleksandrov, in Growth of Crystalline Semiconductor Materials on Crystal Surface, Chapter 1, Elsevier (1984)

44. S. Shimizu, S. Komiya, 18, 765 (1981)

45. Y. Namba, T. Mori, Thin Solid Films 39, 119 (1976)

46. H. Sankur, W.J. Gunning, J. DeNatale, J.F. Flintoff, J. Appl. Phys. 65 (6), 2475 (1989)

47. D. Lubben, S.A. Barnett, K. Suzuki, S. Gorbatkin, J.E. Greene, J. Vac. Sci. Technol. B3 (4), 968 (1985)

48. M. Hanabusa, M. Suzuki, S. Nishigaki, Appl. Phys. Lett. 38 (5), 385 (1981)

49. J. Krishnaswamy, A. Rengan, J. Narayan, K. Vedam, C.J. McHargue, Appl. Phys. Lett. 54 (24), 2455 (1989)

50. J.J. Dubowski, D.F. Williams, Chemtronics 1 (1), 33 (1986)

51. P.K. Bhat, J.J. Dubowski, D.F. Williams, Chentronics 1 (2), 82 (1986)

52. P.K. Bhat, J.J. Dubowski, D.F. Williams, Appl. Phys. Lett. 47 (10), 1085 (1985)

53. C. Girault, D. Damiani, J. Aubreton, A. Catherinot, Appl. Phys. Lett. 54 (20), 2035 (1989)

54. C.C. Chang, X.D. Wu, A. Inam, D.M. Hwang, T. venkatesan, P. Barboux, J.M. Tarascon, Appl. Phys. lett. 53 (6), 517 (1988)

55. O. Eryu, K. Murakami, K. Masuda, A. Kasuya, Y. Nishina, Appl. Phys. Lett. 54 (26), 2716 (1989)

56. P.K. Schenk, D.W. Bonnell, J.W. Hastie, J. Vac. Sci. technol. A7 (3), 1745 (1989)

57. A. Inam, X.D. Wu, T. Venkatesan, S.B. Ogale, C.C. Chang, D. Dijkkamp, Appl. Phys. Lett. 51 914), 1112 (1987)

58. G. Koren, A. Gupta, E.A. Giess, A. Segmuller, R.B. Laibowitz, Appl. phys. Lett. 54 (11), 1054 (1989)

59. C.R. Guarnieri, R.A. Roy, K.L. Saenger, S.A. Shivashankar, D.S. Yee, J.J. Cuomo, Appl. Phys. Lett. 53, 532 (1988)

60. D.B. Geohegan, D.N. Mashburn, R.J. Culbertson, S.J. Pennycook, J.D. Budai, R.E. Valiga, B.C. Sales, D.H. Lowndes, L.A. Boatner, E. Sonder, D. Eres, D.K. Christen, W.H. Christie, J. Mater. Res. 3 (6), 1169 (1988)

Chapter 2

Development of a Laser Photochemical Deposition System for ZnSe

2.1 Development of experimental configuration

As it was not at first known what experimental configuration would ultimately prove most successful for deposition experiments and in view of the wide variety of experimental configurations used by other workers, it was felt initially that the system design chosen should be one that would lend itself to relatively easy modification and redevelopment. The philosophy of an easily alterable experimental configuration, rather than a rigidly fixed one, led directly to the basic aspects of the deposition system, both in design and method of operation.

A conventional MOCVD system operates at atmospheric pressure and utilises a carrier gas (usually hydrogen) to transport organometallic precursors across the substrate and conduct thermal energy rapidly through the reaction volume to aid pyrolytic decomposition.

As it was not known which pressure range would give the best results, the facility to operate at below atmospheric pressure was felt to be highly desirable. A conventional MOCVD low pressure system relies on controlled precursor transport via a carrier gas and computer controlled mass flow controllers up to a constriction upstream of the reactor, which marks the end of the high pressure region. The reactor volume is exposed to a vacuum pump, and the reactor pressure is maintained in the desired range by automatic operation of an exhaust throttle valve in response to a reactor pressure sensor.

This complex arrangement was not felt to be attractive on grounds of complexity and expense and so it was decided to opt for a very simple system, which whilst having some disadvantages would at least offer operation over a wide pressure range and at the same time obviate the need for a carrier gas, which would allow examination of deposition phenomena in the absence or presence of other gaseous species.

The approach selected was for a system in which the organometallic precursors would be stored in containers under their own vapour. The reactor would then be evacuated to a suitable pressure ($\sim 10^{-5}$ Torr), and then sealed off from the vacuum system, after which the gases would then be independently admitted to the cell using the pressure gradient rather than a carrier gas. Gas entry would be manually controlled by operation of a needle valve until the desired partial pressure as measured by capacitance manometer had been reached, at which point the second reactant gas could then be admitted until the total pressure required had been reached. Laser irradiation of the precursor gases would then begin. After a short period of time the reactor would be evacuated and the process repeated.

It was decided to fabricate the reactor itself out of stainless steel rather than the silica usually used in MOCVD. A silica reactor does not lend itself to radical redevelopment, whereas a stainless steel reactor could be built with flanged ports which could accommodate either windows for radiation entry or fittings for gas entry or pressure measurement devices. The configuration could easily be changed if dictated by operational demands.

This early philosophy of built-in adaptability was vindicated during a difficult and protracted development programme in which the experimental design was modified and reconfigured on numerous occasions before the final successful arrangement was reached.

2.11 Choice of Precursors

The choice of a static rather than flowing system immediately precluded use of the standard DMZn/H_2Se precursor combination as the prereaction that occurs between these compounds make them unsuitable for use in a static system. Rapid reductions in gas phase concentrations of DMZn and H_2Se are observed on mixing the compound vapours at room temperature, together with the appearance of polycrystalline ZnSe deposits on reactor walls[1]. This prereaction is minimised in conventional MOCVD systems by separation of the DMZn and H_2Se reactant flows until the susceptor region is reached[2].

DMZn appeared to be an ideal precursor for photochemical processing. It is a liquid at room temperature and has a high vapour pressure, so transfer to a static cell would be straightforward. The UV absorption spectrum of DMZn exhibits the absorption shoulder at ~200nm typical of many organometallics (figure 2.1) with a high absorption cross section at the 193 nm ArF excimer line of 0.27 $Å^2$, or 16260 mol^{-1} l cm^{-1} absorption coefficient (α_{193}). DMZn had also been used to deposit Zn films by photolysis[3,4] and was therefore an obvious choice.

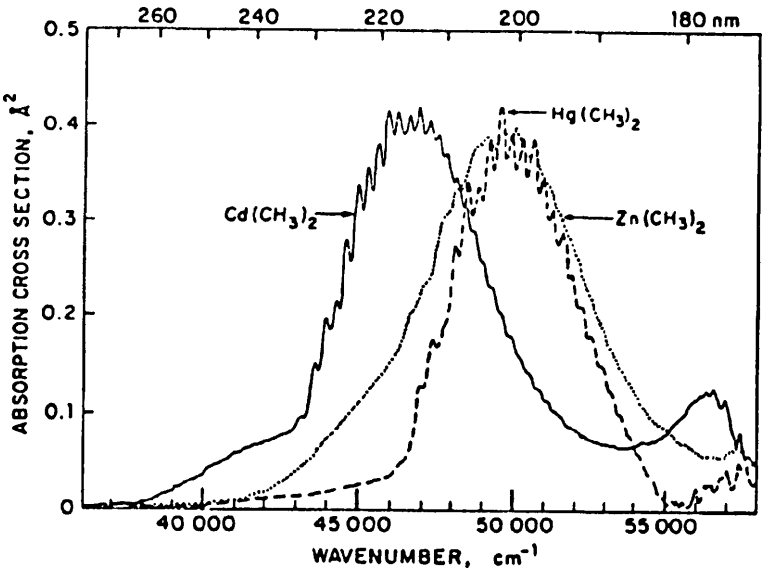

Figure 2.1 UV spectrum DMZn (after Chen and Osgood[5])

The unsuitability of H_2Se as a precursor and the high UV absorption of organometallic compounds indicated that an organometallic Se compound would be a suitable choice. Diethylselenide (DESe) has been used as an alternate Se precursor in some ZnSe MOCVD studies[6,7] and is quoted as undergoing no gas phase reaction with DMZn below 350°C[8], satisfying the requirements for a static system. Assuming that DESe photolysis would be efficient enough to be a useful precursor, the

lack of any prereaction with DMZn meant that deposition experiments could be carried out in the range 20-350°C without any pyrolysis taking place which would otherwise deplete the reactant gas reservoir. Any observed deposition would also unambiguously be due to the effects of UV irradiation. DESe is a liquid at room temperature with a vapour pressure of 15 Torr[9], sufficient for direct entry to the reactor.

2.2 Admittance of Laser Radiation to the Reactor.

Once the outline of experimental method and arrangement had been chosen, one major problem remained, that of admitting laser radiation to the cell for the duration of an experiment. The fundamental problem is of course that as the laser radiation photolyses the precursor gases to generate depositing species. Deposition is just as likely to take place at the window surface as at the substrate, especially as photolysis rates will be highest at the window region because in this area there will have been no appreciable decrease in light intensity due to gas phase absorption.

Because the UV wavelengths required for photolysis result in photon energies much higher than the bandgaps of semiconductor materials, any material deposited on the window will strongly absorb any further laser radiation and the deposition process is rapidly self limiting.

Workers have attempted to overcome this difficulty in a number of ways, the most common being to bleed a purge gas across the window surface to prevent reactant gases from reaching the window itself and

causing deposition there. In a number of cases this has not proved satisfactory[10,11], as any turbulence generated by introduction of the purge stream into the reactor can result in the reactant gases being transported to the window in vortices, with unwanted deposition resulting. Surface selectivity for heterogeneous reactions has also allowed purging to be successful in minimising window deposits in HgTe deposition whereas in the same reactor a CdTe deposit formed more rapidly[12].

In the static system chosen, introduction of a purge gas would have resulted to a continuous change in experimental parameters throughout an experiment, which was unacceptable, and in retrospect it is highly likely that vortice-induced deposition would have resulted anyway.

Other approaches have been to coat window surfaces with low volatility oils to suppress window deposition[13,14]. This has been primarily used with low power density UV lamps with varying degrees of success. An oil coating was not thought to be compatible with the high power density of a laser and could also lead to contamination problems. An ideal solution would avoid the introduction to the cell of nonreactant materials, whether purge gases or oils. Eventually it was decided to pass the beam into the reactor by focussing it a few mm away from the window either externally or within the cell, so that the energy density at the internal window surface would be high enough to remove any deposition due to the preceding pulse and only lose a small percentage of the pulse energy in doing so. The beam profile would then expand downstream of the focal point until it could illuminate the substrate at a sufficiently low energy density to allow deposition.

2.3 Initial Experimental Configuration and Description

The original experimental configuration is shown schematically in figure 2.2.

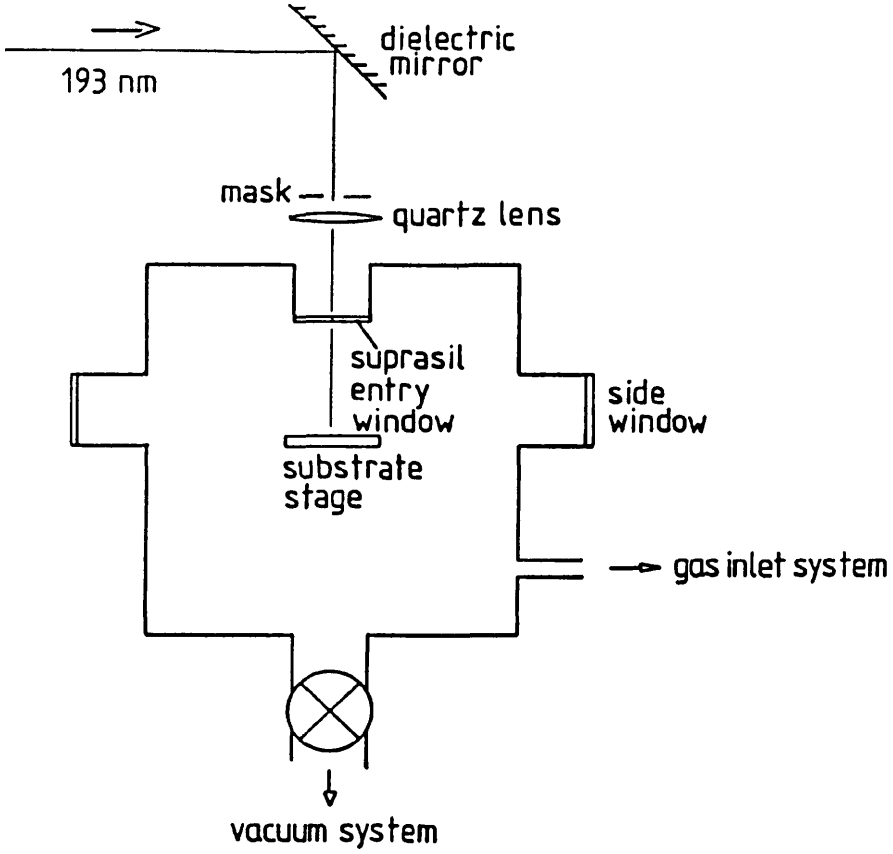

Figure 2.2 Original experimental configuration. For details of gas handling system see figure 2.9. Reactor cap is shown in inverted position adopted to shorten path length (section 2.42).

The apparatus can be broken down into four basic sections:

1. Excimer Laser and Optics
2. Reactor and Sample Stage
3. Gas Handling System
4. Vacuum System

These will now be considered separately.

2.31 EMG 101 Laser

The UV source used throughout this study was a Lambda Physik EMG101 excimer laser. Laser emission is produced through a high voltage discharge plasma in an argon-fluorine-helium gas mixture. Electron impacts in the discharge plasma electronically excite the noble gas molecules which then react with the halogen to produce excimer molecules with lifetimes of a few nanoseconds, which constitute the upper laser level. Following radiative decay to the ground level, excimer molecules dissociate immediately so there is no population of the lower laser level and no ground state reabsorption of the beam.

As a consequence, excimer lasers are termed superradiant and do not actually require an optical cavity to develop a strong coherent laser output, although in practice a cavity is used to improve output quality. Only a small number of passes occur before beam exit from the laser head and the beam is not strongly polarised unlike other laser systems.

The ArF excimer line is 193 nm ($h\upsilon$ = 6.4 eV), and this was used throughout this study although other gas mixtures can be used to vary the wavelength such as KrF (248 nm) and XeCl (351 nm).

The EMG 101 output consists of pulses of nominally 15 nanoseconds duration[15], with a variable operating rate of 0.5 - 50 Hz. Actual pulse energies are quoted as 120 mJ, but in practice maximum energies obtained were of the order of 70 mJ at low rates, the obtainable pulse energy decreasing with increasing operating rate.

Excimer lasers are among the less reliable commercially available lasers, due to the high operating voltages and the corrosive nature of the gases used. The 30 kV discharge in the laser head places a strain on electrical components. Earlier models such as the EMG 101 are prone to failure of the thyratron, a switching element in the high voltage circuit and this in fact failed during use of the laser in this study.

The gas mixture is circulated past the electrodes in the laser head by a large cylindrical fan which rotates in standard ball races. The lubrication in the ball races failed in the corrosive atmosphere, necessitating dismantling of the laser and gas reservoir. Several fan components had seized and required remachining. Exposure of the internal surfaces of the gas reservoir lead to a loss of passivation of areas exposed to the fluorine mix, and after reassembling it took many refills of the gas mixture before an adequate laser output was achieved again.

The output decreased markedly over the course of the experimental programme, possibly due to erosion of the electrodes, to the extent that at a 30 Hz operating rate the maximum pulse energy was 30 mJ, somewhat limiting the range of experiments possible.

2.32 Reactor and Sample Stage

The reactor itself consisted of a stainless steel cylinder with grooved flanges at either end to accept o-rings for vacuum seals. The lower flange was originally clamped onto a baffle valve which

opened onto a diffusion pump. The upper flange o-ring sealed against the reactor cap. Welded in the centre of the cap was a port on which was mounted a 30 x 2 mm Suprasil fused silica window. A collar held the window against an o-ring to form a vacuum seal. In the original experimental configuration (figure 2.2) the ArF laser beam passed vertically through this window to irradiate the sample after reflection from a dielectric mirror.

Four similar ports were positioned at intervals around the diameter of the reactor. As originally envisaged these would act as observation windows or laser windows if the experimental configuration was changed, as eventually happened. A large 5 cm. diameter port in the reactor wall accepted a blanking piece to which was attached the sample stage support arm and electrical leadthroughs for sample heating, temperature sensor and other ancillaries.
A KF10 klein flange was welded to the reactor to which was connected the gas inlet manifold and pressure sensor. Two further connections acted as the inlet and exhaust for flowing hydrogen at atmospheric pressure through the reactor for the purposes of sample pregrowth bakeout.

2.33 Temperature control

The samples were maintained at the required temperature with a resistance heater, consisting of a 0.125 mm stainless steel foil heating element sandwiched between two silica microscope slides. Mica sheets were placed between the element and slides for greater

thermal contact. Another piece of silica acted as the sample support stage. A strip of silica was welded to the sample stage, to which were attached tantalum wire restraint clips. The sample stage was indium bonded to the resistance heater for maximum thermal contact, and held in place with stainless steel spring clips. Samples themselves, either (100) GaAs or microscope slide sections, were indium bonded to the support stage, the Ta wire clips pressing gently at the sample sides, which was necessary to hold the sample in place if it was in a vertical configuration.

Temperature measurement was achieved using a 100 Ω platinum resistance thermometer (Pt 100), which consists of a 2 x 10 mm ceramic plate on to which is evaporated a thin Pt film. The temperature is sensed by measuring increases in the resistance of the film. The shape of the sensor makes it very useful for applications such as this where it is in contact with a flat surface, and there are no spurious thermocouple effects at electrical leadthroughs, as can happen if one side is at a different temperature to the other i.e. during sample bakeout.

The resistance thermometer was indium bonded to a piece of GaAs which in turn was indium bonded to the sample support stage, a stainless steel spring clip holding the arrangement in place. The thermometer was connected to a Newtronics Micro 96 controller, which in turn controlled a thyristor stack in circuit with the variac supplying the resistance heater. Accurate control was possible from room temperature to 600° C.

2.34 Gas Handling system

The gas handling system was very straightforward compared to a conventional MOCVD system. The organometallics DMZn and DESe were both stored in stainless steel bubblers, one arm of which was connected to the gas inlet pipe. DMZn was readily obtainable in a bubbler, but supplier difficulties were continually a problem with regard to DESe. The only form it could originally be purchased in were sealed glass ampules containing 5 cm^3 liquid (Alfa chemicals). To place this in the bubbler, another bubbler body was obtained and one end cut off. A flange was welded to this to accept an o-ring, so a sealing lid could be attached. The lower connection of this bubbler was then attached to a valve placed vertically in place of the redundant dip tube elbow. The entire arrangement was then placed in a glove box which was filled with argon. The DESe ampules were broken and the contents poured into the upper bubbler, which acted as a funnel to the lower bubbler. Once all the material had passed into the lower bubbler, the sealing lid was bolted in place to prevent escape of any residual DESe.

Once both bubblers were installed on the kit, they were immersed in liquid nitrogen for 20 minutes, before opening the bubbler to the vacuum system and evacuating to 10^{-3} Torr. The bubblers were then sealed and the liquid nitrogen bath removed, to leave the organometallic stored under its own vapour.

Whitey valves were originally used but these quickly developed leaks and were replaced with Nupro bellows valves which were found to be vacuum tight and reliable.

Reactant partial pressures were measured with a Baratron capacitance manometer (10^{-3} - 10 Torr range). This instrument was found to be ideal for measuring the reactant pressures as it is insensitive to material properties since it measures absolute pressures, unlike a Pirani gauge which measures ambient thermal conductivity. An Edwards pressure transducer (1-1000 mBar) was also fitted to measure hydrogen pressures during sample bakeout.

2.35 Vacuum System

As stated above, in the original configuration the cell was bolted to a baffle valve directly above a diffusion stack. A Penning gauge was also attached to the baffle valve. An Edwards E2M8 rotary pump was used for roughing and backing. Cold traps were fitted above the diffusion pump and on the roughing line.

2.4 Initial Experimental Programme

Before attempting to deposit ZnSe by the photolysis of DMZn and DESe, the first parameter to consider was the ratio of reactant partial pressures to use. MOCVD experience did not seem useful as a starting point, in view of the fundamentally different deposition processes involved. Assuming that roughly equal atom fluxes of Zn and Se from the photolysed gas volume would generate a ZnSe layer as has been found to be the case in MBE growth of ZnSe[16] and that photolysis of each reactant would be directly proportional to its absorption coefficient at 193 nm, a partial pressure ratio which was the inverse of the absorption ratios of the reactants seemed to offer a reasonable chance of generating equivalent Zn and Se fluxes at the substrate.

2.41 DESe UV absorption spectrum

The UV absorption spectrum was measured in order to obtain the absorption coefficient at 193 nm. A silica cell was connected to the reactor and both were filled to the appropriate partial pressure as measured on the baratron. The quartz cell was then transferred to a UV spectrometer and the absorption spectrum obtained. $Log_{10}\ I_o/I$ values at 0.1 and 0.3 Torr were found to be 0.08 and 0.18 respectively, giving a value of α_{193} of 2800 $mol^{-1}\ l\ cm^{-1}$, or 0.05 $Å^2$ cross section, approximately one sixth the published value for DMZn.

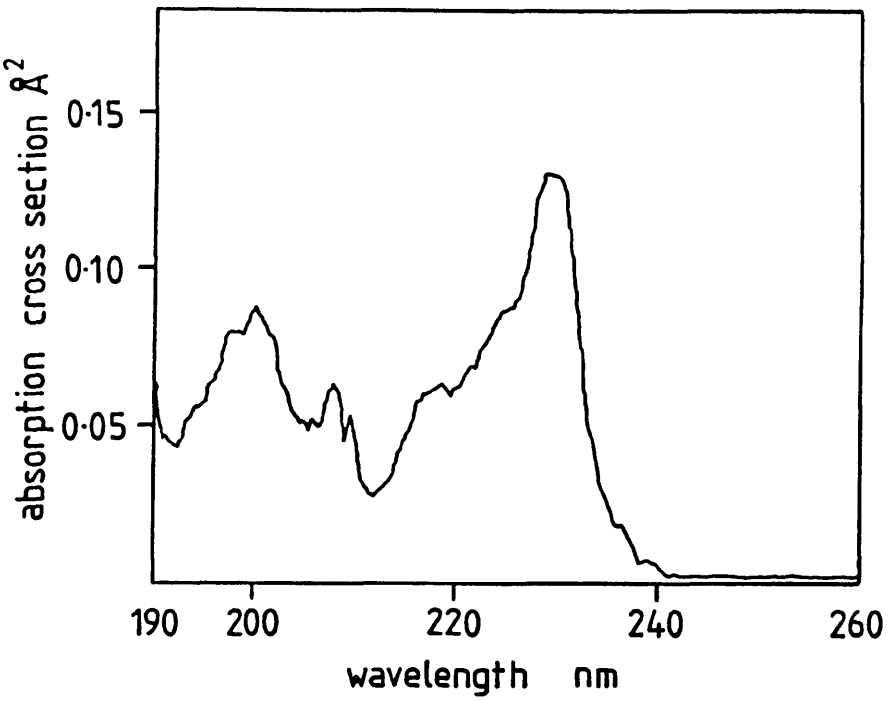

Figure 2.3 The UV absorption spectrum of DESe

2.42 Initial Experimental Results

For the first attempt at layer deposition, reactant partial pressures of 5 Torr P_{DESe} and 0.2 Torr P_{DMZn} were used. The beam was focused above the window to form a 2 x 1 mm image on the window internal surface. The laser was fired for 5 minutes at 5 Hz with a pulse energy of 50 mJ.

No laser induced fluorescence was visible inside the reactor and no deposition was observed on the glass slide substrate. However, a striking deposit was formed on the window around the area defined by the beam profile (figure 2.4).

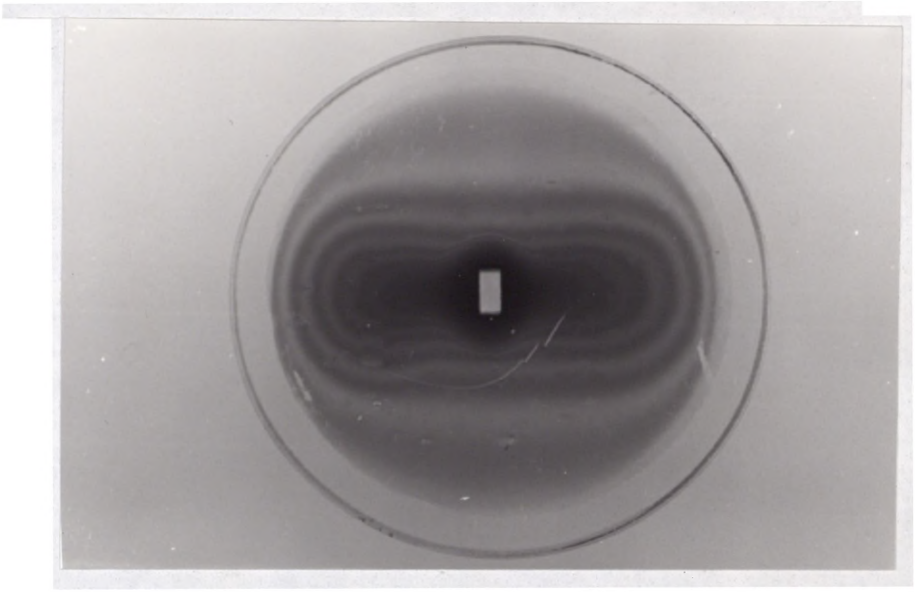

Figure 2.4 Se window deposit. Note elongation of deposit and relation to slot formed by beam.

The deposition pattern did not follow the rectangular beam profile, but instead was extended along the short axis of the beam profile at the window (the profile vertical axis on exiting the cavity). This can be explained as follows:

Although as discussed in section 2.31, excimer lasers are not strongly polarised, the beam was passed into the cell via a dielectric mirror which would result in polarisation, the resulting beam electric vector being aligned parallel with the beam profile short axis.

Two-photon absorption of photolysis generated Se or Zn atoms would result in ionisation (first ionisation energy Zn=9.39, Se=9.75eV)[17].

Any generated ions would interact with the electric vector of the beam and receive extra momentum along that axis, resulting in the extended deposition pattern observed.

An EDAX analysis of the deposited material showed it to be primarily selenium, with any zinc present being below the EDAX detection limit. Interestingly this was not the stable form, 'grey' or tetragonal selenium, which has a semimetallic appearance, but the transparent red monoclinic phase[18].

The lack of any deposit on the substrate or any gas phase fluorescence was attributed to the use of too high a P_{total}, resulting in all the beam energy being absorbed in ablating the window deposit or rapidly absorbed early in the path length.

A series of experiments was undertaken varying all possible experimental parameters. A great deal of trial and error was involved as it quickly became apparent that varying one experimental parameter automatically resulted in others being altered. For example, increasing the reactant partial pressures also resulted in an increase in beam absorption along the path length and a reduction in energy density at the substrate.

A ZnSe layer was finally deposited at the substrate region after decreasing the P_{DESe}:P_{DMZn} ratio to 3:1 and lowering gas phase absorption by both reducing P_{total} and decreasing the path length from 7 to 3 cm by inverting the reactor cap, so the window port protruded into the cell. The energy density at the substrate was also increased by using a different lens of longer focal length to

form a smaller image. The ZnSe deposit grew only in the region irradiated by the beam. Also clearly visible on the glass slide substrate used in the initial experiments was a contaminating deposit of yellow-white dust. The main direction of the project at this point became one of finding an experimental procedure which overcame the particulate contamination, which would be necessary before ordered or epitaxial material could be deposited.

2.5 ZnSe Layer Contamination by Particulate Matter

All the ZnSe layers deposited in the early experimental programme suffered from extreme contamination by micro- and macroscopic 'dust', which proved under EDAX analysis in the SEM to be ZnSe particles. The dust deposits often took the form of streaks radiating outward from the central ZnSe deposit, especially at the 2 Torr P_{total} used for the deposition of the first ZnSe layer.

A Talystep surface profile of the first ZnSe growth is shown in figure 2.5. 'Shoulders' consisting of dust deposits piled at the side of the layer can be seen clearly in the profile.

SEM micrographs of an early specimen deposited on (100) GaAs are shown in figure 2.6 and 2.7. This sample was heavily contaminated with particulates and the resulting granular microstructure is clearly shown in figure 2.7.

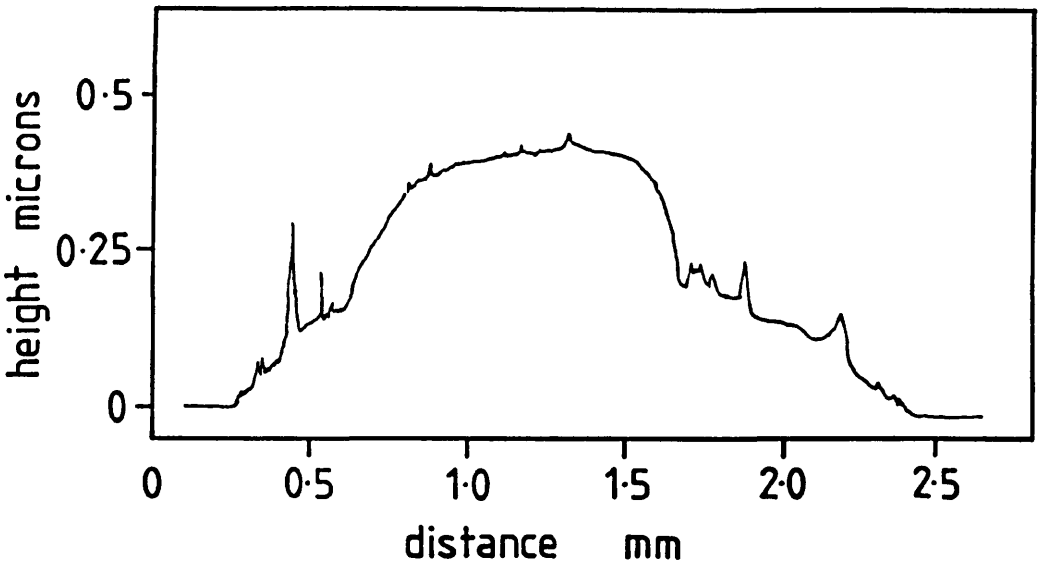

Figure 2.5 Talystep surface profile of original layer. Note 'shoulders' to deposit formed by dust piles.

2.51 Vapour Phase Nucleation

The contaminating particles were thought initially to be formed in the gas phase by homogeneous nucleation processes. Homogeneous nucleation has been reported in a number of photochemical deposition studies. Irvine and coworkers obtained polycrystalline CdTe[19] and CdHgTe[20] as a result of contamination by vapour phase nucleated particles. Fujita et al also observed dust formation in the photolysis of $Cd(CH_3)_2$ and $Te(C_2H_5)_2$ at 193 nm[21] but avoided layer contamination by using an inverted substrate configuration similar to that of Morris[22].

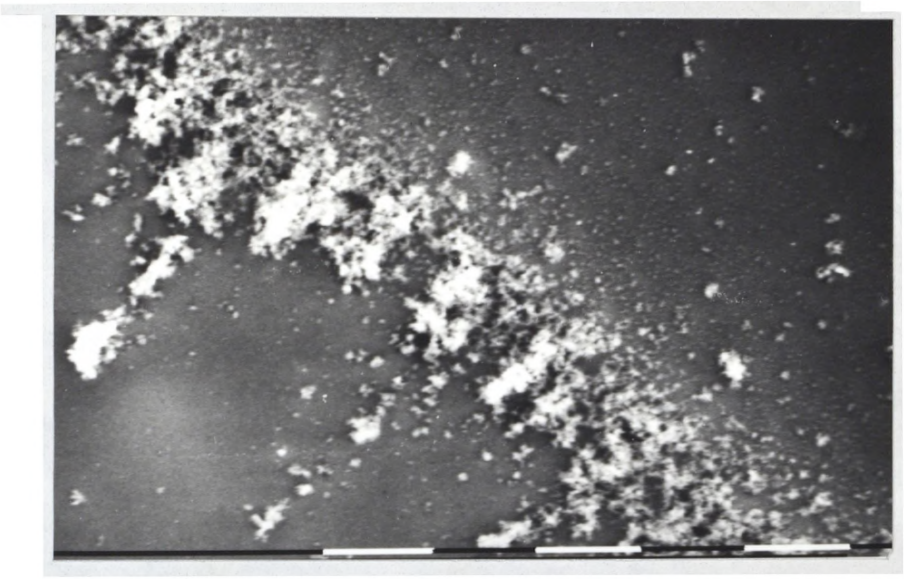

Figure 2.6 SEM micrograph of edge of ZnSe layer photochemically deposited on (100) GaAs. Dust deposits piled at edge of layer are clearly visible (10μm marker)

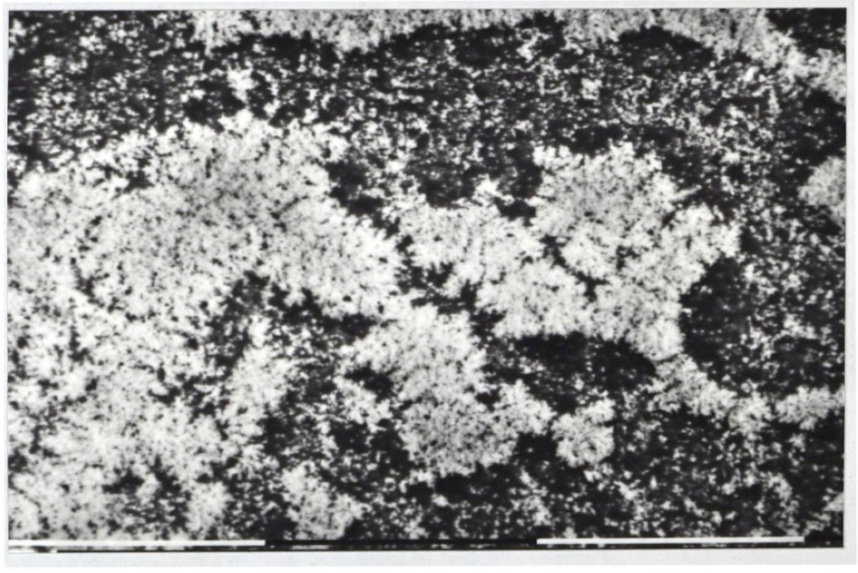

Figure 2.7 Close-up of heavily contaminated region exhibiting coarse granular microstructure (0.1 mm marker)

Efficient photolysis of organometallics at low temperatures can result in high supersaturations and homogeneous or vapour phase nucleation occurs as a result of these high supersaturation levels.

The classical treatment of homogeneous nucleation of a hypothetical nucleus from the supersaturated vapour involves two competing factors. These are a decrease in free energy due to the creation of condensed matter from the vapour phase and a rise in free energy due to the creation of a new surface. The first factor is a volume term and therefore a cubic function, whereas the second is an area term. For a nucleus forming in the gas phase there will be a critical radius above which the reduction in free energy due to formation of solid material is greater than any rise in free energy due to formation of new surface area. Below this critical radius the opposite is the case, and the nucleus must form quickly enough to overcome this nucleation barrier, or it will reevaporate to lower the overall free energy again.

Crystal growth on an already existing solid surface is not governed by the same constraints and can take place under much lower impinging atom fluxes than are necessary for gas phase nucleation.

This treatment indicated that it might be possible to alter the experimental parameters to produce photolysis rates low enough to ensure that only heterogeneous nucleation could take place. In practice this meant lowering laser pulse energies and/or reducing reactant partial pressures. However even by reducing DMZn pressure to as little as 0.03 Torr, and lowering pulse energies to a point barely sufficient to guarantee deposition at the substrate,

conditions for the suppression of dust formation were never reached. As lower partial pressures were used, the observed form of dust deposition altered from radial streaks to an annular ring appearing around the central ZnSe layer. Although the majority of particulates appeared in this ring there was still a high degree of layer contamination.

As flow patterns had been noted in some earlier dust deposits, a magnetically coupled fan was installed in the cell to try and prevent dust falling directly on the substrate, but this proved ineffective.

As it did not appear to be possible to create conditions which precluded dust formation, it was decided to try and observe the gas phase nucleation directly to see if it was restricted to any particular section of the reaction volume or occurred throughout the region above the substrate. If the particulate formation was due to homogeneous nucleation the highest nucleation rates would be found in the region of highest flux generation, i.e. the beam focal region in the section of the photolysis volume directly below the window.

If homogeneous nucleation occurred mainly or was restricted entirely to the most intensely irradiated section of the photolysis volume at the point of beam entry to the cell where supersaturation levels would be highest, it should have been possible to alter the experimental configuration to allow dust to fall away from the substrate rather than towards it.

2.52 Visual Observations of Particle Formation.

In order to determine whether particulate formation was spatially restricted or took place throughout the photolysis volume, direct visual observations were made using a handheld He-Ne laser to illuminate macroscopic particles in the reactor. The beam was positioned to enter the cell through a side window passing just above the substrate and visual observations were made through another side window at right angles to the He-Ne laser beam direction.

Any material which entered the beam was brightly illuminated and it was relatively easy to determine the extent and shape of the dust volume between the ArF entry window and the substrate. The dust was seen very clearly to be falling through the He-Ne beam indicating as expected that it was forming in the upper cell region where photolysis rates are highest.

The majority of the falling particles were observed within an ovoid annular volume centred on the vertical excimer beam, with the extended axis of the relatively dust free central region aligned along the short axis of the rectangular ArF beam profile (figure 2.8).

The elongation of the low dust density region was clearly reminiscent of the deposition profiles observed at the window surface in the initial growth attempts and it was clear that polarisation of the ArF laser beam played a role in determining the geometry of the dust contamination. The most likely explanation at this time seemed to be that ions generated in the intense focal beam regions were

ejected from the photolysis volume in preferential directions as in the case of window deposition. Homogeneously nucleated material would form in a correspondingly ovoid volume, before beginning to fall towards the substrate. Any pressure pulses generated in the photolysis volume would tend to push material further away from the ArF laser beam, forming the dust halos around the layer observed both on the sample and in the gas phase.

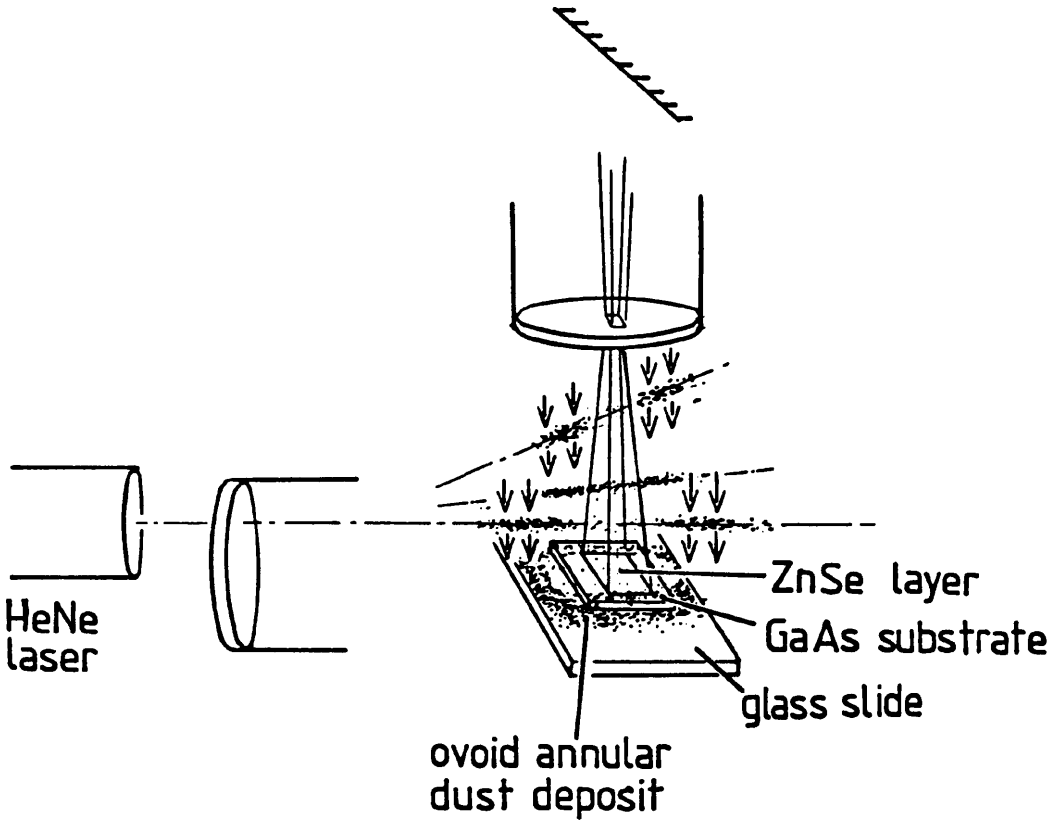

Figure 2.8 Vapour phase particles became brightly illuminated as passed through the He-Ne beam. Arrows indicate observed direction of motion of particles through beam. Particle motion was very apparent, and particles appeared to be falling from upper regions of cell, rather than forming lower down near substrate. He-Ne beam paths 1 and 2 intersected the ArF laser beam, and in these positions a central gap of low dust density was visible. In position 3, passing behind the excimer beam, a continuous line of dust was observed. These observations matched the pattern of the dust deposit on the substrate and glass slide support, with an ovoid region of low dust density centred on the ZnSe layer.

2.53 Horizontal Reactor Configuration

As the direct observations of the dust appeared to confirm that homogeneous nucleation was confined to the upper cell region rather than the entire photolysis volume, this offered the chance to minimise layer contamination by passing the ArF beam into the cell horizontally to strike a vertically positioned substrate. Particles forming in the focal region would then be able fall away from the substrate to the bottom of the cell. An initial experiment was attempted in which the beam was directed by two mirrors to enter a side window, but the combined losses at the mirrors proved too great for this to be practical. The system was therefore reconfigured with the reactor in a raised position to permit direct beam entry through a side window.

A new reactor base was fabricated with a Klein flange connection for an Edwards Speedivalve 25. Stainless steel bellows tubing connected the raised reactor to the vacuum and gas handling system (figure 2.9). Two Speedivalve 10 diaphragm valves were fitted in series to allow the reactor and gas inlet pipes to be sealed and the reactor disconnected from the vacuum and gas handling systems. This allowed the reactor to be taken to a fume hood where sample loading and unloading subsequently took place. Residual adsorbed DESe on the cell walls gave off an unpleasant odour even after reactor purging and evacuating.

Direct observation by He-Ne laser illumination was again employed in order to determine the success of this new experimental configuration in reducing dust contamination.

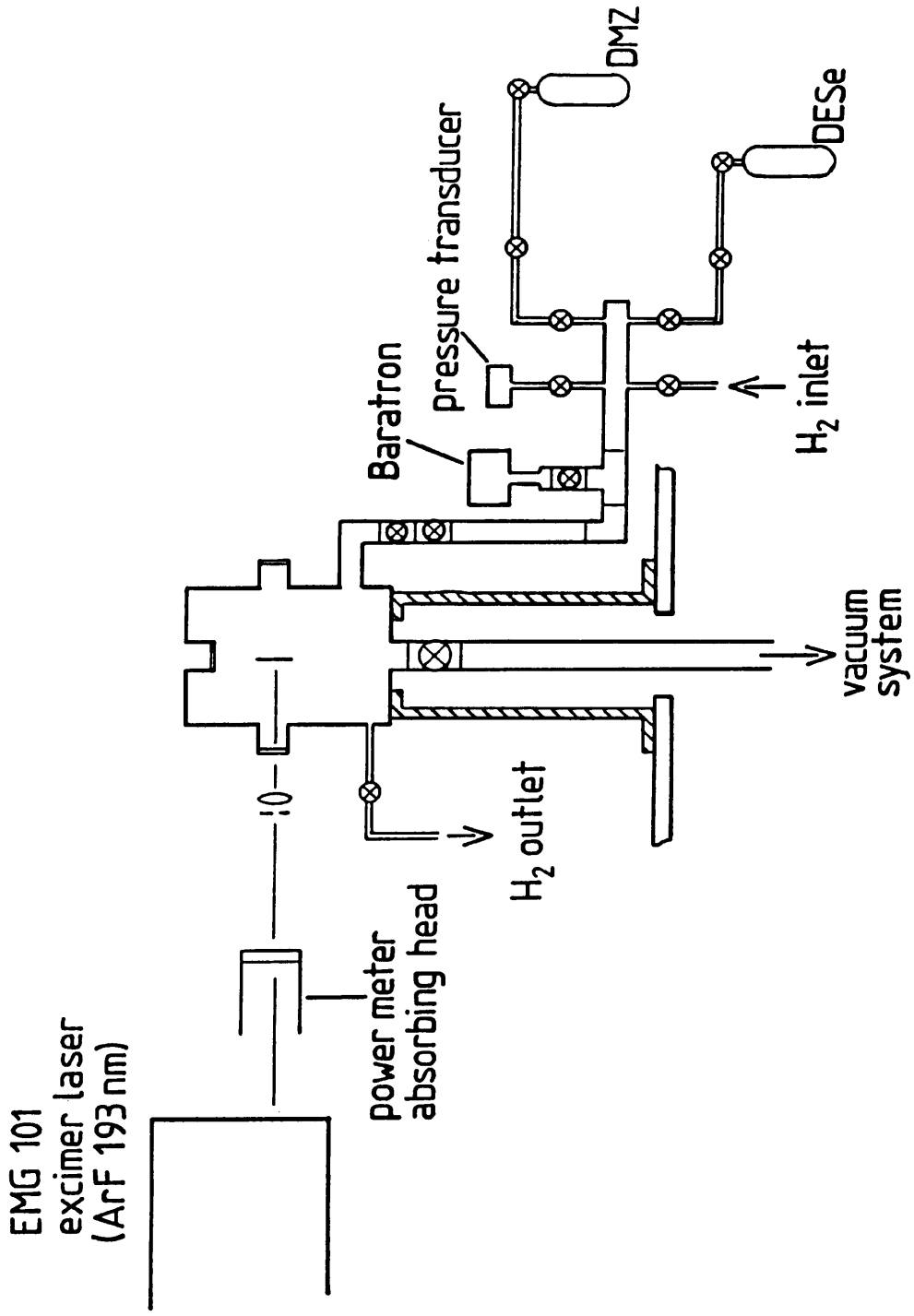

Figure 2.9 Later experimental configuration. Reactor is in raised position relative to laser to allow direct beam entry to cell.

The He-Ne laser beam was directed into the reaction volume through the upper window and visual observations were again made through the side port. It was readily apparent that the entire photolysis region between the laser entry window and substrate was full of particulate material, the dust volume extending almost to the upper window, about 3.5 times the height of the ArF illuminated volume. No central low contamination region was observed unlike the previous vertical configuration, and on removal from the cell the deposition showed severe and uniform particulate contamination around and on the ArF illuminated region.

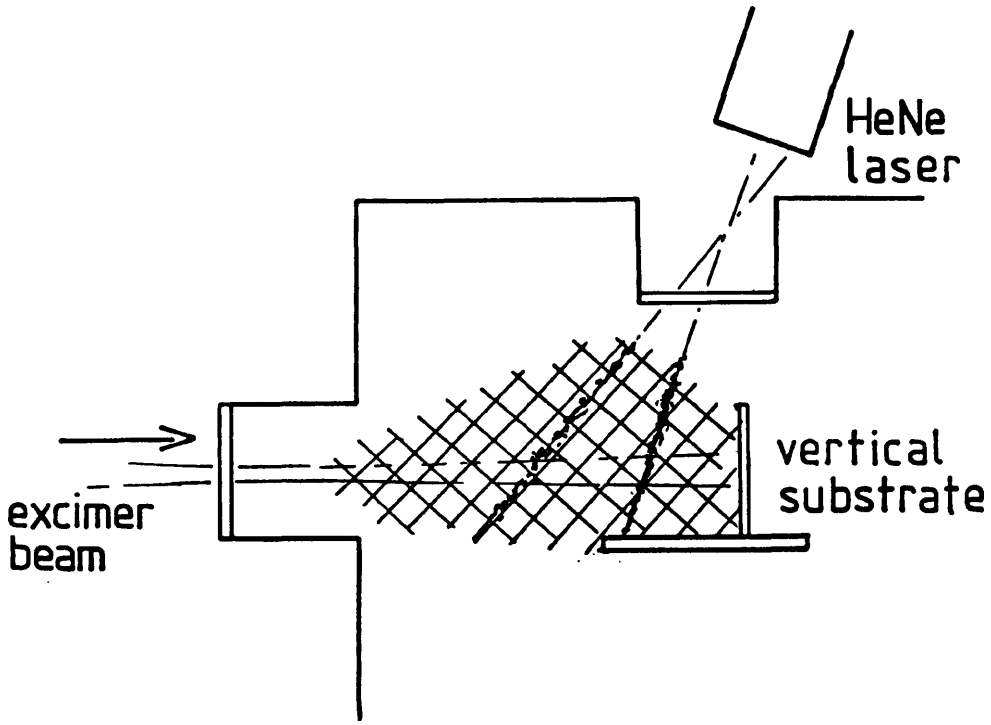

Figure 2.10 Observed dust volume in horizontal reactor configuration. Dust was visible over the cross hatch area (region closer to 193 nm beam entry window and lower cell were not visible through side port) and appeared much denser than in vertical configuration. No central region of low particle density was noted.

These disappointing observations obviously did not support the hypothesis that homogeneous nucleation was restricted to the beam focal region and it was clear that for some as yet unknown reason changing the deposition geometry had adversely affected the contamination problem.

Further attempts were undertaken to observe any change in the extent of dust formation with changes in experimental parameters, and it was during one of these sessions that the true reason for the severity of the particulate contamination was discovered. Whilst making He-Ne laser illuminated dust observations, the ArF beam focusing lens was moved sideways and a large quantity of dust was immediately seen to be generated between the window and substrate.

2.54 Ablation Induced Particulate Formation

The formation of particles in the gas phase clearly had to be a direct consequence of the removal of deposited material from the window by the excimer beam. As the beam profile was moved sideways it contacted the material which was allowed to deposit around the beam profile during the course of the experiment. The realisation that window material was a primary factor in the dust formation allowed the experimental observations to be interpreted in the following way.

Material deposited on the window surface by the preceding ArF laser pulse and subsequently ablated by the following pulse was ejected at high velocity from the window surface directly into the region of

most intense photolysis where saturation levels are highest in the reactor. The ablated particles themselves may have either been sufficiently large to act as condensation surfaces for photolytically generated species, or low mericity ablation products that may have quickly exceeded the critical radius by virtue of a high collision rate resulting from an initially large translational velocity. Whatever the primary mechanism, the gas phase particulate formation appeared to be the result of seeding of the gas phase, or in effect artificial homogeneous nucleation.

In the case of the vertical configuration, the central region of low contamination could now be explained as the result of material ablation into the polarised ArF beam. The highly ionised ablation species interacted with the superimposed beam electric vector resulting in a removal of ablation species from the centre of photolysis volume, forming the annular ring of greatest dust density, the central low density region being extended along the beam electric vector axis. However, in the horizontal beam configuration, the absence of the dielectric mirror meant there were no polarisation effects to aid removal of potential nuclei from the photolysis volume, and the higher power densities at the window may have resulted in higher particle translational energies and higher photolysis rates, compounding the problem and resulting in the severe contamination which was observed in practice.

Now that a coherent theory for the cause of the dust generation had been established, the next step was to use it to develop a practical method of producing a particulate free growth environment.

2.6 Development of an Electrostatic Dust Suppression System

Because experimental observations had shown that as expected material ablated from the window was ionised, the potential appeared to exist for an electrostatic means of suppressing particulate contamination. This route was explored, and a prototype device was made for insertion into the reactor (figure 2.11).The design consisted of a glass envelope of an appropriate diameter to fit inside a window port. Two stainless steel plates (0.5 x 2.5cm) ran the length of the envelope and were separated and supported by two PTFE internal baffles. The baffles were drilled out to a sufficient diameter to allow the laser beam to pass through, and a rectangular slot was cut in the front of the glass envelope to allow the beam to enter the cell.

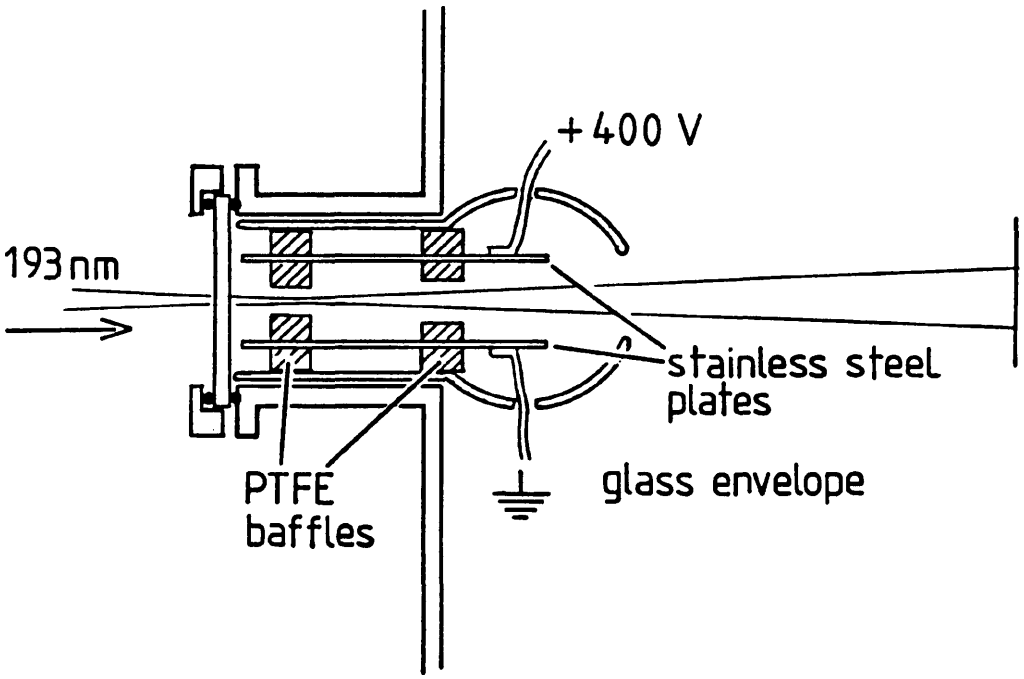

Figure 2.11 Electrostatic dust suppression unit. As ionised particles were projected from the window surface, it was hoped that an applied field across the plates would impart enough angular displacement to the particles to force them into the internal baffles, thus preventing them entering the cell reaction volume.

2.61 Experimental Dust Suppression Tests.

The electrostatic dust suppressor unit was installed in the reactor and connected to a high tension supply. The lower plate was earthed and the upper plate was wired to the positive output. If any positively charged particles did exit the envelope a positive upper plate might still aim them below the substrate region from where any developed dust could fall away without consequence.

He-Ne laser illuminated observations were again made to determine the success of the electrostatic device. Severe dust contamination was again noted in the absence of an applied voltage. The voltage was increased incrementally, and dust was generated in the gas phase until the applied potential reached 400V. At this potential no dust was observed to form in the region between the envelope and the substrate even at high pulse energies and a range of reactant partial pressures up to a few Torr total. Occasional arcing was observed between the plates at 400V, becoming more severe as the potential was raised.

The conditions for avoidance of vapour phase nucleation had now been established and a programme of ZnSe photochemical deposition was carried out. Owing to the relatively long (9 cm) path length in the horizontal reactor configuration, the reactant P_{total} had to be kept relatively low to avoid too high gas absorption levels of the 193 nm beam. The standard conditions used were 3:1 P_{DESe}:P_{DMZn} and a P_{total} of 0.4 Torr.

2.7 Experimental Deposition Procedure

All the layers used for the results section in Chapter 3 were deposited using the following procedure:

1. After the preceding experiment, the reactor was sealed from the vacuum system and gas handling system, before disconnecting from those sections by undoing the appropriate Klein flange connections. The hydrogen exhaust line was also disconnected from the Nupro bellows valve attached to the reactor.

The reactor was then transferred to a fume hood. The cap sealing bolts were undone and air admitted, allowing the cap to be removed. The heater and Pt100 electrical connections were severed and the heater/sample stage removed from the reactor. The heater was then reconnected to a variac in order to melt the In thermal bond and remove the previous sample.

2. The GaAs slice was degreased in refluxing IPA for rinsing in Millipore deionised water (18 MΩ cm^{-1}). The substrate was then etched in 5-1-1 H_2SO_4-H_2O_2-H_2 for 2 minutes, before rinsing again in Millipore water for 5 minutes and blow drying in N_2.

3. A small piece of indium was placed on the heated sample stage. Once the indium was molten, the GaAs substrate was pressed onto the blob and tantalum wire clips were moved into position at the sample edges. The stage was then disconnected from the variac and

repositioned in the reactor. All electrical connections were made and the cell transferred back to the cabinet. The vacuum, gas handling and H_2 exhaust lines were then reconnected.

4. After evacuation of the kit to ensure leak tightness, the vacuum system was closed off and hydrogen admitted to 1200 mBar. The Baratron was sealed off from the reactor to prevent damage occurring due to stress at the elevated pressure. The excess pressure prevented any chance of a suck back from the exhaust bubbler on opening the reactor H_2 exhaust. Once the exhaust line was open, a pure hydrogen flow was established through the reactor. The heater temperature was then raised to 550° C for 10 minutes to remove the substrate oxide layer. After the bakeout the heater temperature was allowed to fall to the required growth temperature under flowing H_2. The H_2 inlet and exhaust valves were then sealed.

5. The Baratron was reopened and the reactor evacuated. Once the cell pressure measured by the Penning gauge had fallen below the minimum Baratron reading (10^{-3} torr) the Baratron was adjusted to read zero. The electrostatic dust suppressor was set to +400 V, and the DESe and DMZn bubblers were opened to the needle valves. The laser was switched on, and brought up to operating pulse rate and power output, as measured on a Scientech 365 power/energy meter placed directly in front of the laser.

6. Once the laser output had stabilised, the reactor was sealed from the vacuum system and 0.3 Torr of DESe were admitted. The DESe pressure usually dropped slightly due to adsorption on the reactor walls, and a small quantity was admitted if necessary to bring P_{DESe} back to 0.3 Torr. DMZn was then admitted to bring the total cell pressure to 0.4 Torr.

7. After a final check on laser power, the shutter was closed and the power meter removed. The shutter was then reopened and laser radiation admitted to the reactor for 2 minutes 30 seconds. This time was chosen because no visible decay in laser induced fluorescence was observed in this time, indicating that there was no major decay in the reactant reservoir. After the irradiation period, the shutter was closed, and the reactor evacuated by roughing via the cold trap followed by opening to the diffusion pump until the Baratron read zero again. Reactants would then be readmitted. The laser power was measured every other gas fill and readjusted if any drift had occurred.

2.8 Material Characterisation Techniques

This section briefly describes the techniques used to characterise the ZnSe layers grown by laser photochemical deposition and also material deposited by the laser ablation technique described in chapter 5 onwards.

2.81 Microscopy

Optical microscopy was routinely used to determine layer thickness. An Olympus metallurgical microscope was used, which had an optional Nomarski interference contrast objective. Layer thickness was determined by cleaving the substrate and examining the substrate -layer interface side on. A calibrated graticule allowed thickness measurements to be resolved to ± 0.2 μm. A sharply detailed interface between layer and substrate was visible and no staining of the layer was required.

For more detailed observations of surface features a Philips 505 scanning electron microscope (SEM) was used. The high magnification and great depth of field of this instrument were invaluable in examining features of small scale and/or high topographic variation. Although all thin films were grown on n-type GaAs, sample charging was noted demonstrating high material resistivity. Conducting carbon coatings were occasionally used to overcome charging on particularly difficult samples. This SEM instrument had an EDAX facility which allowed approximate values of material composition to be established.

2.82 X-Ray Diffraction

Material crystallinity and orientation were measured using X-ray diffractometry. The instrument used was a 'θ-2θ' diffractometer. The sample is rotated with respect to the X-ray source through an angle θ, during which time the X-ray counter is also rotated at twice the rate through an angle 2θ. This arrangement always maintains an equivalent angle between the incident beam and the sample surface and the reflected beam and the surface. Any reflections due to planes of spacing d_{hkl} can only come from those planes lying parallel to the sample surface, so preferred orientation of material deposited on a substrate can be readily determined.

2.83 Dynamic SIMS

Dynamic SIMS (secondary ion mass spectrometry) was used to depth profile ZnSe layers yielding information regarding distribution of impurities through a layer. In particular carbon, which cannot be detected with EDAX, could be examined with SIMS. Because SIMS has a great variation in sensitivity from element to element, and also for the same element in different matrices, standards of known impurity levels must be used for quantitative studies. Standards were not available for this study and, therefore, quantitative information about carbon levels could not be obtained, although trends between different samples could be established.

References

1. J.I. Davies, Ph.D. Thesis, University of Manchester (1985)

2. W. Stutius, J. Crystal Growth **59**, 1 (1982)

3. D.J. Ehrlich, R.M. Osgood Jr., T.F. Deutsch, Appl. Phys. Lett. **38** (11), 946 (1981)

4. D.J. Ehrlich, R.M. Osgood Jr., T.F. Deutsch, J. Vac. Sci. Technol. **21** (1), 23 (1982)

5. C.J. Chen, R.M. Osgood Jr., J. Chem. Phys. **81** (1), 327 (1984)

6. K. Ohmi, I. Suemune, T. Kanda, Y.Kan, M. Yamanashi, Jap. J. App. Phys. **26** (12), 2072 (1987)

7. H. Mitsuhashi, I. Mitsuishi, M. Mizuta, H. Kukimoto, Jap. J. App. Phys. **24** (8), 578 (1985)

8. K. Sritharan, T. Jones, J. Crystal Growth **68**, 656 (1984)

9. Alfa Products Catalogue, Ventron GMBH, W. Germany (1986)

10. S.Rolt, personal communication.

11. P. Balk, H. Heinecke, N.Putz, C. Plass, H.Luth, J. Vac. Sci. Technol. **A4** (3), 711 (1986)

12. S.J.C. Irvine, J.B. Mullin, Chemtronics **2** (2), 54 (1987)

13. H. Ando, H. Inuzuka, M. Konogai, K. Takahashi, J. Appl. Phys. **58** (2), 802 (1985)

14. Y. K. Bhatnagar, W.I. Milne, University of Cambridge, B.A.C.G. Photochemical Processing Workshop presentation (1988)

15. EMG101 operating manual, Lambda Physik, Göttingen (1980)

16. J. Kleiman, R.M. Park, H.A. Mar, J. Appl. Phys. **64** (3), 1201 (1988)

17. Handbook of Chemistry and Physics, CRC press, 54th edition (1973)

18. E.M. Elkin, in Encyclopedia of Chemical Technology, ed. R.E. Kirk and D.F. Othmer, Vol.20, p. 525 (Wiley, New York, 1982)

19. S.J.C. Irvine, J. Giess, J.B. Mullin, G.W. Blackmore, O.D. Dosser, J. Vac. Sci. Technol. **B3** (5), 1450 (1985)

20. S.J.C. Irvine, J.B. Mullin, J. Crystal Growth, **79**, 371 (1986)

21. Y. Fujita, S. Fujii, T. Luchi, J. Vac. Sci. Technol. **A7** (2), 276 (1989)

22. B.J. Morris, Appl. Phys. Lett. **48**, 867 (1986)

Chapter 3

Laser Photochemical Deposition Results and Discussion

3.1 Sample Appearance and Morphology

All the samples grown over the temperature range 25-350°C exhibited a characteristic appearance. The actual 'layer' formed as a rectangular deposit reproducing the beam profile at the substrate. Around this well defined central region was a 'halo' of interference fringes extending 5-10 mm from the irradiated region. This film was not visible in cross section under the optical microscope and could not be measured by Talystep, but the presence and wide spacing of interference colours demonstrates that these films were extremely thin, probably of the order of 100 Å or less. These very thin deposits were formed by photoproducts diffusing outwards from the photolysis volume and as such are the result of purely gas phase deposition.

The edge of the irradiated region was usually well defined and can be seen as the abrupt step in the Talystep profile shown in figure 3.1.

All the layers deposited exhibited specular morphology (figures 3.2, 3.3) and did not exhibit the hazy appearance that is often seen in MOCVD grown ZnSe, which has been attributed to hillocks running parallel to the (110) cleavage plane[1]. A good or improved surface morphology is commonly reported for irradiated growth surfaces[2-4]. Both Hg lamp and 248 nm excimer irradiation have been shown to result

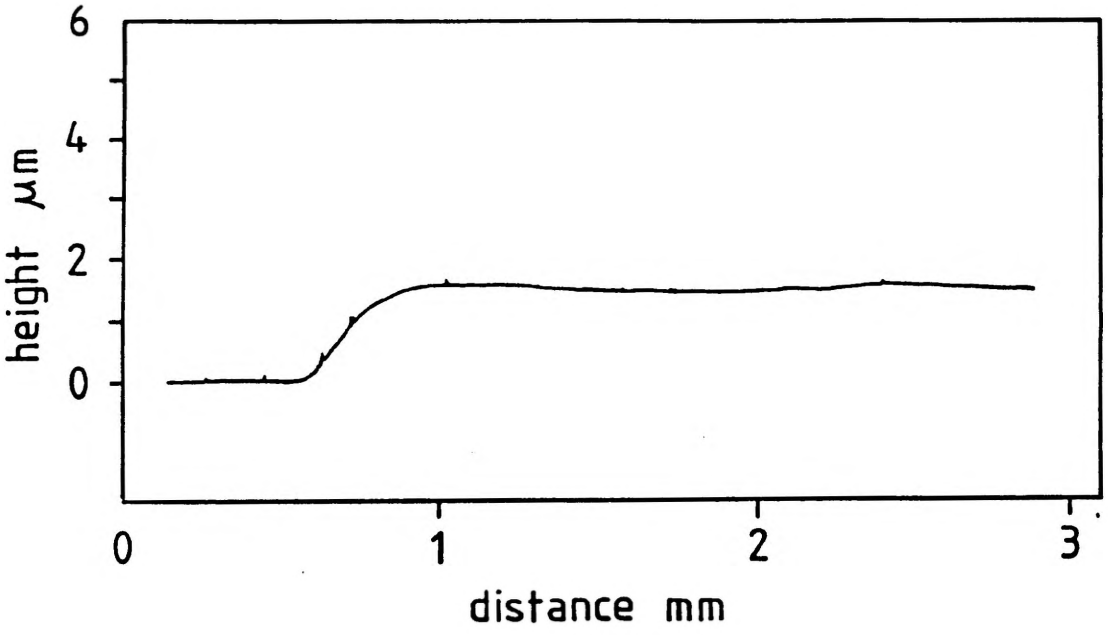

Figure 3.1 Talystep surface profile of photochemically deposited ZnSe layer

Figure 3.2

Figure 3.3

Specular surfaces of photochemically deposited ZnSe shown in Nomarski interference contrast optical micrographs.

in improved surface morphology during molecular layer epitaxy of GaAs[4], and this was attributed to the enhanced migration of adsorbates on the surface.

In the nearest comparable work to this present study, Shinn et al obtained specular ZnSe of excellent morphology at 200°C and above by photolysis of DMZn and DESe at 193 nm[5]. However this was carried out in a parallel illumination configuration with no direct illumination of the substrate. An attempt at growing material at 100°C resulted in a powdery deposit, unlike the specular material which has been obtained in this study at room temperature. The first photolytically deposited ZnSe reported by Johnson and Schlie[6] exhibited a very poor irregular flake/ball morphology, but this material was deposited under very weak Hg lamp illumination.

3.2 Growth Rate Studies

The growth rate in a laser photochemical deposition system will be due to a variety of factors, many of which are interdependent. This problem has already been addressed to some extent in the preceding chapter, where it was shown that the photolysis product flux at the substrate is a function of the reactant partial pressures and the laser energy density at that point, which in turn is a function of path length and reactant partial pressures. Therefore to minimise difficulty in interpretation of the results, all the data presented in this section was obtained at a fixed reactant partial pressure ratio of 3:1 P_{DESe}:P_{DMZn} and a total partial pressure P_{total} of 0.4

Torr. The deposition parameters that were varied were laser pulse energy, laser operating rate and ambient temperature, and experiments were carried out at various combinations of these parameters in order to elucidate their effects on growth mechanisms in a fixed pressure regime.

3.21 Laser Power

Figure 3.4 shows the variation in growth rate with pulse energy at a fixed ambient temperature of 100°C and a fixed laser operating rate of 10 Hz. As growth is initiated by the laser pulses, and is not a continuous process as in a conventional pyrolytic system, growth rates are presented here and generally in terms of the growth rate per pulse rather than growth rate per unit time. This is found to be more instructive in indicating trends in the deposition process. The pulse energy is presented in terms of the energy density at the substrate (E_{ds}, mJ cm^{-2}). These are not calculated values and were obtained experimentally by direct power measurements through a transmission cell, as is covered in detail in Chapter 4. The growth rate plot in figure 3.4 not unexpectedly rises with pulse E_{ds}, and begins to level off at the highest energies.

The layer grown at the highest E_{ds} showed evidence of thermal damage in the form of layer delamination, both from the substrate and within the layer itself. The reduction in growth rate increase may also be the result of the removal of deposited material at the damaging higher irradiances. This is considered further in Chapter 4.

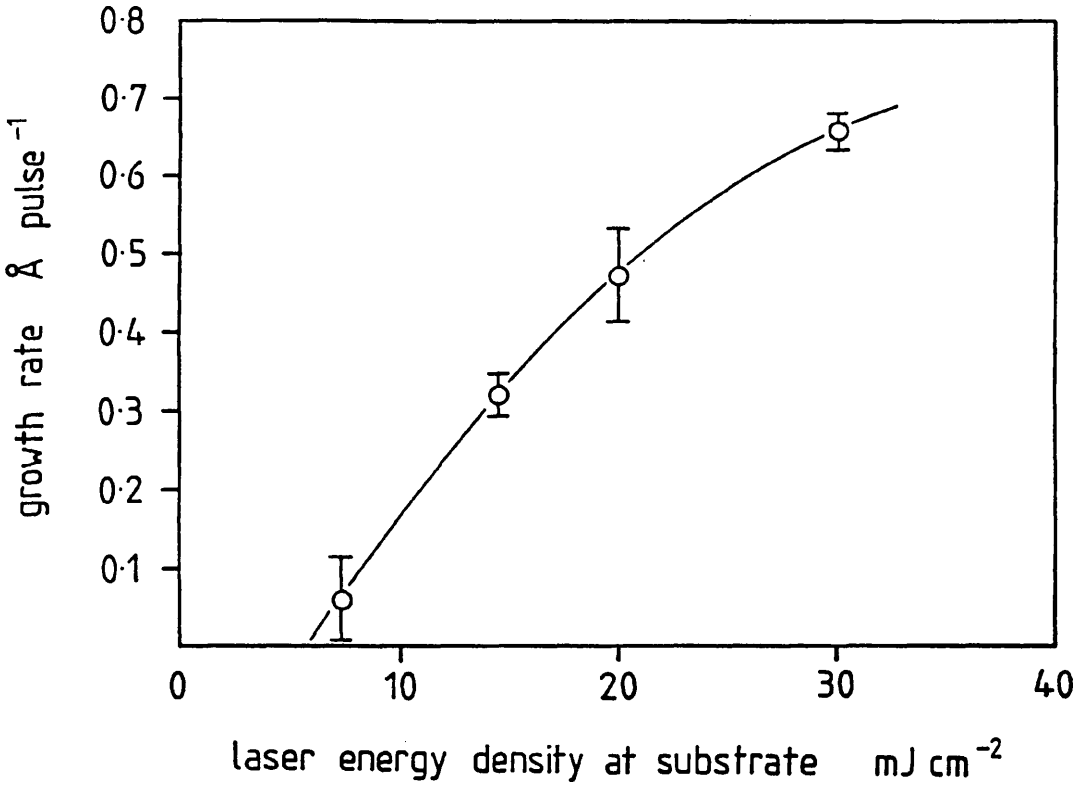

Figure 3.4 Variation in growth rate with pulse energy. 10 Hz laser operating rate and 100°C ambient temperature.

The error bars are calculated from layer thickness measurements assuming a reading error of ± 0.1 μm on the optical microscope. The deposition rate plot does not pass through the origin, but intersects the x-axis at a pulse energy of E_{ds} of ~5 mJ cm^{-2}, which would therefore appear to be the minimum necessary to generate a sufficient photolysis product flux at the substrate for layer nucleation.

3.22 Laser Operating Rate

Figure 3.5 shows the variation in growth rate against laser operating rate at a fixed E_{ds} of 10.5 mJ cm^{-2} and an ambient temperature of 275°C. The growth rate per second is shown and can be seen to rise

overall with operating rate, but when the deposition rate is plotted as Å pulse^{-1}, the opposite trend is displayed. This is indicative of a decrease in available reactants for photolysis, but does not in itself demonstrate whether gas phase or adsorbate layer photolysis is the dominant mechanism.

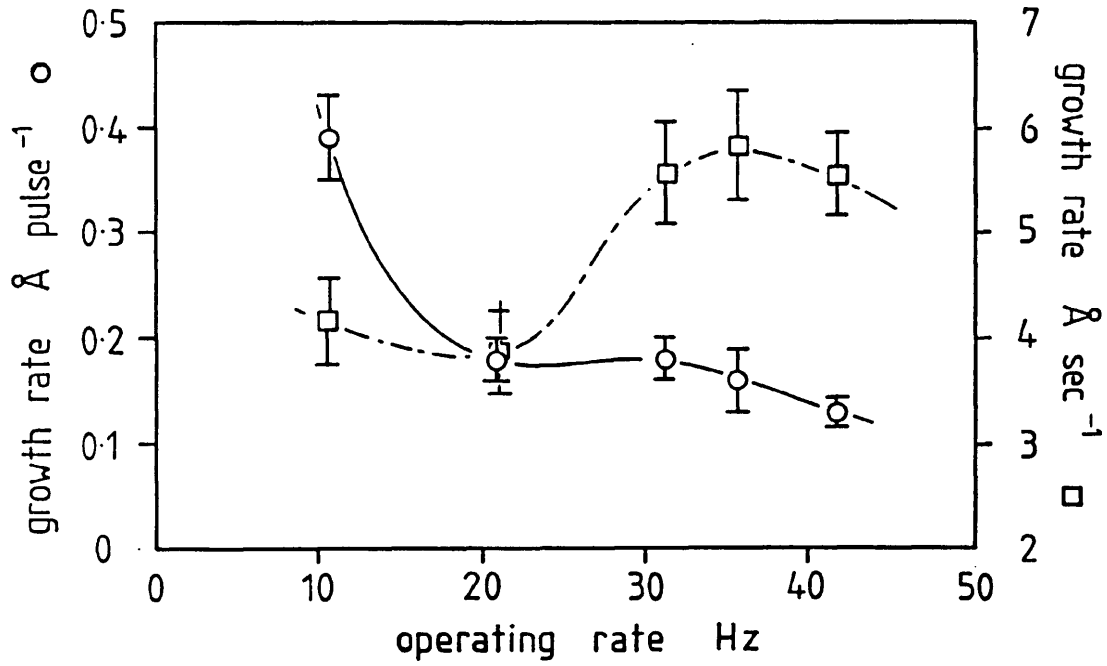

Figure 3.5 Variation in growth rate with laser operating rate. Growth rate in Å s^{-1} shows overall rise, but rate as Å pulse^{-1} shows decline with increasing operating rate.

The decreasing deposition rate per pulse could be due to two factors, either a diffusion rate limit for reactant transport into the photolysis volume, or a decrease in extent of a reactant adsorbed layer again due to reactant depletion or furthermore laser induced thermal effects which will be considered in more detail later.

3.23 Effect of Ambient Temperature

Figure 3.6 shows the variation in growth rate with increasing temperature at a fixed E_{ds} of 14.6 mJ cm^{-2} and 10 Hz laser operating rate. Interestingly, the growth rate does vary with ambient temperature, although the gas phase photolysis rate is

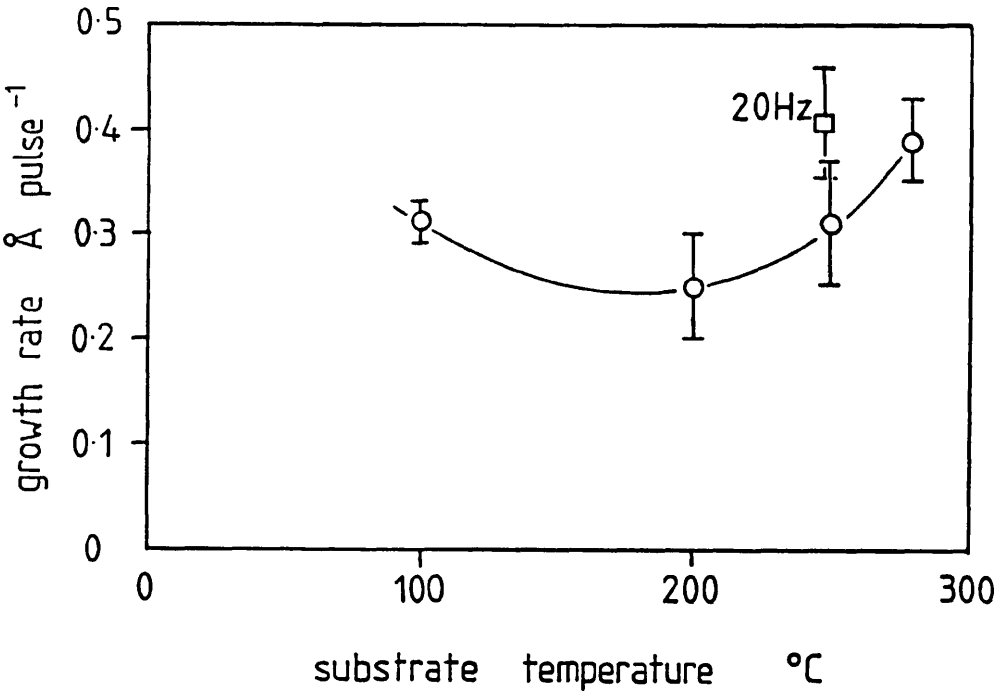

Figure 3.6 Variation in growth rate with ambient temperature

a constant factor and all layers were grown at well below the published value of 350°C necessary for gas phase pyrolysis of DMZn and DESe[5]. A decrease in growth rate is observed between 100 and 200°C, followed by a significant rise between 200 and 275°C. The initial decrease in growth can be explained by the reduction in thickness of an adsorbate layer with increasing temperature, suggesting that adsorbate layer photolysis contributes significantly to the growth rate at least for lower ambient temperatures.

The decreasing trend in growth rate is reversed above 200°C, and any further decrease in the contribution of adsorbate layer photolysis to the overall deposition rate is outweighed by another contributing factor which results in a 60 % rise in deposition rate between 200 and 275°C. As the gas phase photolysis rate should be constant for all temperatures, and the adsorbate layer photolysis rate presumably decreases further in this temperature regime, it would appear that pyrolytic effects were contributing to deposition, although as stated the ambient temperatures were below those normally necessary.

3.24 Pyrolytic Effects

Apparently heating effects caused by the UV laser striking the substrate were raising the surface temperature to the point necessary for pyrolysis. If this is the case, the true deposition temperature is actually the sum of the ambient temperature and any increase due to thermal effects of pulsed UV irradiation. This is consistent with the results in figure 3.6 and would indicate that below ~200°C the increase in surface temperature was not sufficient to result in any significant degree of pyrolysis, but above this point the combined effects of ambient temperature and laser heating were sufficient to drive the local surface temperature above the threshold for pyrolysis. As the laser was pulsed, a thermal response from the material to irradiation would take the form of a rapid heating and cooling cycle following each pulse and the surface temperature would perhaps only be raised above the pyrolysis threshold temperature for a short period following each pulse. As the ambient temperature is

raised, after a laser pulse the material surface would reach a higher temperature and also spend a longer time between pulses above the 350°C pyrolysis threshold temperature, resulting in the increase in deposition rate observed between 200 and 275°C.

As further evidence for pyrolytic behaviour, a data point for a layer grown at 250°C but at 20 Hz repetition rate is included. A 30% increase in deposition rate per pulse is observed, which suggests that the degree of laser induced temperature rise effects, in this case pyrolysis, rises with increasing pulse rate, as was subsequently shown to be the case (see section 4.42).

However, reference to figure 3.5 shows that at a higher ambient temperature of 275°C, this trend is reversed and an equivalent increase in repetition rate results in a decrease in deposition rate. This observation lends further weight to the dominance of adsorbate layer deposition as a primary growth mechanism. Pyrolysis could take place in the gas phase, as in conventional MOCVD, or in the adsorbed layer. If in the gas phase, pyrolysis must be very localised anyway due to the limited heating potential of the very small thermal mass of the layer surface region, as opposed to a massive heated susceptor, and the poor thermal conductivity of the gaseous ambient. Assuming that most pyrolysis is of the adsorbate, laser heating effects would result in increased reactant desorption as well as pyrolysis. Diffusion of reactants into the photolysis volume will be a constant factor for both 20 Hz layers in figures 3.5 and 3.6, so gaseous photolysis and pyrolysis would result in an increase in deposition rate with pulse rate seen in figure 3.6, but not the

decrease seen in figure 3.5.

At the higher ambient temperature the decrease in deposition rate due to an increase of thermally induced reactant desorption appears to outweigh the effects of an increase in pyrolysis temperature.

These results are significant in that they offered the first evidence in this study that laser-induced thermal effects were appreciable and important. This led to the thermal response investigation covered in Chapter 4.

3.25 Adlayer Thermal Desorption

The hypothesis that deposition rate is governed by the combined effects of ambient temperature and laser-induced thermal effects on the extent of adlayer coverage, and subsequent photolysis and pyrolysis, is further supported by figures 3.7 and 3.8. Figure 3.7 shows the variation in growth rate with pulse energy at 275°C at a fixed operating rate of 30 Hz. The deposition rate peaks at ~10 mJ cm^{-2} E_{ds}, decreasing at higher levels. Again this decrease in deposition rate is consistent with the increasing desorption of an adsorbed layer due to the laser heating effects of the higher pulse energies.

Figure 3.8 shows a similar trend obtained by increasing the substrate temperature rather than laser induced heating. Depositions were carried out at a fixed repetition rate of 30 Hz and a pulse energy of 30 mJ, giving an E_{ds} of 7.5 mJ cm^{-2}. In the temperature range shown,

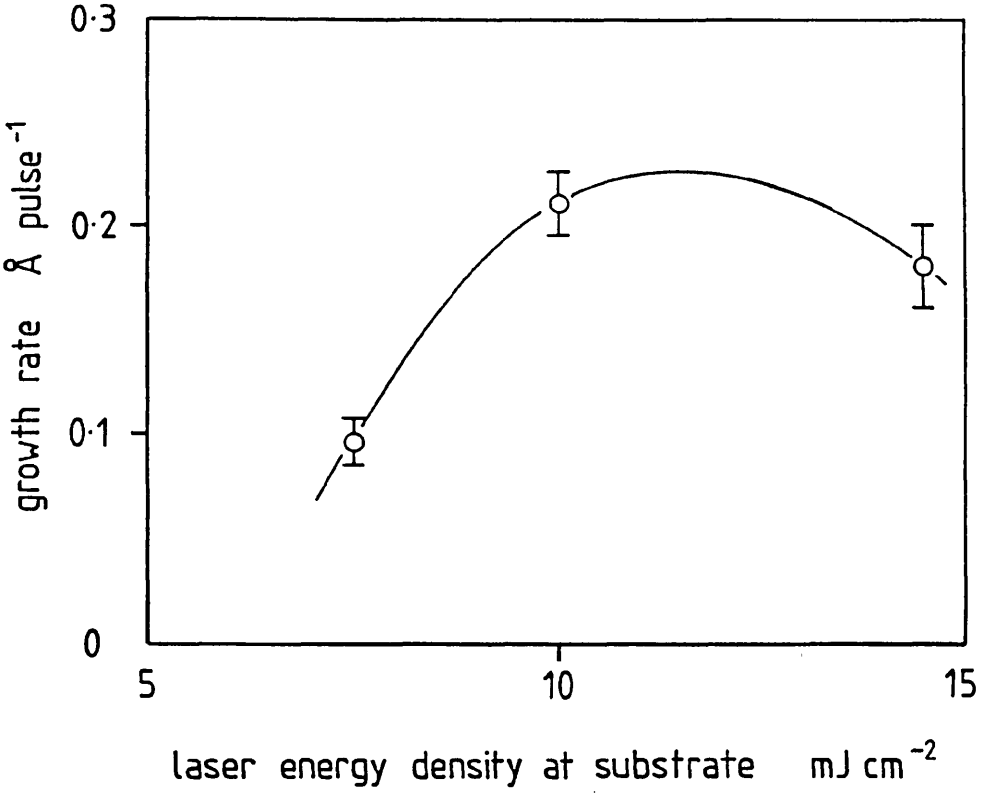

Figure 3.7 Variation in growth rate with laser power. 30 Hz operating rate, 275°C ambient.

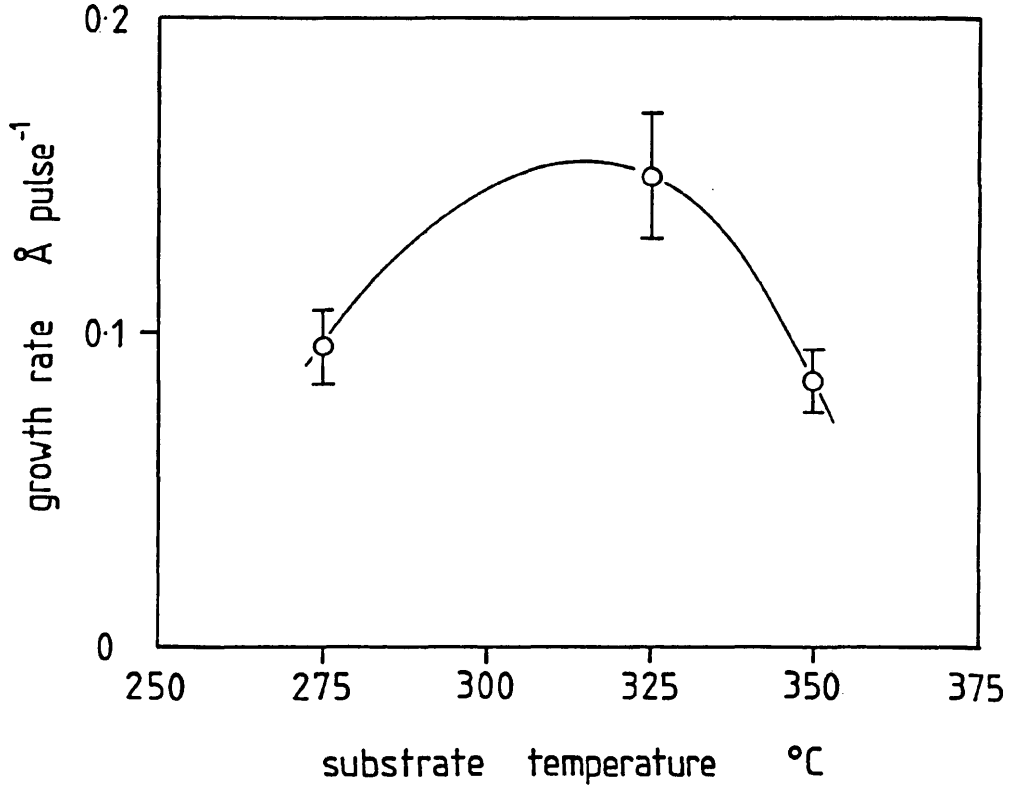

Figure 3.8 Variation in growth rate with substrate temperature, 30 Hz operating rate, 7.5 mJ cm^{-2} E_{ds}.

the growth rate initially increases, again indicative of pyrolytic effects as in figure 3.6, and peaks at 325°C followed by a 40% decrease at 350°C. The increase in substrate temperature appears to have the same thermal effect as the increase in pulse energy in figure 3.7, resulting in an initial increase in pyrolytic deposition followed by an overall decrease in photolytic and pyrolytic deposition due to loss of the adsorbate phase. The overall trends displayed in figure 3.5 also exhibit this behaviour, with an initial large drop in deposition rate as the operating rate is increased, followed by a levelling off as surface temperatures result in some pyrolysis, and then a decline again as adlayer coverage is further reduced.

The dominance of adsorbed layer as opposed to gas phase mechanisms may also explain the difference between the ratios of reactant partial pressures necessary to deposit ZnSe and the ratios of reactant absorption values at 193 nm. As stated in the preceding chapter, $a_{DMZn}:a_{DESe}$ is 30:1, whereas stoichiometric deposition was achieved at a ratio of 3:1 $P_{DESe}:P_{DMZn}$. This partial pressure ratio may not have been reflected in the reactant ratios of the adsorbed layer due to the wide variation in the partial pressures of DMZn and DESe (section 2.1). DESe is far less volatile than DMZn, and would therefore be expected to constitute a far higher percentage of the adlayer composition than the 3:1 gas phase ratio, thus increasing the DESe photolysis rate at the substrate.

3.26 Summary of Contributing Effects to Growth Rate

The growth rate of nominally photolytically deposited ZnSe at a given temperature has been shown to be the sum of three contributing factors, adsorbate layer photolysis, gas phase photolysis, and adsorbate layer pyrolysis, the extent of each depending on the particular experimental condition. The trends these factors are believed to exhibit for the temperature range studied are shown schematically in figure 3.9. The dominant mechanism is deposition from the adsorbed layer, and as the extent of adlayer coverage decreases with increasing temperature, so does the adlayer photolysis rate. At higher ambient temperatures, the sum of the background temperature and laser induced heating in the sample is sufficient to result in some pyrolysis of the adsorbed layer, but further temperature increases result in sufficient desorption to lower the pyrolysis rate.

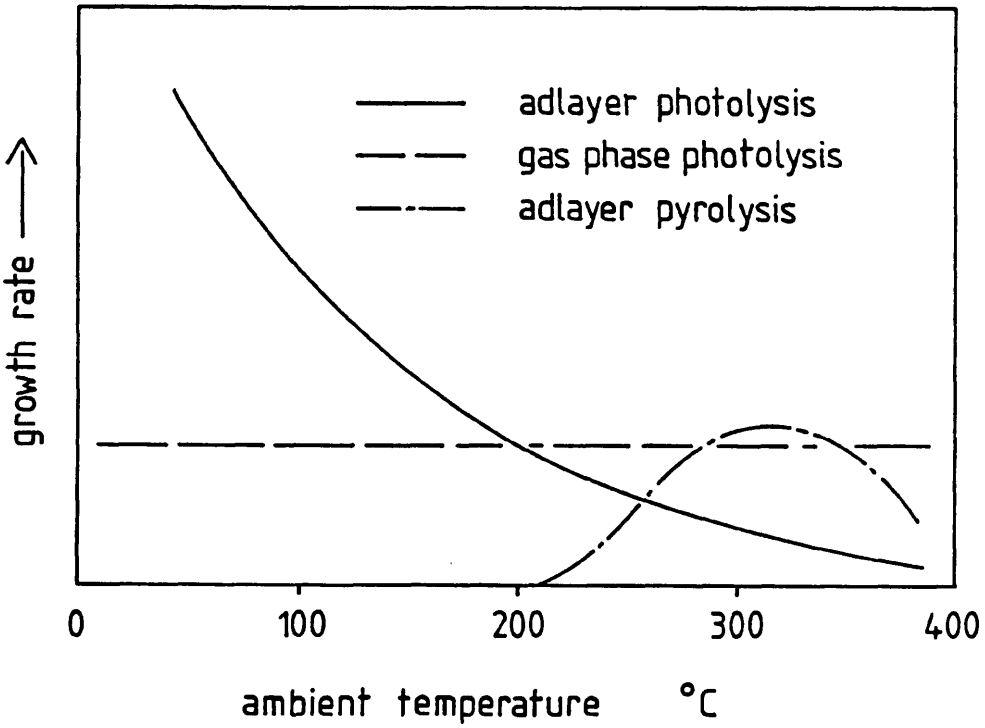

Figure 3.9 Proposed variation with temperature of contributing factors to deposition rate

3.3 Layer Orientation and Crystallinity

All ZnSe layers were deposited on (100) GaAs substrates and were therefore expected to reproduce a (100) orientation. The crystallinity, measured in terms of the full width at half maximum (FWHM) of the (400) reflection, of all the layers grown was found to be disappointing in comparison to MOCVD material deposited at equivalent temperatures from DMZn and H_2Se.

The best quality MOCVD and MBE grown epitaxial material is produced at ~280°C[7], with FWHM (400) values of 0.18 degrees being typical for MOCVD layers[7]. In contrast, epitaxial material was not grown by laser photochemical deposition at this temperature, and FWHM (400) values of ~4-6 degrees were obtained in the 280°C temperature regime, actual values depending on the laser pulse energy/operating rate. No significant improvement was noted in FWHM (400) values for the majority of samples grown at temperatures in the range 25-275°C.

A marked characteristic of many samples grown at 275°C and below is an intense (111) reflection. Reference to the ASTM powder file for cubic ZnSe shows that for a randomly oriented sample the most intense peak (100% I/I_1) is the (111), but the (220) and (311) are also dominant at 70% and 44% I/I_1 respectively. (220) and (311) reflections were observed in some samples but always at lower ratios to the (111) signal than would be given by a random orientation, indicating a preferential (111) orientation.

3.31 Preferential (111) orientation

Figure 3.10 shows three x-ray diffraction patterns for samples A012, 013 and 014 grown at respective pulse energies of 10.5, 20.5 and 24 mJ cm^{-2} and fixed conditions of 150°C and 10 Hz. The ratio of (111)/(400) intensities varies from 0.2 to 20 with increasing irradiance. This can be partially attributed to differences in thickness between the samples. Figure 3.11 shows two layers deposited under equivalent experimental conditions but at different growth times (t_g) of 15 and 45 minutes.

The 15 minute t_g layer exhibits a broad (400) reflection and a weak (111) signal, whereas the second thicker sample exhibits a much more intense (111) reflection.

It is apparent from this result that the initial layer grows reproducing the (100) substrate orientation, but the crystallinity is so poor that eventually any register with the initial (100) substrate orientation is lost to material subsequently deposited. Once the constraint to reproduce a (100) orientation is removed, the layer then grows along the [111] axis, the preferred orientation under UV irradiation. This is clearly demonstrated by depositing on an amorphous substrate, which presents no crystalline order to define the initial layer orientation. Figure 3.12 shows the XRD pattern of a layer deposited on a glass slide, which exhibits an intense (111) reflection. No (400) signal is observed, but slight (220) and (311) signals indicate a small degree of random orientation.

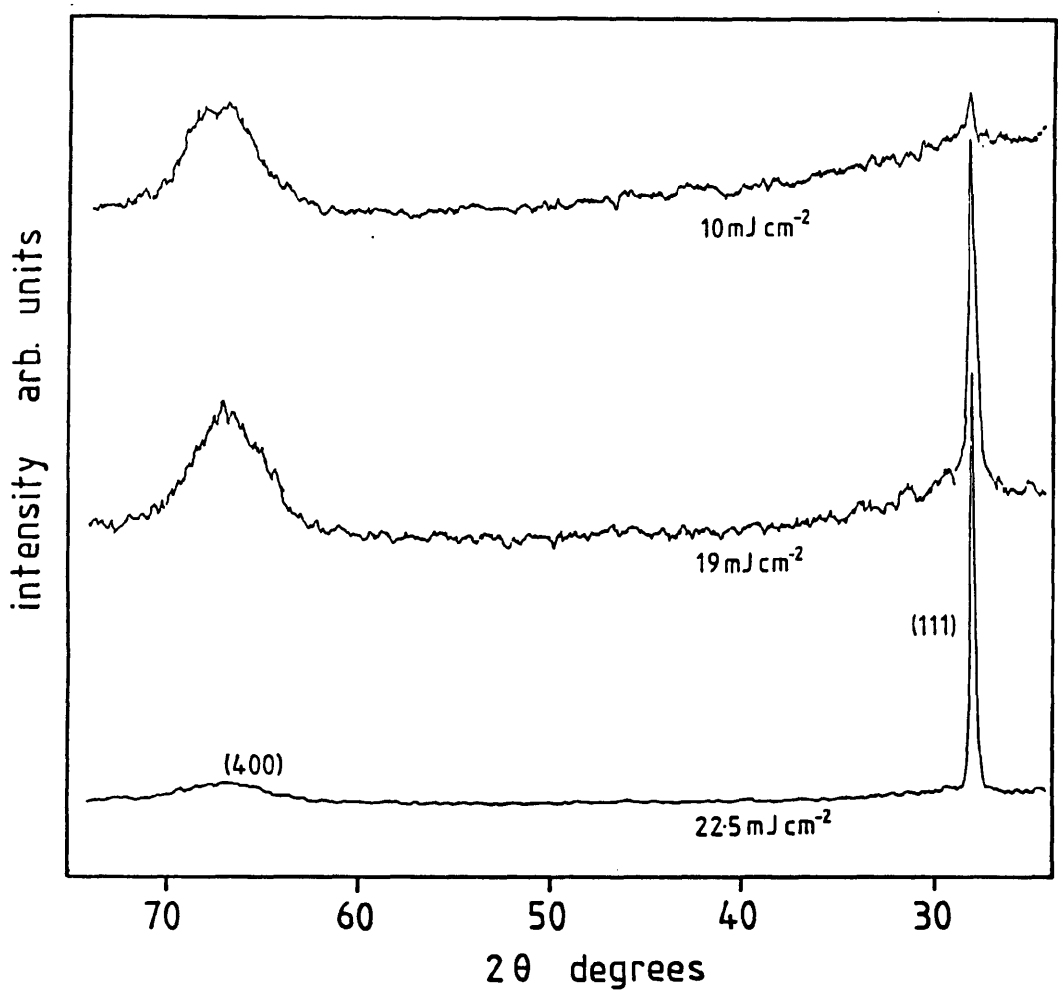

Figure 3.10 Variation in relative intensities of (400) and (111) reflections with increasing E_{ds} for three layers grown at 275°C. Note difference in FWHM (400) between (400) and (111)

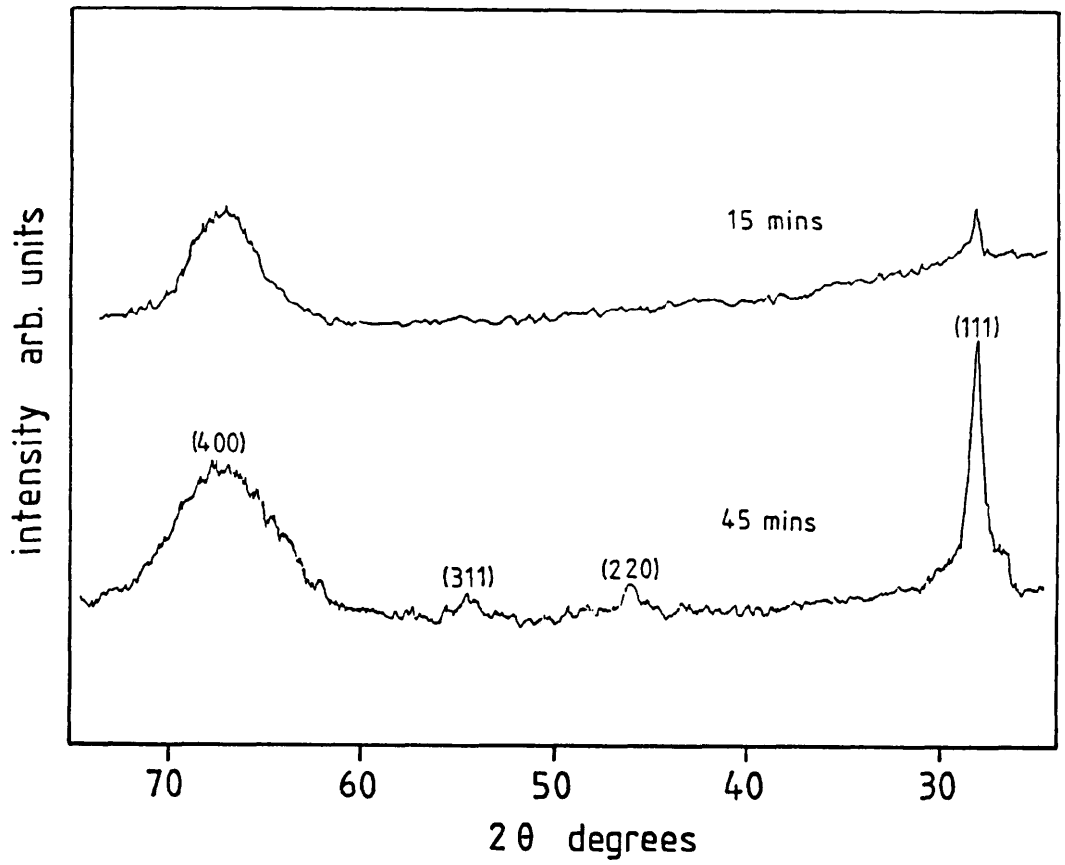

Figure 3.11 XRD patterns for layers grown under identical conditions for growth times of 15 and 45 minutes

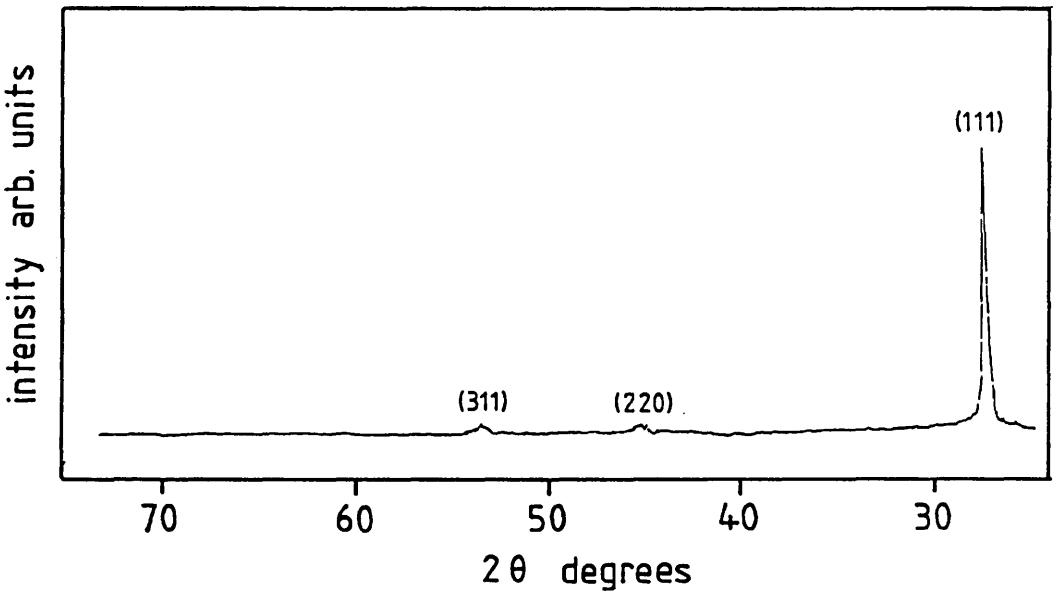

Figure 3.12 XRD pattern of material deposited on glass slide. Note absence of (400) reflection and intensity of (111) reflection

A preferential (111) orientation has also been observed by Ando et al for ZnSe deposited on glass from DEZn and DMSe under Hg lamp illumination[8]. Non-irradiated pyrolytic material deposited under equivalent conditions exhibited random orientation[8]. There are two questions to be addressed here; why does UV irradiation result in a preferred (111) orientation, and why is the (100) oriented material of such poor crystallinity compared to the (111) material deposited during the same growth run under exactly the same experimental parameters?

The FWHM(400) is observed to be several degrees wide at growth temperatures where equivalent MBE and MOCVD material exhibits values of 0.11 degrees. The lattice is so disrupted as to be considered virtually amorphous. This is also found to be the case with 'halo' material deposited around the irradiated region so the poor crystallinity cannot be attributed to radiation induced damage.

In the case of conventional MOCVD deposition, the most popular Se precursor is gaseous H_2Se[9], which undergoes a parasitic reaction with DMZn. As already discussed, epitaxial material is grown with these precursors at 280°C. When ZnSe is grown pyrolytically from DMZn and DESe, it is generally performed at 400°C and above[10]. Whilst this no doubt reflects the need for higher pyrolysis temperatures due to the lack of a parasitic reaction between the organometallics equivalent to that between DMZn and H_2Se, it may also indicate the need to thermally desorb alkyl group reaction byproducts from the layer surface to obtain epitaxial material. Yokogowa et al have reported that a temperature of 400°C is necessary to grow single crystal material from the pyrolysis of DMZn and DESe[11].

It is apparent that from comparison with high quality DMZn/H_2Se MOCVD and MBE grown material, that the most probable source of lattice disruption and the extremely broad (400) reflections is the incorporation of carbon that is not removed by thermal desorption or reaction routes available in MOCVD. What this cannot explain, however, is the striking difference in crystallinity between (100) oriented and (111) oriented material.

3.4 Carbon Incorporation in ZnSe and GaAs

Carbon incorporation during MOCVD semiconductor growth has been much more widely studied in the case of GaAs than ZnSe, and pertinent results for GaAs are considered in this section as they are also useful in demonstrating potential C incorporation mechanisms in this study.

In all known cases of group IV incorporation in II-VI compounds, the group IV atom resides on the group II site as has been demonstrated by electron paramagnetic resonance[12,13]. This is chemically reasonable in the case of ZnSe because carbon forms strongly bound compounds with Se and not Zn. Although identification of carbon in ZnSe by photoluminescence was thought impossible, a peak at 2.7920 eV has recently been attributed to carbon, and this lies very close to the previously unidentified I_3 peak often observed when DESe is used[14]. In a recent MOMBE study using H_2Se/DMZn, a peak was observed in this position only when both sources were cracked before deposition[15], indicating that the presence of both methyl radicals and Se atoms was necessary for its appearance in PL spectra.

The presence of CH_3-Se therefore appears to be a significant factor in carbon incorporation, and compounds that contain it or processing conditions that allow it to be formed will result in increased carbon levels.

The contribution of ethyl groups to C incorporation is not so clear. It is well known that substituting TEGa for TMGa reduces carbon incorporation in MOCVD grown GaAs[16], but this is believed primarily to be due to the so-called ß-elimination process in the decomposition of TEGa. $Ga(C_2H_5)_3$ decomposes stepwise into components $GaH(C_2H_5)_{3-n}$ with the simultaneous formation of C_2H_4[17]. Ethene has a very low sticking probability on GaAs and desorbs instantly at room temperature[18]. This route to the suppression of the adsorption of carbon bearing species is not available for photodissociated ethyl groups. The spontaneous decomposition of surface bound ethyl groups to form a gas phase ethene molecule and leaving a surface hydrogen atom is believed to operate[19,20].

Experimentally, all carbon has been shown to be removed from an adsorbed TEGa layer on (100) GaAs by soaking in vacuo at 400°C for 5 minutes[21], presumably by ß-elimination. A route therefore does exist for alkyl desorption provided a carbon-carbon double bond can be formed, which is only the case if the group contains two or more carbons, i.e. a ß-carbon[22], but this process will become increasingly unfavourable with decreasing growth temperatures.

3.41 Crystallographic Dependence of C Incorporation

The crystallographic orientation dependence of carbon incorporation in the MOCVD of GaAs has been studied experimentally, the highest carbon levels being obtained on (111)B (As) surfaces and the lowest on (111)A (Ga), the (100) levels being intermediate between the two close packed surfaces.[23] The alkyl radicals (CH_3 in this case) have the highest affinity for As sites and the carbon levels reflect the density of group V sites on the particular crystallographic orientation. The increase in adsorbed AsH_3 on the Ga terminated (111)A surface also provides a greater source of hydrogen for transfer to the methyl radical resulting in subsequent desorption[23].

The removal of methyl radicals is thought to be accomplished by reaction with AsH_3 adsorbed on or present near the surface which acts as a source of atomic hydrogen to create methane. The presence of hydrogen carrier gas has been shown to play a minimal role in the creation of CH_4 from the CH_3 radical during alkyl/hydride MOCVD[23,24], the dissociation barrier of molecular hydrogen apparently being too great[18].

3.42 Carbon Incorporation in Laser Deposited material

Films grown by the photolysis of trimethylaluminium (TMA) at temperatures below 200°C have been shown by Motooka et al to consist of porous pure Al with occluded hydrocarbon species CH and CH_3[25], and in material deposited above this temperature Al-C bonding was observed by Auger electron spectroscopy (AES)[25]. The authors

concluded (indirectly from mean free path calculations) that Al, and not $Al(CH_3)_n$ radicals were responsible for deposition. However Zhang and Stuke found that the main photolysis product of TMA to be $AlCH_3$ in a laser mass spectrometric study[26]. This same study also included work on the photolysis of adsorbed Al precursors. Interestingly, all the photolysis products Al, AlH^+, $AlCH_3$, found at 248 nm and 193 nm were also found at 308 nm XeCl laser light, even though they were not detected from isolated gaseous Al alkyls. This demonstrates the influence of environment on the process,and also that dissociation occurs most probably at the surface. This result was obtained with both Si and UV transparent quartz substrates, demonstrating a photochemical rather than photothermal process as the main component. Importantly, a much higher abundance of $AlCH_3$ was found from adsorbed layer photolysis against the isolated gaseous photolysis value.

3.44 DMZn, DESe and Related Compound Photoproducts

The photolysis of dimethylzinc and other group IIb organometallics such as dimethylcadmium and dimethylmercury has been investigated quite thoroughly[27-31], demonstrating that these molecules undergo complete dissociation to three fragments on absorption of a single photon of ~250 nm or less. In the case of DMZn and DMCd, after loss of the first methyl group, the second methyl is known to dissociate well within the molecule rotational period as has been shown by anisotropic fragmentation[29] and spectroscopic[31] observations. The methyl radicals have been pictured as either leaving simultaneously from a bent excited state of the parent molecule[31], or sequentially after activation of the M-C asymmetric stretch[30].

No work has been found in the literature on the photofragmentation of diethylselenide, but there is evidence to suggest that the photolysis of alkyltellurides is not a simple one-stage process. The flash photolysis of dimethyltelluride (DMTe) performed by Connor et al[32] demonstrated the presence of the CH_3Te, believed to be a primary photoproduct. It was also shown that collision of a Te atom with a DMTe molecule resulted in the formation of Te_2 and two methyl radicals or C_2H_6 at almost every collision. Mullin and Irvine[33] demonstrated that photolysed DETe did not deposit Te in the high UV intensity region of their reactor, but only further downstream after absorption of additional radiation, indicating that also in the case of DETe decomposition is not a simple one step process.

The metal-carbon bond strengths, properly described by the mean bond disruption enthalpy D[M-R], are somewhat higher for the group VI organometallics than for the corresponding group II compounds:

Group II metal	D(M-R)(kJ mol^{-1})	Group VI metal	D(M-R)(kJ mol^{-1})
$Zn(CH_3)_2$	186.4	$Se(C_2H_5)_2$	240.3
$Cd(CH_3)_2$	148.5	$S(C_2H_5)_2$	293.5
$Cd(C_2H_5)_2$	110.6	$S(CH_3)_2$	303.6
$Hg(CH_3)_2$	130.0	$Te(C_2H_5)_2$	235.0
$Zn(C_2H_5)_2$	145.0	$Te(C_2H_5)_2$	483.0

(all values from reference 34 apart from DMTe, DETe, reference 33)

A further measure of the relative stabilities of DMZn and DESe is given by the enthalpies of formation of the compounds, 20.8 and -90 kJ mol^{-1} for DMZn and DESe respectively[34].

Although there is enough energy in a 193 nm photon (6.4 eV) to break both bonds in a DESe molecule (2 x 2.5 eV), energy is also distributed to translational motion and vibrational states of the photofragments, and referring to the similar bond strengths of DESe and DETe. It is highly probable that a primary photoproduct of DESe is the ethylselenide radical C_2H_5Se. The flash photolysis of CSe_2 was shown some years ago by Callear and Tyerman[35] to produce CSe and atomic selenium. Reaction with gaseous Se atoms and ethylene produced ethylene selenide, and in a similar manner to DMTe and Te[32], fast abstraction of Se from C_2H_4Se by collision with free Se to form Se_2 was highly efficient (the dimer is the majority vapour species for all group VI elements[36]). It is therefore reasonable to suppose that the major photoproducts of DESe are C_2H_5Se, C_2H_5, Se and Se_2.

3.45 Surface and Gas Phase Reactions

The reactions below are the primary gas and adsorbate phase reactions that lead to products that may then incorporate in the depositing ZnSe layer:

$$Se(C_2H_5)_2 \xrightarrow{h\upsilon} Se(C_2H_5) + Se$$

$$Se(C_2H_5) \xrightarrow{h\upsilon} Se + C_2H_5$$

$$Zn(CH_3)_2 \xrightarrow{h\upsilon} Zn + 2CH_3$$

$$Se + Se(C_2H_5)_2 \rightarrow Se_2 + 2C_2H_5 \quad ?$$

$$Se + Se \rightarrow Se_2$$

Primary DMZn photoproducts are therefore expected to be Zn, CH_3

Primary DESe photoproducts are expected to be $(C_2H_5)Se$, Se, Se_2, C_2H_5

3.5 Carbon Incorporation Routes in Laser Deposited ZnSe

By comparison with carbon incorporation studies in conventional MOCVD and MOMBE and precursor photolysis studies, several potential routes for carbon incorporation in laser deposited ZnSe can be identified. Physisorbed $Se(C_2H_5)$ generated as a primary photoproduct could incorporate directly at a Zn site. Physisorbed TMGa molecules are known to be prone to chemisorption once scission of one or more Ga-CH_3 bonds occurs by photo-dissociation[37]. If the same process occurs with DESe after removal of an alkyl group, the lattice will be terminated at the point of incorporation with a C_2H_5 group .

This would cause gross local distortion and disruption of the lattice which would be consistent with the XRD profiles obtained.
Se atoms could combine with photogenerated methyl or ethyl groups either on or close to the surface[20] and then incorporate.
Alternatively alkyl groups could chemisorb directly at Se sites.

3.51 Radical Removal Routes

At the low deposition temperatures used in this study the conversion of an ethyl group to ethene by hydrogen removal was not available as a reaction route as this needs 500°C. Methane and ethane generation by radical reactions such as

$$CH_3 + C_2H_5 \longrightarrow C_2H_6 + CH_2$$

would be a means of reducing alkyl radical concentration but still result in formation of a reactive species.

Methyl radicals could also combine to form ethane:

$$CH_3 + CH_3 \longrightarrow C_2H_6$$

Atomic hydrogen could be generated by further photolysis of alkyl groups:

$$CH_3 \xrightarrow{h\upsilon} CH_2 + H$$

A radical is of course still left, although any atomic hydrogen generated could remove methyl or ethyl radicals. Deposition under an overpressure of hydrogen (10 Torr H_2) was found to give no appreciable improvement in the crystalline quality of deposited ZnSe FWHM (400), suggesting that the presence of atomic and not molecular hydrogen at the layer surface is necessary for efficient suppression of radical incorporation, as is the case in conventional MOCVD.

3.52 Thermal Desorption

SIMS depth profiles of samples grown at varying deposition temperatures shows that carbon levels fall progressively with increasing deposition temperature (figure 3.13) The mean adsorption time of alkyl groups decreases exponentially with increasing temperature[38]. This reduction in alkyl density reduces the potential either for direct incorporation into the lattice, or for the formation of alkyl containing Se species which could then incorporate into the layer. The primary photoproduct $Se(C_2H_5)$ may also desorb increasingly before incorporation. This would result in a decrease in growth rate as is observed with increasing temperature. In a similar manner, desorption of the pyrolysis product $Ga(C_2H_5)$ is

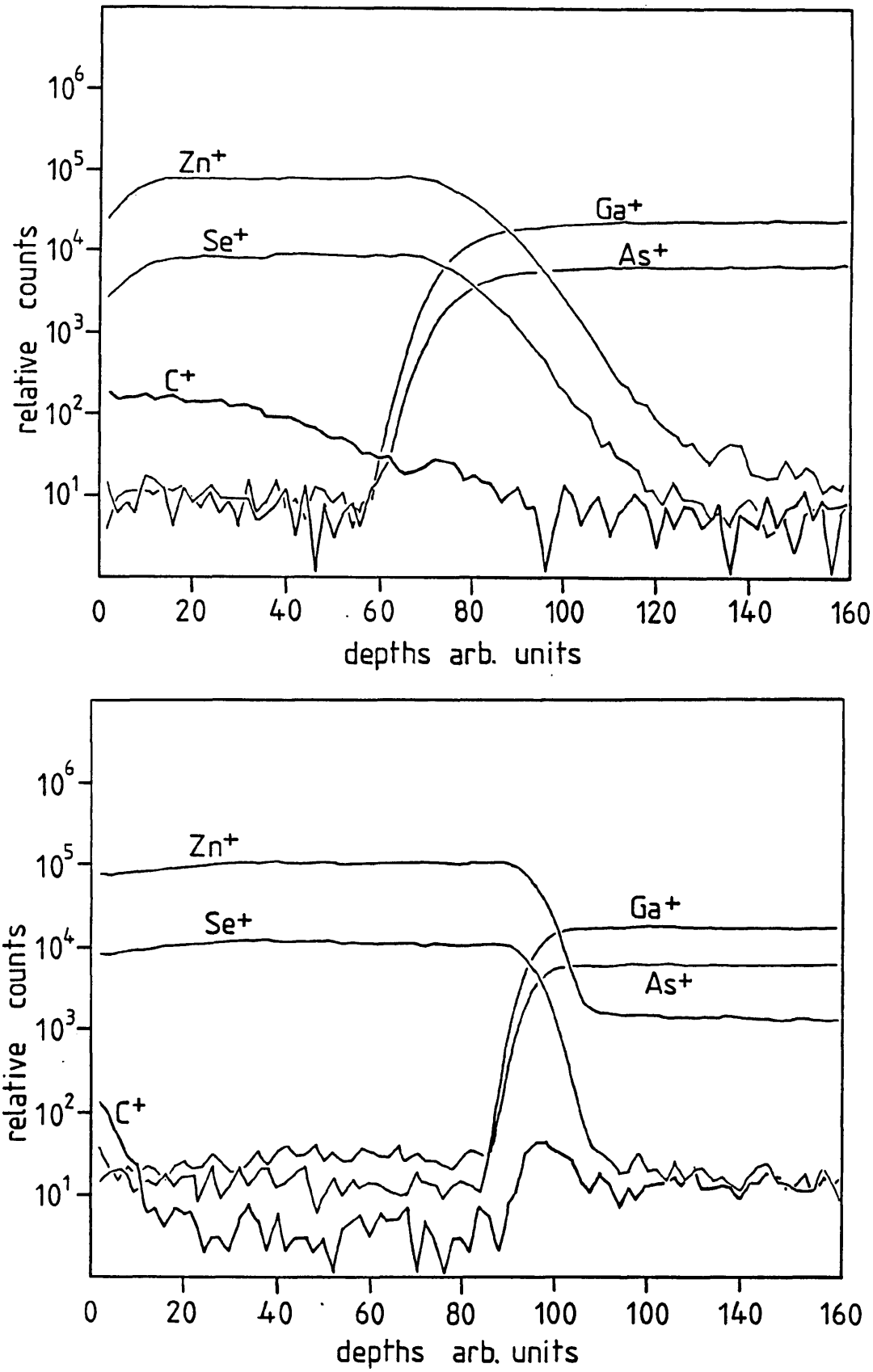

Figure 3.13 SIMS depth profiles for layers grown at 325°C (upper) and 350°C (lower). Note decrease in carbon level for layer grown at higher temperature. Both layers grown at 30 Hz operating rate, 7.5 mJ cm^{-2} E_{ds}.

believed to lower the deposition rate of GaAs in chemical beam epitaxy of TEGa and As_2[20]. Together with the decrease in carbon levels from 275-350°C there is a corresponding increase in material crystallinity, measured by FWHM (400) (figure 3.14). The improvement in crystallinity is exponential with temperature and this is immediately suggestive of a direct link with the exponential decrease of the mean adsorption time of alkyls with increasing temperature.

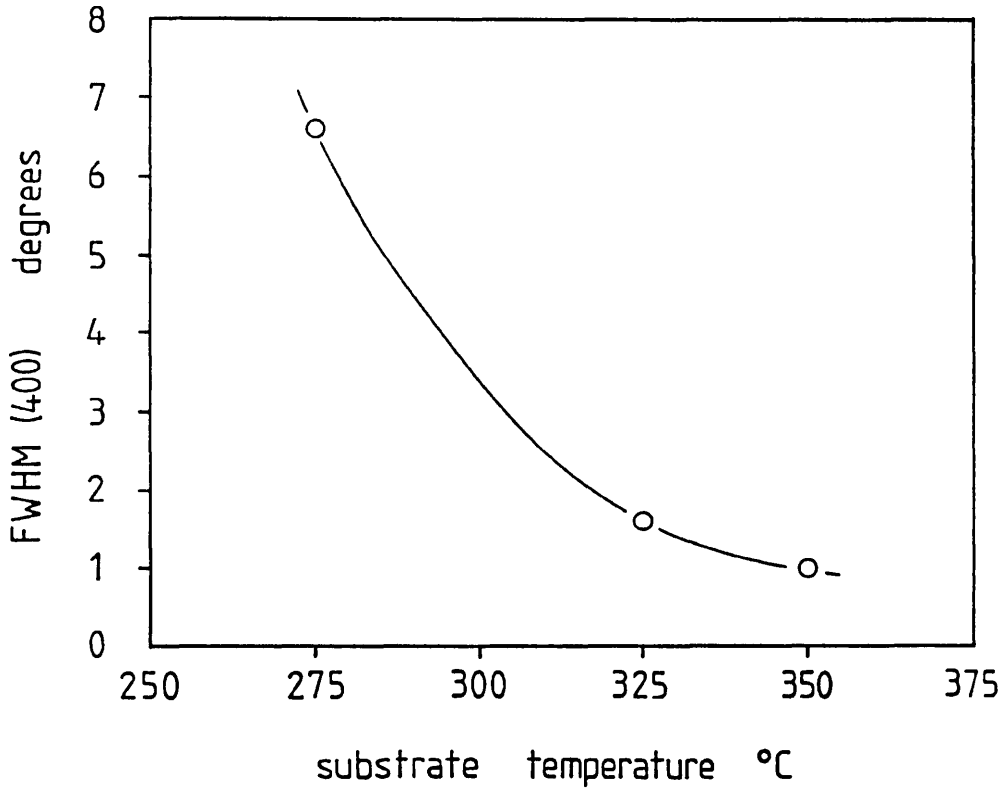

Figure 3.14 Increase in crystallinity with increasing growth temperature

The net result in either or both of these processes is that the competitive incorporation of Se atoms as opposed to Se-alkyl groups or lone alkyl groups moves in favour of Se at raised growth temperatures. The improved crystallinity of the layers results in fully oriented (100) material at 325°C, the (100) orientation of the substrate being reproduced sufficiently well to suppress the preferred [111] axis growth.

3.53 Reduction of C Levels by UV Irradiation

Donnelly et al[39] found that 193 nm irradiance of InP layers deposited by photolysis of $In(CH_3)_3$ and $P(CH_3)_3$ was particularly successful at reducing carbon levels to below AES detection limits, allowing epitaxial material to be deposited at 320°C. Non-irradiated areas were amorphous with very high (40 %) carbon levels. This success was not repeated with GaAs deposited at 193 nm from $Ga(CH_3)_3$ and $As(CH_3)_3$[40]. The films were randomly oriented and polycrystalline, and this was attributed to the high measured carbon content (1-3at.%) preventing epitaxy.

Al films deposited on sapphire by 248 nm photolysis of a TMA adsorbed layer under vacuum have been shown to have very high levels of methyl contamination[41], but under similar conditions 193 nm radiation was demonstrated to be very effective at removing methyl contaminants[42]. However this success was not repeated when an overpressure of 0.1 Torr TMA was used, the methyl desorption process being unable to compete with increased adsorption.

Similar effects have been observed in this study. Figure 3.15 shows XRD patterns for two layers grown at 325° C under different total reactant partial pressures of 0.4 and 0.8 Torr. To obtain an equivalent E_{ds} of 7.5 mJ cm^{-2} at both pressures the laser pulse energy was raised from 30 to 50 mJ to allow for greater gas phase absorption at 0.8 Torr. As discussed in section 3.2, these values have been obtained experimentally as covered in Chapter 4. The layer grown under a P_{total} of 0.4 Torr is fully oriented (100) with a FWHM (400) of 1.6 degrees.

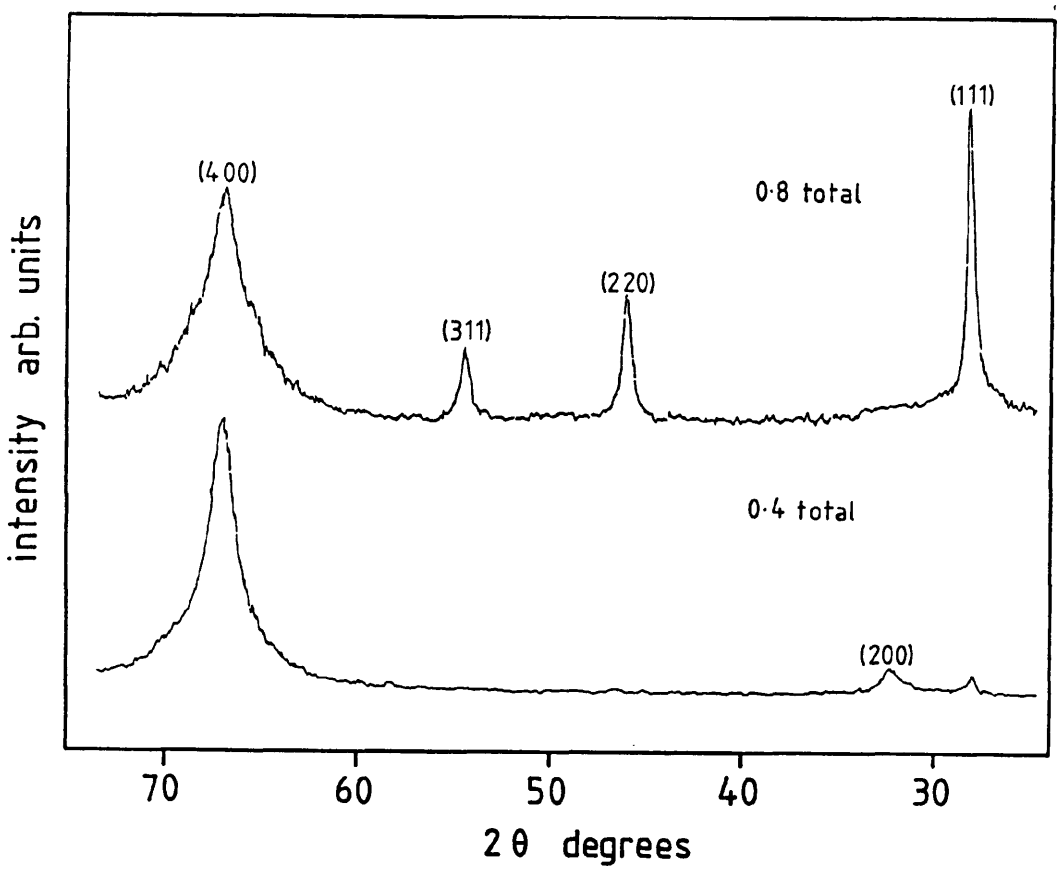

Figure 3.15 Reduced crystallinity with increasing P_{total}.

The material deposited under a P_{total} of 0.8 Torr has a poorer FWHM (400) of 3 degrees and exhibits some random (220), (331) and (111) orientation. This is consistent with laser stimulated alkyl desorption processes being unable to compete sufficiently with alkyl adsorption at the higher P_{total} to result in a fully oriented (100) layer. This result also indicates that irradiation does indeed suppress carbon incorporation and that crystallinity would be worse without direct UV layer illumination.

An improvement in FWHM (400) with increasing laser power levels was observed in samples deposited at 275°C and 40 Hz laser operating rate. A sample grown at an E_{ds} of 7.5 mJ cm^{-2} exhibited a FWHM (400) of approximately 6.5 degrees, whereas a sample grown at an increased E_{ds} of 14.6 mJ cm^{-2} exhibited a greatly improved FWHM (400) of approximately 3 degrees (figure 3.16). The extent of (111) growth was correspondingly reduced. This improvement in crystallinity could be the result of an increase in alkyl desorption simply due to increased surface temperatures at the higher irradiance, or possibly photolytic removal of carbon bearing species as appears to be the case in the reported Al deposition[42]. Alternatively further effects may be responsible and these will be explored in section 3.7.

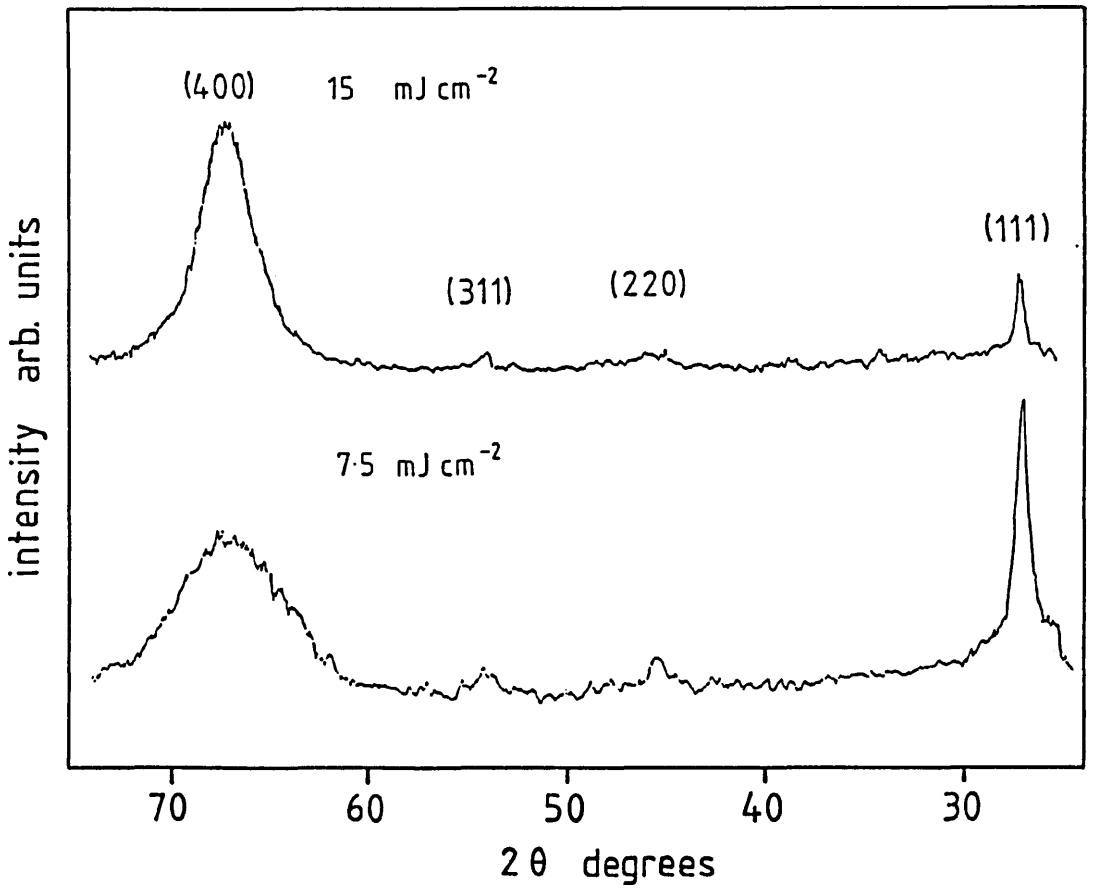

Figure 3.16 Improvement in crystallinity with increasing E_{ds}. 275°C ambient, 40 Hz operating rate.

3.6 Difference in (111), (100) Crystallinity

The wide disparity in crystallinity between (100) and (111) oriented material has yet to be addressed. It is clearly the case that the poor crystallinity of (100) oriented material is the result of excessive carbon incorporation. Apparently alkyl incorporation on (111) surfaces is suppressed or a mechanism of preferential alkyl removal operates on this plane. As discussed previously, GaAs deposited on substrates of different orientation exhibits lowest C levels on (111)Ga material, but this has been attributed to the high density of adsorbed AsH_3 on this surface providing a hydrogen source for alkyl removal. In terms of C affinity for Zn and Se, a (111)Zn surface would favour a minimal level of direct alkyl incorporation, but $Se(CH_3)$ and $Se(C_2H_5)$ could still readily incorporate. A (111)Se surface would provide the highest density of sites for direct alkyl incorporation. In the absence of an equivalent mechanism as exists for GaAs hydride MOCVD, there is no obvious reason why (111) ZnSe surfaces should exhibit a markedly different carbon incorporation to (100) planes.

3.7 Potential Non Photolytic or Photothermal Growth Mechanisms

Studies of the laser assisted growth of GaAs under Ar ion laser illumination have been performed by several groups, and large enhancements in deposition rates due to irradiation have been reported. The 514.5 nm Ar ion line is well away from the gas phase absorption regions of TMGa, TEGa and AsH_3[43], and the absence of a direct photolytic decomposition mechanism has lead to somewhat contradictory interpretations of the observed growth enhancements. Karam et al have reported growth of GaAs at 250°C[44]. The thermal rise due to irradiation was estimated at 50°C, leaving the surface well below the pyrolytic decomposition temperature for TEGa and AsH_3. The 2.3 eV photon energy was stated as not being great enough to break the Ga-C bond, and an unspecified 'photocatalytic reaction' at the substrate surface was invoked to explain the observed deposition. This has been interpreted as a photochemical lowering of the activation energy for pyrolysis by the absorption of 514 nm radiation by surface species[45], but no evidence, either theoretical or experimental, has been produced for this mechanism.

The reduction in carbon incorporation in GaAs by Ar ion laser illumination has also been reported recently[46]. SIMS depth profiles revealed presence of H and C in the layer which was taken as evidence of the incorporation of CH_x groups. The proposed incorporation route was the abstraction of hydrogen from adsorbed methane by ethyl radicals to produce methyl radicals which then incorporate into the lattice. It was not stated why ethyl radicals could not directly incorporate. The reduction in carbon levels in irradiated material was ascribed to 2.5 eV photons 'easily' breaking the Ga-CH_x bond.

3.71 Deposition By Carrier Photogeneration

In a study of the deposition of ZnS and ZnSe by Xe arc lamp photolysis of DMZn, DMSe and DMS, Fujita et al[47] obtained information on the wavelength dependence of the growth rate for both materials by selective use of filters and monochromators. It was found that the growth rate of ZnSe increases abruptly at threshold energy values of 2.5 eV (500 nm) and for ZnS at 3.5-3.7 eV (350-335 nm), corresponding approximately to the respective band gap values at the growth temperatures used. Direct gas phase dissociation is not expected at these wavelengths, suggesting that a surface electronic response to above band gap radiation was responsible for the increase in growth rate.

Ritz-Froidevaux et al reported that the photo-absorption edge of organometallics extends to longer wavelengths when adsorbed at a surface, compared to the gas phase[48]. This also seems to be the case in the work of Zhang and Stuke on adsorbed TMA on SiO_2[26], where longer wavelength photolysis could not be attributable to a surface electronic process. However in the case of the results of Fujita et al, the extension of the absorption band to 500 nm would be particularly extreme, and the abrupt growth rate increase at the appropriate band gap value of each material appears to offer conclusive proof that the observed enhancement of growth rate is not photolytic in nature, but is due to the generation of e-h pairs in the layer. It has been suggested that this carrier generation promotes some surface reaction such as the elimination of alkyl groups from adsorbed species.

3.72 Reappraisal of Reported GaAs Photodeposition

The possibility of photogenerated carriers dissociating TEGa molecules adsorbed on GaAs was considered by Sugiura et al[49] to explain the growth enhancement of Ar ion laser irradiation, but was discounted because the carrier concentration due to irradiation, calculated at 10^{16} cm^{-3}, was a minimal percentage of the 10^{18} cm^{-3} carrier concentration due to doping. However, carriers excited across the GaAs band gap by 2.3 eV photons possess an excess ~1 eV kinetic energy which is not available to dopant carriers, and may allow them to catalyse reactions such as the decomposition of adsorbed molecules.

The important results of Fujita et al demonstrate the possibility of stimulating reactions in an adsorbate by carrier generation at a semiconductor surface. This process will now be considered in more detail, as will its potential relevance to the results obtained in the present study.

3.8 Reaction Stimulation by Photogenerated Carriers

Transition metal and main group metal-carbon sigma bonds are commonly cleaved on electrochemical oxidation and reduction.[50] In particular, the electrochemical reduction of organo-Hg compounds has been investigated more thoroughly than any other main group metal organic species[51-53]. Dialkyl Hg compounds of the type [HgR_2] generally

reduce in an irreversible two electron process at a dropping mercury electrode with concomitant metal-carbon bond cleavage.

It has been known for some time that the illumination of semiconductor surfaces by photons of hu > E_g can lead to chemical reactions when samples are immersed in aqueous solution[54-56]. Reactions occurring due to the photogeneration of electron hole pairs followed subsequently by one of the carriers leading to or catalysing a reaction at the semiconductor-liquid interface, are in some ways analagous to the photostimulation of reactions at a semiconductor-adsorbate interface.

Most early treatments of semiconductor-electrolyte systems considered the photogeneration of thermalised minority carriers (holes in n-type material, electrons in p-type) in a surface depletion region (formed due to contact with the electrolyte) which are then swept toward the surface due to band bending in the depletion region[54-56]. Once at the surface the carriers are able to stimulate oxidation (holes) or reduction reactions (electrons). Hot carrier injection into electrolytes was considered by Boudreaux et al[57], who considered the photogeneration of a hot electron which subsequently tunneled through a surface potential barrier into a potential well representing an adsorbed OH^- ion. The criteria for hot carrier injection were identified as the tunneling and effective relaxation time in the electrolyte being faster than the thermalisation time of carriers in the semiconductor i.e. once generated in the solid the hot carrier is able to reach the electrolyte and give up its kinetic energy there rather than lose its energy to the lattice as phonons[57].

The capacity for photostimulation of oxidation of semiconductor surfaces in gaseous environment has also been apparent for several years. The enhancement of thermal oxidation of Si and GaAs by above band gap visible illumination was the subject of several early studies[58-60] and the increase in oxidation rate was generally attributed to the weakening of surface bonds by hole generation, leaving more open to attack by oxygen. An alternative explanation was proposed by Petro et al[61] who considered the oxidation of p-type GaAs in terms of the presence of photogenerated electrons dissociating physisorbed O_2. This was further supported by Bartels[62] and Mönch[62,63] who in a surface science study measured increased oxygen uptake on GaAs (110) under Xe lamp illumination. A filter was used to prevent photodissociation of O_2 and the increased oxygen uptake was attributed to generation of O_2^- by attachment of hot electrons which dissociates at lower energies than O_2 and can then physisorb once dissociated.

More recently the wavelength dependence of photostimulated oxidation of GaAs in aqueous[64] and gas phase[64,65] ambients has been studied. In oxides grown in deionised water, visible 514 nm illumination was found not to produce a significant change in oxidation kinetics, but 257 nm UV illumination resulted in a three fold increase in oxidation rate. Similar wavelength dependent enhancements were observed for oxidation in air. The wavelength dependence was suggested as being due to photons of increasing energy being absorbed in different sections of the Brillouin zone and generating electrons and holes of different energies, which are then able to stimulate reactions unavailable to lower energy photocarriers. This concept will now be covered in more detail and its possible relevence to the

present study will be considered.

Applying this argument to the present study, it is possibly the case that alkyl elimination by photogenerated carriers occurs preferentially on (111) oriented ZnSe, due to a difference in the surface electronic response of this plane to the (100).

3.9 Carrier Generation in GaAs and ZnSe

Although the room temperature bandgaps of GaAs and ZnSe are generally quoted as 1.4 eV and 2.68 eV respectively[40], these values represent the minimum possible energy transition from valence to conduction band that define the fundamental absorption edge, and do not reflect the range of transitions possible at photon energies greater than these values. In direct band gap semiconductors such as GaAs and ZnSe visible and ultraviolet photons are absorbed in different parts of the Brillouin zone, generating electrons and holes of different energies.

The optical properties of semiconductors can be summarised by the complex dielectric function[66]. This has been obtained experimentally by Kramers-Kronig transformation of reflectance measurements[67] and has also been evaluated by theoretical treatments of the electronic band structure[68,69]. The imaginary part of the dielectric constant, ϵ_2, is the extinction coefficient and is sharply structured between 3 and 7eV for GaAs and ZnSe (figure 3.17).

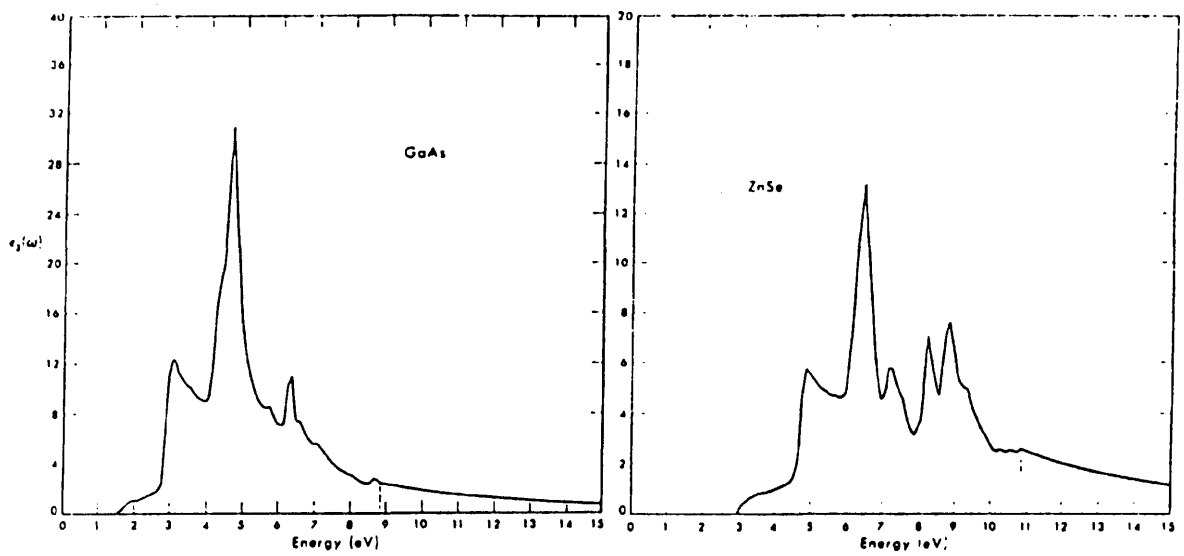

Figure 3.17 Imaginary part of dielectric constant for GaAs and ZnSe (after reference 68)

The peaks in the ϵ_2 curve are due to transitions from the valence to the conduction band in different sections of the Brillouin zone. Figure 3.18 shows the E-k diagram for ZnSe (GaAs is shown in figure 1.1). The ϵ_2 peak in the 4.9 eV region corresponds to L-edge transitions at 4.6 eV and Λ ([111] axis) transitions at 4.7 eV. The peak at 6.45 eV is caused by Δ ([100] axis) transitions at 6.2 eV, X-edge transitions at 6 eV and Σ ([110] axis) transitions at 6.6 eV[68] (these values will be reduced somewhat at elevated temperatures). The low energy optical spectrum of GaAs is similar to ZnSe,~ 3 and ~5eV photons induce L and X edge transitions in the GaAs Brillouin zone[70].

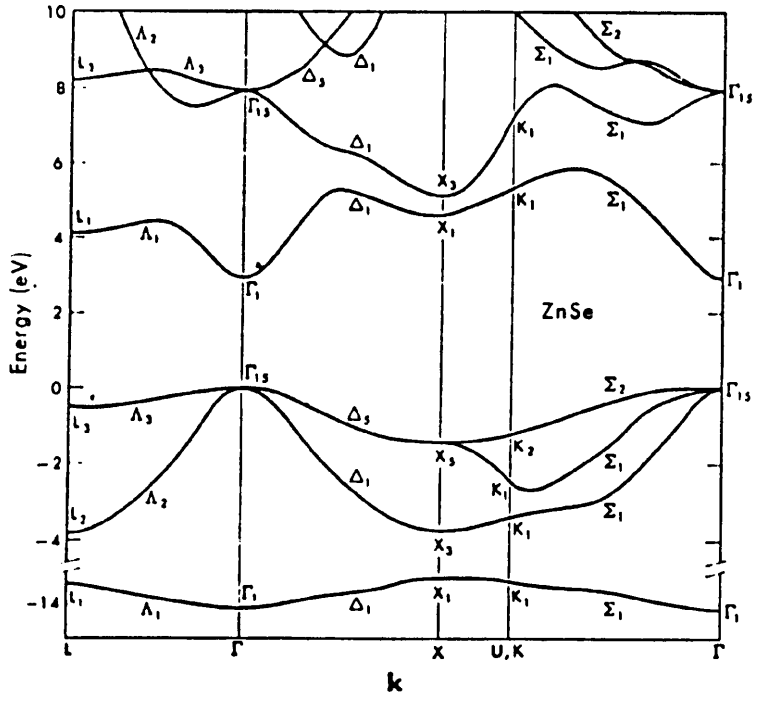

Figure 3.17 Reduced zone E-k diagram for ZnSe (after reference 68)

These interband transitions which occur at higher energies than the fundamental absorption edge result in a steep rise in the absorption coefficient of the semiconductor moving into the UV. The wavelength dependent optical absorption coefficient for GaAs has also been extracted from the Kramers-Kronig transformation of reflectance data[71]. (figure 3.18). Moving further into the UV from the fundamental absorption edge, there is a 100 fold increase in α due to higher energy interband transitions described above.

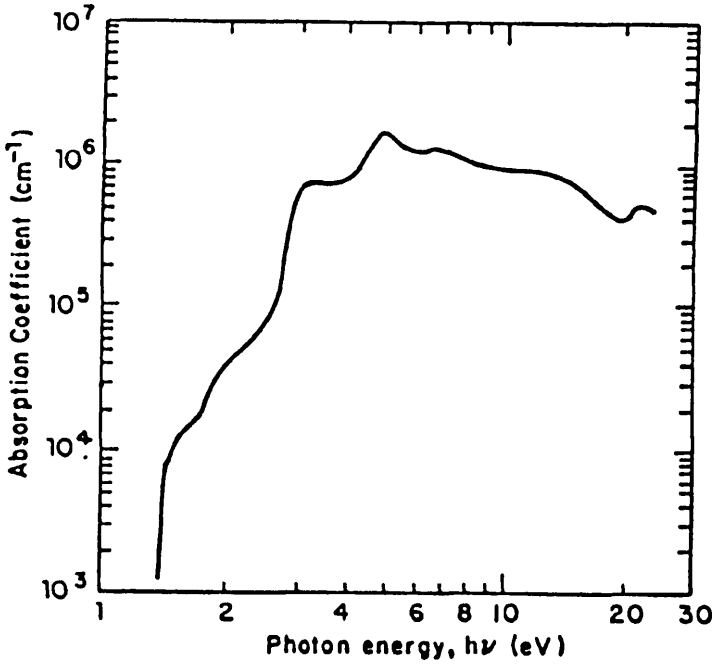

Figure 3.18 Wavelength dependence of absorption for GaAs (after reference 71)

The increase in absorption efficiency is due to the fact that for UV wavelengths the valence and conduction bands are more or less parallel for a range of k values, whereas it is only at the critical point for the fundamental Γ transition that $d^2E/dK^2=0$ for both bands. There is a much higher density of states available at the higher energy transitions and therefore a much higher transition probability. As a result of this very high α at 6.4 eV/193 nm, the absorption depth for GaAs is of the order of 50 Å, and carrier photogeneration is confined to this region. Over this short distance, near ballistic carrier transport to the surface is possible[65].

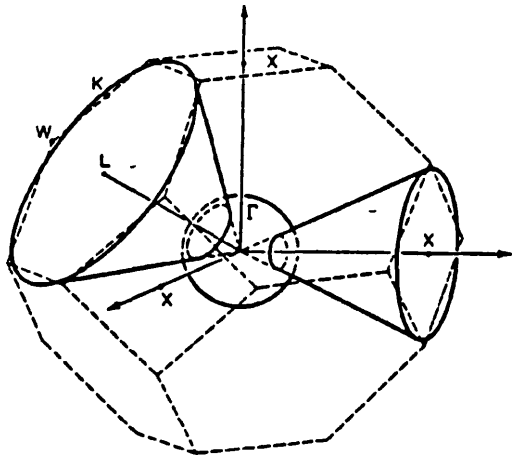

Figure 3.19 Γ, X and L regions of the sphalerite Brillouin zone (after reference 72)

The separate contributions of the various sections of the Brillouin zone to the complex dielectric constant have been calculated by Kahen and Leburton[72] for GaAs. The Brillouin zone was partitioned into the Γ, X and L regions (figure 3.19). The spherical Γ region at the zone centre corresponding to the band gap is isotropic and independent of zone orientation, but the integration volumes of the L and X regions are approximated by cones along the <111> and <100> regions. The relative volume of the L region is greater than that of the X, and the L regions display 8-fold degeneracy as opposed to the 6-fold degeneracy of the X volumes. The relative contributions of the regions to the dielectric constants are given as L=6.01, X=1.25 and Γ=0.41. Interband transitions in the L region therefore determine most of the optical properties of the semiconductor above the band gap. Although this was calculated for GaAs the basic result applies

to ZnSe as both materials share the sphalerite crystal structure. This predominance of <111> transitions may be a determining factor in any differential electronic response to irradiation of the (100) and (111) surfaces.

One factor that has not been addressed in the literature is the relevance of crystal (and therefore bond) orientation to the probability of exciting a given transition in the Brillouin Zone. If there is indeed an orientation dependence this will be a determining factor in the nature of electronically stimulated processes on a given surface plane.

For a (100) surface, two <100> axes and one <110> are in plane and perpendicular to normal illumination. The electric vector of the UV photons will be parallel to the (100) face, whereas in this orientation the <111> axes are inclined at 54.7° to the surface[73]. If this degree of inclination from the electric vector of the radiation results in L and Λ transitions becoming unfavourable, X, Δ and Σ transitions in the <100> and <110> directions may become preferred. The primary transitions are in fact the higher energy Δ and Σ, the low density of states at the 6 eV X edge resulting in a small contribution to ZnSe optical properties in this region[68]. Reference to the ZnSe E-K diagram (figure 3.18) shows that these interband transitions take > 6 eV leaving the promoted electron with a minimum excess energy. A photocarrier produced by 193 nm radiation in this section of the Brillouin zone therefore appears with negligible kinetic energy.

For an exposed (111) surface, the shallowest inclination of the <111> axes is 19.5°, much closer to a parallel condition with the electric vector of the UV light. If L and Λ transitions are predominant, then the photogenerated electrons are left with an excess of ~2 eV kinetic energy, and may be much more capable of stimulating surface reactions such as the removal of alkyl groups bound to Se atoms, which would otherwise incorporate into the lattice as is believed to occur on (100) surfaces.

Although a comprehensive study of orientation dependent photocarrier generation has not been carried out for ZnSe and GaAs, anisotropy has been observed in GaAs multiphoton absorption studies[74].

If anisotropic energetic photocarrier generation does indeed result in the (111) surface being the most reactive under UV illumination, leading to enhanced alkyl group desorption and improved crystallinity over the (100) surface, it is then straightforward to see why the layer becomes completely (111) oriented. Assuming that layer growth begins with initially randomly oriented nuclei on an amorphous substrate, any exposed (111) planes will grow more quickly than any other regions. The highest UV irradiance will be experienced by those (111) surfaces which are aligned (presumably accidentally) nearest to a perpendicular orientation with the beam axis, and any regions that satisfy this condition will grow at the expense of other areas further from the favourable alignment. Soon the entire layer adopts the (111) orientation, resulting in the marked preferred orientation observed experimentally.

References

1. W. Stutius, J. Crystal Growth **59**, 1 (1982)

2. N. Putz, H. Heinecke, E. Veuhoff, G. Arens, M. Heyen, P. Balk, J. Crystal Growth **68**, 194 (1984)

3. P. Balk, M. Fischer, D. Grundmann, R. Luckerath, H. Luth, W. Richter, J. Vac. Sci. Technol. **B5** (5), 1453 (1983)

4. J. Nishizawa, H. Abe, T. Kurabayashi, Naoki, Sakurai, J. Vac. Sci. Technol. **A4** (3), 706 (1986)

5. G. B. Shinn, P.M. Gillespie, W.L. Wilson,, W.M. Duncan, Appl. Phys. Lett. **54** (24), 2440 (1989)

6. W.E. Johnson, L.A. Schlie, Appl. Phys. Lett. **40** (9), 798 (1982)

7. N. Maung, Ph.D. thesis, University of Manchester (1988)

8. H. Ando, H. Inuzuka, M. Konogai, K.Takahashi, J. Appl. Phys. **58** (2), 802 (1985)

9. B. Cockayne and P.J. Wright, J. Crystal Growth, **68**, 225 (1984)

10. H. Mitsuhashi, I. Mitsuishi, M. Mizuta, H. Kukimoto, Jap. J. Appl. Phys. **24** (8), 578 (1985)

11. K. Yokogawa, M. Ogura, T. Kajiwara, Appl. Phys. Lett. **50** (16), 1065 (1987)

12. K. Suto and M. Aoki, J. Phys. Soc. Jpn. **24**, 955 (1968)

13. K. Suto and M. Aoki, J. Phys. Soc. Jpn. **26**, 287 (1969)

14. K.P. Giapis, K.F. Jensen, J.E. Potts, S.J. Pachuta, Appl. Phys. Lett. **55**(5),463(1989)

15. H. Onimaya, S. Yamaga, A. Yoshikawa, H. Kasai, J. Crystal Growth **93**, 679 (1988).

16. T.F. Kuech, R. Potemski, Appl. Phys. Lett. **47** (8), 1985

17. D.C Tuck in Comprehensive Organometallic Chemistry,p. 47, vol. 1, ed. G. Wilkinson, G.A. Stone, E.W. Abel (Pergamon, New York, 1982)

18. H. Lüth, J. Vac. Sci. Technol. **A7** (3), 696 (1989)

19. L.M. Fraas, P.S. McLeod, L.D. Partain, J.A. Cape, J. Vac. Sci. Technol. **B4** (1), 22 (1986)

20. A. Robertson Jr., T.H. Chiu, W.T. Tsang, J.E. Cunningham, J. Appl. Phys. **64** (2), 877 (1988)

21. M.E. Pemble, S.M. Francis, D.S. Buhaenko, P.A. Goulding (to be published)

22. M. Yoshida, H. Watanabe, F. Uesugi, J. Electrochem. Soc. **132** (3), 677 (1985)

23. T.F. Kuech, E. Veuhoff, J. Crystal Growth **68**, 148 (1984)

24. G. Arens, H. Heinecke, N. Pütz, H. Lüth, P. Balk, J. Crystal Growth **76**, 305 (1986)

25. T. Motooka, S. Gorbatkin, D. Lubben, D. Eres, J.E. Greene, J. Vac. Sci. Technol. **A4** (6), 3146 (1986)

26. Y. Zhang, M. Stuke, J. Crystal Growth **93**, 143 (1988)

27. C.F. Yu, F. Youngs, K. Tsukiyama, R. Bersohn, J. Preses, J. Chem. Phys. **85** (3), 1382 (1986)

28. J.O. Chu, G.W. Flynn, C.J. Chen, R.M. Osgood Jr., Chem. Phys. Lett. **119** (2), 206 (1985)

29. C. Jonah, P. Chandra, R. Bersohn, J. Chem. Phys. **55** (4), 1903 (1971)

30. S.L. Baughcum, S.R. Leone, Chem. Phys. Lett. **89** (3), 183 (1972)

31. C.J. Chen, R.M. Osgood, J. Chem. Phys. **81** (1), 327 (1984)

32. J. Connor, G. Greig, O.P. Strausz, J. Am. Chem. Soc. **91**, 5965 (1986)

33. J.B. Mullin, S.J.C. Irvine, J. Vac. Sci. Technol. **A4** (3), 700 (1986)

34. G. Pilcher and H.A. Skinner, in The Chemistry of the Metal-Carbon Bond, ed. F.R. Hartley and S. Patai (Wiley, New York,1982), Vol. 1, Chapter 2.

35. A.B. Callear, W.J.R. Tyerman, Trans. Faraday Soc. **62**, 371 (1966)

36. Landolt Bornstein, N.S., Vol 17b, Springer, Berlin (1982)

37. P.K. York, J.G. Eden, J.J. Coleman, G.E. Fernandez, K.J. Beernink, Appl. Phys. Lett. **54** (19), 1866 (1989)

38. P.W. Atkins, Physical Chemistry, chapter 29, p. 1012, Oxford, (1982).

39. V.M. Donnelly, D. Brasen, A. Appelbaum, M. Geva, J. Vac. Sci. Technol. **A4** (3), 716 (1986)

40. V.M. Donnelly, V.R. McCrary, A. Appelbaum, D. Brasen, W.P. Lowe, J. Appl. Phys. **61** (4), 1410 (1987)

41. G.S. Higashi, L.J. Rothberg, C.G. Fleming, Chem. Phys. Lett. **115**, 167 (1985)

42. G.S. Higashi, L.J. Rothberg, J. Vac. Sci. Technol. **B3** (5), 1460 (1985)

43. V.R. McRary, V.M. Donnelly, J. Crystal Growth, **84**, 253 (1987)

44. N.H. Karam, H. Liu, I. Yoshida, S.M. Bedair, Appl. Phys. Lett. **53** (9), 767 (1988)

45. A. Doi, S. Iwai, T. Meguro, S. Namba, Jap. J. App. Phys. **27** (5), 795 (1988)

46. R. Iga, H. Sugiura, T. Yamada, K. Wada, Appl. Phys. Lett. **55** (5), 451 (1989)

47. S. Fujita, A. Tanabe, T. Sakamoto, M. Isemura, S. Fujita, J. Crystal Growth, **93**, 259 (1988)

48. Y. Ritz-Froidevaux, R.P. Salathe, H.H. Gilgen, H.P. Weber, Appl. Phys. **A27**, 133 (1982)

49. H. Sugiura, R. Iga, T. Yamada, M. Yamaguchi, Appl. Phys. Lett. **54** (4), (1989)

50. C.J. Pickett, in The Chemistry of the Metal-Carbon Bond, ed. F.R. Hartley and S. Patai, Vol. 2, Chapter 1.

51. K.P. Butin, M.T. Ismail, O.A. Reutov, J. Organomet. Chem. **175**, 157 (1979)

52. K.P. Butin,I.P. Beletskaya, A.N. Kashin, O.A. Reutov, J. Organomet. Chem. **10**, 197 (1967)

53. L.I. Denisovich, S.P. Gubin, J. Organomet. Chem. **57**, 87 and 99 (1973)

54. H. Gerischer, J. Vac. Sci. Technol. **15**, 1422 (1978)

55. H.J. Hoffman, J.M. Woodall, Appl. Phys. Lett. **38**, 564 (1981)

56. F.W. Ostermayer, P.A.Kohl, Appl. Phys. Lett. **39**, 76 (1981)

57. D.S. Boudreaux, F. Williams, A.J. Nozik, J. Appl. Phys. **51** (4), 2158 (1980)

58. S.A.Schafer, S.A. Lyon, J. Vac. Sci. Technol. **19** (3), 494 (1981)

59. E.M. Young, W.A.Tiller, Appl. Phys. Lett. **42** (11), 63 (1983)

60. I.W. Boyd, Appl. Phys. Lett. **42** (8), 728 (1983)

61. W.G. Petro, I. Hiro, S. Eglash, I. Lindau, C.Y. Su, W.E.Spicer, J. Vac. Sci. Technol. **21** (2), 82

62. F. Bartels, W. Mönch, Surface Science, **143**, 315 (1984)

63. W. Mönch, Surface Science, **168**, 577 (1986)

64. D.V. Podlesnik, H.H. Gilgen, A.E. Willner, R.M. Osgood Jr., J. Opt. Soc. Am. **3** (5), 775 (1986)

65. C.F. Yu, M.T. Schmidt, D.V. Podlesnik, R. M. Osgood, J. Vac. Sci. Technol. **B5** (4), 1087 (1987)

66. J.I. Pankove in Optical Properties in Semiconductors, chapter 18, p.392, Dover (1975)

67. H.R. Philipp, H. Ehrenreich, Phys. Rev. **129** (4), 1550 (1963)

68. J.P. Walter, M.L. Cohen, Phys. Rev. **183** (3), 763 (1969)

69. J.R. Chelikowsky, M.L. Cohen, Phys. Rev. B **14** (2), 556 (1976)

70. M. Cardona, in Semiconductors and Semimetals, ed. R.K. Willardson, A.C. Beer, vol. 3, p.125, Academic, New York (1966)

71. H.C. Casey, D.D. Sell, K.W. Wecht, J. Appl. Phys **46** (1), 250 (1975)

72. K.B. Kahen, J.P. Leburton, Phys. Rev. B **32** (8), 5177 (1985)

73. Table of Interplanar Angles, Appendix 3, p. 460 in Elements of X-Ray Diffraction, B.D. Cullity, pub. Addison Wesley

74. V. Nathan, A.H. Guenther, S.S. Mitra, J. Opt. Soc. Am. **B2** (2), 294 (1985)

Chapter 4

The Thermal Response of ZnSe and GaAs to 193 nm Radiation.

4.1 Introduction

As noted in the preceding chapter, it was apparently the case that thermal effects were playing a role in the nominally photolytic deposition of ZnSe. Furthermore this was taking place at ambient temperatures below that reported to be necessary for the pyrolysis of DMZn and DESe. It should again be emphasised that no pyrolytic or non beam-induced deposition was noted on the sample or stage at regions remote from the photolysis volume. It was therefore concluded that beam induced thermal effects at the substrate and depositing layer were raising the irradiated surface temperature above that of the ambient, causing some pyrolysis of the adsorbate species. It was therefore decided to undertake a study of the thermal response of GaAs and ZnSe to pulsed UV radiation in order to quantify if possible the extent to which thermal effects were responsible in determining the overall growth rate. It is the surface temperature which determines adatom mobility and crystallinity of depositing material as well as the desorption of reaction products and, therefore, knowledge of the extent to which radiation can separate surface temperature from that of the sample bulk is clearly important.

The approach adopted was to experimentally determine where possible the extent of pulsed UV laser induced surface temperature rises, together with thermal calculations for comparison with and expansion of the scope of the experimental work.

The absorption of above-band gap radiation by ZnSe and GaAs has been covered in section 3.9 and is also covered in further detail in section 6.8. The important factors regarding both induced temperature rises and their calculation are the following.

1. The timescale of energy transfer from the beam to the lattice (i.e. timescale of material heating) is very short compared to the pulse duration.

2. The volume over which the laser radiation is absorbed is determined by the material absorption depth (α^{-1}) and is extremely shallow.

The very high absorption depths (α^{-1}) of ZnSe and GaAs at 193 nm result in the energy of a laser pulse being distributed initially in a very shallow volume. The photocarriers generated by interband transitions lose energy and momentum to the lattice on a picosecond timescale and thermal equilibrium between lattice and carrier plasma is attained on a timescale much shorter than the pulse duration. The transfer of energy from laser light to the lattice can be regarded as instantaneous for the purposes of temperature rise calculations.

An 'instantaneous' rise in surface temperature due to a laser pulse will be followed by a subsequent drop at the end of the pulse, the surface temperature eventually reaching its original value as heat is dissipated into the sample bulk and the surrounding environment.

As the sample volume will be many times greater than the very shallow skin absorption region, the actual rise in overall sample temperature will be negligible compared with the surface temperature rise values. For a given amount of energy absorbed, the extent of the initial temperature rise and the subsequent decay rate will be governed by the thermophysical properties of the material concerned.

If the surface temperature of the sample is above the ambient by some value DeltaT when the next pulse arrives, the following temperature transient will be raised accordingly and the surface temperature will rise in a stepwise manner at a rate given by DeltaT x (1/pulse separation). As the sample surface temperature becomes elevated above the bulk (or ambient) value heat will flow into the overall sample volume until an equilibrium surface temperature is reached depending on the laser pulse energy, operating rate and the material thermodynamic properties.

A hypothetical surface temperature-time profile for a series of pulses would take the form of figure 4.1. Here the final overall temperature rise is governed by two factors, the laser operating frequency, and the shape of the decay curve which is governed by the material properties and which also determines DeltaT at a given time following a pulse.

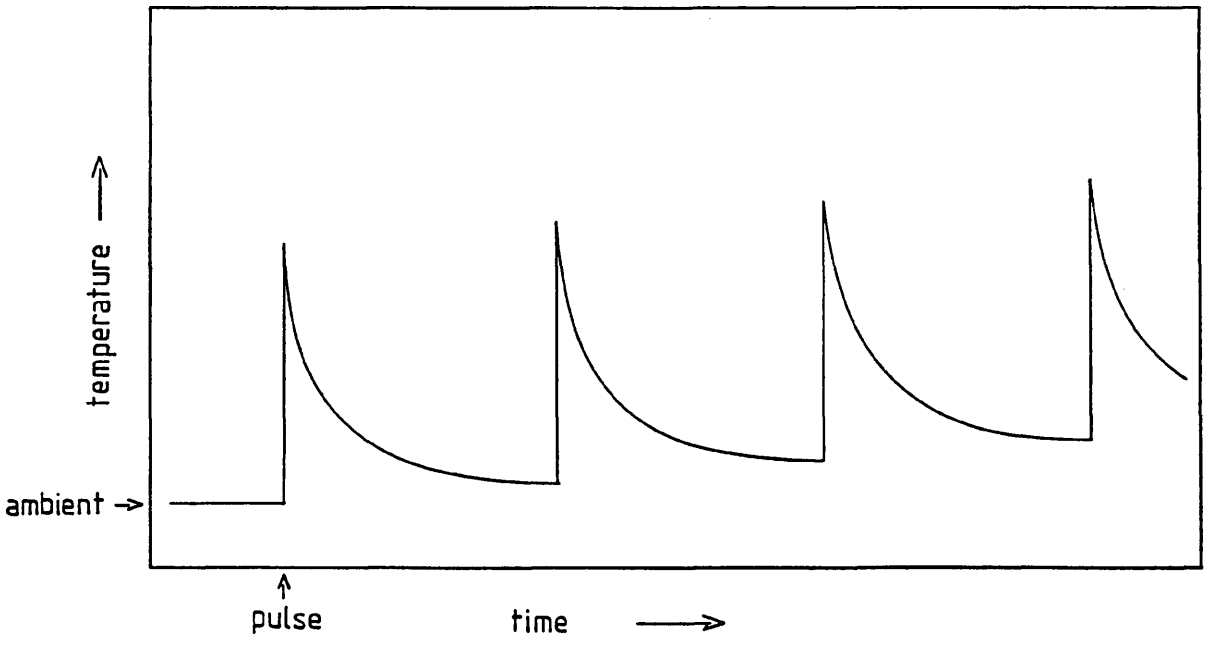

Figure 4.1 Hypothetical surface temperature-time profile for pulsed laser heated sample.

4.2 Experimental Approaches to Determination of Thermal Response

The experimental work carried out in this study fell into two main categories.

1. Attempted direct measurements of beam-induced surface temperature rises using two techniques, infrared optical pyrometry and thermocouple measurements.

2. Determination of actual laser pulse energy densities at the sample during deposition experiments by gas phase absorption studies.

In order to determine the beam-induced heating effects during deposition studies, it was necessary not only to determine the thermal response of ZnSe and GaAs at a given energy density, but also to accurately determine beam energy densities actually encountered at the sample. A short experimental study was undertaken to discover if a simple Beer's Law calculation was adequate in determining gas phase beam absorption. This will be described in a later section.

4.21 Direct temperature measurement.

Surface temperature measurement using a thermocouple, although experimentally straightforward, immediately presented drawbacks as a result of the limitations of sample attachment. Attaching the thermocouple tip to the front face suggested two problems, the first being that the thermocouple tip shadows the local sample region from the laser radiation causing the heating, so any heat being detected must diffuse from the surrounding surface region. The second drawback is that of the minimal contact area of a roughly spherical

thermocouple tip in contact with a microscopically smooth substrate face, reducing heat transfer efficiency from sample to probe.

In view of these drawbacks, it was decided to explore the use of infrared optical pyrometry to measure surface temperature rises. As a non-intrusive technique, simply detecting radiation emitted from the heated body, it appeared to be promising, possessing none of the drawbacks of thermocouple attachment.

4.22 Emission of Radiation and Pyrometry

The radiative process occurs when a temperature differential exists between a sample and the local environment. Although the sample is not in thermal equilibrium with its surroundings, if it has a uniform temperature it may be considered to be in equilibrium within itself. A blackbody distribution of radiation will be maintained inside the sample as a result of a dynamic process in which the rate of absorption of photons at a given frequency must be balanced by an equivalent rate of re-emission. Therefore, at frequencies for which the absorption coefficient is high, the rate of emission is also high[1]. A fraction of radiation exits the sample and is not balanced by an equivalent influx of radiation unless the sample and environment are in thermal equilibrium. Spectral or monochromatic emittance ϵ is defined as the ratio of radiant flux (watts) leaving the surface of a body at a given temperature and wavelength to that of a blackbody radiating at the same conditions. If ϵ is weighted over the spectral distribution of the blackbody the wavelength independent or total emittance ϵ_t is obtained.

Semiconductor behaviour departs from that of a blackbody due to the presence of the forbidden energy gap and a corresponding cutoff in emitting frequencies. Pyrometers detect a certain bandwidth of radiation, and the emissivity setting is actually the spectral emittance, given by

$$\epsilon = \frac{(1-R)(1-\exp(-\alpha.t))}{(1-R)\exp(-\alpha.t)}$$

where R = reflectivity, α = absorption (cm^{-1}) and t = sample thickness (cm)

This equation has two limits of interests defined by the absorption behaviour of the semiconductor. At wavelengths shorter than the bandgap where the material is highly absorbing, $\epsilon = (1-R)$. In this region, GaAs can be treated as a "grey body" emitter. The emittance of GaAs above the band gap is found experimentally to vary with wavelength from 0.6 - 0.68, with a corresponding change in reflectivity[2], and this is insensitive to temperature and doping level. For wavelength bands greater than the bandgap, GaAs is not strongly absorbing, and spectral emittance is given approximately by $\epsilon = \alpha.t$. The main absorption process in the near-infrared region is free carrier absorption (FCA), which is dependent on temperature and particularly doping level.

4.23 Initial experiments

The first pyrometer that became available for use was a Minolta Cyclops 33. This device has an operating bandwidth of 8 - 12 µm, the spectral region in which GaAs emittance is governed by FCA processes. A short experimental programme was carried out to determine whether any meaningful results could be obtained until a more suitable pyrometer became available.

Initially an attempt was made to calibrate the pyrometer against a piece of GaAs at a known temperature. This was complicated by the fact that one could not observe a sample pressed against a heater, because of the IR transparency of the GaAs the heater temperature was measured rather than that of the sample. This was overcome by the method shown in figure 4.2. A heater consisting of a movable wire wound silica tube furnace was employed.

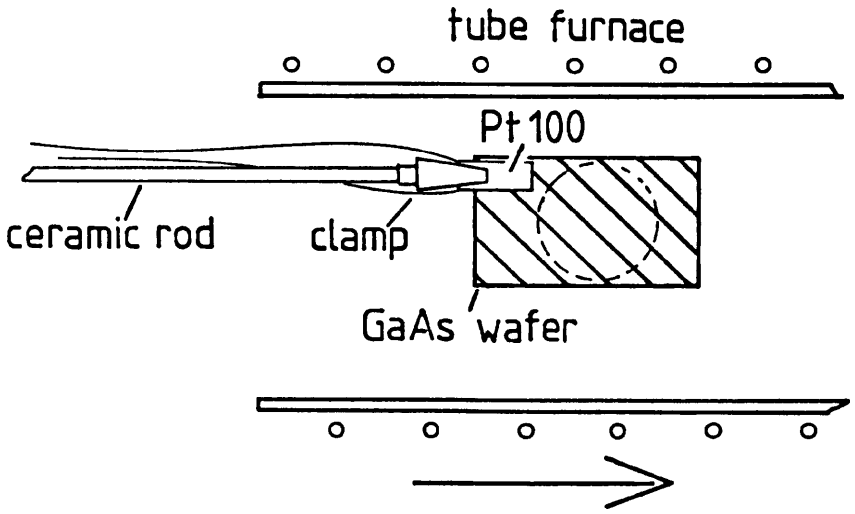

Figure 4.2 The tube furnace was slid in direction indicated to reveal hot sample to pyrometer. The ring shows region of sample visible to pyrometer.

The Cyclops 33 pyrometer was used in much the same way as a camera, the sample being observed through a viewfinder and the main lens adjusted until the sample was brought into focus. A target graticule in the viewfinder defined the area over which radiation was detected, and at the minimum focussing distance of 75 cm the measurement spot had a 13 mm diameter.

A wafer of n-type GaAs (10^{18} cm^{-3}) was cut to a 15 x 25 mm rectangle to ensure the sample filled the detection area, and was held at the end of a fixed arm. A platinum resistance thermometer was attached

to an upper corner of the sample out of view of the pyrometer. The pyrometer was aligned before the furnace tube was slid into place, and the sample raised to an appropriate temperature. An emissivity setting between 0 and 1 has to be dialled into the pyrometer, and a value of 0.6 was chosen initially. Temperature measurements were made by reading the temperature value displayed digitally in the viewfinder. Once at temperature, the furnace tube was slid away and pyrometer readings were taken as the Pt100 values passed through 10°C increments.

Figure 4.3 shows that equivalent readings were obtained in the 80°C region, the pyrometer giving the lower reading at greater temperatures and the higher reading at lower temperatures.

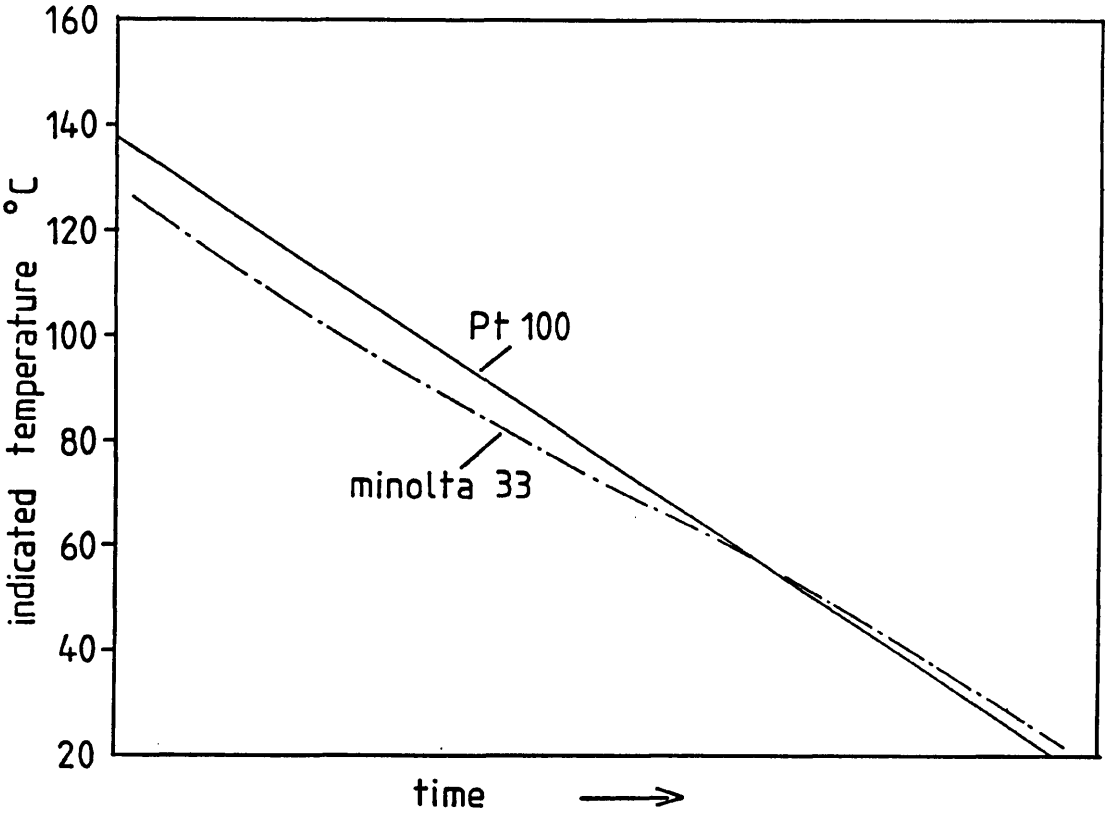

Figure 4.3 Pyrometer reading of GaAs wafer temperature with linear projection of equivalent Pt100 resistance thermometer.

This result is in overall agreement with the calculated results of Jordan[2] for n-type GaAs emittance in the 8-12 μm range. For a thickness-doping product of 5 x 10^{16} cm^{-2} the spectral emittance in this region was calculated as being approximately 0.6. The GaAs substrate thickness was 450 μm, and provided the wafer is hot over its entire depth, a 10^{18} cm^{-3} doped sample has an effective thickness-doping product of ~5 x 10^{16} cm^{-2}.

Measurements of GaAs under irradiation by pulsed excimer laser were then undertaken. The Cyclops 33 integrates readings taken over 1 second, and then displays the average value during that period, and so it was not be possible with this instrument to directly observe transient profiles such as figure 4.1.

A schematic of the experimental arrangement is shown in figure 4.4. The GaAs sample was held at the centre of the vacuum chamber, the beam focus positioned to ensure that the entire front face of the sample was irradiated. The sample was observed through a side port, the usual silica window having been replaced by an infrared transparent KBr window.

4.24 Experimental Results

The experimental results are summarised in figure 4.5. As the emissivity is determined by the absorption-thickness product, the emissivity increases throughout the experiment as the heated depth increases. The initial rate of rise given by this method cannot, therefore, be taken as reflecting the true rate, but the equilibrium temperature can be taken as an approximation to the true equilibrium

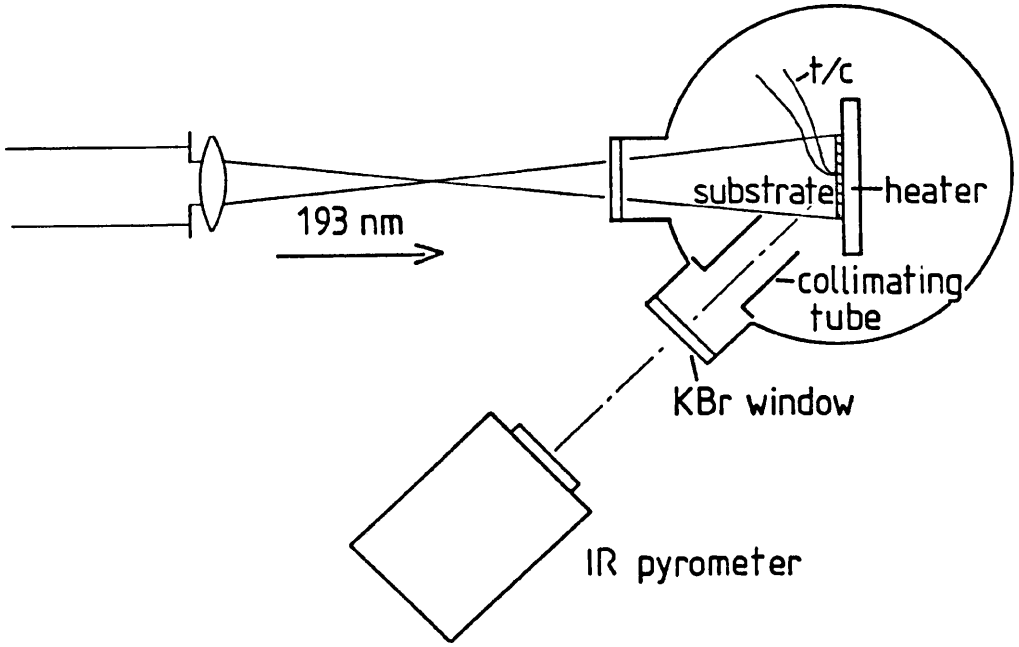

Figure 4.4 Schematic of experimental arrangement of pyrometric temperature measurements of pulsed laser irradiated sample. Position of thermocouple used for later thermocouple measurements is also indicated (section 4.4)

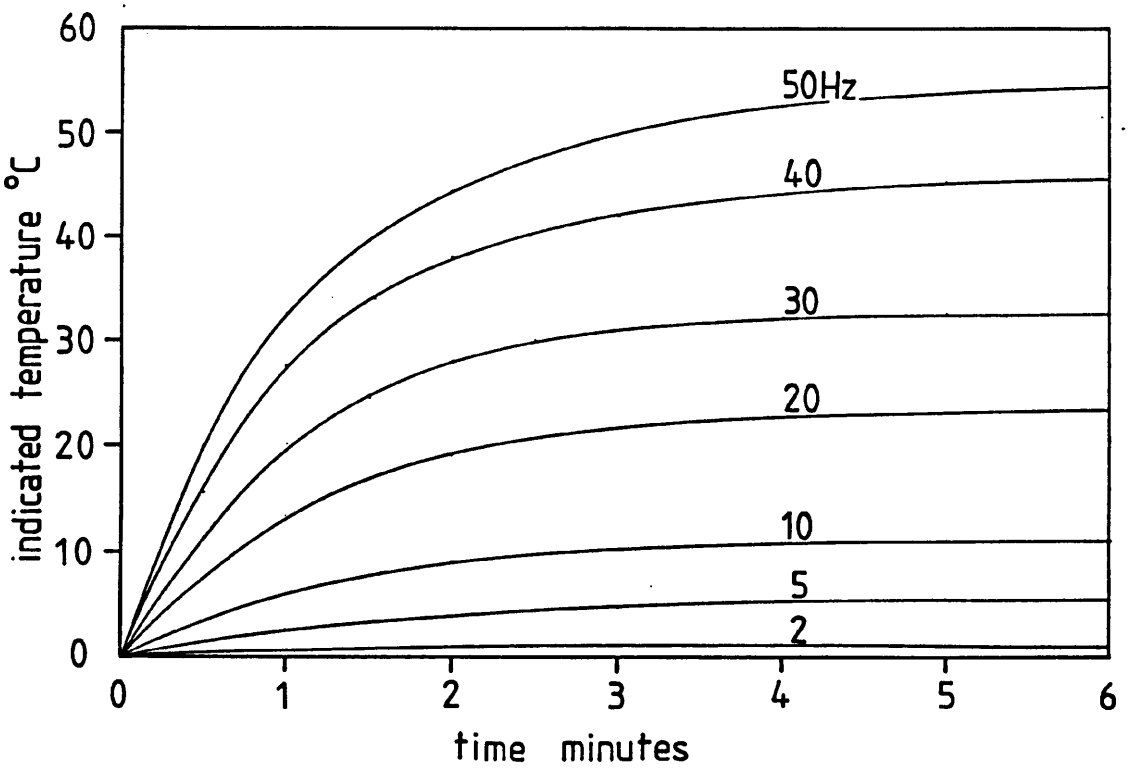

Figure 4.5 Temperature increases of GaAs wafer indicated by Minolta 33 pyrometer. E_{ds} = 15 mJ cm^{-2}, ambient temp ~20°C.

temperature, although a decreasing temperature gradient from the front to rear sample surface will reduce the overall emission from the sample and lower the indicated temperature.

4.3 Temperature Measurement using the IRCON 4000

The second pyrometer to become available for use was an IRCON model 4000. This device is usually installed in an MBE system[3,4] and has an operating bandwidth of 0.7 - 0.95 μm, corresponding to photon energies of 1.31 to 1.77 eV. The room temperature band gap of GaAs is 1.42 eV, but the band gap is temperature dependent and is given by[5]

$$E_g\ (T) = E_g\ (0) - [aT^2/(T + B)]$$

where $E_g(0) = 1.519$ eV, $a = 5.405 \times 10^{-4}$ eV K^{-2} and $B = 204$ K

Although at low temperatures GaAs is partially transparent to the detector, the band gap progressively decreases with temperature. At 300° C the band gap is 1.29 eV and the GaAs is therefore opaque to the detector. The minimum accurate operating temperature of the IRCON 4000 is still higher at 440° C as it operates at the edge of the blackbody distribution. This defined the minimum experimental temperatures that could be used and was obviously a major limitation.

4.31 Experimental results

GaAs temperature measurements with the IRCON 4000 were made using the same experimental configuration shown in figure 4.4. During preliminary attempts at measuring the temperature of a resistance heated sample, great discrepancies were noted between the pyrometer and Pt 100 readouts. It was apparent that infrared radiation from the heater was being reflected from the cell walls and was swamping radiation emitted from the sample, preventing accurate measurement.

This was overcome to some extent by shielding the heater with stainless steel foil, to prevent radiation from the windings being transmitted through the silica heater plates, and fitting a collimating tube inside the cell between the KBr window and the sample, to minimise stray radiation reaching the detector (figure 4.4). With these modifications, results typified by figure 4.6 were obtained. This shows simultaneous pyrometer and Pt100 readings plotted against time from switch on of the resistance heater.

The initial transparency of the GaAs results in a ~400°C discrepancy in readings. The pyrometer reading immediately begins to drop as the sample rear face opacifies. When the resistance thermometer gives a reading of 300°C, at which point the sample front face should be opaque, there is still a ~100°C gap in readings due to stray radiation.

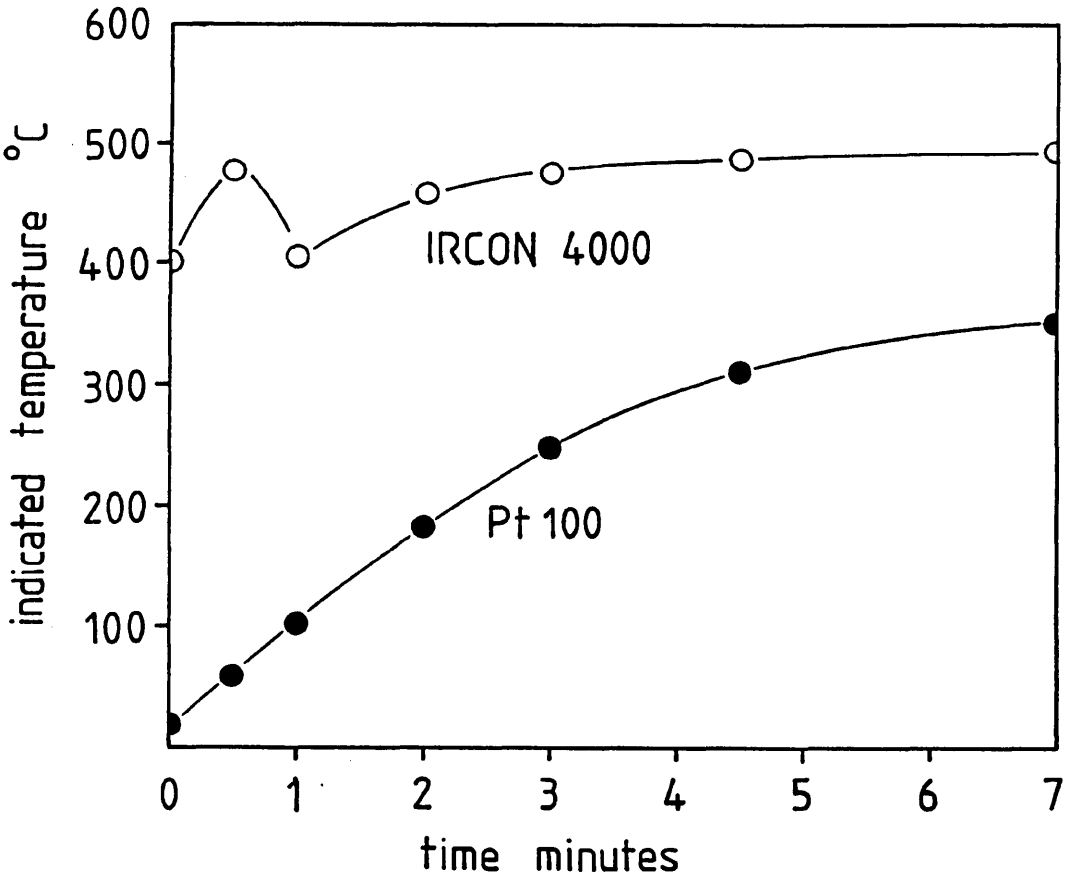

Figure 4.6 IRCON 4000 IR pyrometer and Pt100 temperature readings for same sample. Note drop in pyrometer reading as sample rear face opacifies.

The sample was taken to a temperature of 440°C (Pt100 reading) to ensure that the radiation emitted by the sample was within the pyrometer detection limits, at which point the sample was subjected to pulsed laser radiation. At maximum power conditions of 20 mJ cm^{-2} energy density (E_{ds}) and an operating rate of 30 Hz, a minimal rise of 2°C was observed.

The infrared pyrometry work performed with the Minolta Cyclops demonstrated that GaAs substrate temperatures could be made to depart appreciably from low ambient temperatures at representative laser pulse energy densities. However, the instrument detection wavelength

bandwidth gave results which could not be accurately interpreted. The IRCON 4000 pyrometer was restricted to a high minimum operating temperature, but even allowing for background interference seemed to show that at ~450° C ambient laser induced temperature rises were negligible.

4.4 Thermocouple Measurements

In view of the limitations of both sets of measurements it was decide to undertake thermocouple measurements in spite of the limitations outlined in section 4.21. The thermocouple did have the advantage that a full set of measurements could be taken over a wide ambient temperature range, and any trends in temperature rise over the complete range determined. ZnSe on GaAs could also be studied.

4.41 Experimental

A chromel-alumel thermocouple of minimal tip diameter was fabricated from 0.125 mm wire. The tip was dipped in molten Ga until a small blob attached itself to the contact area. Whilst warm the thermocouple was pressed against the sample face so that the Ga wetted the surface, increasing the contact area. Care was taken to ensure that no excess Ga emerged from around the tip, increasing the shadow area. Thermocouple measurements were performed on a 1 μm ZnSe on GaAs epilayer grown by MOCVD. Measurements were obtained over an ambient temperature range of 40-350°C, pulse energy densities of 5-20 mJ cm^{-2}, and operating rates of 2-50 Hz. All results were obtained in vacuo apart from some measurements performed under an ambient atmosphere of 0.4 Torr Ar to approximate deposition conditions.

4.42 Thermocouple Measurement Results

All the thermocouple measurements are displayed in table 4.1. and are presented as the equilibrium surface temperature reached under laser irradiation and the initial rate of rise of the thermocouple reading. Representative results and trends exhibited are displayed in figures 4.7 - 4.9. The effect on surface temperature of irradiating at a fixed pulse energy (10 mJ cm^{-2}) and varying the laser operating rate from 2-50 Hz is shown in figure 4.7. The curves displayed are chart recorder readings of the thermocouple output. The pulsed heating effect of the laser is not reflected in the curves which show a smooth rise in temperature, the thermocouple being unable to respond to the brief temperature transients. Not unexpectedly the rate of rise and equilibrium temperature rise with operating rate. The surface temperature rises steeply on opening the laser shutter, particularly at the higher operating rates, with the equilibrium temperature attained within 20 seconds at low rates and 50 seconds at the higher rates. Although the rate of rise in $^{\circ}C\ s^{-1}$ increases with operating rate, figure 4.8 shows the rate of rise per pulse stays roughly constant over the range 2-50 Hz.

As mentioned in section 4.1, this rate of rise is determined by the extent to which the surface temperature has cooled between pulses. The temperature rise per pulse (i.e. the temperature to which the surface has cooled to before the next pulse arrives) is roughly constant from 2-50 Hz, demonstrating that the temperature decay curve is quite flat over the 20 - 500 ms range, and the pulse energy is distributed evenly over the bulk of the substrate well within a 20 millisecond time interval (the shortest period that could be

ZnSe on GaAs 40°C ambient

5 mJ cm^{-2}

	2	5	10	20	30	40	50
R_{in}	0.11	0.34	1.02	2.13	3.53	4.56	—
T_{eq}	2.5	7.0	20.0	37.5	57.5	72.5	—

10 mJ cm^{-2}

	2	5	10	20	30	40	50
R_{in}	0.39	0.73	1.88	4.45	6.57	7.38	12.0
T_{eq}	6.5	13.5	32.5	64.5	85.5	113.0	126.0

15 mJ cm^{-2}

	2	5	10	20	30	40	50
R_{in}	0.30	0.92	2.23	3.56	6.85		
T_{eq}	4.5	16.5	32.5	64.0	89.0	117.5	131.0

20 mJ cm^{-2}

	2	5	10	20	30	40	50
R_{in}	0.48	1.47	2.89	4.04	6.50	10.78	—
T_{eq}	9.0	11.0	40.0	76.0	107.0	129.0	—

100°C ambient

5 mJ cm^{-2}

	2	5	10	20	30	40	50
R_{in}	—	0.26	0.64	1.63	2.55	4.36	4.41
T_{eq}	—	6.0	11.0	22.0	37.0	53.0	55.5

7.5 mJ cm^{-2}

	2	5	10	20	30	40	50
R_{in}	0.25	0.5	1.24	2.4	3.53	—	—
T_{eq}	4.0	7.0	17.5	36.0	49.0	—	—

10 mJ cm^{-2}

	2	5	10	20	30	40	50
R_{in}	0.28	0.73	1.37	3.16	4.90	7.54	9.14
T_{eq}	5.0	11.0	22.5	45.0	65.5	83.0	96.5

15 mJ cm^{-2}

	2	5	10	20	30	40	50
R_{in}	0.22	—	1.80	—	6.45	11.1	—
T_{eq}	3.0	—	26.0	—	70.0	91.0	—

Table 4.1 Thermal response of ZnSe layer/GaAs substrate. Equilibrium temperature rise (T_{eq}) and initial rate of rise (R_{in}).

200°C

5 mJ cm^{-2}

	2	5	10	20	30	40	50
R_{in}	0.18	0.60	1.37	3.15	4.93	6.16	7.04
T_{eq}	2.0	7.5	16.0	30.5	48.0	—	

10 mJ cm^{-2}

	2	5	10	20	30	40	50
R_{in}	—	1.03	1.67	3.33	5.81	7.41	—
T_{eq}	—	12.0	18.5	36.0	57.5	74.0	—

275°C

5 mJ cm^{-2}

	2	5	10	20	30	40	50
R_{in}	—	—	0.65	1.78	2.31	3.05	—
T_{eq}	—	—	6.5	14.0	19.0	24.5	—

7.5 mJ cm^{-2}

	2	5	10	20	30	40	50
R_{in}	—	0.52	0.83	1.85	4.27	—	—
T_{eq}	—	5.0	11.0	22.0	36.0	—	—

325°C

20 mJ cm^{-2}

	10	30
R_{in}	1.39	5.82
T_{eq}	11.0	45.5

350°C

15 mJ cm^{-2}

	10	30
R_{in}	1.78	4.87
T_{eq}	9.5	33.5

0.4 Torr 300°C ambient

5 mJ cm^{-2}

	5	10	20	30	40	50
R_{in}	—	0.65	1.45	—	2.53	—
T_{eq}	—	3.5	8.0	—	13.0	—

15 mJ cm^{-2}

	5	10	20	30	40	50
R_{in}	0.76	1.38	4.48	6.34	8.13	—
T_{eq}	4.0	9.0	16.0	24.5	33.2	—

Table 4.1 (cont.) Results for an ambient atmosphere of 0.4 Torr are included. Values are slightly reduced compared to sample in vacuo.

'observed', defined by the 50 Hz maximum laser operating rate).

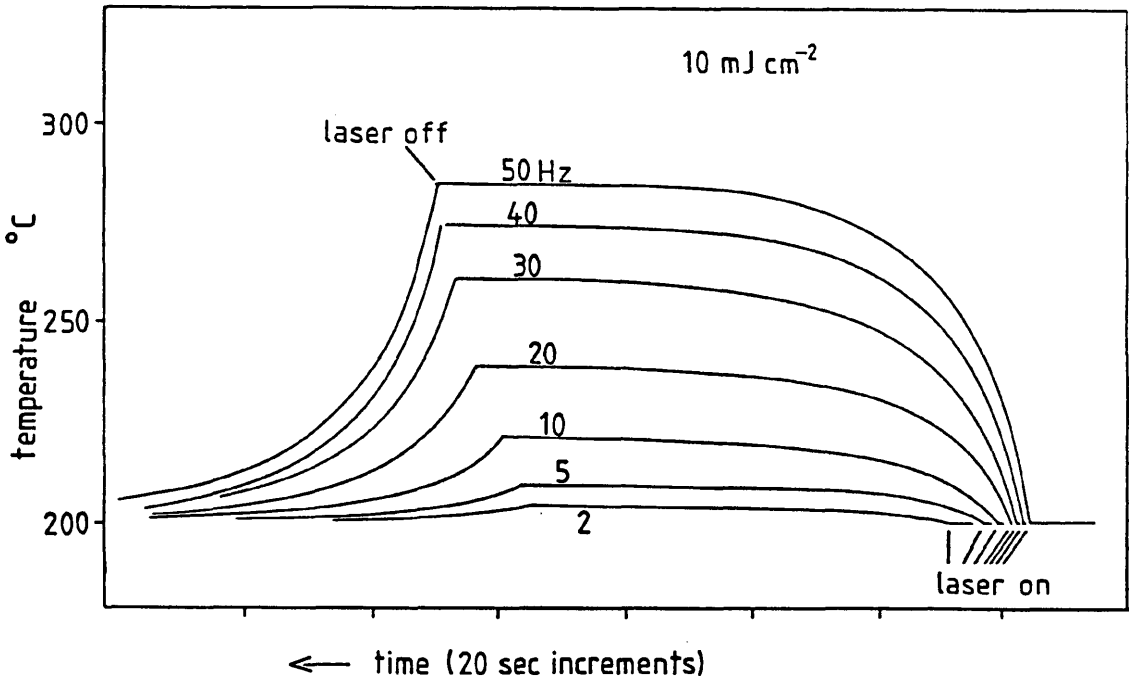

Figure 4.7 Chart recorder readings of thermocouple outputs of ZnSe on GaAs surface. Energy density fixed at 10 mJ cm^{-2}, 200°C ambient.

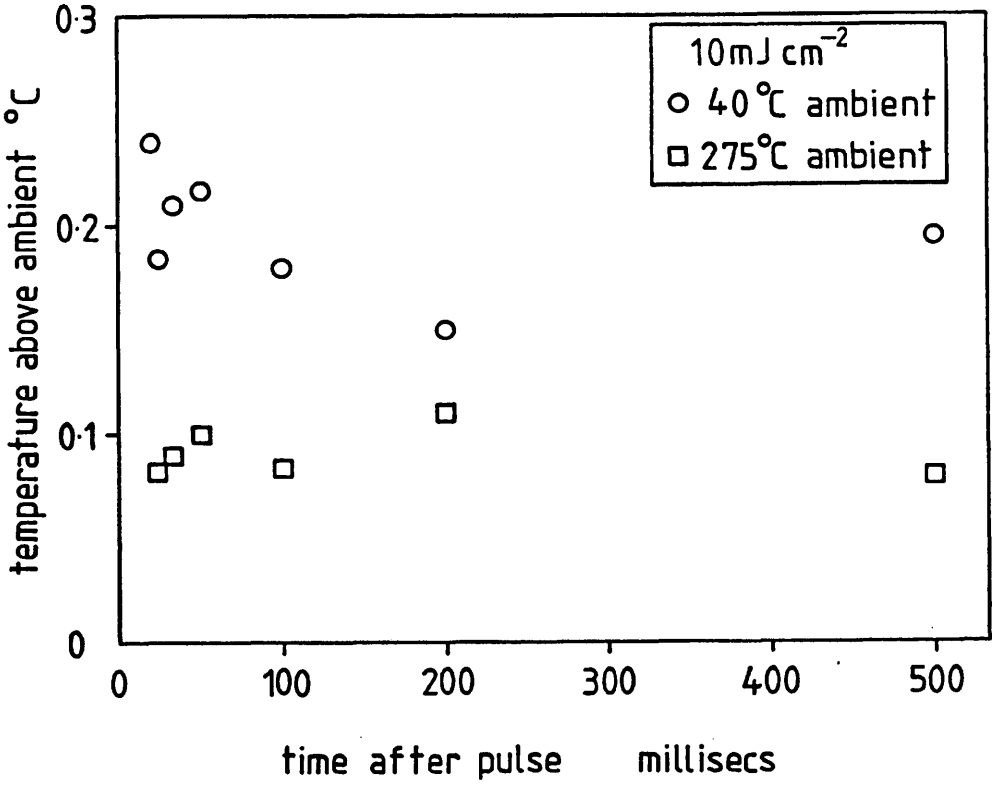

Figure 4.8 Initial rate of rise at fixed E_{ds} of 10 mJ cm^{-2} and varying operating rate from 2-50 Hz. Rates are divided by laser frequency to give rate of rise per pulse and are presented against pulse separation to give an approximation to temperature decay curve for a single pulse.

Figure 4.9 shows chart recorder temperature-time profiles for a fixed operating rate of 30 Hz and energy densities varying from 5-15 mJ cm^{-2}. The rate of rise and equilibrium temperature increase as more energy is delivered to the sample in a given time.

The effect of varying the ambient temperature on the laser-induced temperature rise is shown in figure 4.10. Interestingly the change in ambient temperature has a marked effect on the final rise, which decreases from 90°C to 30°C over the ambient range 40 to 350°C at the laser parameters given. This decrease in rise with increasing ambient temperature was observed for all laser operating conditions studied and the change in rise with increasing ambient is shown graphically in figure 4.11 for 30 Hz operating rate and 20 mJ cm^{-2} E_{ds}. The 440°C point was the result obtained using the IRCON 4000 IR pyrometer and this result is shown to be clearly of the right order.

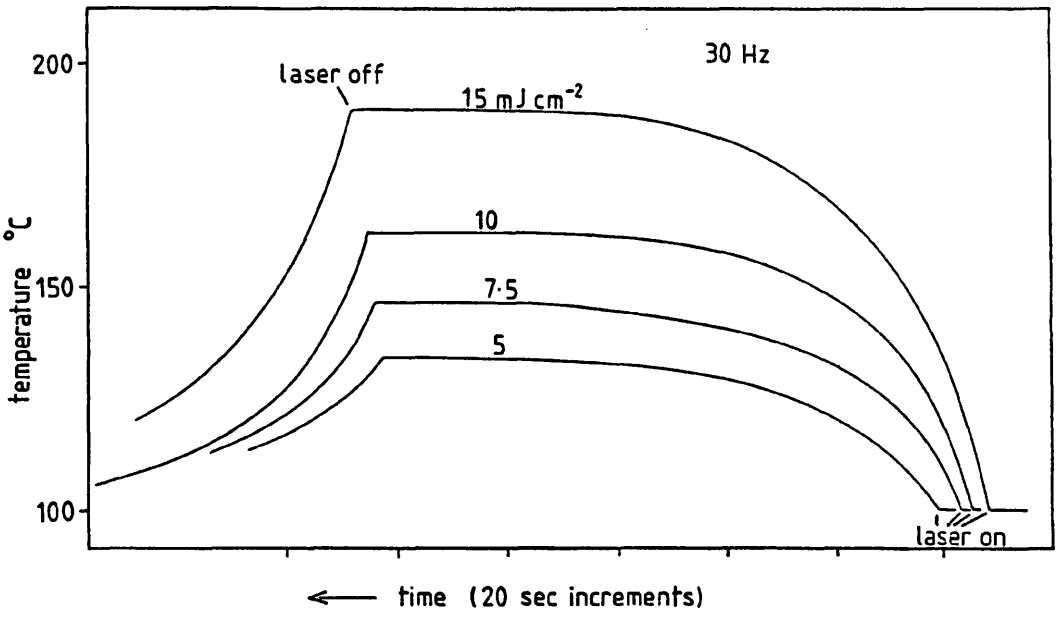

Figure 4.9 Increase in equilibrium surface temperature with increasing pulse energy, 100°C ambient, 30 Hz operating rate.

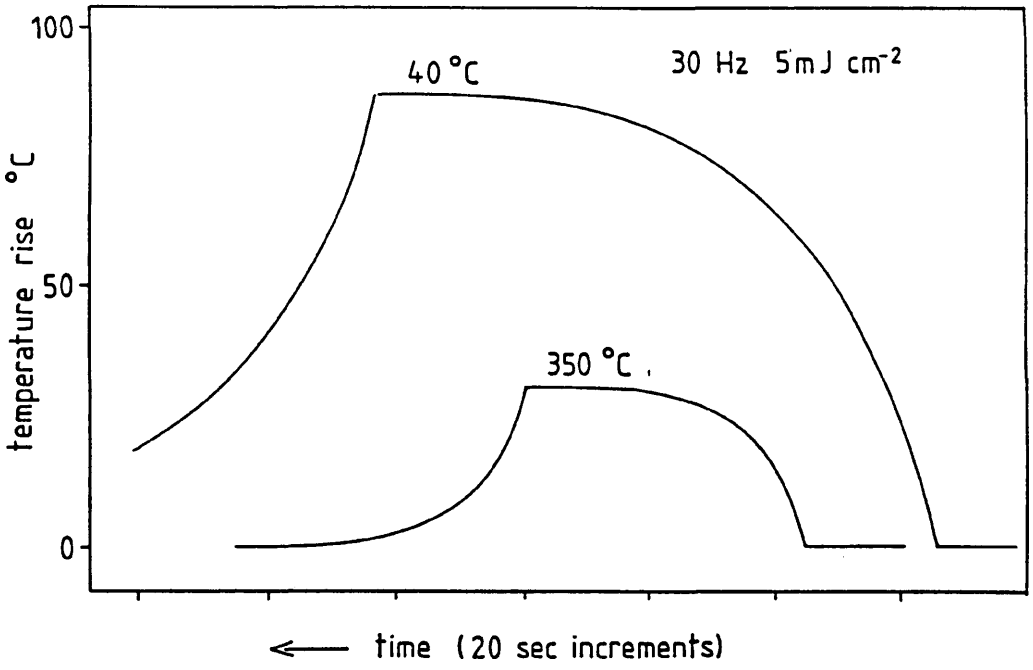

Figure 4.10 Effect of increasing ambient temperature on extent of laser-induced temperature rise.

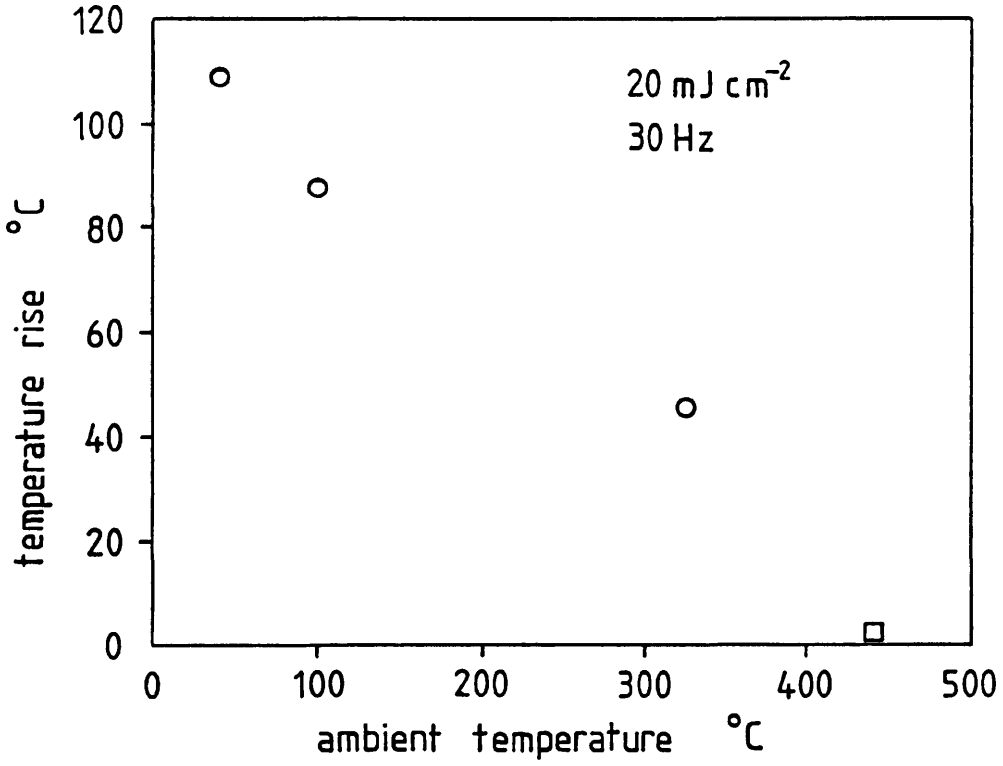

Figure 4.11 Equilibrium temperature rises at 30 Hz, 20 mJ cm^{-2} from 40°C - 440°C ambient. Square point is IRCON 4000 reading.

4.43 Comparison to Minolta 33 readings

A comparison with the Minolta 33 pyrometry results obtained at equivalent energy densities and operating rates shows as expected that the pyrometer was underreading due to the temperature gradient through the sample, resulting in bulk emissivities lower than the irradiated surface value. The pyrometer readings are < 0.5 x equilibrium thermocouple values, and the rates of rise are ~0.05 thermocouple values.

4.5 Determination of Deposition Energy Levels

In order to simulate, either experimentally or by calculation, actual beam induced temperature rises, it is of course necessary to know values of actual energy densities at the substrate during deposition. Gas phase absorption values for DMZn and DESe are known, as well as deposition partial pressures, which allows a Beer-Lambert calculation to be made for the cell path length. The validity of this approach was questioned because the measurements of gas phase absorption are made with lamps operating at much lower power densities than the laser power levels encountered during deposition. Non linear processes occurring under laser illumination, such as laser induced fluorescence and ionisation, do not occur or do not contribute to the spectrometer derived gas phase absorption values. Attempting to calculate absorption taking into account these extra effects was not felt to be practical, and a direct measurement of gas phase absorption at deposition power levels was necessary.

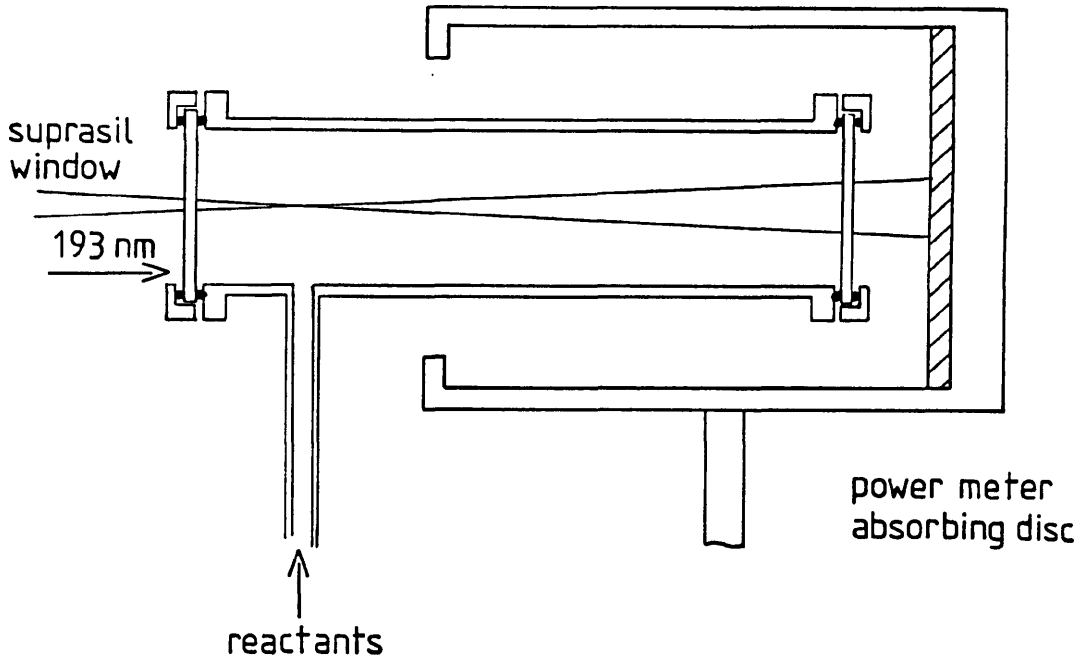

Figure 4.12 Transmission cell for gas phase absorption measurements

A diagram of the experimental configuration used for absorption studies is shown in figure 4.12. The deposition reactor is simulated with a stainless steel tube fitted with flanges to mount suprasil windows. The separation between window inner surfaces was 9 cm, equivalent to the deposition reactor path length. A 1/4" stainless steel pipe ending in a VCR male fitting was welded to the tube to allow direct attachment to the deposition system vacuum and gas handling equipment. DMZn and DESe could then be admitted to the cell after evacuation, reactant partial pressures being measured with the Baratron in the same way as deposition experiments. The gas entry pipe was fixed to one end of the transmission tube, so most of the tube could be inserted into the body of the power meter absorbing head to minimise air transmission losses.

The deposition geometry was reproduced with the beam focusing lens and 10 x 5 mm mask being positioned at the same distance from the entry window front surface resulting in equivalent beam cross section dimensions at the entry and exit windows of the transmission tube and the entry window and the substrate in the deposition cell.

4.51 Experimental Procedure

During irradiation, deposition occurred on the rear window surface, so power readings were taken as quickly as possible and the evacuated cell transmission was measured before and after every absorption measurement. Gas phase absorption was determined by taking the power meter reading at the point of closing the laser shutter, and calculating the decrease in transmission using the subsequent evacuated cell transmission. Laser power levels were measured before and after each absorption reading to ensure no drift in output had occurred. Three readings were taken at each power level/$P_{reactant}$ combination and averaged.

4.52 Results

The results are summarised in table 4.2. A comparison with Beer-Lambert calculated absorptions shows that transmission was actually higher than predicted (15% for 0.1 Torr DMZn, 40% 0.3 Torr DESe), and the percentage transmission increased with increasing power levels. Both these results suggest that for the laser power/$P_{reactant}$ regime studied, absorption processes saturated at the high cell entry power

densities used. This is also consistent with analyses of the deposited material on the entry window during ZnSe growth studies.

pulse energy mJ cm^{-2}	0.3 Torr DESe	%trans	0.1 Torr DMZn	% trans	0.4 Torr P_{tot}	%trans	0.8 Torr P_{tot}	% trans
30	61	(40)	68	(15)	56		19	
50	67	(40)	75	(15)	66		29	
70	73	(40)	77	(15)	68		34	

Table 4.2 Measured transmissions of DMZn and DESe at laser energies used during deposition experiments. Note transmission increases with increasing pulse energy. Bracketed values are calculated from absorption coefficients.

Although the layer material deposited in the 7.5-30 mJ cm^{-2} energy density range used was stoichiometric, EDAX analysis of the window material showed it to be 80-90% Se, the remainder Zn.

It appears that the initially low DESe photolysis rate increased when moving toward the high intensity beam focal region, resulting in the excess Se:Zn ratios found in the window deposits. There are apparently enough quanta in the beam focal region to photolyse the majority of all species and, therefore, the reactant partial pressures determine the photolysis rates in the saturated condition and not the relative α values.

The actual energy densities used during deposition conditions of 3:1 $P_{DESe}:P_{DMZ}$, 0.4 Torr P_{total}, were found to be 7.5, 14.5, and 20.5 mJ cm^{-2} for pulse energies of 30, 50 and 70 mJ respectively.

Section 4.6 Thermal Response Calculations

The thermal response of ZnSe on GaAs to pulsed UV laser radiation was also calculated in order to determine the temperature-time profile of individual thermal transients which could not be obtained experimentally and also to act as a comparison with the experimental results that were obtained.

A computer program was developed to calculate the surface temperature transients using an adaptation of the method described by Baeri and Campisano[6]. The calculation is 2-dimensional, i.e. heat is assumed to only flow in the z direction from a surface uniformly heated in the x-y plane. This assumption is valid if the beam cross-section is much greater than the heated sample thickness, as is the case experimentally in the present study.

A numerical calculation allows the effects of thermal parameters which are temperature dependent to be incorporated. One of these is thermal conductivity k, which for GaAs varies from 0.55 - 0.2 W cm^{-1} K^{-1} over the range 300 to 600 K[7]. The GaAs specific heat C_p also increases from 325 - 350 J g^{-1} K^{-1} over this range. The thermal properties of ZnSe display similar trends[8].

The 'sample', consisting of a ZnSe epilayer and GaAs substrate is divided into slices i-n in the x-y plane of DeltaZ thickness. For a time increment DeltaT the energy transferred from one slice to the next by conduction is calculated, the driving force for heat transfer being the thermal gradient between slices, $(T_{i-1} - T_i)/DeltaZ$. One iteration of the calculation leaves each slice at a temperature

T_i. Given that temperature the thermal conductivity of each slice is calculated. The thermal conductivity of each face of a slice is then obtained by averaging the thermal conductivity of a slice and the particular adjoining slice. The energy $DeltaQ_{out}$ lost from slice i as heat is conducted further into the sample to slice i+1 is given by

$$\frac{(T_{i-1} - T_i)}{DeltaZ} \times \frac{(k_{i-1} + k_i)}{2} \times Deltat = DeltaQ$$

The energy $DeltaQ_{in}$ entering slice i from slice i-1 is similarly evaluated, and the total change in thermal energy $DeltaQ_{tot}$ is obtained. A new temperature is then calculated from

$$T = T + \frac{DeltaQ_{tot}}{C_p.density.volume}$$

4.61 Stability Constraint to Calculation

Calculations of this kind are subject to a stability constraint given by

$$\frac{k \cdot Deltat}{C_p.density.(DeltaZ)^2} < 0.5$$

The calculation is not valid if the driving force for heat transfer, the thermal gradient, changes significantly over the timescale of Deltat. Deltat must therefore be small compared to the rate at which the slice temperature alters. Outside of this constraint the simulation becomes unstable, with too much heat being lost from one slice and gained by the next, leading to temperature oscillations that can become divergent. The stability criterion imposes a constraint on minimum slice thickness of ~0.5 μm at which point thermal gradients are so high that a Deltat of ~1 nanosecond is required to stabilise the calculation. This slice thickness is

greater than the absorption depth α^{-1} for ZnSe and GaAs which is of the order of 50 Å. The volume of material over which the laser energy is absorbed is therefore much smaller than can be accommodated in the calculation. However the fact that heat flows rearward into the sample during the pulse duration allows a good approximation to be made even when using 0.5 μm slices.

The rate at which heat is dissipated into the solid is governed by the thermal diffusivity of the material $D=k/C_p.density$. If the light absorption depth α^{-1} is smaller than the heat diffusion length $(Dt)^{0.5}$, the depth to which heat flows during a laser pulse can be approximated by a characteristic heat diffusion length $(2Dt)^{0.5}$, where t is the pulse duration (figure 4.13).

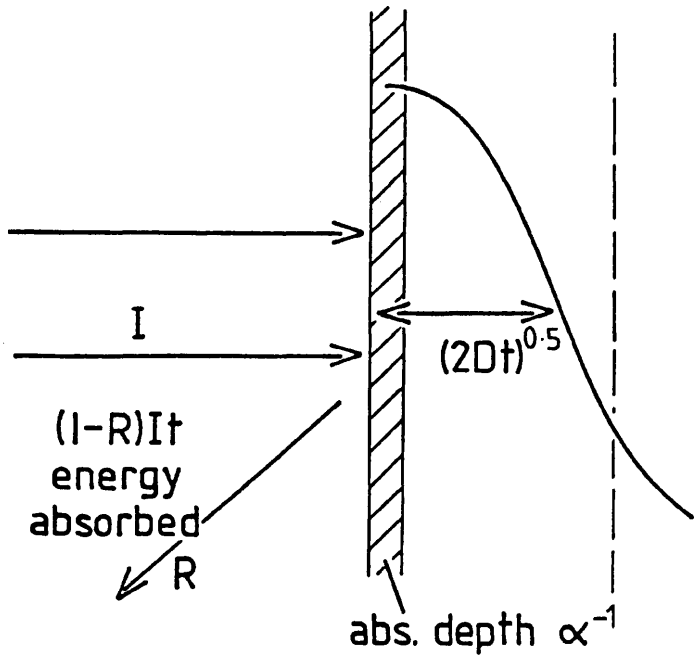

Figure 4.13 The characteristic heat diffusion length $(2Dt)^{0.5}$

For a 15 nanosecond excimer laser pulse and ZnSe $(2Dt)^{0.5}$ is ~0.4 μm. A reasonable approximation can therefore be made by starting the calculation at the end of the pulse and assuming that the energy is distributed over the first 0.5 μm of the epilayer. The maximum surface temperature reached during the pulse will of course be underestimated. The temperature reached at a time t at the surface of a material (z=0) is given by

$$T(o,t) = (2I_o/k)(Dt/\pi)^{0.5}(1-R)$$

Provided $(Dt)^{0.5} > a^{-1}$, the beam cross section is much greater than the sample heated thickness and the irradiance is constant over time t. This latter criterion is not met by the excimer so the temperature given by the above equation will be approximate, but a 20 mJ cm^{-2} pulse gives a temperature rise of ~200 °C, whereas the computer programme gives a rise of 100°C. The temperature given by the above equation is therefore of the right order and are taken as approximately correct. The thermal gradients are so high that the discrepancy in temperatures in the different calculations would actually makes very little difference to the calculated transient profile, as the approximated condition will be reached on a very short (~10 nanoseconds) timescale.

4.62 Calculation Results

Results of the computer simulations are shown in figures 4.14 and 4.15.

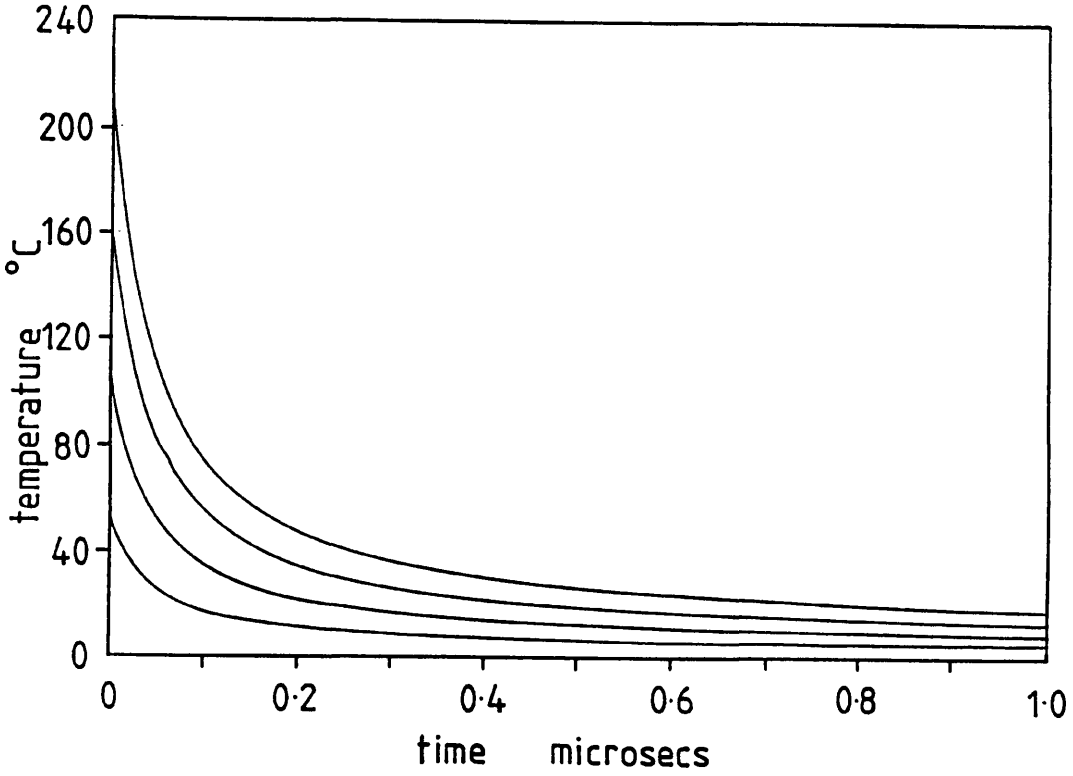

Figure 4.14 Simulated surface temperature-time profiles for pulse E_{ds} 5-40 mJ cm^{-2}. Because calculation underestimates extent of rise, actual pulse energies to create equivalent rise would be ~ 50% those indicated (section 4.61)

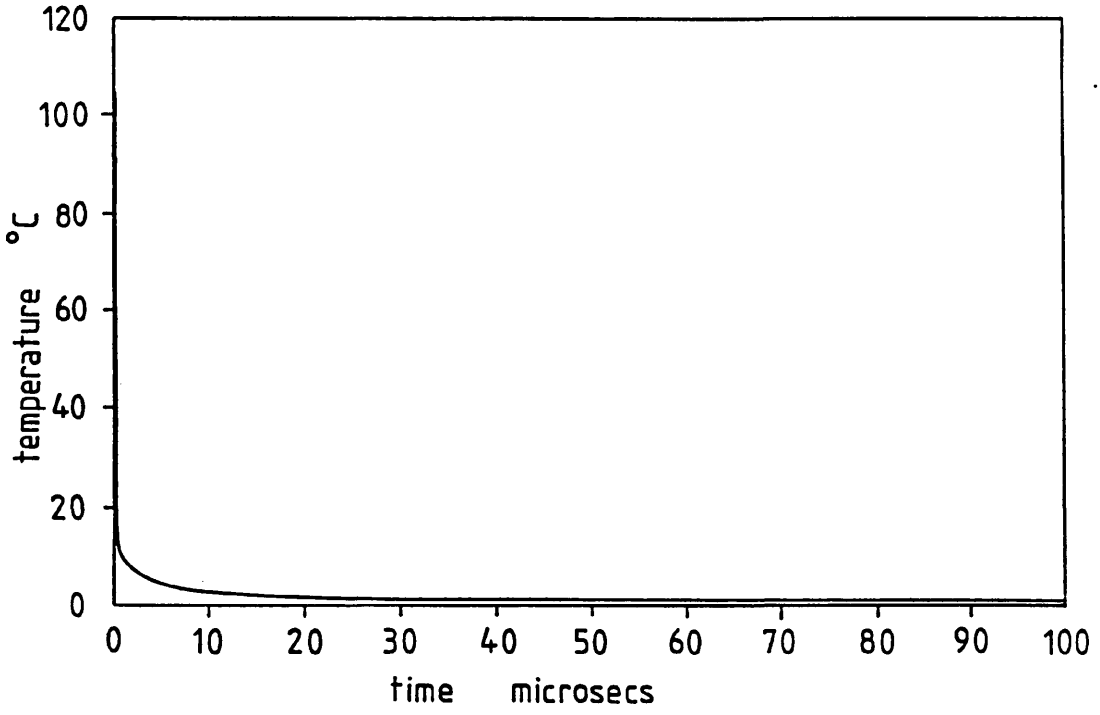

Figure 4.15 Temperature-time profile of 20 mJ cm^{-2} over 100μs after pulse.

The striking feature of the calculated temperature-time profiles is the extremely rapid rate of fall of the surface temperature, with initial rates of the order 2 x 10^9 °C s^{-1}. The 200°C rise due to a 20 mJ cm^{-2} laser pulse falls to 10°C above ambient after ~1μs, and further calculation gave 1°C above ambient at 50 μs, the temperature at a depth of 100μm rising to 0.2°C at this time. The rapid decay and flattening of the decay curve as the heat is distributed evenly over the sample matches the experimental results of figure 4.8. The energy of a 20 mJ cm^{-2} distributed over the depth of a 450μm wafer gives an overall temperature rise of 0.25°C, which matches the experimental results particularly well.

4.63 Decreasing Rise With Increasing Ambient Temperature

As described in section 4.4, the overall equilibrium laser-induced temperature rise decreases markedly with increasing ambient temperature. This is due to a small extent to the increase in specific heat C_p over the temperature range studied. Figure 4.15 shows calculated temperature time profiles for a 40 mJ cm^{-2} pulse at 40°C and 350°C ambients. The temperature rise due to the laser pulse decreases by 8% at 350°C due to the increase in C_p, but this is not sufficient to cause the decreases seen experimentally.

The major factor in the observed reduction is the increase in the fraction of energy emitted as radiation by the sample at elevated ambient temperatures. Treating the sample solely as a piece of GaAs (a good approximation as the IR transparent ZnSe layer represents a minimal fraction of the sample mass), a piece of heavily doped n-type

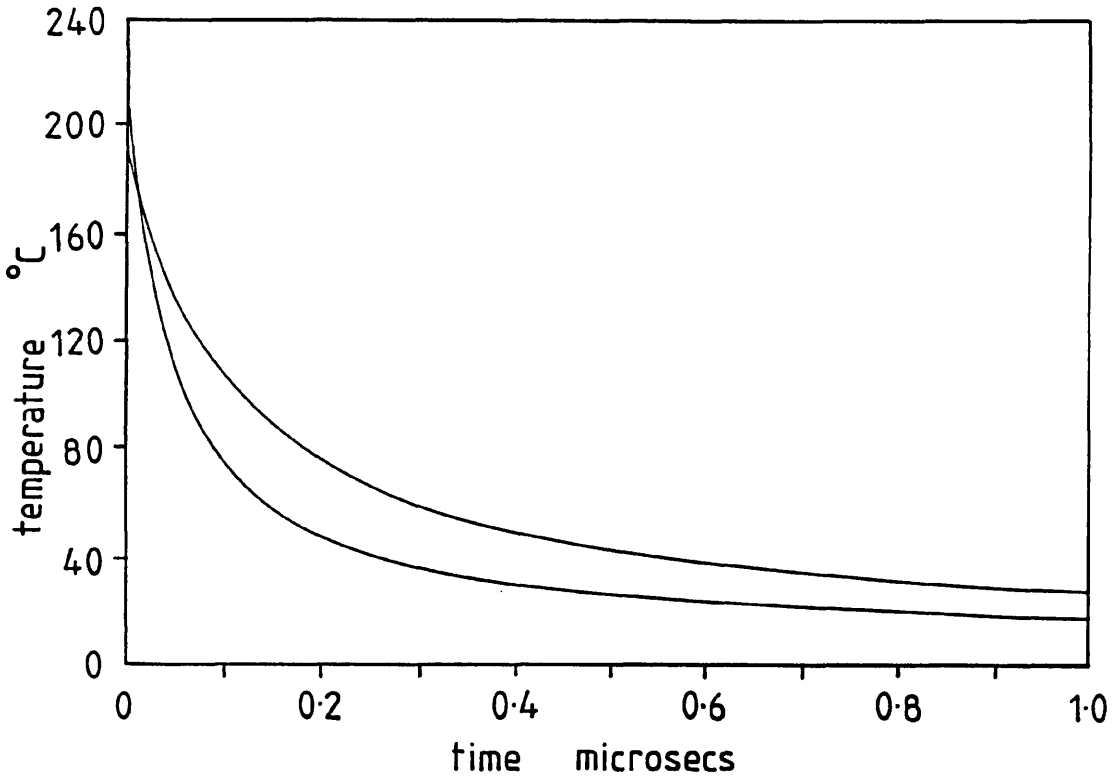

Figure 4.16 Effect of ambient temperature on temperature-time profiles. Note slight difference in maximum temperature due to change in C_p, and reduced temperature fall rate due to decrease in thermal conductivity at 350°C.

GaAs at 40°C will radiate enough energy to cause a drop in temperature of ~0.02°C in 20 ms, the gap between laser pulses at 50 Hz. Emittance of radiation scales with T^4, and the sample at 350°C radiates enough energy to result in a ~0.2°C drop in temperature over 20 ms. The situation is complicated by the flow of heat into the sample from the heater to balance the loss of radiated energy, but this figure agrees closely with observed decreases in the initial rate of rise of ~0.1°C $pulse^{-1}$ (table 4.1).

4.7 Comparison With Growth Rate Results

Referring to figure 3.6, the indicated ambient temperature values are lower than the actual ZnSe average surface temperatures by ~30°C for the 100°C sample, to ~15°C for the 275°C sample, on the basis of the results presented in table 4.1. The onset of pyrolysis appears to be in the ~250°C ambient temperature region, or ~265°C actual. A 15 mJ cm^{-2} pulse will result in a transient of ~150°C, resulting in a surface temperature peak of ~415°C, well above the reported DMZn and DESe pyrolysis threshold temperature of 350°C[9]. The surface temperature would pass below 350°C within 0.1 μs of the laser pulse (figure 4.16). For pyrolysis to occur on this timescale, adsorbate layer pyrolysis is the only route by which it could occur to an appreciable extent. Adlayer coverage will not be greatly affected by the laser temperature transients as the microsecond timescale of those is minimal compared to the surface exposure time between pulses.

4.8 Thermal Shock Damage

Both MOCVD grown thermal test samples and photochemically deposited layers showed no visible signs of damage at the maximum energy densities of 20 mJ cm^{-2} used. However, samples deposited at energy densities not far above this level exhibited delamination due to severe transient thermal stresses. Figures 4.17 and 4.18 show micrographs of a ZnSe layer deposited under an E_{ds} of 30 mJ cm^{-2}.

Internal delamination of the layer and separation from the substrate has taken place. The underlying substrate shows no sign of damage. The ZnSe layer is unable to mechanically withstand the stresses due to transient heating. The maximum temperature rise reached at 30 mJ cm^{-2} is ~ 300°C, establishing a temperature gradient into the layer at the end of the pulse of 6 x 10^6 °C cm^{-1} (300° drop over ~0.5 μm) which established high stresses within the layer resulting in mechanical damage.

The resistance of materials to rapid heating or thermal shock can be considered by comparing the relative thermal shock resistances under specified conditions[10]. The resistance to thermal shock at a constant rate of heating, R, is defined as the heating rate required to effect fracture.

For a constant rate of change of surface temperature the maximum heating rate ϕ_{max} at the point of fracture occurs when the thermal stress σ^{ϕ} equals the fracture stress σ_f.

$$\phi_{max} = R \times \text{shape factor}$$

$$R = \frac{\sigma_f (1-u) D}{E \alpha}$$

where u= Poisson's ratio (dimensionless), D = thermal diffusivity $m^2 s^{-1}$, E = Young's Modulus N m^{-2}, α = linear expansion coefficient C^{-1}, σ_f is in N m^{-2} and shape factor has dimension of m^{-2}.

Although σ_f is not available for ZnSe and GaAs, it can be approximated by yield stress σ_y which for ZnSe[11] is 20 MN m^{-2}. Although values of σ_f or σ_y have not been found, a similar value has been assumed for GaAs although this probably underestimates the true GaAs value.

Evaluating $\sigma_f(1-u)D/E\alpha$ for ZnSe and GaAs we have:

$$R_{ZnSe} \quad \frac{20 \times 10^6 \times (1-0.38) \times 4.2 \times 10^2}{4.78 \times 10^{10} \times 6.84 \times 10^{-6}} = 16000 \ ^\circ C\ s^{-1}\ m^2$$

$$R_{GaAs} \quad \frac{20 \times 10^6 \times (1-0.31) \times 3.2 \times 10^3}{8.55 \times 10^{10} \times 5.73 \times 10^{-6}} = 90000 \ ^\circ C\ s^{-1}\ m^2$$

The shape factor affects the magnitude but not the ratio of these values.

ZnSe scores poorly principally by virtue of its low thermal diffusivity. GaAs scores higher by a factor of ~6 due to its more favourable thermophysical characteristics. As a result GaAs and other III-V compounds such as InP can be subjected to much higher heating rates without damage. As the heating rates are themselves dependent on thermal diffusivity the laser powers these materials can be subjected to are even higher than the above comparison suggests.

The high thermal shock resistance of InP allowed Donnelly and coworkers to deposit epitaxial InP with 100 mJ cm^{-2} ArF 193 nm pulses which were found necessary to completely desorb reaction byproducts[12]. Roth et al[13] deposited epitaxial GaAs by pyrolytic surface heating using a 530 nm pulsed Nd-YAG laser and found the optimum energy density to be 120 mJ cm^{-2}. Below this level polycrystalline material was obtained. The pulse width was 3 ns, and the calculated temperature rise was 1000°C, giving a heating rate of 3×10^{11} °C s^{-1}, whereas the ZnSe layers in this study were damaged at a heating rate of 2×10^{10} °C s^{-1}.

The unfortunate combination of thermophysical properties for ZnSe restricted usable laser energy densities to particularly low levels when compared to those used in other studies and it is probable that material of much higher quality would have been prepared if higher

laser powers could have been used to flash desorb carbon-bearing species. The poor thermal shock resistance encountered imposes a considerable restraint on the available power window for the pulsed laser processing of ZnSe .

Figure 4.16 SEM micrograph of ZnSe layer damaged during growth by thermal shock of 30 mJ cm^{-2} laser pulses (1mm marker)

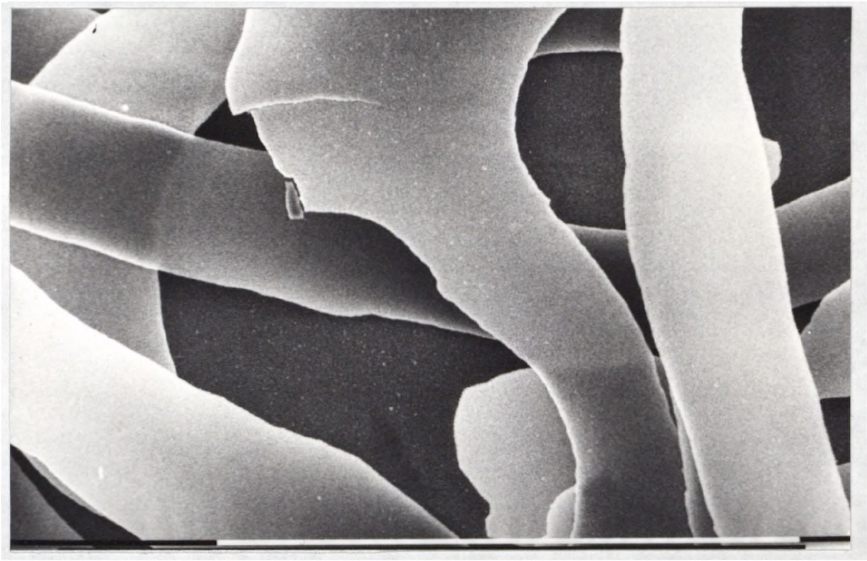

Figure 4.17 Close-up of delaminated material (0.1mm marker)

References

1. Emission of Radiation from Semiconductors, Chapter 7 in Semiconductor Opto-Electronics, ed. S. Moss, Burrell, Ellis.

2. J.S. Blakemore, J. Appl. Phys. 53, R123 (1982)

3. W.E. Hoke, P.S. Lyman, W.H. Labossier, J.Vac. Sci. Technol. B5 (3), 734 (1987)

4. S.L. Wright, R.F. Marks, W.I. Wang, J. Vac. Sci. Technol. B4 (2), 505 (1986)

5. S.L. Wright, R.F. Marks, A.E. Goldberg, J.Vac.Sci. Technol. B6 (3), 842 (1988)

6. P. Baeri and S.U. Campisano, Chapter 4 in Laser Annealing of Semiconductors, ed. J.M Poate and J.W. Mayer, Academic Press 1982.

7. J. Blakemore, J. Appl. Phys. 53 (10), R123 (1982)

8. Landolt-Bornstein, N.S., Vol 17b, Springer, Berlin, 1982, and references therein.

9. G.B. Shinn, P.M. Gillespie, W.L. Wilson, W.M. Duncan, Appl. Phys. Lett. 54 (24), 2440 (1989)

10. personal communication, R. Taylor.

11. Y.A. Ossipyan, Inst. Phys. Conf. Ser. 67 section 1, 11 (1983)

12. V.M. Donnelly, D. Brasen, A. Appelbaum, M. Geva, J. Appl. Phys. 58 (5), (1985)

13. W. Roth, H. Krautle, A. Krings, H. Beneking, in Laser Diagnostics and Photochemical Processing for Semiconductor Devices, MRS Symp. Proc. Vol. 17, p. 193 (1983)

Chapter 5

Laser Induced Plasma Studies Experimental

5.1 Experimental Programme

The laser induced plasma experimental study fell into two main categories:

1. A study of the actual laser induced plasmas consisting of electrical measurements to obtain time of flight information and the variation in plasma behaviour over a range of laser powers.

2. Thin film deposition from the plasmas to determine the potential of this method for depositing epitaxial ZnSe.

All experimental studies were conducted in the same vacuum chamber which was reconfigured as appropriate for the relevant experiment.

5.2 Experimental Apparatus For Thin Film Deposition

The experimental apparatus is shown schematically in fig 5.1. It consisted of four main sections:

1. Lambda Physik EMG 101 excimer laser and optics.
2. Vacuum chamber and sample/target stage.
3. Vacuum system
4. Pure hydrogen supply for sample bakeout.

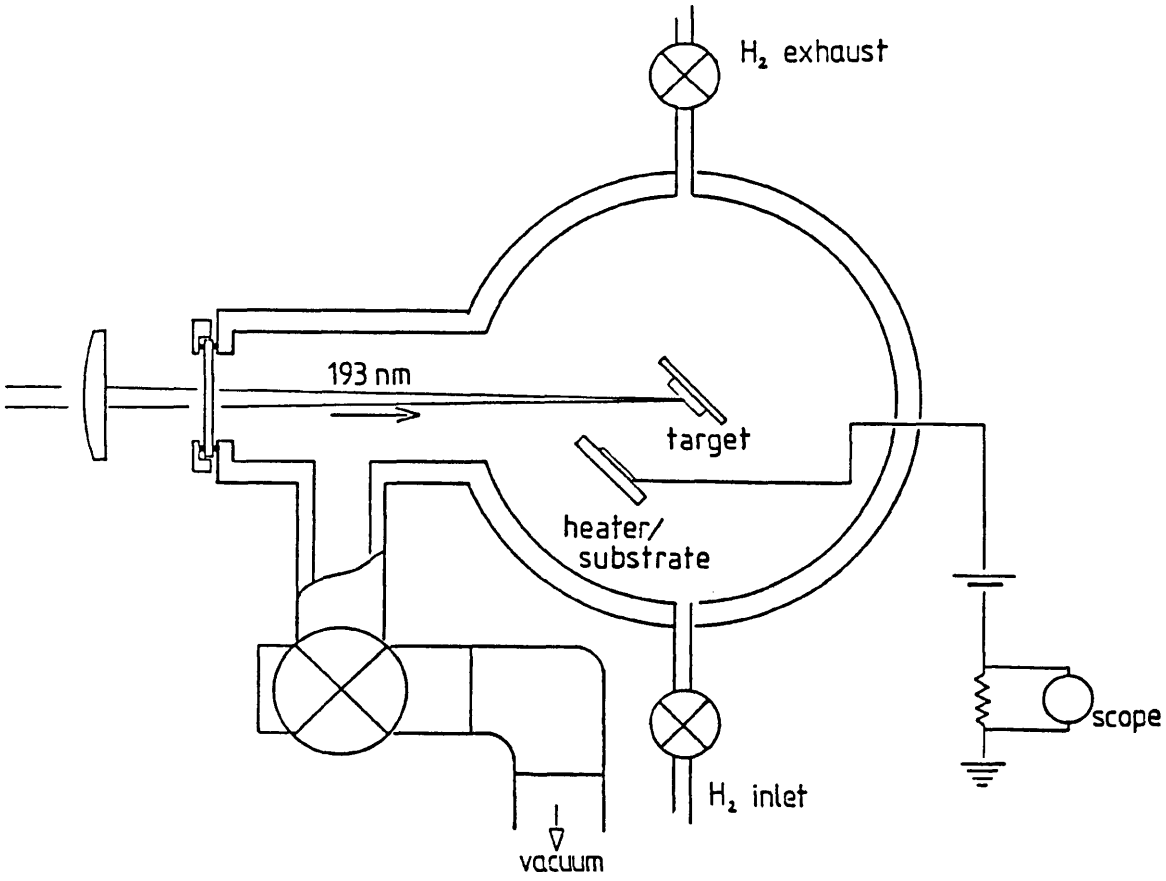

Figure 5.1 Experimental Apparatus

5.21 Excimer Laser and optics

For the laser plasma study as well as the photolytic deposition study covered in chapters 2-4 the EMG 101 laser was operated using the ArF line giving an output wavelength of 193 nm (6.4 eV). A description of this laser is given in section 2.31.

In a laser evaporation study the experimental configuration is to a large degree determined by the target material. Some compound materials exhibit non-congruent vaporisation, the composition of the target surface becoming increasingly depleted in the higher vapour

pressure constituent with successive laser pulses. For these materials either the target must be moved between pulses to allow fresh material to be struck (usually a rotating target) or the beam can be tracked (wobbling lens) across the target surface. Single element targets or compounds that display congruent evaporation can can be struck successively at the same position.

Because of the directional nature of the plasma, it may also be necessary to the move the substrate to deposit over a large enough area.

ZnSe was found in this study to vaporise congruently (section 7.4) allowing the laser to strike a fixed point on the target surface and therefore avoiding experimental complexity. To cover a wide enough area at the substrate surface the lens/aperture was moved at intervals during a growth run. The aperture dimension (10 x 5 mm) was somewhat smaller than the rectangular beam dimension at the point of striking the aperture (25 x 10 mm). Moving the aperture and lens horizontally and vertically within the cross section of the beam had the effect of tracking the beam across the target surface, and moving the plasma plume across the substrate to cover a reasonable area.

5.22 Vacuum chamber

The vacuum chamber and deposition geometry are shown in figure 5.1. The vacuum chamber consisted of a cylindrical body with a T-piece attached. The T-piece ended in a flange and O-ring against which was held the suprasil fused silica laser entry window. At the side arm

of the T-piece was a bellows valve which sealed the vacuum chamber from the vacuum system when the cell was brought up to atmosphere for sample removal or bakeout under hydrogen.

A removable internal support frame was used to hold both the ablation target and the substrate heater stage in position (see figure 5.2).

The substrate sat on a silica stage, to which it was thermally bonded with indium bond and held in place by tantalum wire clips. A platinum resistance temperature sensor (Pt100) was mounted on a piece of GaAs thermally bonded to the sample stage, which in turn was attached to a resistance heater of the same type used in the photolysis experiments described in section 2.33. One of the Ta wire clips which pressed against the sample front face was connected to an electrical leadthrough to allow the substrate to be electrically biased for reasons described in chapter 7. Further leadthroughs were provided for heater and Pt100 connections.

The target was fastened by stainless steel spring clips to a microscope slide which was held above the sample stage by ceramic rods placed in the support frame. The mounts for the sample stage were also attached to these rods and could be slid up and down, allowing the separation between target and substrate distance to be varied as appropriate.

The deposition geometry used is shown in fig 5.2. The target surface was oriented at 45 degrees to the beam axis and the substrate held such that a normal drawn from the substrate surface intersected the target at the irradiated region. This geometry was chosen in the

expectation that vaporised material would stream perpendicularly from the target surface towards the substrate. The 45 degree angle was selected simply because given the relatively small internal diameter of the cell, any smaller angle would have resulted in the heater stage interrupting the beam.

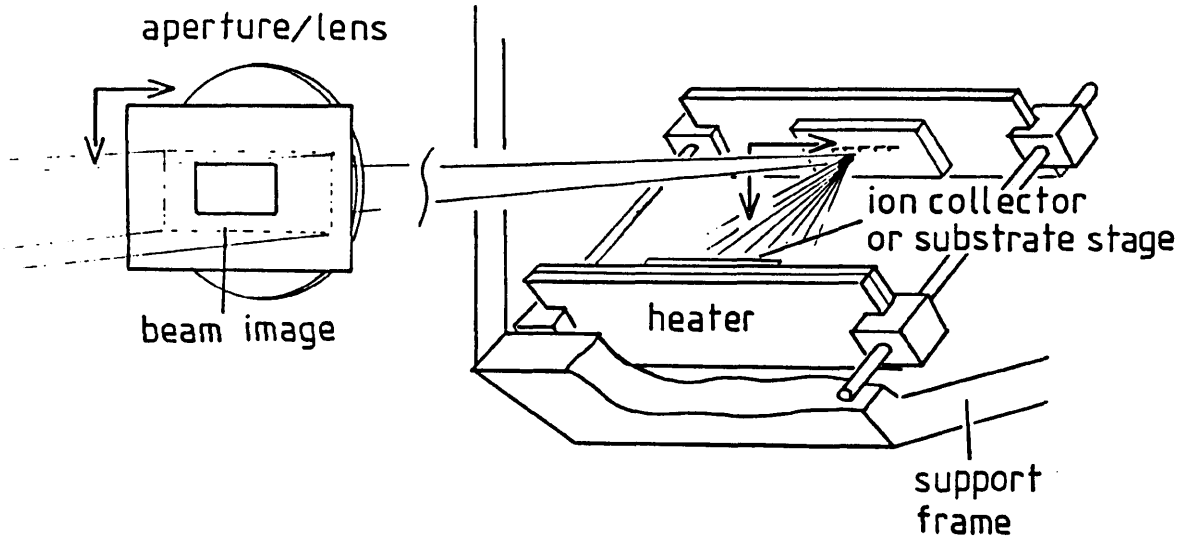

Figure 5.2 Internal configuration of vacuum chamber. Target and prepared substrate were placed in position and support frame was then inserted in reactor. Aperture/lens combination was moved relative to beam profile as indicated to track beam across target.

The excimer laser radiation passed through a 10 x 5 mm rectangular aperture fastened in front of a 25 cm focal length fused silica lens and the beam was brought to a focus at the target surface held at the centre of the vacuum chamber. An observation window was fitted to the reactor side wall, which separated from the chamber to allow removal of the sample stage/target support frame.

5.23 Vacuum System

The vacuum system was essentially the same as that used in the photolysis study, and is described in section 2.35.

5.24 Hydrogen

The vacuum chamber was also connected to a Pd hydrogen diffuser via a Nupro bellows needle valve, and a corresponding outlet valve allowed pure hydrogen to be flowed through the chamber at 1 atm. pressure for the purposes of sample pregrowth bakeout.

5.3 Film Deposition Experimental Procedure

1. A 'standard' pretreatment was followed for the n-type GaAs (100) substrates (see section 2.7):

    a. A fifteen minute IPA degrease under reflux, followed by a rinse in deionised (18MΩ) millipore water.

    b. A two minute etch in 5-1-1 H_2SO_4-H_2O_2-H_2O.

    c. A final rinse in millipore water preceded blow drying in nitrogen.

2. The targets were prepared by sectioning bulk ZnSe infrared window material (supplied by Alfa CVD Ltd.) on a diamond wire saw into 20 x 10 x 1 mm blocks. The targets were cleaned ultrasonically in Aristar IPA to remove contaminants before refluxing in IPA and rinsing in millipore water.

For optimum results it was found necessary to etch the target to remove the surface layer mechanically damaged by the diamond saw (section 7.31). The ZnSe was etched for 5 minute periods in 1% Bromine in methanol followed by ultrasonication in CS_2 to dissolve the brown bromoselenide reaction products. The total etching time was 20 mins, which removed 40 μm of material.

3. The prepared target and substrate were positioned with the support frame ex-situ. The heater stage was removed from the support frame and connected to a Variac, in order to melt a blob of indium on the sample stage. The prepared substrate was pressed onto the indium, and any excess removed. The heater was disconnected and once cool, retaining clips were placed over the sample edges. The heater stage was then remounted on the support frame.

4. Once the substrate and target were correctly positioned, the support frame was slid into the vacuum chamber and once in place all electrical connections were made. Final laser alignment then took place. The lens/aperture combination was placed in its initial position (top left of the beam profile looking from the laser cavity) and the laser briefly fired at a low power level to show a visible flash at the target surface. Beam position on the target was adjusted in azimuth by sliding the support frame back and forth within the reactor and beam elevation was adjusted if necessary by altering the height of the excimer laser using the trim wheels on the laser legs, together with appropriate adjustments to the height of the lens and aperture. The initial position for the aperture was the upper left corner of the beam image looking along the beam direction.

5. Once the beam was striking the target at the correct starting position, the reactor side wall was bolted in place and the cell evacuated to 10^{-6} Torr. The cell was then closed off from the vacuum system. Hydrogen was admitted to 1 atm. and then flowed continuously through the reactor. The sample was baked out at 550°C for 10 minutes, to remove the oxide layer present and expose the clean GaAs surface. The sample was allowed to cool to the appropriate growth temperature under flowing hydrogen before the cell was again evacuated to 10^{-6} Torr.

6. The excimer laser was brought up to operating pulse rate and power, and ablation of the target begun. After a period of time (usually 4 minutes) the lens/aperture combination was tracked 1 mm to the right across the target to strike fresh material. Once 5mm of target had been traversed, the lens and aperture were lowered 1 mm and then sequentially rastered back across the target in the opposite direction (figure 5.2). A further pass back across the target was then made. The combination of moving the point of ablation across an area of 5 x 4 mm, together with subsequent expansion of the generated plasma resulted in even area coverage of roughly 1 cm^2 at a substrate separation of 1 cm.

5.4 Plasma Electrical Studies Experimental

The experimental apparatus for the plasma electrical studies consisted of the deposition system described above, with the modification of a 2 x 2 cm. stainless steel foil plate which acted as an ion collector when placed on the heater instead of the substrate stage. This allowed the collector to be positioned at separations varying from 1 to 4 cm from the target. The foil collector plate was attached to an electrical leadthrough. Both the wire attached to the foil and the retaining clips were insulated so that ions could not strike them and generate spurious signals. The plate was connected to an external variable D.C. source (1.5 amp. max current) which in turn was earthed via a 10 ohm resistor. Any current passing to or from earth due to negative or positive species condensing on the foil were sampled by measuring the voltage drop across the resistor. Voltages measured this way were displayed directly on an oscilloscope (Tektronix type 549), the time base of which was activated by an external trigger pulse taken from the excimer laser firing circuit.

The current/time profiles obtained by this method therefore gave a direct reading of the time of flight of ionised species from target to substrate following a laser pulse, and allowed the effects of varying the substrate bias voltage to be investigated. The profiles shown in chapter 7 are taken directly from Polaroid photographs of the oscilloscope screen. An exposure time of three seconds was always used, and all profiles shown were obtained at a laser repetition rate of 10 Hz.

Operation of the EMG 101 laser at lower repetition rates can result in wide variations in pulse to pulse stability, and exposing over three seconds gave a resulting image composed of ~30 superimposed profiles. This automatically weights the image to the profile produced at the mean pulse energy, and any profiles generated from pulses not at the mean energy appeared faint on the Polaroid. The plasma current profiles were always 'well behaved' and varied pulse to pulse only in height rather than shape, the height variation clearly being the result of laser output instability.

Chapter 6

Characterisation of Laser Induced Plasmas

A series of experiments was undertaken to study the Time of Flight (ToF) characteristics of the laser induced plasmas obtained by irradiating ZnSe with 193 nm laser light. The method and experimental apparatus used to measure the ToF of ejected species from the target to the collector probe are described in section 5.4. As electrical currents were being measured it was not possible to study the ablation characteristics of any ejected neutral species but significant details of the ablation process were obtained by studying the generation of ionised species.

6.1 Positive ion currents

Figure 6.1 shows a ToF oscilloscope trace obtained with zero electrical bias on the collector. A net positive current is observed. This result is in contrast to other published studies which have found plasmas generated from laser evaporation of solid targets to exhibit overall electrical neutrality. In a similar study Lubben et al obtained no net current at zero biases when ablating Si with 248 nm KrF radiation at equivalent energy levels[1]. Overall equivalence in positive and negative currents was also found by Bhat et al[2] in laser plasmas generated by ablating CdHgTe with a 1.06 μm Nd:YAG laser at an energy density of 4.2 J cm^{-2} .

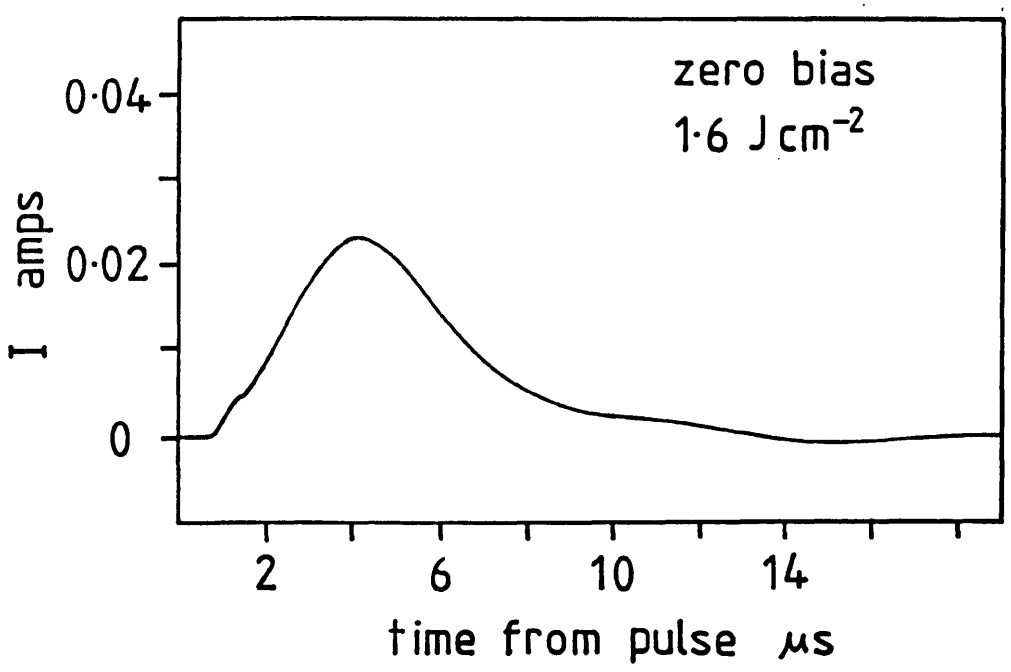

Figure 6.1 Net positive current observed at zero electrical bias proving ZnSe laser plasmas did not exhibit electrical neutrality.

There were originally thought to be two possible explanations for this anomalous result: it was either an artifact of the experimental geometry or a result of the ablation mechanism, and these possibilities are investigated in section 6.5.

Figure 6.2 shows the response in positive current profile with varying negative collector bias for energy densities at the target of 1.6 J cm^{-2} and 0.6 J cm^{-2} respectively. As an increasing negative potential is applied to the collector, the peak currents obtained rise accordingly, the peak current I_{max} saturating at -80 V. The zero bias result is included on this scale for comparison. A marked three peak structure to the plasma ToF profile is exhibited at these energy densities. The peaks are labelled a, b and c in order of their appearance with increasing laser power (section 6.2).

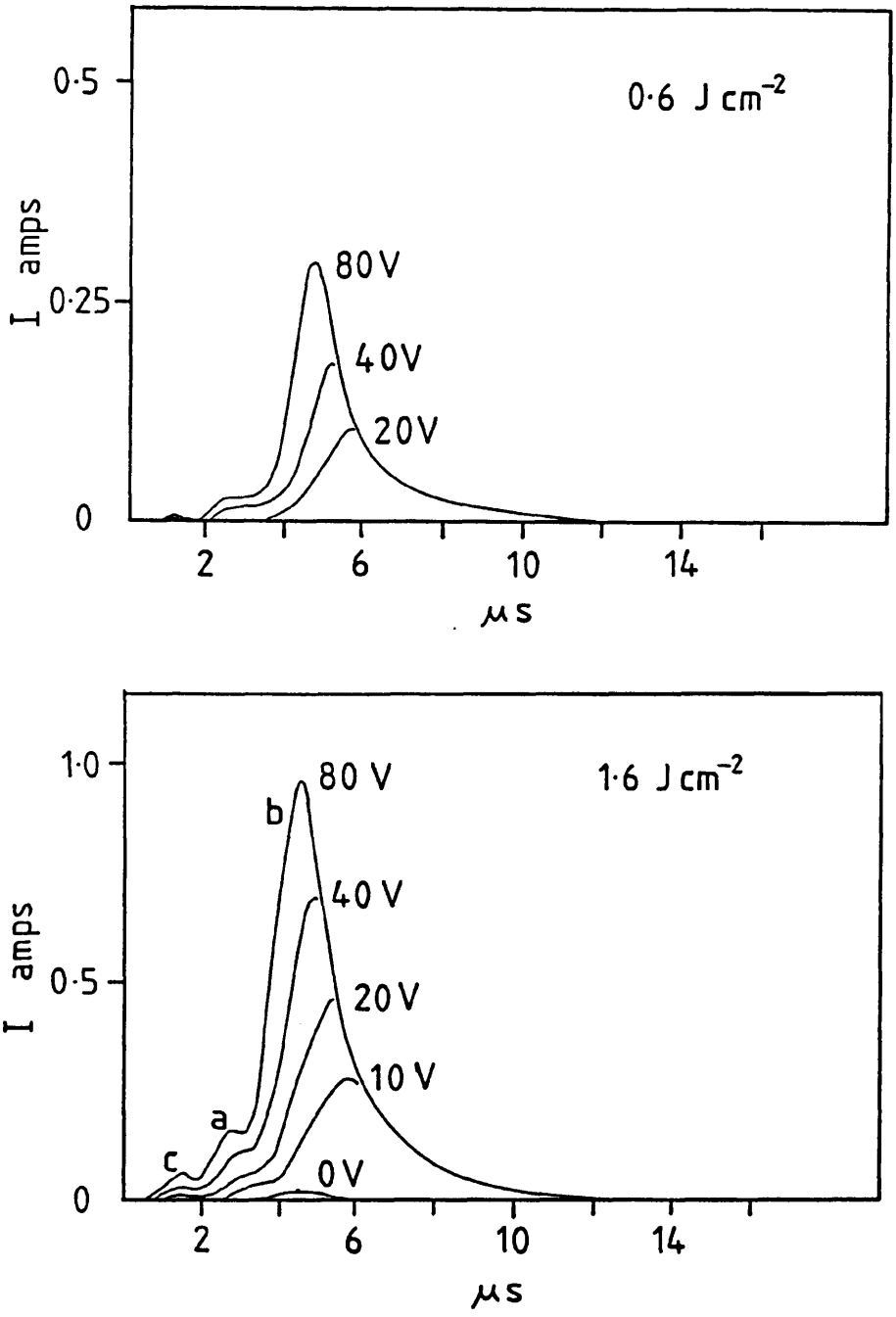

Figure 6.2 Response in current profile with varying collector bias for energy densities 0.6 and 1.6 J cm^{-2}

The delay following the laser pulse at which I_{max} of the peak b reaches the collector is 4.4 μs for both 0 and -80 V collector bias, demonstrating that the peak b current/time measurements are a true

representation of the plasma expansion velocity, and are not perturbed by acceleration toward the biased collector. This result is probably due to the screening effects of the very high space charge density plasma[1]. It is possible that the low current peak a and b profiles are shifted to shorter delay times by the collector bias.

6.2 Threshold Energy Densities for Ablation

Figure 6.3 shows a series of profiles obtained from an experiment to determine the laser energy density threshold for ablation of ZnSe. The target collector separation and bias used were 1 cm and -80V respectively. A current was first detected at an energy density at the target of ~90 mJ cm^{-2}. Operating the EMG 101 laser at very low power levels resulted in wide variations in pulse-to-pulse stability. Although the laser was operated at a nominal 5mJ $pulse^{-1}$, actual power meter measurements indicated variations in output from ~3 to ~7 mJ $pulse^{-1}$ (corresponding energy densities 90 and 210 mJ cm^{-2} respectively) resulting in the series of current profiles shown.

At the ~90 mJ cm^{-2} threshold only a single peak (peak a) is observed, As the laser power fluctuated to ~210 mJ cm^{-2} the profile transitioned abruptly to the two peak structure, the new peak appearing at a longer delay time than the first. When the second peak (peak b) appeared it displayed a greater I_{max} than the first, and as the laser output was increased, I_{max} of this new peak increased in actual and relative intensity to the first to become the dominant peak in figure 6.2. I_{max} for the second peak appeared at a

delay of 5.2 μs, shifting to 4.4 μs as the energy density was increased to 300 mJ cm^{-2} and remaining at this ToF for all higher laser outputs investigated.

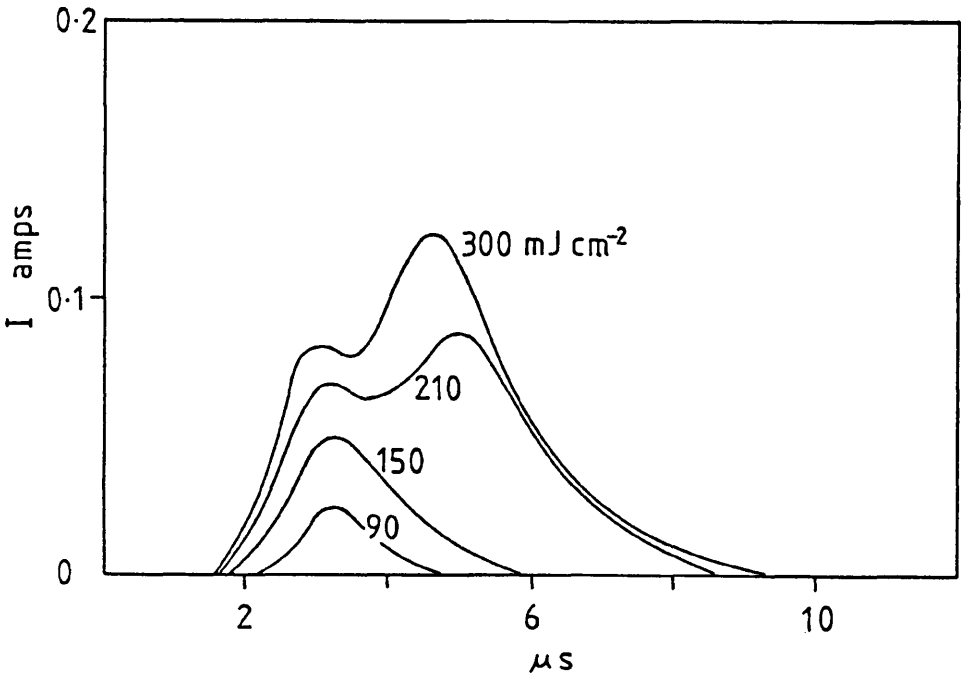

Figure 6.3 Variations in current profile at ablation threshold energies. Transition from single peak 90 mJ cm^{-2} profile to twin peak structure at 210 mJ cm^{-2} was not observed to be gradual, the second peak appearing abruptly at the height indicated.

At 300 mJ cm^{-2} energy density the plasma plume was well established as an intense white spark at the surface and a jet of blue fluorescence expanding away from the target.

At a threshold of around 0.6 J cm^{-2}, the third peak (peak c) of minimum time of flight appeared at the position indicated in figure 6.2.

6.3 Multiple Peak ToF Profiles

Other published current/time measurements of silicon[1], germanium[1] and cadmium mercury telluride[2] laser plasmas exhibit simple single peak profiles, which have been taken to demonstrate ablation of the solid to a vapour of ionised species all at an equivalent temperature. The question now arises as to the nature of the laser driven solid-plasma transition which results in the more complex profiles obtained in this study. The possibilities include:

1. Each individual peak represents the time of flight envelopes of different species, whether in terms of mass or charge, generated during the ablation process.

   2.The separate peaks are actually the same species but are generated at different temperatures by different mechanisms during ablation, or by variation in power during an individual pulse.

3. Different species may be formed not only during the ablation of the solid but also by reactions in the vapour phase to form higher mericity species of lower velocity during expansion of the plasma toward the substrate.

4. A combination of some of the above.

5. The complexity of the current profiles is not due to different species but is an artifact of laser/plasma interaction.

The last possibility refers to processes such as the following:

If the plasma generated during the early stages of the pulse is optically dense, it will absorb further incoming radiation and interrupt the ablation process, which can only then recommence when the plasma has reduced sufficiently in density to allow transmission of radiation again and generate a further pulse of ablation products. There are, however, two reasons why plasma absorption of radiation

and an ensuing oscillation in the rate of ablation could not lead to multiple peak profiles. The ArF pulse duration is 15 ns, and assuming the majority of species are generated within that timescale, any variation in rate of ablation during that time would not result in the μs scale gaps separating the peaks.

Furthermore, it can be seen from all the current profiles obtained over the range of laser irradiances used that the actual I_{max} delay times are generally invariant with power. Using higher input powers, therefore, does not result in higher ion translational kinetic energies, but instead produces a larger population of ionised species at an equivalent temperature. This observation demonstrates that once sufficient energy has been injected into the target to produce an ablation species, that species is ejected at the minimum possible energy. This indicates that for pulse energies greater than the ~210 mJ cm^{-2} threshold for the high energy ablation mechanism, the major factor which the pulse energy determines is the rate of ablation, i.e. the rate at which the plasma/ solid interface moves rearwards into the target during the pulse lifetime.

As varying the pulse energy still generates species of the same temperature, then altering energy densities within a single pulse would have no observable effect.

Reaction in the vapour phase to form new species can also be discounted. In figure 6.3, I_{max} of peak a appears at a delay of 3.2 μs. If these positive ions then combined with neutrals to form higher mass particles of lower kinetic energy, a peak would appear at a longer delay time, as is observed as the ablation rate is in-

creased. However the second peak to appear is at all times larger than the first, which it could not be if it was due to products of the original ablated species.

It would therefore appear that the three peak profiles of figure 6.2, and particularly the transition from peak a to peak a and b in figure 6.3 indicate the existence of at least two separate ablation mechanisms. It is assumed that the majority species for these peaks is Zn^+ as this will presumably be the easiest to ionise given the ionic nature of the ZnSe lattice. Mass spectrometric studies of laser ablated metal and semiconductor surfaces show that the vapour consists of single atoms. For the II-VI compounds no detectable quantities of molecular species $(AB)_n$ exist in the vapour at elevated temperatures[3].

The appearance of peak c at higher energy densities may be tentatively assigned to multiply ionised Zn^{2+}. The ToF of 1.6 μs was the minimum observed for a positively charged species at the 1 cm target/ collector separation.

6.4 Effects of Increasing Target/Collector Separation

Figures 6.4 and 6.5 show oscilloscope traces of positive current ToF spectra obtained at target/collector separations of 2 and 4 cm respectively. The three peak structure is still apparent in figure 6.5 but the FWHM of peak b has expanded to almost envelop peak a. Peak c is still clearly visible.

The non-structured single peak evident in figure 6.6 demonstrates that if the plasma plume is allowed to expand 4 cm. away from the target, the leading edge of peak b sweeps past both peaks a and c, leaving an apparent single peak profile.

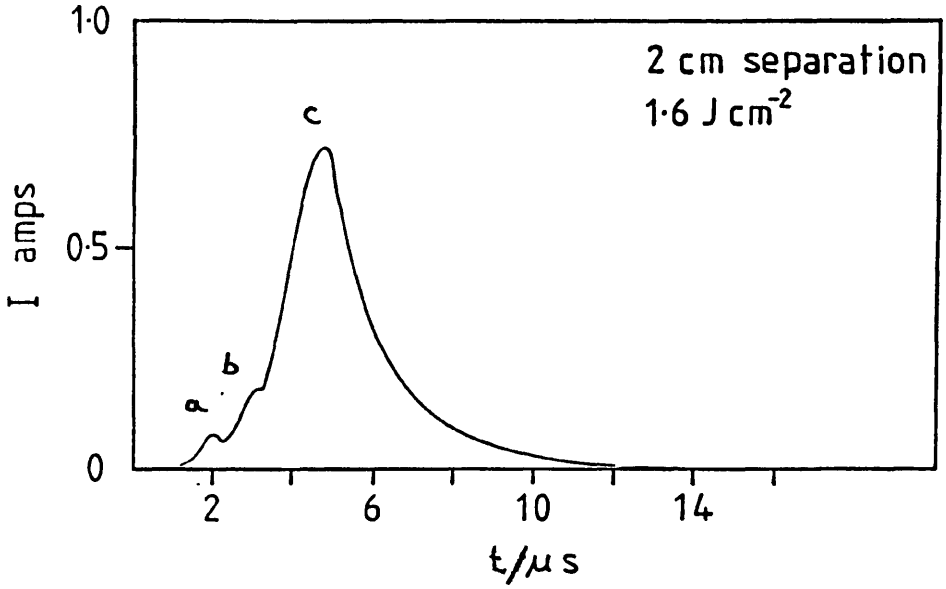

Figure 6.4 Positive current ToF profile, 2 cm target-collector separation

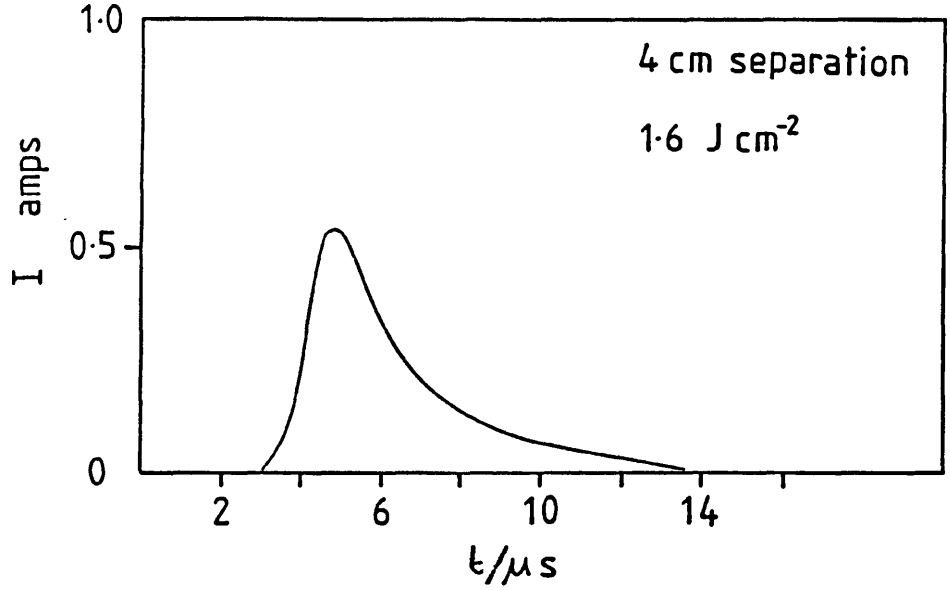

Figure 6.5 Positive current profile, 4 cm target-collector separation.

In figure 6.6 mean velocities for each peak are plotted against target-collector separation. The mean velocities are obtained by dividing the target-collector separation by delay time for I_{max} of peaks a,b, and c. The mean velocity of I_{max}a effectively doubles with distance. This surprising result is again in contrast with those of Lubben et al[1] who obtained constant velocities at varying

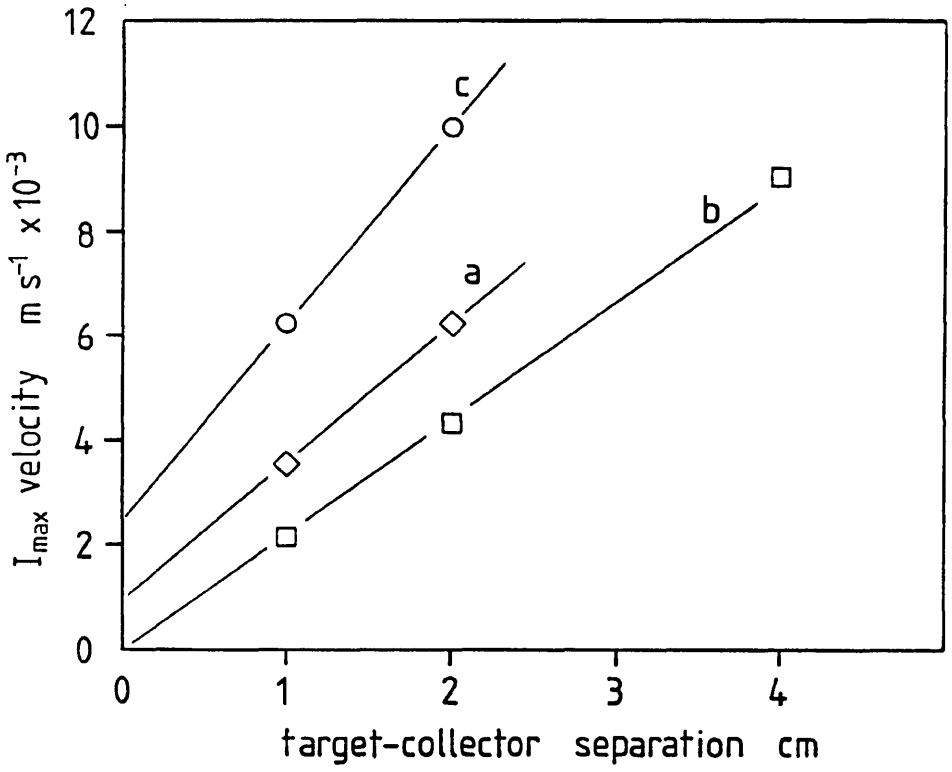

Figure 6.6 Mean Peak velocity vs. target-collector separation

separations for KrF excimer laser ablated Si ions. It is noteworthy that the peak b plot in figure 6.6 passes close to or through the origin, suggesting that whatever mechanism is responsible for acceleration of the plasma, ablation products leave the target with negligible thermal energy of < 1eV. This apparently self-contradictory result is in complete contrast to any other published work, all of which obtain ion energies falling in the range ~10 - 100 eV.[1,4,5,6,7,8]

6.5 Negative charge ToF spectra

Experiments were conducted to obtain ToF spectra of negatively charged ablation species by reversing the collector bias to repel positive species. It was expected initially that an electron current would be detected, and possibly negatively charged particulates which had been reported by other workers[1].

At low positive biases up to +3 V, a net positive current was still observed as positive ions were not sufficiently repulsed to suppress their arrival at the collector surface. At +7 V, no net current was observed, and at higher voltages a signal due to negatively charged particles impinging on the collector was obtained.

The negative charge ToF spectra were characterised by current maxima falling at longer delay times than those of the positive current signals, and a flat profile trailing current several tens μs broad.

Figure 6.7 shows oscilloscope traces of negative ToF spectra obtained at 1 cm target/substrate separation, as well as positive current signal as comparison. The mean velocity at I_{max} is 1400 m s^{-1}, and the velocity of the trailing species is of the order of 200 m s^{-1}.

The very wide distribution in velocities suggests a flux of particles of equivalently wide mass range, many of which would not be low mericity species but rather more massive particulates. This was confirmed by examination of the collector surface. After positive ion detection experiments a specular deposition pattern was evident

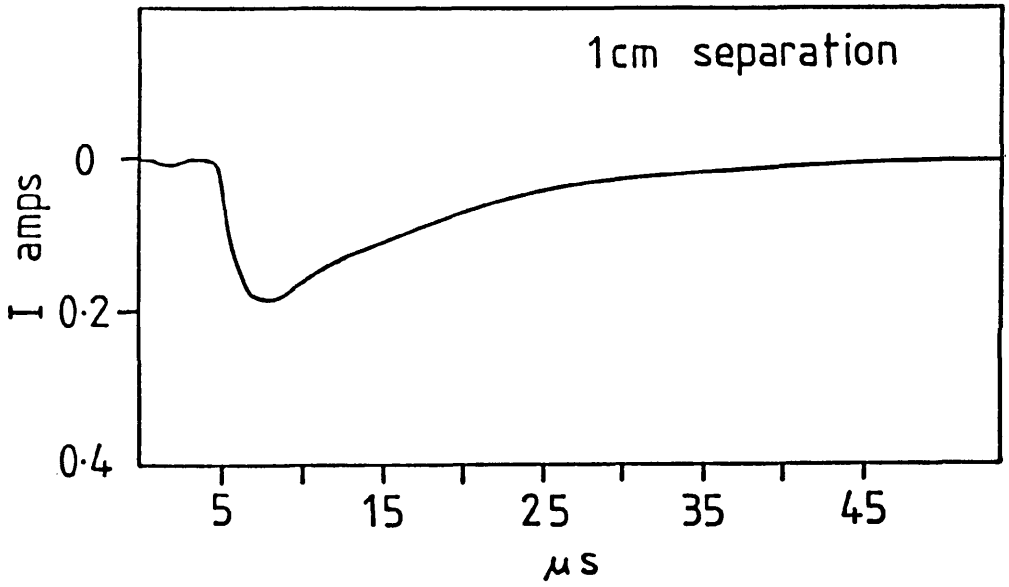

Figure 6.7 Negative current profile. Note how broad profile is compared to positive current. Small signal ahead of main peak is believed to be small electron current.

but on biasing the collector positive a non-specular dust-like particulate deposit visible to the naked eye was obtained, proving that the broadband negative signal was at least due in part to particulates.

The composition of the species represented by the negative current profiles was later shown by deposition experiments to be that of the target. Deposition studies were conducted with a negative bias applied to the substrate so any deposition was due to positive and neutral species condensing on the substrate. The composition of the deposited layers always reproduced the non-stoichiometric target composition of $Zn_{0.56}Se_{0.44}$ (section 7.33). The repelled negative species must therefore have also been of the same composition as the target because any deviation from the target composition in the non-depositing target species would have been reflected by an equivalent change in composition of the ZnSe films. This result indicates that

potential negatively charged species such as Se^- or Se_2^- are not present to any extent in the vapour.

Particle formation and the origin of the negative charge are covered in more detail in sections 7.31 and 6.8 respectively.

6.51 Electron Detection Experiments

Some of the negative spectra obtained exhibited very small amplitude signals at delay times corresponding to velocities of the order of 13000 m s^{-1}. This is the highest velocity obtained for any species negative or positive and as such was probably due to an outer corona of electrons expanding ahead of the dense positive ion plasma.

The most striking feature of this signal is the very small current it represents, a minimal percentage of the positive current values. Bhat et al[2] obtained rough parity in electron and ion currents for a CdHgTe target ablated with a Nd:YAG laser (1.06 μm) at 4 J cm^{-2}, and a somewhat larger electron current at 1.9 J cm^{-2}. This energy density is equivalent to those used in this study, but the ablation process will be determined by the infrared Nd:YAG laser wavelength.

As mentioned in section 6.1, the minimal electron current observed in these experiments was thought originally to be the result of two possible factors:

1. The ablation of ZnSe by 193 nm radiation results in the generation of an electron deficient plasma, the electrons remaining in the target.

2. The plasma as formed has parity in electron and ion populations but interaction with the electric vector of the reflected beam results in an angular separation of electron and ion currents resulting in most electrons missing the collector which is positioned to detect maximum positive current.

As is discussed in section 7.1, it is apparently the case that polarisation of the reflected beam results in positive ions receiving extra momentum along an axis parallel to the incident beam direction, and a further extension of this phenomenon could result in electrons present in the expanding plasma being accelerated much more efficiently by the beam electric vector due to the much lower electron mass and inertia. It was thought that if the plasma electron population was much more susceptible to acceleration away from the original direction of flight by the laser field an angular separation of electrons and ions could result as shown in figure 6.8. The expanding electron cloud would, therefore, be directed away from the collector, resulting in a very low signal as observed experimentally. Electrons deflected to the other side of the beam would strike the target again, resulting in the region around the crater charging negative, as is also observed.

In order to verify if plasma/beam interaction was responsible for removal of electrons from the expanding ion volume, the biased collector was repositioned appropriately as shown in figure 6.8.

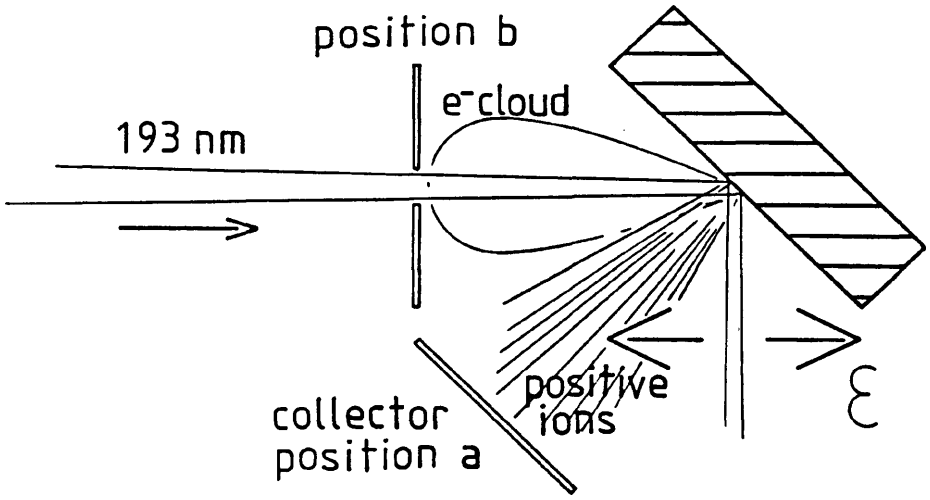

Figure 6.8 Experimental configuration to determine if electron and ion currents underwent angular separation. Collector (with slot to allow beam passage) normally placed at position a to detect positive ions was placed at position b to determine if electron flight direction differed from that of ions.

A 1 mm deep slot was cut in the collector to allow passage of the laser beam to the target.

With the collector in this position, no enhancement of the electron signal at all was noted over the signal obtained with the collector in the normal position. This result indicates that the plasma was electron deficient as originally generated.

6.6 Degree of Vapour Ionisation

As the time of flight studies were current measurements, no direct evidence could be obtained about the behaviour and density of neutral species ejected from the target by electrical measurements alone.

However, it was possible to determine approximately the degree of ionisation of the vapour by comparing the total current produced by one pulse (number of ions) and the volume of material deposited (numbers of ions + atoms) by one pulse. An experiment was performed to determine the distribution of material deposited from the laser plasmas and this is described fully in section 7.1. The ovoid (in plan view) deposit was found to approximate in cross-section to a $\cos^{30}\theta$ and a $\cos^{6}\theta$ distribution along the short and long axes respectively. Using these distributions the volume of the deposit was obtained by numerical integration and found to be 2.2×10^{-5} cm^3. This volume of material was deposited over 2500 laser pulses, giving a volume deposited per pulse of 1.7×10^{-9} cm^3. One ZnSe unit cell has a volume of 182.3 $Å^3$ and contains 8 atoms[9]. Therefore the total number of atoms deposited per pulse is 7.6×10^{13}.

Using the area under the positive ToF spectra (figure 6.2) to obtain a value for the total charge transported results in a value of 2.6×10^{-6} coulombs. Assuming that all positive ionised species are monatomic, this gives a total of 1.6×10^{13} ions, which represents 20% ionisation of depositing species on the basis of the above figure.

6.7 Laser Ablation Mechanisms

The various proposed mechanisms for laser ablation or evaporation can be divided into two broad categories:

1. Thermal Processes

The laser radiation is considered to act as a very high intensity heat source as regards the manner in which energy is transferred to and distributed within the solid target. The resulting melting, vapourisation and ionisation of the target are driven by thermal energy in the lattice, and the evaporating species display a thermal velocity distribution related to the thermal energy of the target.

2. Non-Thermal Processes

The monoenergetic laser radiation is efficiently coupled into the target as a result of the excitation of specific systems. This concentration of the laser energy into high energy states of the target material results in a non-thermal distribution which is reflected in the lack of equipartition of thermal energy throughout the lower energy modes of the solid. The resulting evaporating species are highly energetic and do not display a velocity distribution reflecting the thermal energy of the lattice or melt, or a percentage ionisation governed by thermal statistics.

This second approach is more related to ion or electron beam sputtering, for which processes it is well established that the contribution of thermal energy in the lattice to the rate of material desorption is minimal. The velocity distributions of ion sputtered species are non-Maxwellian, as is the degree of ionisation.

In the case of laser ablated material, the velocity distributions of vapour species have been shown in several studies to be either Maxwellian or non-Maxwellian. A Maxwellian distribution does not necessarily reflect a thermal evaporation process, but may instead be the result of formation of a dense gaseous plasma, the resulting high

collision rate producing a thermal distribution amongst species initially in a 'top-heavy' high energy distribution.

Maxwellian distributions have been found by Namiki and coworkers, who studied the ToF spectra of ions ejected from CdS irradiated with a nitrogen laser[10]. The ion yields of Cd^+, S^+ and S_2^+ saturated at 100 mJ cm^{-2}. At this energy density non-thermal distributions and very high kinetic energies of 100 eV were observed for the majority species Zn^+ and also S^+. At a higher energy density of 300 mJ cm^{-2} a stable broadband ToF spectra for Cd^+ developed which fitted a Maxwell-Boltzmann distribution and was assigned to the formation of a laser generated plasma.

Hanabusa et al observed non-Maxwellian distributions for Si vapour obtained by irradiating Si with a frequency doubled 530 nm Nd:YAG laser[11]. The Si velocity distribution was found to have a FWHM half that of a Maxwellian distribution for a most probable speed of 8 x 10^5 cm s^{-1}.

In a recent study by Arlinghaus et al of ZnS ablation by 308 nm XeCl excimer laser[12], Maxwell-Boltzmann distributions were obtained for Zn atoms ablated at energy densities of 17 and 80 mJ cm^{-2}. The most probable velocities were 1000 and 2200 m s^{-1} respectively at these values. Despite the latter velocity corresponding to a temperature of 9250 K, a thermal process such as sublimation was proposed as ablation mechanism. These velocities are consistent with the peak a velocities obtained at a 1cm separation and equivalent energy densities in this study.

6.71 Maxwell-Boltzmann Distribution Fitting

In order to determine whether the ZnSe laser plasmas exhibited thermal or non-thermal distributions, it was decided to determine whether or not Maxwell-Boltzmann distributions could be fitted to the ion current ToF profiles obtained in this study. As discussed, a thermal distribution would not necessarily indicate a thermal ablation process but a non-thermal distribution would indicate a non-thermal ablation mechanism.

If the velocity distribution of the ejected ions follows the Maxwell-Boltzmann law, the ToF spectra as a function of time should fit the following function[13] :

$$F(t) = \text{const}\ \frac{1}{t^5}\ \exp\left(\frac{-ml^2}{2kT_{eff}t^2}\right)$$

where m is the ion mass, l the flight length, k is Boltzmann's constant and T_{eff} represents the effective temperature of the translational kinetic motion.

Using data points taken from the oscilloscope traces, a curve fitting computer program (using the Gauss-Marquardt non-linear method) was used to obtain best fits using an automated search for a least mean squares value. Three parameters were used, the constant in the above equation which in effect represents the gain used on the oscilloscope, the constant term - $ml^2/2kT_{eff}$ within the exponential term and a delay time offset which had the effect of shifting the x-axis origin for the best fit.

A shift in the origin was necessary to obtain a fit because delay times taken directly from the oscilloscope traces represent mean velocities and not the true plasma expansion velocity at the point of striking the collector. As described in section 6.4, the velocity obtained by dividing the target-collector separation with I_{max} ToF increased with increasing separation, so the plasma plume was clearly accelerating. The above equation is for a constant translational velocity, which will result in a shorter calculated ToF than for an accelerating plasma, given equivalent velocities at the point of impacting the collector. Therefore, it would not be possible to fit the equation to profiles in this study using the origin on the oscilloscope trace. Allowing the programme to shift the time origin for the best fit gives ToF values for the ablating species as if they had a fixed translational kinetic energy, allowing the true expansion velocity at the collector to be determined.

Figure 6.10 shows data points and corresponding simulated fits for peak b profiles obtained at 1,2 and 4 cm target-substrate separations. The value of $ml^2/2kT_{eff}$ calculated by the programme to give the best fit to the experimental data is shown together with a value for $ml^2/2kT_{eff}$ obtained by calculating T_{eff} from the equation for the most probable speed $v=(2kT/m)^{0.5}$. Using the new delay time for I_{max} given by the best fit program to obtain the most probable speed

$$\text{most probable speed} = \frac{\text{original ToF - best fit x-axis shift}}{\text{target/collector separation}}$$

and assuming m = atomic mass Zn $=1.06 \times 10^{-25}$ Kg, the recalculated values of $ml^2/2kT_{eff}$ are somewhat larger than the best fit values as calculated originally. These larger values would have the effect of broadening the distribution of velocities, so the experimentally

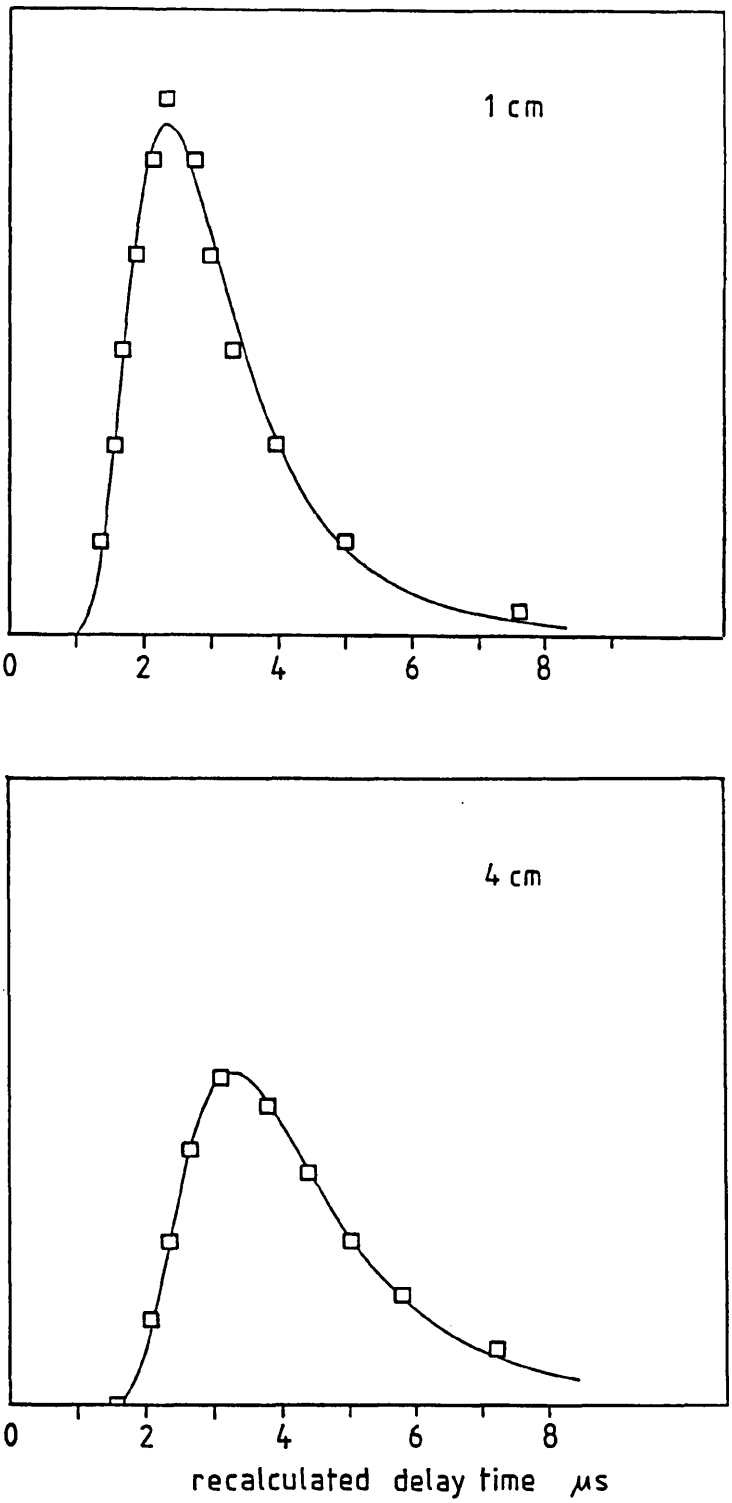

Figure 6.10 Computer fittings to positive ion ToF profiles. X-axes are recalculated flight times for species travelling at constant velocity. Most probable speed $(2kT_{eff}/m)^{0.5}$ for 1 cm target-collector separation is 4100 m s^{-1}, giving T_{eff} of 65000 K (5.6eV). Putting T_{eff} back into $(ml^2/2kT_{eff})$ gives 5.9×10^{-12} against computed value of 12×10^{-12}. 4 cm separation results are most prob. speed = 12000 m s^{-1}, T_{eff} = 550000 K (47eV), $(ml^2/2kT_{eff})$ = 11.2×10^{-12} against computed value of 29×10^{-12}.

observed profiles indicate a deviation from a Maxwell thermal distribution in that there is a greater population of high energy states than would be predicted by a Maxwell-Boltzmann distribution.

Other than this discrepancy, the profiles do behave in a Maxwellian fashion in that as the target/substrate separation is increased and T_{eff} of the plasma at the collector increases, the FWHM of the profile broadens as a result of indicating a wider distribution of thermal energy/velocities at the higher temperature, as predicted by the Maxwell-Boltzmann distribution.

6.72 Recalculated Plasma Expansion Velocities

Plasma expansion velocities taken from the recalculated Time-of-Flight values are plotted against target-collector separation in figure 6.11. Instead of the constant acceleration suggested by the equivalent mean velocity plot, a rapid initial acceleration is followed by a period of decreasing acceleration towards a constant velocity. It is notable that the recalculated velocities still pass through the origin within limits of experimental error, demonstrating minimal thermal velocity on ejection from the target. As the true velocity after 1 cm has been calculated at ~4350 m s^{-1}, and the mean velocity taken straight from the oscilloscope trace was ~2300 m s^{-1}, a best estimate for the ejection velocity from the target would be 250-500 m s^{-1}, representing surface temperatures in the range 200-1600° C.

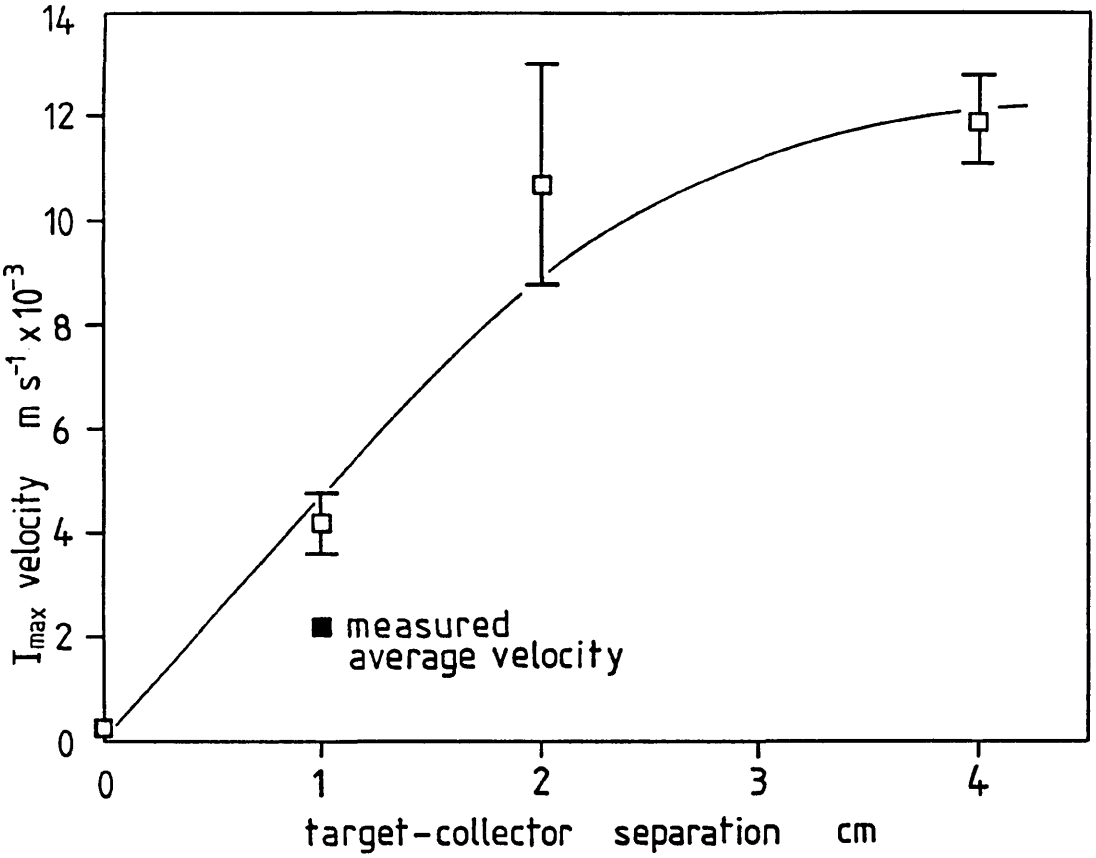

Figure 6.11 Recalculated plasma expansion velocities on basis of Maxwell-Boltzmann fits to ToF profiles. Initial velocity obtained by taking observed 1 cm delay time to give the average velocity over that distance. Linear acceleration was assumed to obtain initial velocity from calculated (final) and average velocities. Note that initial velocity is still very low as for figure 6.6 (uncorrected values) although velocity now approaches constant value at longer separations. Error bars taken from computed error to flight time shifts. Large error to 2 cm value is believed due to modification of profile leading edge by peak a (see figure 6.4) making accurate measurement difficult.

6.8 Proposed ZnSe Ablation Mechanisms

Before considering a potential mechanism to account for the extremely non-thermal equilibrium ablation of ZnSe demonstrated by the very low initial plasma temperatures coupled with the high occupancy of ionised and excited states, the mechanisms by which laser radiation is coupled into a semiconductor lattice will be considered.

6.81 Energy Transfer From Laser Radiation to the Solid

The transfer of energy from laser light to a crystalline semiconductor lattice is quite well understood in the case of low to medium photocarrier concentrations, as are the timescales for the processes involved. Absorption of light by interband transitions of the semiconductor creates photocarriers with a range of energy and momentum. This non-thermal distribution of carriers scatters into a thermal distribution on a timescale of 100 femtoseconds or less through carrier-carrier interactions[14].

At low carrier densities ($< 10^{17}$ cm^{-3}) the timescales for carrier energy transfer to the lattice have been estimated to be between 0.5 and 10 picoseconds depending on carrier and lattice temperatures and carrier density. Photocarriers are most energetically coupled with longitudinal optical (LO) phonons, and emission times for polar LO phonons by photocarriers have been shown experimentally to be less than a few tenths of a picosecond.

The population of the LO phonons increases upon receiving energy from

the carriers and this phonon system then attempts to reach equilibrium with other phonons in the lattice by scattering processes, leading to thermal equilibrium between the phonon modes and a raising of the lattice thermodynamic temperature. This has been estimated to take 10^3 phonon-phonon scattering events[14]. Because of the high LO phonon-carrier coupling and correspondingly high non-equilibrium LO phonon population, phonon 'bottlenecks' can occur if the equilibrium time exceeds the emission time[15]. If the population of LO phonons builds up quickly enough energy can be reabsorbed by carriers, slowing the carrier cooling rate. The carrier cooling rate timescale can also be decreased by other processes which become important at high carrier densities. Auger (three body) processes can raise the carrier temperature by transferring the recombination energy of two carriers to a third carrier.

Carrier relaxation mechanisms in polar and non-polar semiconductors have been considered in detail by Yoffa[16,17]. A theoretical study of screening effects on the phonon emission rate indicated that material parameters were important in determining the critical density of photocarriers at which screening effects become important. It was argued that the hot carrier cooling rate in Si would not be significantly affected until the density of photoelectrons in the conduction band (N_c) reached 10^{21} cm^{-3}, whereas in GaAs the carrier cooling rate would begin to decrease at $N_c = 6 \times 10^{16}$ cm^{-3}, reducing by a factor of 25 at 10^{18} cm^{-3}. Similar trends would be exhibited by other non-polar and polar compounds. Time resolved near-band transmission measurements made by Leheny and co-workers[18] and Shank and coworkers[19] provided information on changes in occupancy of near band edge states after a photoexcitation laser pulse, and showed a

significant slowing down in optical phonon emission rate above 10^{16} cm^{-3}. In this carrier density range the energy loss timescale shifted from 1 to 10 picoseconds. The photoelectrons themselves have also been shown to exhibit non thermal equilibrium distributions at high carrier concentrations[20]. High temperatures also favour optical phonon reabsorption by carriers, extending carrier temperature decay timescales[21].

Carrier recombination events are not well understood but are much less frequent than phonon scattering. At liquid helium temperatures GaAs recombination times are of the order of 100 nanoseconds[22]at low excitation powers, falling typically to less than 10 nanoseconds at plasma densities greater than $10^{19}cm^{-3}$.

Above these carrier density ranges, theoretical and experimental study becomes difficult because of lack of detailed knowledge of the many interactions possible between carriers and other carriers or the lattice, and the variations in rate of the interactions at excessive carrier densities. However, it can be stated that the trends established for polar compounds at low to medium carrier densities are for carrier cooling rates to be delayed with increasing carrier concentration and screening effects, and for carrier temperatures to be kept high by phonon reabsorption and Auger processes, and these trends would be expected to continue at higher carrier densities.

What relevance does this have for laser ablation? Before considering that question, a theory proposed at the beginning of this decade by Van Vechten for the mechanism of laser annealing of amorphous ion implanted silicon will be outlined. Laser melting of amorphous

silicon was shown in the 1970s to produce very high quality crystalline material[23,24]. Although the term laser annealing came into use, this is a somewhat misleading description as the melting and solidification rates ($\sim 10^9$ k s^{-1}) of the melted surface regions are extremely rapid and in metallurgical terms are quenches rather than anneals, which suggests a gentle process. One of the factors that lead to questioning of a thermal melting and quenching was the very high material quality produced despite the massive cooling rates.

Van Vechten and coworkers[25,26] proposed a non-thermal process, arguing that in the laser annealing of ion implanted silicon, recrystallisation was not due to thermally driven melting followed by cooling and recrystallisation, but instead to a "plasma annealing" process dependent on the creation of a sufficiently high density of electron-hole pairs (broken bonds) to allow atomic rearrangement at lattice temperatures well below the melting point. It was proposed that time resolved surface reflectivity measurements made during annealing experiments were not evidence of a molten phase as was (and is) the conventional interpretation[27,28,29,30] but instead were due to a high density carrier plasma producing a metallic reflection.

A second order phase transition was proposed to occur if more than a critical number of electrons (8×10^{21} cm^{-3} for Si) were to be excited out of the bonding states of the valence band to the antibonding states of the conduction band. This new phase was said to consist of a fluid but cool lattice and a hot electronic system which retained the energy of the irradiating laser pulse. It was proposed that sufficient electrons were promoted from bonding to antibonding

orbitals by radiation for the bond charges to become depleted to such an extent that the crystal could no longer resist shear stresses and behaved not as a crystalline solid but as a fluid. This proposed transition from the solid to a liquid phase was quite distinct from the normal melting process, which is a strictly first order transition driven by the violent thermal motions of the constituent atoms at high temperatures. In the annealing process, the atoms were then proposed to rearrange themselves to the epitaxial single crystal before covalent bonding was reestablished as the plasma density decreased, as long as carrier relaxation was slow enough to allow this.

In support of a low lattice temperature model, Raman surface temperature measurements made by Compaan and coworkers[31,32] and von der Linde[33] appeared to show actual temperatures well below the Si melting point. The interpretation of these results has been questioned, and predicted optical properties of later versions of the plasma annealing model[34,35] were not found experimentally[36]. The basic aspects of the thermal model, i.e. transfer of energy from carriers to lattice on a picosecond timescale and carrier densities of less than 10^{20} cm^{-3} have not been disproved and are accepted by the majority of researchers[37].

Even if as seems likely the overall approach of a thermal model is satisfactory in the case of laser annealed Si, the plasma annealing model is still important on the basis of its main principle; if carrier densities are reached that represent a high fraction of bonding orbitals depopulated, phase transitions could be driven by much lower temperatures than would be necessary for a cohesive

lattice.

6.82 Ablation by Valence Band Depopulation

Referring again to fig 6.3, the transition from an isolated peak to twin peak structure is highly significant in that as the pulse energy rises, the second peak appears at a longer ToF indicating species of lower effective temperature and thermal velocity. These are possibly higher mericity species at the same temperature as the peak a species although this is highly unlikely. The appearance of a late broadband reported by Namiki and coworkers in the Cd^+ ToF spectra attributed to the formation of the gaseous plasma is also highly unlikely to account for the observed results[11]. In the case of the Cd^+ plasma the maximum current was less at all times than that of the primary peak from which the plasma was forming, as would of course be expected.

The crucial factor in the ZnSe results is that peak b displays a greater I_{max} than peak a at first appearance, so it cannot be formed from peak a species. A different ablation mechanism operating above the 210 mJ cm^{-2} threshold appears to be the only way to explain the experimental observations, and the model proposed above is consistent with the increased peak b delay time and the jump in obtained current. The reduction in thermal velocity and the increase in ionisation efficiency are both a consequence of retention of energy in the carrier system. At and above the threshold energy density the critical value is reached for valence band depopulation resulting in lattice decohesion. The surface material can now vaporise before thermal equilibrium is reached between the lattice phonon modes or between the lattice and carrier population is reached. Electron

diffusion into the sample means that electron-hole recombination does not take place within the ablated volume. The excess hole population in the ablated volume results in the highly ionised and electron deficient plasma.

An injection of electrons from the surface into the bulk solid at a faster rate than the plasma/surface interface moves rearward into the target should result in a negatively charged volume of material around the etched hole. This result was observed experimentally, and is described in more detail in the deposition section (chapter 7).

Considering the ablation process in terms of valence band depopulation also explains why thermal ion velocities are invariant with energy density once the "cold ablation" is established as the primary vaporisation mechanism. The material vaporises at the threshold value and therefore cannot receive any more energy from the laser pulse via carrier/lattice thermalisation.

The main criteria for 'cold ablation' to take place are that the hole density at the material surface must be sufficiently high that the lattice can be driven to disintegration on a timescale $\leq$ carrier recombination time and that much of the laser energy is still retained in the electronic system on the timescale of vapourisation. A simple consideration can show that in the case of ZnSe and 193 nm radiation these conditions can be reached easily without moving away from accepted timescales for carrier energy transfer and recombination rates.

6.83 Carrier Densities During Ablation

The absorption coefficient of ZnSe for 193 nm radiation is extremely high. Using the formula for an absorption coefficient

$$\alpha_{193} = \frac{4 \pi \epsilon_2}{n_{193}}$$

where ϵ_2 is the imaginary part of the complex dielectric constant and n the refractive index[5],

a value of 0.23 nm^{-1} for α_{193} is obtained using the published value of 12 for ϵ_2[38].

The observed threshold laser pulse energy density for low temperature ablation is 210 mJ cm^{-2}. Making an estimate for reflectivity at high carrier concentrations rising to 0.6, absorption in the vapour of the order of 20%, and assuming that around the pulse peak 10% of the pulse energy is delivered to the sample in 0.5 nanosecond, i.e. ~20 mJ cm^{-2}, gives a total absorbed energy density of 6.4 mJ cm^{-2}. Using the above absorption value 12% of this energy will be injected into the carrier system within a unit cell depth (5.67 Å). For a 1 x 0.5 mm irradiated surface area, the total energy absorbed within a unit cell depth is 1.2×10^{-5}J. This equals 7.5×10^{13} photons and therefore an e-h pair density of 4.1×10^{22} cm^{-3}.

There are 4.4×10^{22} atoms in 1 cm^3 ZnSe. The actual carrier population, or more specifically the hole density, will depend on the carrier recombination rate and the decrease in carrier density due to diffusion. If the recombination time is of the order of 0.5 nanoseconds then the hole density would be ~2×10^{22}, which represents an average of 2 broken bonds per atom. Hole diffusion

will reduce this figure further so values of this order may only be reached in the first monolayer or so. The recombination time is an estimate, but times of the order of 10 nanoseconds have been reported for plasma densities of 10^{19} cm^{-3}, and will be expected to rise with carrier density, so the figure chosen is not unreasonable.

The proposed radiation induced failure of covalent bonding at the surface is extensive enough within the absorption depth that stresses within the surface region cannot be contained and the surface volume disintegrates. The driving force for this might be thermal motions of the atoms or mutual coulombic repulsion of (predominantly) Zn ions created by the very high local hole density in the surface monolayers, or acceleration down a Madelung potential due to the ionicity of the original lattice resulting in an explosion of the surface. The interaction of ions at the surface with the laser field resulting in ion motion is also a possibility.

In a sense this process can be regarded as a pseudo-second order sublimation driven by a non-thermal route. Whether the tendency of II-VI compounds to sublime is reflected in the observed results is a matter for conjecture.

The extent to which a latent heat is involved in the vapourisation, or if instead the 'cold' laser ablation of ZnSe is closer to a second order phase transition is also a matter for conjecture, but obviously the energy distribution within the vapour is highly non-thermal and is retained in the excited states of the vapour species.

6.84 Carrier Diffusion and Target Charging

As described in section 3.9, for ZnSe irradiated by 193 nm UV light, the 6.4 eV photons can be absorbed at various points over the Brillouin zone. Transitions at the X point (band gap =~6eV) and L point and region (band gap =~4.5 eV) points will leave generated photocarriers with an excess of~0.5 and ~2 eV respectively, the excess energy appearing as carrier kinetic energy. The excess kinetic energy of the carrier results in the energy of the light not being delivered to the lattice at the point of absorption as the photoelectron rapidly diffuses into the sample.

Electron diffusion will be enhanced by high carrier density screening effects which delay the transfer of kinetic energy to the lattice.

A constraint to diffusion of the electron population into the sample is the establishment of internal electric fields or Dember fields[39] between the negatively charged electron and positively charged hole populations. However, electrons will still diffuse into the target at a faster rate than the plasma/solid interface moves rearward into the target, leaving the plasma with an overall positive charge and the target with a negative charge.

The rate of diffusion of holes away from the high N_v density surface region may also be affected by bottlenecking, as a result of the considerable depletion of valence band electrons which are necessary for hole migration.

6.9 Increase in Effective Plasma Temperature

The increase in plasma temperature as measured by the most probable speed $v=(2kT/m)^{0.5}$ taken from the velocity distributions can be explained by quenching of the excited states by collisions with other vapour species. Collisions in the plasma are an alternative route to excited state depopulation (and repopulation) other than radiative decay. Fluorescence was clearly visible to the naked eye over the entire flight length of the plasma at a 2 cm target-collector separation demonstrating that energy was still present in excited states at these distances from the target. The redistribution of energy from a highly non-thermal top-heavy population of electronic excited states is achieved by scattering down to the thermal modes of the system by collisions in the dense plasma, resulting in an increase in the effective temperature of the vapour species.

As the thermal velocity of the major plasma volume increases, the full width at half maximum height of the major current peak increases accordingly and follows the Maxwell-Boltzmann distribution. Eventually it overtakes the smaller peaks leaving the single peak profile obtained at a 4 cm separation.

It is of course reasonable to ask why the results of Lubben and coworkers for Si ablated at 248 nm do not demonstrate similar characteristics to this study, but instead exhibit constant and high initial thermal velocities for ejected species. The explanation must lie with the indirect band gap of Si, giving a much greater absorption depth than that of ZnSe and reducing the attainable hole density at the surface by several orders of magnitude.

References

1. D. Lubben, S.A. Barnett, K. Suzuki, S. Gorbatkin, J.E. Greene, J. Vac. Sci. Technol. **B3** (4), 968 (1985)

2. P.K. Bhat, J.J. Dubowski, D.F. Williams, Chemtronics 1, 82 (1986)

3. Landolt-Bornstein, N.S., Vol. 17b, Springer, Berlin, 1982

4. H. Sankur, W.J. Gunning, J. DeNatale, J.F. Flintoff, J. Appl. Phys. **65**(6), 2475 (1989)

5. H. Sankur, J.G. Nelson, A.T. Pritt, W.J. Gunning, J. Vac. Sci. Technol. **A5**(1), 15 (1987)

6. A. Namiki, K. Watabe, H. Fukano, S. Nishigaki, T. Noda, J. Appl. Phys. **54**, 3443 (1983)

7. O. Eryu, K. Murakami, K. Masuda, A. Kasuya, Y. Nishina, Appl. Phys. Lett. **54**(26), 2716 (1989)

8. P.K. Schenck, D.W. Bonnell, J.W. Hastie, J. Vac. Sci. Technol. **A7** (3), 1745 (1989)

9. J. Blakemore, J. App. Phys. **53** (10), R123 (1982)

10. A. Namiki, K. Watabe, H. Fukano, S. Nishigaki, T. Noda, J. Appl. Phys. **54** (6), 3443 (1983)

11. M. Hanabusa, M.Suzuki,S. Nishigaki, Appl. Phys. Lett.**38**(5), 385 (1981)

12. H.F. Arlinghaus, W.F. Calaway, C.E. Young, M.J. Pelin, D.M. Gruen, L.L. Chase, J. Vac. Sci. Technol. **A7**(3), 1766 (1989)

13. S. Tomoda, I. Kusunoki, S. Matsumoto, Mass Spectroscopy **23**(2), 133 (1975)

14. H.M. van Driel, Transport Properties of Laser-Generated Non-Equilibrium Plasmas in Semiconductors, in Interfaces Under Laser Irradiation, ed. L.D. Laude, D. Bauerle, M. Wautelet, Nato ASI Series E, no.134 (1987)

15. H.M. Van Driel, Phys. Rev. B **19**, 5928 (1979)

16. E.J. Yoffa, Phys. Rev. B, **21**, 2415 (1980)

17. E.J. Yoffa, Phys. Rev. B, **23**, 1909 (1981)

18. R. F. Leheny, J. Shah, R.L. Fork, C.V. Shank, A. Migus, Solid State Commun. **31**, 809 (1979)

19. C.V. Shank, R.L. Fork, R.F. Leheny, J. Shah, P:hys. Rev. Lett. **42**, 112 (1979)

20. J. Shah and R.F. Leheny, Hot Carriers in Semiconductors Probed by Picosecond Techniques, Chapter 2 in Semiconductors Probed by Ultrafast Laser Spectroscopy, ed. R.R. Alfano, Academic Press (1984)

21. P.A. Maksym and C.J. Hearn: Ultrafast Relaxation Processes of Hot Excited Carriers, Chapter 3 in Semiconductors Probed by Ultra Fast Laser Spectroscopy, ed. R.R. Alfano, Academic Press (1984)

22. H.M. van Driel, Physics of Pulsed laser Processing, Chapter 16 in Semiconductors Probed by Ultrafast Laser Spectroscopy Vol.II, ed. R.R. Alfanso, Academic Press (1984)

23. A.G. Klimenko, E.A. Klimenko, V.I. Donin, Soviet J. Quant Electron. 5, 1289 (1986)

24. G. Vitali, M. Bertolotti, G. Foti, E. Rimini, Phys. Lett. **63A**, 351 91977)

25. J.A. Van Vechten, R. Tsu, F.W. Saris,Phys. Lett. **74A** (6),422; J.A. Van Vechten, R. Tsu, F.W. Saris, D. Hoonhout, Phys. Lett. **74A** (6), 417 (1979)

26. J.A. Van Vechten, J. de Phys. **41** c-15 (1980)

27. D.H. Auston, J.A. Golovchenko, P.R. Smith, C.M. Surko, Appl. Phys. Lett. **33**, 539 (1978)

28. M.E. Roulet, P. Schwob, J. Appl. phys. **50** (8), 5537 (1979)

29. D.H. Auston, C.M. Surko, T.N.C. Venkatesan, R.E. Slusher, J.A. Golovchenko, Appl. Phys. Lett **33**, 437 (1979)

30. D.J. Wouters, H.E. Maes, J. Appl.Phys. **66**(2), 900 (1989)

31. A. Compaan, H.W. Lo, Phys. Rev. Lett. **44**, 1604 (1980)

32. A. Compaan, H.W. Lo, Appl. Phys. Lett **38**, 179 (1980)

33. V. von der Linde, G. Wartman, G., XII IGEC, Munich, 1982

34. J.A. Van Vechten, A.D. Compaan, Solid State Commun. **39**, 867 (1981)

35. J.A. Van Vechten, Solid State Commun. **39**, 1285 (1981)

36. S.A. Lyon, Y.H. Chen, J.F. Lin, J.M. Worlock, Appl. Phys. Lett. **42**(11), 978 (1983)

37. M. Bertolotti, Presentation on Reordering Processes in Laser Irradiated Semiconductors in Cohesive Properties of Semiconductors Under Laser Irradiation, NATO ASI Series

38. J.P. Walter, M.L. Cohen, Phys. Rev. **183** (3), 763 (1969)

39. J.I. Pankove, in Optical Processes in Semiconductors, Chapter 14, p.320 (Dover, New York, 1976)

Chapter 7

Laser Plasma Film Deposition Results

7.1 Deposition Geometry

The plan-view shape of the deposited film as formed by the cross-section of the plasma plume was not a circular deposit but rather was ovoid, the long axis aligned parallel to the beam direction. This was reminiscent of the window deposits of the photolysis study and suggested that a polarisation effect was distorting the plasma profile. As the laser light was not reflected from a mirror the polarisation was presumably occurring on reflection from the target surface, with preferential reflection occurring for light with the electric vector aligned parallel with the beam axis. The 45 degree target angle also maximised the polarisation condition. The observed distribution also indicated a high degree of ionisation in the ejected species and also that material was ejected throughout the pulse duration, confirming the results of the Time-of-Flight studies (chapter 6).

7.11 Deposit $Cos^n \theta$ distribution

In order to realise the technological potential of laser ablation as a means of producing electronic device structures, a very high degree of control over the spatial uniformity of the deposition will of course be necessary. The highly directional nature of the plasma

plume results in a very high degree of efficiency in material transfer from target to substrate, but as a consequence the deposit is localised and non-uniform as defined by a $\cos^n \theta$ distribution, where θ is the angle between an angle of vapourisation and a normal to the point of ablation (deposits from thermal evaporation sources exhibit cos θ distributions[1]).

To achieve uniform deposition over a large area or the control of deposition on a nanometre scale, well characterised material transport parameters will be required, both in terms of material flux per pulse and the spatial distribution of the deposit. It was therefore decided to measure the $\cos^n \theta$ distribution of both the short and long axes of the ovoid ZnSe deposits.

7.12 Experimental Determination

The method used to obtain the spatial distribution of the deposit was to measure the surface topography of a layer using a Talystep stylus profiler. In order to obtain an accurate baseline for the measurement it was decided to deposit through a mask consisting of 1 mm dia. holes spaced at regular intervals in order to be able to use the substrate surface as a reference for the layer height measurement. The mask was held in place over GaAs substrate and both biased positive to +80 V. A target-substrate separation of 10 mm was used. As described in section 5.1, the plume angle tilted from being normal to the target after ~4 minutes (10 Hz, 1.6 J cm^{-2}), limiting ablation to this period in order not to distort the deposit distribution.

In order to obtain a sufficiently deep deposit for an accurate measurement, five separate runs of four minutes duration (10 Hz laser operating rate) were used. After each run the target was carefully moved without disturbing the alignment of the substrate in order for the laser to strike fresh material but maintain a fixed ablation point.

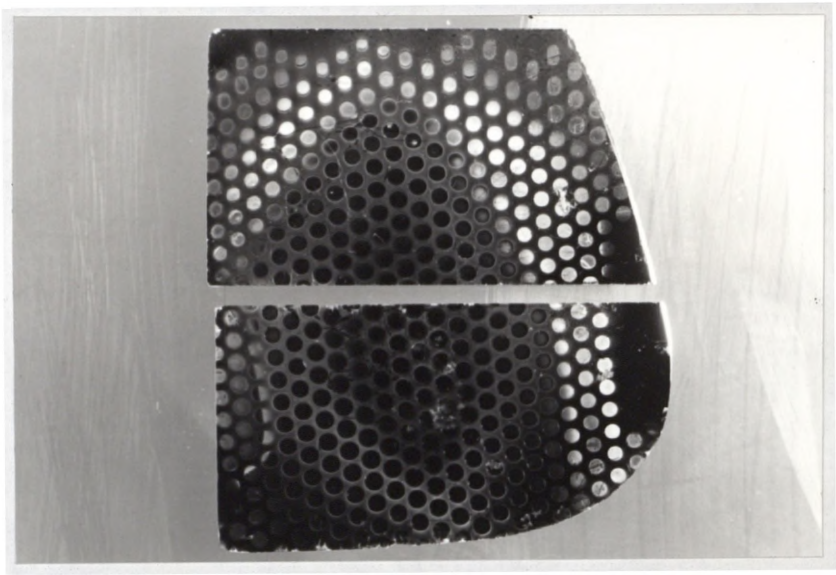

Figure 7.1 Patterned ZnSe deposit on (100) GaAs substrate. Growth was carried out with the pattern placed directly on the substrate. Non-circular form of deposit is clearly evident.

A micrograph of the deposit is shown in figure 7.1. The non-circular form of the deposit is readily apparent. Figure 7.2 shows a composite of the separate Talystep profiles for the deposit long axis, and figure 7.3 shows the computer fits to the obtained profiles for both axes. The Gauss-Marquard method was used to determine the parameters of the non-linear fit.

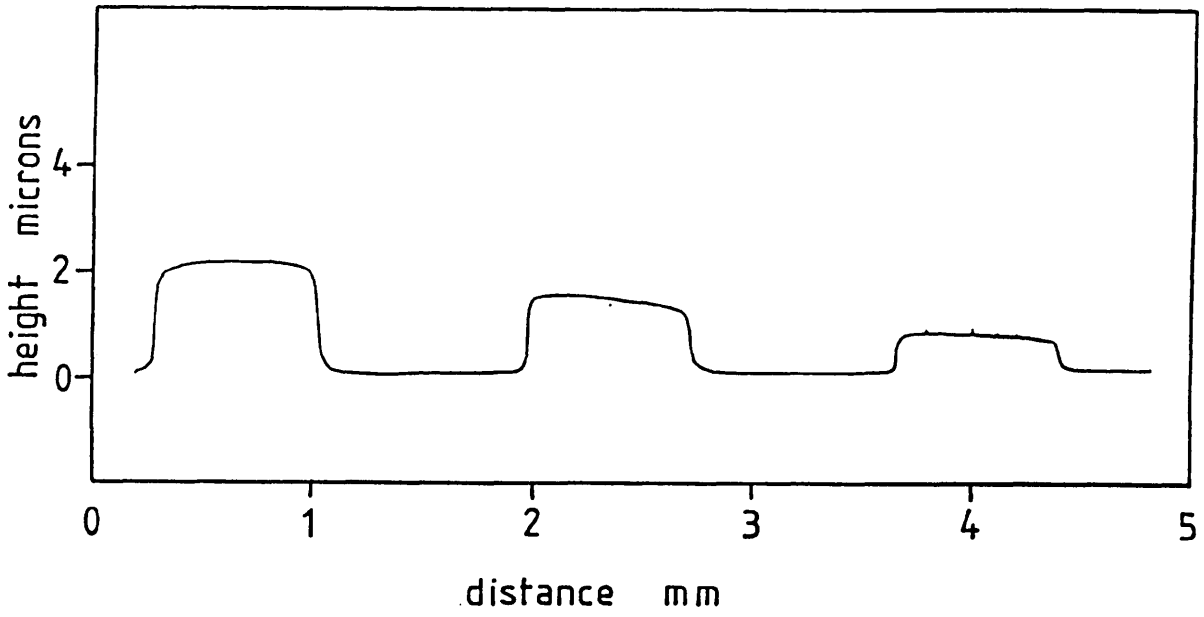

Figure 7.2 Talystep surface profile of ZnSe patterned deposit.

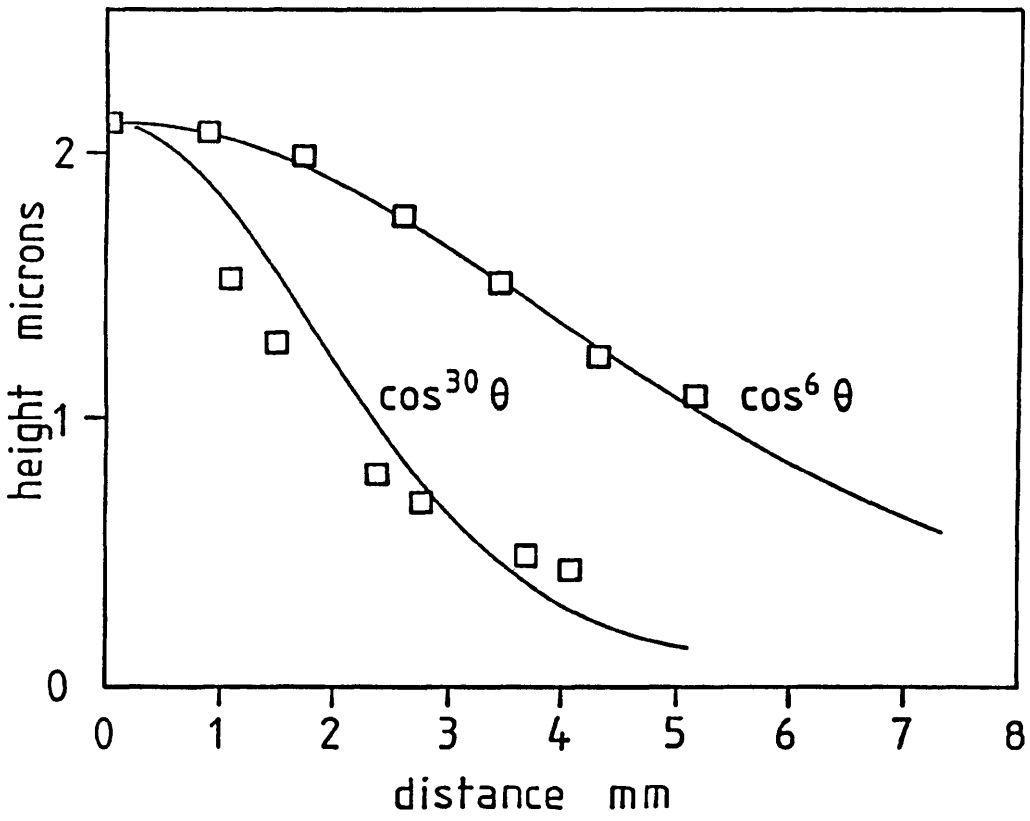

Figure 7.3 Computer curve fits to long and short axes of ovoid deposit. The short axis profile approximates to a $\cos^{30}\theta$ distribution, and the long axis to a $\cos^{6}\theta$ distribution.

7.2 Deposition Study

A series of deposition experiments was undertaken at substrate temperatures varying from ~20°C to 400°C. The original experiments were carried out with a target-substrate separation of 10 mm. It was known from the plasma electrical measurements that particulate material ejected from the target was negatively charged, and all deposition experiments were carried out with a negative bias applied to the conducting n-type GaAs substrate via the wire retaining clips. This also had the effect of earthing the substrate, allowing the depositing positive ions to be neutralised at the layer surface, preventing a positive charge build-up at the layer surface which would then repel further depositing species.

7.21 Layer Morphology

The most striking feature of the laser plasma ZnSe films was the very highly specular morphology characteristic of layers deposited over the entire temperature range 20-400°C from targets prepared in the method described in section 5.3. The surfaces appeared perfectly smooth to the naked eye and this smoothness was confirmed by Talystep profiles and transmission electron microscopy (TEM) cross section studies (figure 7.18). The mirror like surface of the layers is demonstrated in figures 7.4 and 7.5. MOCVD grown ZnSe often exhibits a hazy non specular morphology which has been attributed to hillocks running parallel to (110) cleavage planes[2]. The absence of such features suggests a different growth mechanism, and the mirror-like morphology also indicates a high degree of adatom mobility as would be expected from the elevated temperature of the depositing species.

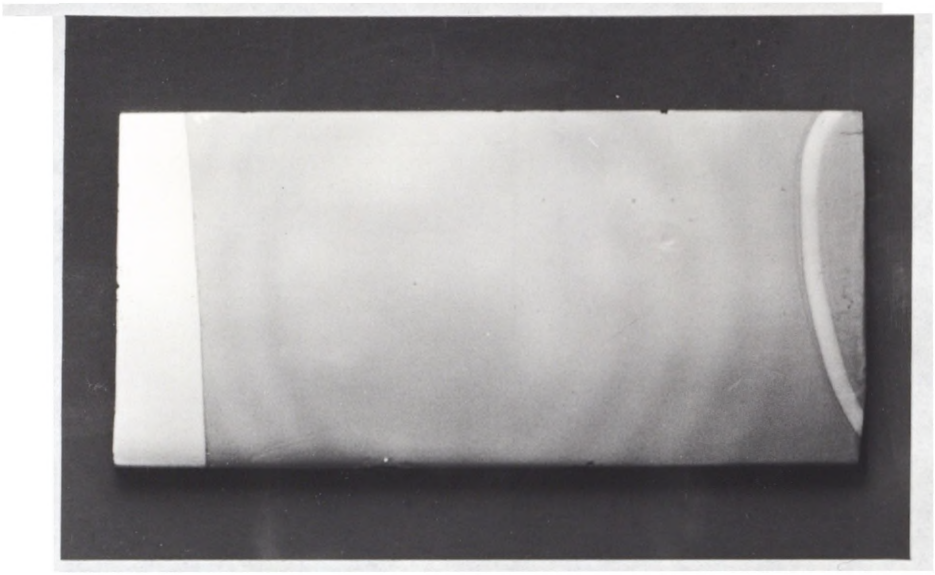

Figure 7.4 Laser plasma deposited ZnSe on (100) GaAs substrate. Lighter areas are the exposed GaAs surface ion regions where retaining clips contacted sample. Electrical bias was applied to the sample at these points.

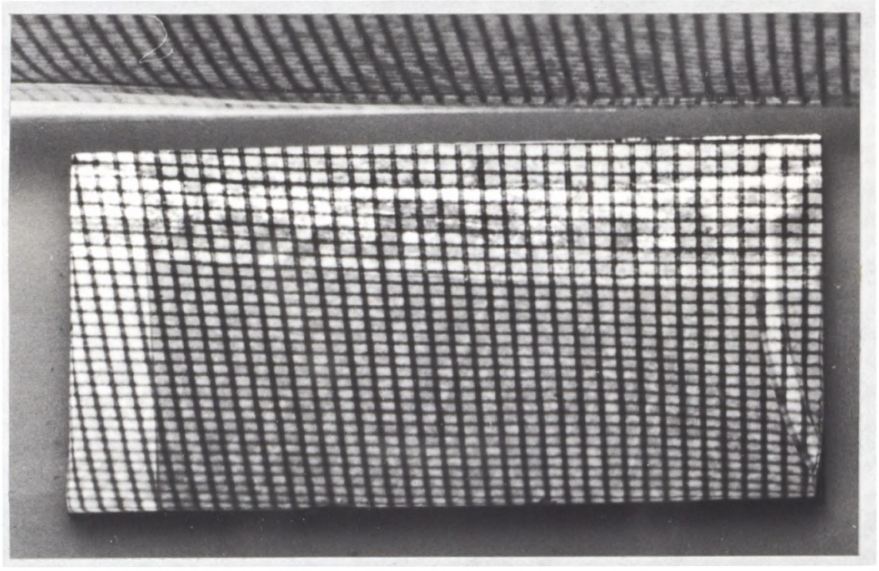

Figure 7.5 Specular reflections from the same sample demonstrate high quality of the ZnSe surface

The first layers were deposited using targets etched in 1% bromine in methanol to remove contamination and mechanically damaged material resulting from sawing the original ZnSe block. It was decided to deposit a layer using an unetched target to determine whether the etch was in fact necessary. The two layers deposited using an unetched target did not exhibit the mirror-like surface morphology of the preceding samples, and were non-specular over most of the layer area. The layer transparency was destroyed by what appeared to be gross particulate incorporation in the upper layer region.

This was confirmed by a TEM cross sectional examination study which showed that layer ABL 04 (300°C deposition temperature) consisted of an epitaxial lower ZnSe layer capped with an amorphous/very highly polycrystalline upper region, with an undulating surface morphology caused by particles embedding in the upper layer regions (figure 7.18, 7.19).

The layer regions around the negatively biased retaining clip were still specular as the particles were deflected from these regions.

7.3 Target morphology

SEM micrographs of etched and unetched target surfaces reveal two very different morphologies. The etched sample exhibits a polycrystalline microstructure but a relatively smooth coherent surface with no irregularities (figure 7.11). In contrast the unetched as-cut surface exhibits a flake-like morphology (figure 7.6). After a deposition experiment the unetched target also had a

liberal covering of bright yellow ZnSe dust clearly visible to the naked eye (figure 7.7). This dust covered the entire target surface apart from a region extending 1-2 mm around each laser dip hole.

It was apparent that the irregular flake morphology of the unetched targets was responsible for the greatly increased generation of particulates from the target. This indicates that the particulate generation process in this case was mechanical break up of the flake structures, possibly due to shock of the laser pulse generating a rapid localised thermal expansion in the target area.

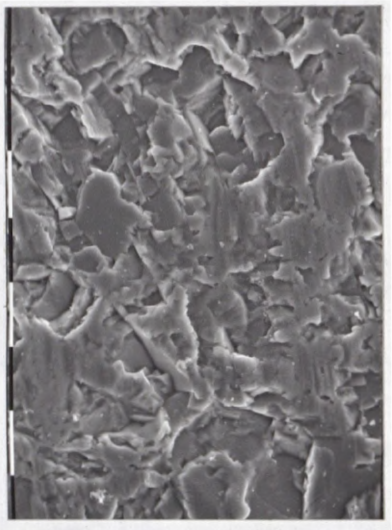

Figure 7.6 Irregular fractured surface of as-cut target. (10µm marker)

Figure 7.7 Particulate coating in area few mms away from point of ablation (10µm marker)

As these particles had already been shown to be negatively charged by electrical studies and their absence from the region of the biased retaining clips, the fact that they were also absent from the region around the dip holes demonstrated that the ablation process left these regions with a remnant negative charge.

The absence of dust from the crater areas was proved to be due to charge effects rather than other causes such as mechanical shock due to ablation. The dust was absent from all dip holes including those drilled earliest in the experiment and did not resettle in these regions after a period of time. This also demonstrated the semi-insulating nature of the target material which was also reproduced in the deposited layers.

The heavy particle incorporation in the upper region of the layers also demonstrated that the ZnSe films were insulating. The negative substrate bias was only effective up to film thicknesses of ~1 μm, after which a positive charge built up at the surface due to the overall positively charged plasma. Negatively charged particulates were then attracted to the surface rather than repelled as the effects of negative substrate bias were suppressed.

7.31 Particle Formation Mechanisms

It is widely accepted in the literature that the particle formation which has been reported in most studies of the laser evaporation of solid targets[3,4,5] is the result of subsurface explosive boiling. Particles have been claimed to be ejected from the target when subsurface regions are superheated before the surface itself has reached the vaporisation temperature, resulting in the 'spitting' of molten particles from the target[6]. Whether this is really the case is open to conjecture. For subsurface regions to become superheated before the surface vaporises, low beam absorption at the surface region is necessary so that heating is not restricted to the surface.

This is difficult to envisage for very high absorption values in the case of above bandgap radiation. However, if as may be the case in the ZnSe/193 nm system, much of the laser energy may still be retained in the expanding carrier plasma thereby increasing the effective absorption depth. Carrier relaxation may therefore result in a degree of subsurface heating, but a temperature inversion is still difficult to envisage.

One possibility that has been ignored up to now is that after the vapour stream has departed a sub-vaporisation temperature molten layer remains. However there will be a sudden pressure drop to the vacuum level after radiation pressure and ablation recoil ceases to exert any pressure on the surface. Sudden decompression as the molten surface is exposed to the vacuum could result in explosive surface boiling and 'spitting' of molten particles. This could be the case in the present study, as the target surfaces do show evidence of melting. Whether they would exhibit such smooth surfaces after an explosive decompression is debatable.

Other possibilities include the mechanical generation of particulates. Extremely rapid localised heating resulting in high temperature differentials could result in localised stresses at the target surface, which could lead to microcracking and fracturing in the region of the etch hole. Loose solid or semi-molten particles could then be transported out of the etch hole with the rising vapour stream.

It was proved during deposition experiments that target surface preparation was a very important factor in minimising the generation

of particulates (section 7.21) and this result favoured a mechanical shock explanation being responsible for at least some particulate formation rather than spitting molten material.

7.32 Particle charge.

Lubben et al[2] assumed the particles generated during Ge and Si ablation to be negatively charged because particle incorporation decreased with increasing negative bias. It was assumed that as originally ejected from the target they were electrically neutral, and became charged up to the plasma potential whilst coexisting with the plasma near the target for ~1 μs after the pulse.

A similar explanation is not appropriate to this study due to the highly positive space charge nature of the ZnSe laser plasmas. It is certain that the particulates are negatively charged as formed. It has already been proved that the ablation process left the etch hole walls and local region negatively charged (section 7.3). As a consequence of being ejected from this region either by mechanical stress or boiling, the particles themselves were, therefore, negatively charged.

7.33 Distribution of Mass Between Positive and Negative Species

The number of charged and neutral species depositing at the substrate due to a 1.6 J cm^{-2} pulse has been shown to be ~7.6×10^{13} (1.6×10^{13} positive ions). The distribution of matter between

positive charged, negative and neutral species can be established by comparing this figure with the total amount of material removed by one laser pulse. The balance will be the negatively charged species removed from the target but rejected from the film. The volume of a laser drilled hole was obtained by measuring the depth of a hole and approximating the somewhat complex hole shape to triangular sided wedge. The depth was measured by calibrating the fine focusing wheel on the optical microscope. Using this somewhat crude technique the volume of a hole (1.6 J cm^{-2}, 2500 pulses) was estimated at 0.031 mm^3. This represents an average 1.24 $Å^3$ $pulse^{-1}$ or 5.4 x 10^{14} atoms (182.3 $Å^3$ per unit cell, 8 atoms per unit cell). This figure is seven times the amount of the positive and neutral species depositing. The distribution of mass is consistent with the total amount of negative charge obtained during ToF studies. The area under the negative charge ToF profile in figure 6.7 represents a total charge of 2 x 10^{-6} coulombs, or 1.25 x 10^{13} electrons. This figure is 80% of the total of positive charges obtained, but experimental observation has shown that many of these particles are relatively massive and the distribution of material is therefore not surprising. The remainder of the negative charge remains with the target as has already been shown.

7.34 Morphology and Composition of Laser Drilled Holes

The pattern of laser drilled holes created by moving the beam aperture is shown in figure 7.8. An SEM micrograph of a single hole is shown in figure 7.9. The surfaces of the pulsed laser evaporated ZnSe regions are notably smooth, without surface roughness or

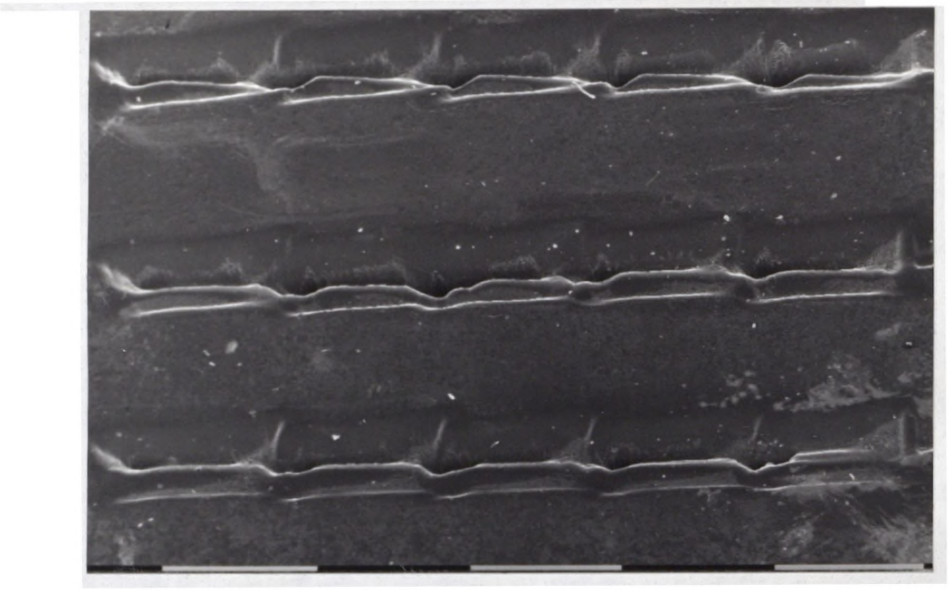

Figure 7.8 Pattern of ablation holes formed by moving lens/aperture every 3000 pulses (1mm marker)

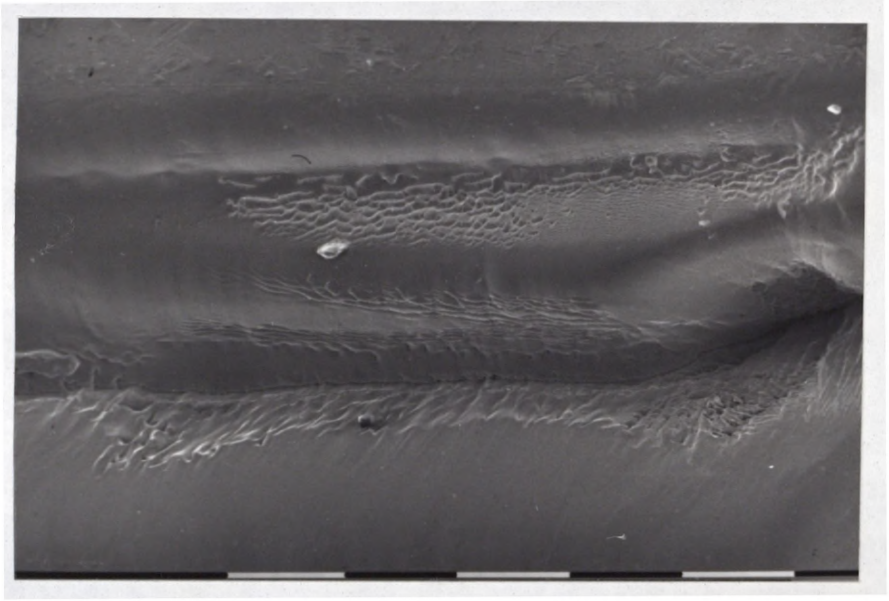

Figure 7.9 Micrograph of ZnSe laser drilled hole (0.1mm marker)

structures often characteristic of laser ablated surfaces. Nd:YAG laser vaporised CdTe has been shown by Dubowski et al to exhibit an 'orange peel' microstructure with random ripples and cracks thought to be a response of the material to significant thermal stresses[7]. EDAX analysis of this material showed it to retain the same composition as the bulk.

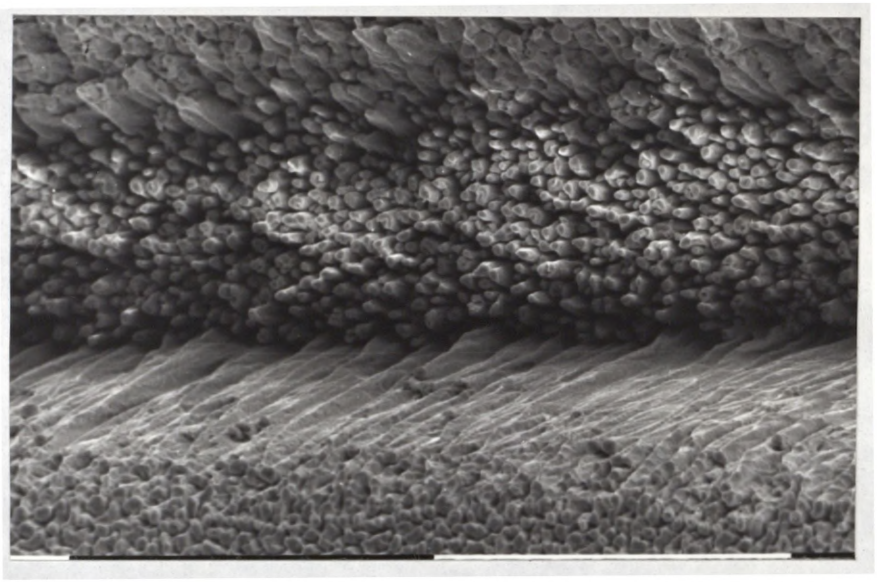

Figure 7.10 Surface structure produced by ablation of PLZT, a material which undergoes non-congruent vapourisation (0.1mm marker)

Materials which exhibit non-congruent vaporisation develop pronounced structures due to the preferential loss of one or more components from the surface. This has been shown for InSb[6], and also for $Pb_{1-1.5y}La_yZr_zTi_{1-z}O_3$[8] as shown in figure 7.10 which is included as a comparison to the ZnSe surface morphologies. The lack of surface structure in the case of ZnSe is in part due to congruent vapourisation characteristics. EDAX analysis has shown the target composition to be non-stoichiometric $Zn_{0.56}Se_{0.44}$ and this composition was consistently repeated in laser drilled regions and chemically etched or unetched non-irradiated surfaces. The non-stoichiometry was due to the fact that the target was sectioned from

infrared window material, for which application a large deviation from stoichiometry is probably an advantage as the free carrier concentration is minimised and, therefore, IR transmission is maximised.

7.35 Terrace Formation in Laser Drilled Holes

The dip holes shown in figures 7.11 and 7.12 exhibit terracing which appears to have been subsequently eroded at a later stage in hole formation. Each hole is formed by 3000 laser pulses, so each terrace is too large to represent the action of an individual pulse. It is proposed that terraces are formed by the forcing of molten material up the side of the hole wall either by expansion of material or ablation recoil pressure.

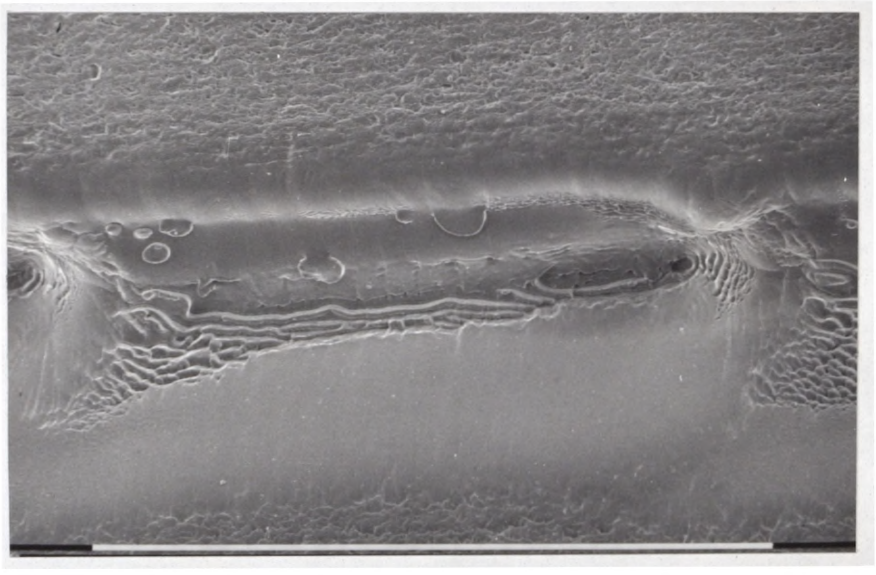

Figure 7.11 Micrograph of ablation hole which displays terracing. Also visible are convex base to hole, and polycrystalline microstructure of surrounding target revealed by chemical etching (1mm marker)

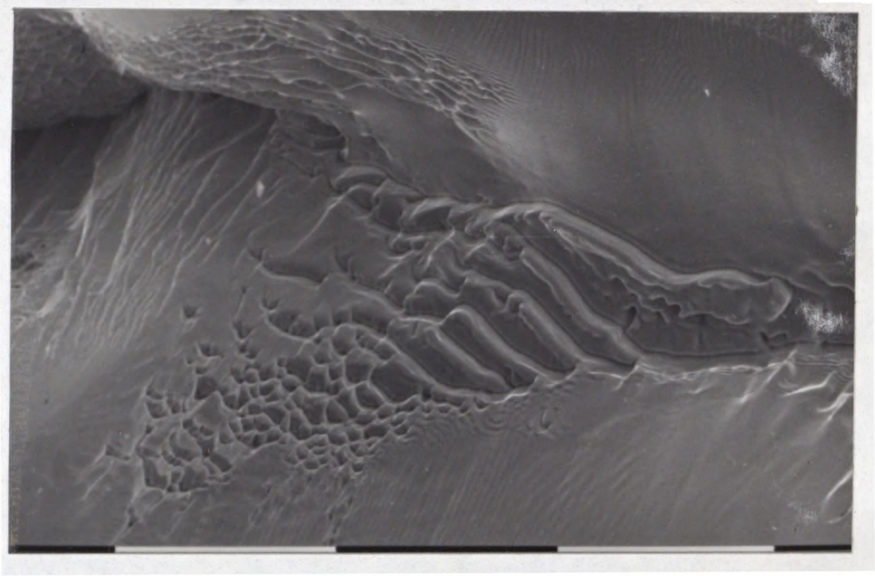

Figure 7.12 Region of terracing in laser drilled hole (0.1mm marker)

Figure 7.13 SEM micrograph of terraces. Raised inner lip is evident as are ripples which are believed to represent actions of individual pulses (0.1 mm marker)

Several terrace features are displayed in figure 7.13. Each terrace exhibits a raised inner lip, ripple features and a gap between the terrace and the inner wall of the next terrace. As the molten or semi-fluid material that forms a terrace is forced up the crater wall, a decreasing temperature gradient from the inner to the outer region of the flow results in an increasing viscosity gradient. The outer region solidifies first, contracting from the wall of the preceding terrace. The still fluid inner wall of the forming terrace is driven further upward and forms the raised inner lip.

The ripple structure evident on the outer terrace boundary is of sufficiently fine dimension that it probably does represent the action of individual pulses. The terrace formation process is not a continuous action but is pulsed in response to the laser. The ripples are conspicuous in the outer terrace regions of highest viscosity and become frozen in position as warmer material is sheared past solidifying older material. Ripples are absent in the inner lip where higher temperatures mean material is still fluid enough to remove artifacts of individual pulses. Eventually the laser cuts deeper into the target, moving the heat source and driving force further from the cooling terrace, which solidifies allowing a new terrace to form.

A diagram of the proposed terrace formation process is shown in figure 7.14.

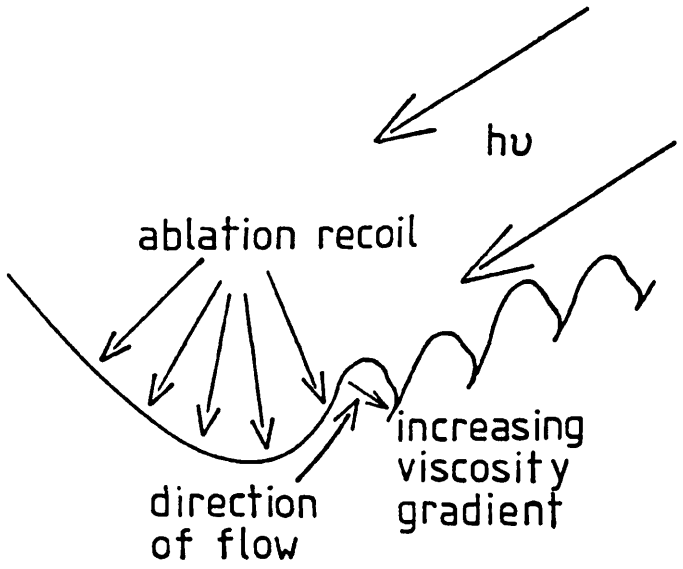

Figure 7.14 Diagram of terrace formation process. Molten material is forced up the sides of the crater by pressure of ablation recoil, Lower viscosity of innermost material forms the raised terrace lip, Eventually terrace solidifies and a new terrace starts to form.

7.36 Convex Wall

The base of the dip hole is convex as is evident in figures 7.9 and 7.11. This is probably due to two effects. Attenuation of the beam due to absorption in the rising plasma jet lowers the etch rate in the central region of the ablation surface. This has also been observed in laser etch holes drilled in Y-Ba-Cu-O high temperature superconductor targets[9]. Redeposition of evaporated material may also contribute to formation of the hump. Interference fringes were visible around each etched hole demonstrating that redeposition did occur.

7.4 Composition and Crystallinity of Deposited films

All layers grown over the temperature range studied gave a composition of $Zn_{0.56}Se_{0.44}$ from EDAX analysis. This non-stoichiometric composition resulted in semi-insulating electrical properties and weak broadband luminescence characteristics. However this result is encouraging in that a 1:1 transfer of material from target to substrate is demonstrated, reproducing the target composition. ZnSe has also been deposited by MBE at 1:1 Zn:Se fluxes[10].

The use of a stoichiometric target would therefore result in a stoichiometric film. On the basis of this result laser ablation of ZnSe has great potential as a method of depositing high quality material given the availability of suitable targets. The congruent vapourisation properties allow a single target of the desired composition to be used and irradiated at a fixed point. Target surface contamination problems will therefore be minimised as clean material is immediately exposed. Use of a rotating target would result in transfer of surface contamination with each pulse, rather than one in several thousand pulses.

7.41 Non Random Orientation

Figure 7.15 shows the XRD patterns of ZnSe layers ABL 01 and 02 deposited on (100) GaAs at 100° and 200° C respectively. The ABL 01 pattern shows random orientation in the form of the (111), (220) and

(311) signals, as well as a (400) peak due to the preferential (100) orientation. However the ratio of the (220) peak to the (311) and (111) peaks is lower than that predicted by the published intensity ratios for a polycrystalline randomly oriented ZnSe sample.

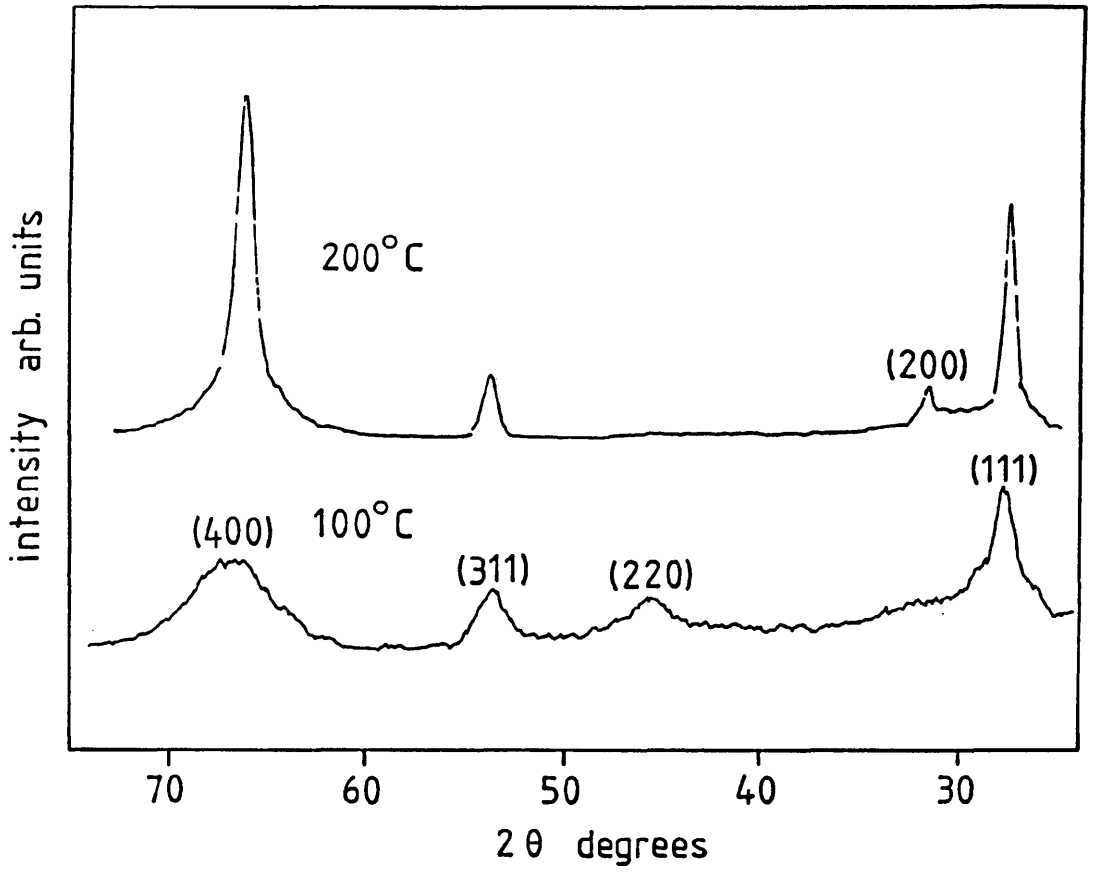

Figure 7.15 XRD patterns for samples deposited at 100 and 200°C. Note absence of (220) reflection in 200°C sample.

In the ABL 02 pattern the (220) reflection is completely absent, despite the presence of strong (311) and (111) signals, which would appear at first to indicate some random orientation.

In the case of randomly oriented material a (220) signal of intensity 70% that of the (111) should be present, but is in fact completely absent. The (311) is present but at a slightly reduced intensity. The non random orientation as evidenced by the absence of the (220)

peak is believed to be due to deposition of the ZnSe layer under the applied electric field used to repel negative charged particulates.

The (110) plane in the sphalerite structure is completely non polar, having equivalent numbers of Zn and Se atoms in the same plane. In an attempt to lower the energy of the material in the applied field, atomic arrangement takes place to minimise the effect of the field by growth on polar rather than non-polar planes, the resulting electric field in the crystal reducing the local effect of the applied field.

The (100) plane of the sphalerite structure does have a polar nature but not to the extent of the (111) and it may be possible that the degree of (100) orientation would have been higher in the absence of the applied field at this temperature.

7.42 Layer crystallinity

The layer crystallinity as measured by the FWHM of the (400) reflection improves with increasing deposition temperature up to 280°C. An x-ray rocking curve of the (400) reflection of a layer deposited at 280°C is shown in figure 7.16. The ZnSe $K\alpha_1$ reflection is seen as a shoulder to the GaAs substrate peak. Unfortunately the layer was rather thin and so the reflection is not strong, but the FWHM (400) taken from the rocking curve is ~0.2 degrees. This is an upper limit as the ZnSe reflection is undoubtedly broadened to some extent by the GaAs peak shoulder beneath it. This result therefore compares favourably with MOCVD-grown material deposited at 280°C, which exhibits a FWHM (400) of 0.18 degrees[11].

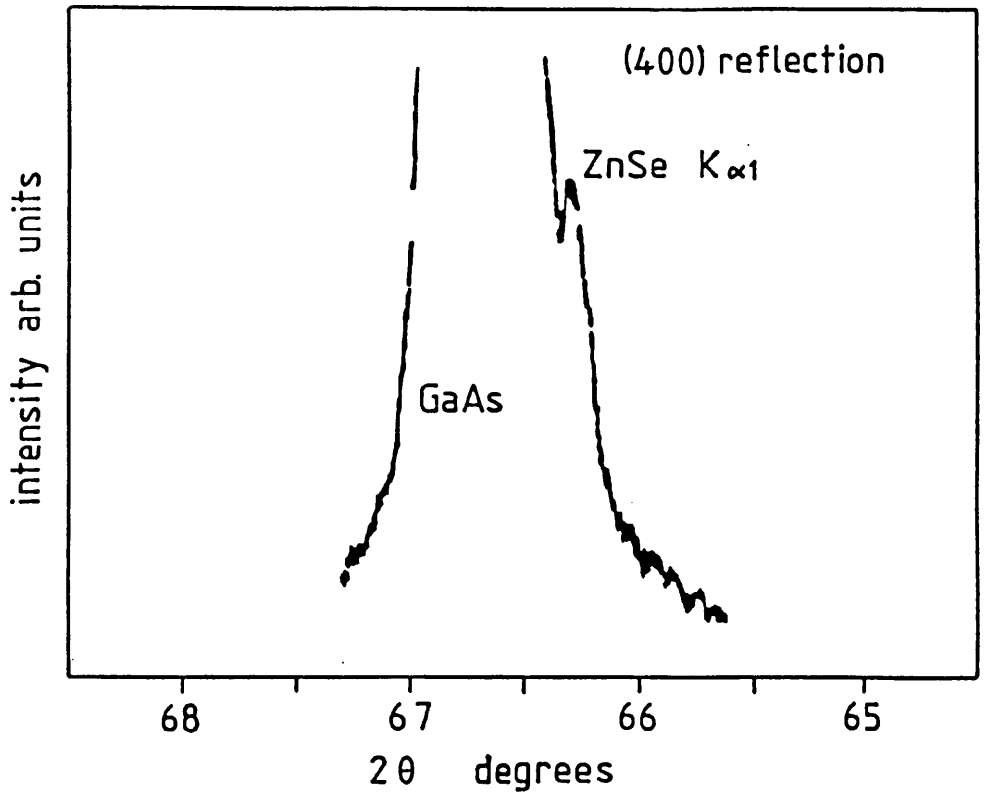

Figure 7.16 X-ray rocking curve of 280°C layer. The ZnSe (400) reflection produced by the Cu $K\alpha_1$ radiation appears at the side of the GaAs $K\alpha_1$ (400) peak, which obscures the ZnSe $K\alpha_2$ peak.

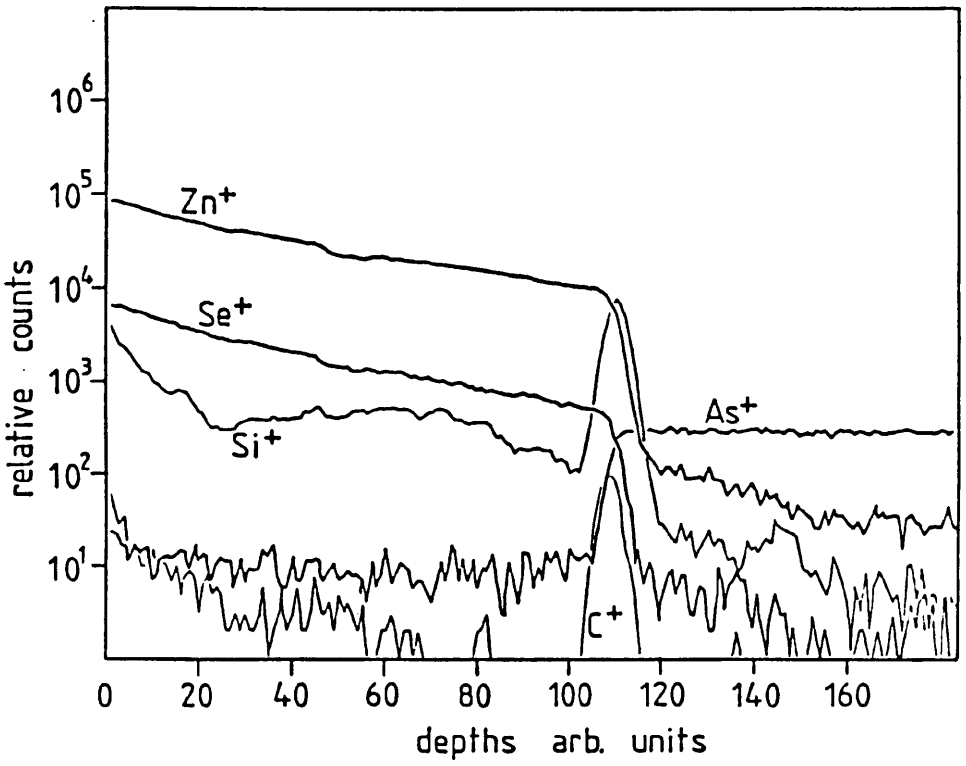

Figure 7.17 SIMS depth profile of laser plasma deposited ZnSe. Si contamination is evident, both in layer and large spike at interface. There is also a carbon spike at the interface.

The FWHM (400) for the laser deposited material is even more encouraging in view of the deviation from stoichiometry of the layer, and the fact that deposition did not take place in an ultra-high vacuum environment but instead in a conventional vacuum. SIMS depth profile studies show silicon contamination levels within the ZnSe layer, and a large silicon spike at the ZnSe/GaAs interface (figure 7.17). The presence of silicon was probably due to silicone grease used to seal vacuum joints. A carbon spike is also present at the interface, possibly as a result of hydrocarbon vapours in the background chamber atmosphere. The best results will obviously not be achieved without a clean environment and minimal interfacial contamination.

Transmission electron microscopy studies confirmed the single crystal nature of the laser plasma deposited films. Figure 7.18 shows a cross sectional micrograph of ZnSe deposited on (100) GaAs at 280°C. The sample was prepared by cleaving the substrate on {110} planes to create a wedge shaped specimen which is electron transparent at the tip of the wedge.

[100] axis diffraction patterns taken from the ZnSe sample are shown in figure 7.19. The diffraction pattern taken from the middle of the layer is representative of high quality single crystal material, whereas the pattern taken from the top of the layer shows a degree of polycrystallinity. This demonstrates that particle incorporation occurred at later stages of growth when the substrate electrical bias was ineffective. The upper left surface region of the ZnSe layer in figure 7.18 shows undulations resulting from particle incorporation in the upper layer.

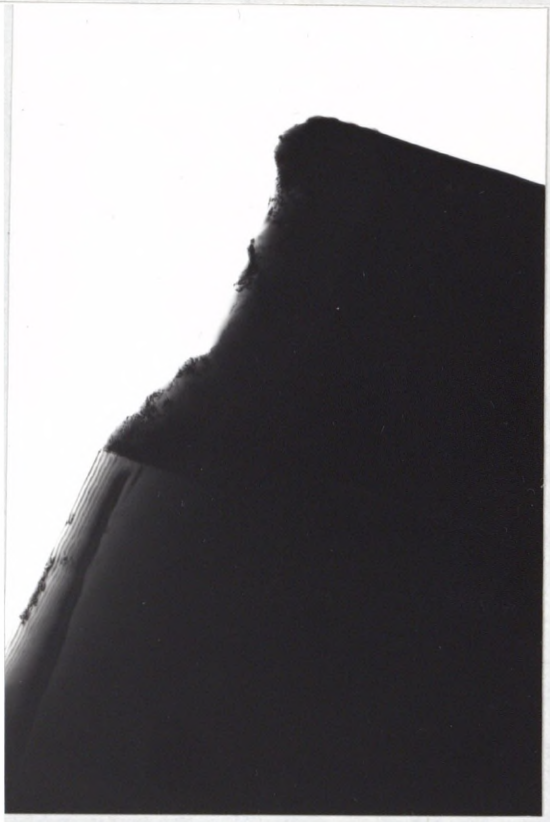

Figure 7.18 TEM micrograph of epitaxial ZnSe (top of picture) on GaAs substrate.

Figure 7.19 [100] axis diffraction patterns from upper layer (top) and and middle layer (bottom)

7.5 Alternate Particulate Suppression Methods

The experimental results of using substrate biasing as a means of preventing the incorporation of negatively charged particulates exposed two factors which led to the search for alternate methods of particle repulsion:

1. The semi-insulating nature of the ZnSe films deposited resulted eventually in a build up of positive charge at the layer surface, rendering the negative substrate bias ineffective and reducing the deposition rate.

2. The observation of non-random orientation at low growth temperatures apparently due to a response of the material to deposition in an applied electric field raises questions as to the nature of the effect of an electric field on film quality. In the case of ZnSe on (100) GaAs, the (100) plane does not represent the lowest energy orientation as it is not the most polar surface. Can defects possibly be induced in the material in the form of local deviations from correct atom positions to counter the presence of the applied field? Furthermore, in the case of laser ablation deposition of insulating ionic material such as oxide films, would the build up of positive charge at the surface due to electron repulsion result in deviations from stoichiometry as a result of cation vacancy formation to achieve electrical neutrality?

On the basis of the above observations it would be desirable to deposit a layer which remains unbiased and electrically neutral and still be able to repel negatively charged particulate matter. With these aims in mind it was decided to electrostatically repel the particulates by means of a negative biased mesh placed above the substrate, thus obviating the need for substrate bias. The major requirement for such a mesh is high transmissivity for the positive ions of the plasma. This depends on two factors:

1. A high hole-to-wire projected area ratio.

2. A wire separation of greater dimension than the induced angular displacement of the positive ions i.e. the majority of ions are not deflected sufficiently from their original path by the negative mesh bias to actually hit the wire, but are transmitted instead.

7.51 Mesh Transmission tests.

Transmission tests were conducted with the mesh placed between the ZnSe target and a stainless steel collector probe. The mesh was biased negative and the collector probe was capable of being biased

negative or positive to determine the efficiency of negative charge repulsion and positive charge transmission. A 2 cm. target-collector separation was used and the mesh placed 1 cm from the target. A series of meshes of relatively small wire separations were tested for transmission and proved unsuitable due to their very low transmission. Images of the meshes were also produced in the deposit at the collector probe. A suitable large wire separation mesh was eventually found which possessed good transmission characteristics and no apparent modulation of the deposit.

The dimensions of the successful mesh were 98% open area, a wire separation of 0.4 mm and a wire diameter of 20 µm. The mesh transmission characteristics are summarised in figure 7.20, which shows oscilloscope traces of positive current time of flight. The positive ion transmission was extremely dependent on voltage. Although a positive current was detected at the collector with +10 V mesh bias, transmission levels at low negative voltages were low. The most striking feature of the current profiles is the truncated appearance of the current profiles, which suggests saturation of transmission at the currents indicated. This is consistent with an instantaneous build up of positive charge on the mesh repelling further positive charges. After turning off the D.C. source to the mesh whilst striking the target the oscilloscope trace gradually decayed from the upper profile to the severely truncated low voltage profile. The saturated transition plasmas apparently do not have a great enough time interval to return to a Maxwell-like distribution before striking the collector, although the tilted flat tops suggest a degree of rethermalisation.

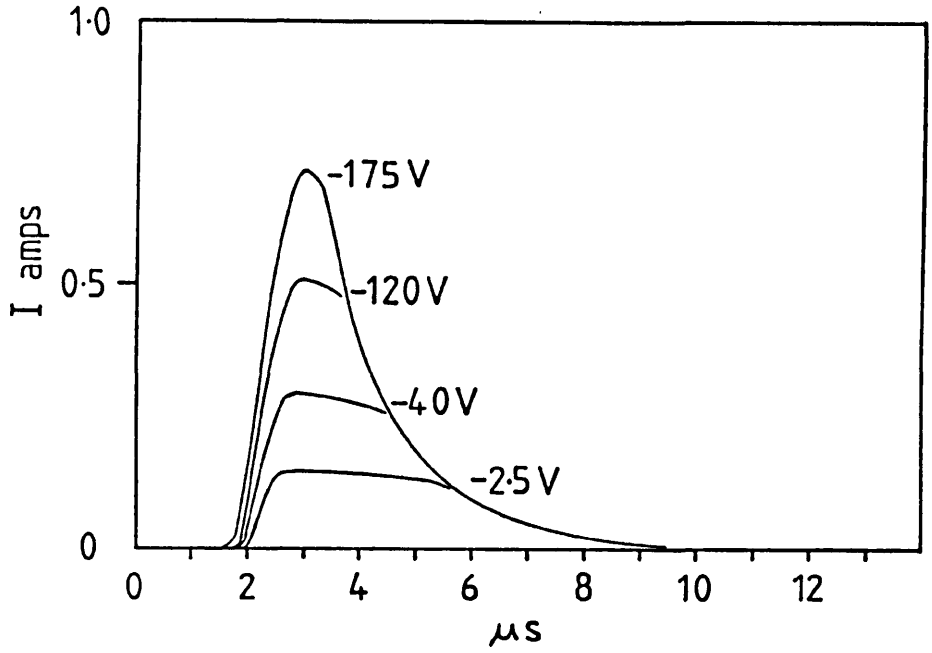

Figure 7.20 Positive ion currents obtained after transmission through negatively biased mesh. Note truncated appearance of profiles consistent with saturation of transmission.

7.52 Deposition Results.

A ZnSe layer was deposited using the mesh to repel particulates. The n-type GaAs substrate was biased as usual to reduce a positive charge build up at the layer surface. The target-substrate separation was 2 cm as for the mesh test and the bias used was originally -120 V, although this was reduced to -90 V during the course of the experiment as some arcing was observed in the chamber at the higher voltage.

On removing the sample from the chamber it was readily apparent to the naked eye that particles were incorporated in the layer. As well as being disappointing this result was highly surprising because up to that point all particles produced were of sub-micron dimensions

and quite invisible to the naked eye. Observation under the SEM showed the particles deposited in this case to be about 50 - 100 μm diameter (figures 7.22, 7.23). As the substrate was still biased negative in this test, the only explanation for the appearance of these relatively massive particles was that as small negatively charged micron-size particulates left the target, they were repelled back toward the target by the mesh field. Trapped electrostatically between the mesh and the negatively charged target, the particles grew in size as they were deposited on by successive plasma jets. To grow to such dimensions quickly the particles must have been held close to the point of ablation where deposition rates would be very high. The particles then acquired a positive charge and were attracted to and accelerated through the mesh to be incorporated in the layer.

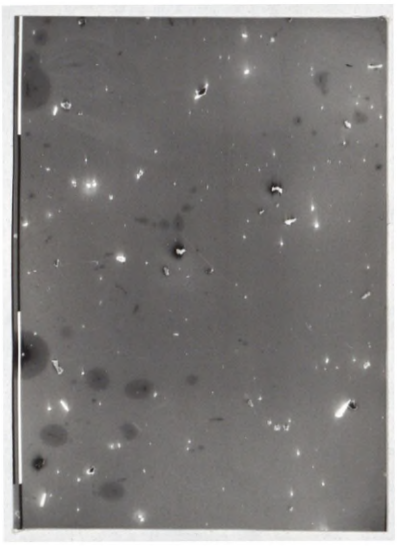

Figure 7.21 SEM micrograph of film deposited through mesh. Note large particulates are clearly visible (1mm marker)

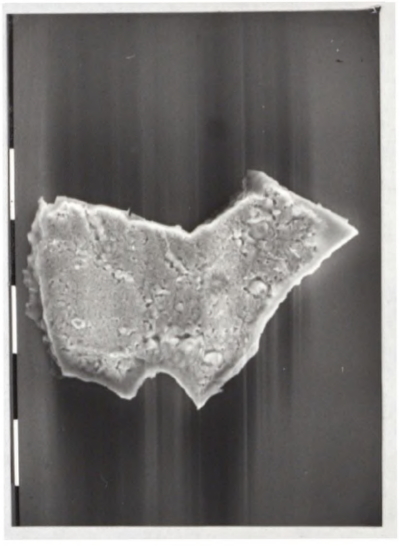

Figure 7.22 Close up of particulate (10μm marker)

7.6 Window Deposition

One surprising and unexpected observation was the appearance of a visible deposit on the inner surface of the laser entry window. The deposit was extremely thin as the beam transmission was not obviously hindered during an experiment, but necessitated removal and cleaning of the window between experiments. The interesting feature of this deposit was the fact that it reproduced the rectangular beam profile at the window and was absent in the regions where the laser did not pass. The deposit was presumably due to the background cell atmosphere of Zn and Se species and the delineation is consistent with the UV enhancement of nucleation rates at the window due to enhanced adatom mobility.

References

1. L. Aleksandrov, Growth of Crystalline Semiconductor Materials on Crystal Surfaces, Elsevier, Amsterdam (1984)

2. W. Stutius, J. Crystal Growth **59**, 1 (1982)

3. D. Lubben, S.A. Barnett, K. Suzuki, S. Gorbatkin, J.E. Greene, J. Vac. Sci. Technol. **B3** (4), 968 (1985)

4. D.B. Geohegan, D.N. Mashburn, R.J. Culbertson, S.J. Pennycook, J.D. Budai, R.E. Valiga, B.C. Sales, D.H. Lowndes, L.A. Boatner, E. Sonder, D. Eres, D.K. Christen, W.H. Christie, J. Mater. Res. **3** (6), 1169 (1988)

5. C.C. Chang, X.D. Wu, A. Inam, D.M. Hwang, T. Venkatesan, P. Barboux, J.M. Tarascon, Appl. Phys. Lett. **53** (6), 517 (1988)

6. H. Sankur, W.J. Gunning, J. DeNatale, J.F. Flintoff, J. Appl. Phys. **65** (6), 2475 (1989)

7. J.J. Dubowski, Chemtronics **3**, 66 (1988)

8. J. Simpson and J.O. Williams, work in progress.

9. A. Inam, X.D. Wu, T. Venkatesan, S.B. Ogale, C.C. Cheng, D. Dijkkamp, Appl. Phys. Lett. **51** (14), 1112 (1987)

10. J.M. DePuydt, H. Cheng, J.E. Potts, T.L. Smith, S.K. Mohapatra, J. Appl. Phys. **62** (12), 4756 (1987)

11. N.M. Maung, Ph.D. Thesis, University of Manchester, 1988.

Chapter 8

Conclusions and Further Work

In this chapter each results chapter is summarised in turn, and where appropriate suggestions are made for further work.

8.1 Laser Photochemical Deposition of ZnSe

In chapter 2 it is shown that ZnSe thin films can be deposited on GaAs and silica substrates by the photolysis of DESe and DMZn with 193 nm ArF excimer laser radiation at substrate temperatures of 20°C and above. Laser entry to the reactor throughout the course of an experiment was achieved by the removal of window deposits with the laser beam loosely focused at the window surface. This inadvertently resulted in heterogeneous nucleation or 'seeding' in the gas phase and particulate contamination in the depositing layer. To avoid this an electrostatic trap was installed which prevented ionised material, projected from the window, from entering the gas phase.

The effects of varying deposition parameters on the growth rate are presented in chapter 3. The overall trends are a decrease in growth rate over the approximate range 20-275°C followed by a subsequent rise and further decrease from 300-350°C, the exact figures dependent on experimental conditions. The initial decrease in growth rate is consistent with the reduction in adsorbate layer coverage at the layer surface. The subsequent rise in growth rate is believed to be due to pyrolysis of the adsorbate layer by surface thermal transients as the surface is struck by the 15 ns laser pulse. The further

decrease in growth rate is consistent with pyrolysis being restricted to the adsorbate layer. Gas phase photolysis is believed to make only a minor contribution to the growth rate.

At temperatures in the 280°C regime the crystallinity of the material deposited on (100) GaAs was poor, whereas layers deposited by MOCVD using DMZn and H_2Se are epitaxial at this temperature. The poor crystallinity of laser deposited material is attributed to the incorporation of carbon as a result of the inability to remove alkyl group reaction byproducts from the growth surface. This is believed to occur in MOCVD by atomic hydrogen (provided by H_2Se) acting as a radical scavenger. If photolytic ZnSe deposition is to match the quality of MOCVD grown material, an efficient means of alkyl removal must be found. The presence of dihydrogen was not found to be successful in increasing material crystallinity.

In retrospect a better precursor combination might have been DEZn and DESe. The absence of any $M-CH_3$ bonds may give improved results as the weaker $M-C_2H_5$ should allow easier alkyl desorption, either photolytically or via ß-elimination routes.

ZnSe layers deposited under UV on silica substrates and on GaAs at low temperatures exhibited a marked tendency to preferential (111) orientation, which increased with increasing pulse energy. In samples where mixed (111) and (100) orientations are exhibited, the crystallinity of the (111) planes (FWHM (400) ≈0.2 degrees) is markedly better than (100) oriented ZnSe (FWHM (400) several degrees) The remarkable tendency towards (111) oriented growth of ZnSe under UV irradiation, together with the great difference in crystallinity

between (100) and (111) growth surfaces is interpreted in terms of the anisotropic generation of energetic photocarriers which stimulate precursor cracking and alkyl group desorption. This result also indicates that the actions of photogenerated carriers are an extremely significant factor in photochemical deposition.

This phenomenon should certainly be studied in greater detail as this effect may provide a greater insight into photodeposition mechanisms. In particular a study of the wavelength dependence of ZnSe preferred orientation growth would be very useful. This could be achieved by depositing on amorphous substrates and irradiating with lamp and monochromator or filter combinations. The wavelength dependence could be useful in determining any interband transitions that may be linked with the observed preferred (111) orientation. Certainly if the proposed mechanism is correct to any degree, no preferred orientation should be observed at photon energies just above the band gap as the isotropy of the Γ region of the Brillouin zone will result in equivalent (hkl) surface reactivities and random orientation.

Chapter 4 dealt with the thermal response of ZnSe and GaAs to UV irradiation. Computer simulation of thermal transients showed that surface temperatures were briefly raised 100-200°C above ambient at the relatively low energy densities used. However these temperatures resulted in enormous thermal gradients at the sample surface which resulted in mechanical failure of the ZnSe layer at the low energy density of 30 mJ cm^{-2}. The low thermal diffusivity of ZnSe results

in a very poor thermal shock resistance compared to other semiconductor materials such as GaAs and InP. The low thermal shock resistance of ZnSe represents a great handicap to the pulsed laser processing of this material. Had the use of higher energy density pulses been possible, this would have undoubtedly led to improved material quality by increasing the removal of alkyl groups either by thermal flash desorption or by photon effects.

UV photochemical deposition of ZnSe is, therefore, probably better carried out with constant flux lamp sources which will can deliver equivalent numbers of UV photons to the sample over a greater period of time and avoid extreme thermal stresses due to pulsed laser sources.

8.2 Laser Plasma Deposition of ZnSe

Pulsed UV laser radiation focused on a ZnSe surface results in a highly ionised jet of vapour expanding away from the target surface. In chapter 6 the results of electrical measurements performed on ZnSe pulsed laser plasmas are presented. Two modes of ablation for ZnSe by 193 nm radiation were identified. The first begins to operates at a threshold energy density of 90 mJ cm^{-2}. The second begins to operate at a higher energy density of 210 mJ cm^{-2}, at which point there is an abrupt jump in ion yield. The effective temperature of species produced at the higher energy, measured by their translational velocity, is found to be lower than species produced at lower pulse energies. The time of flight of ablated positive ions

over varying distances was measured. The ion velocity was found to increase with increasing target-detector separation. The initial velocity and effective temperature of the plasmas produced at 210 mJ cm^{-2} and above was found to be very low indeed.

A mechanism for the ablation of ZnSe by pulsed 193 nm radiation is proposed, involving the depopulation of the valence band as a result of electron-hole pair generation at the target surface. The very high UV absorption of ZnSe results in the creation of a dense photocarrier plasma in the sample absorption depth and importantly a high hole density at the surface. There is also evidence to suggest that in direct band gap materials screening effects at high carrier densities delay carrier recombination, again increasing the hole population. Each hole represents a charge depleted bond, and at a sufficiently high hole density the material bonding fails to stabilise thermal atomic motion.

As a result of the failure of covalent bonding, the solid disintegrates at low thermodynamic temperatures to form a highly ionised and electronically excited vapour. The failure of the solid lattice is not driven by atomic motion as in a conventional melting or sublimation process and represents a second order or partial second order phase transformation. As a result the vapour has a low initial thermodynamic temperature (< 2000 K), much of the pulse energy being retained in electronic excited states. This excited state population, and the degree of ionisation of the vapour ($\geq 20\%$) represent a large departure from thermal equilibrium.

The energy retained initially in excited states eventually scatters

into thermal modes in the vapour and an increase in thermodynamic temperature represented by an increase in translational velocity is observed.

Diffusion of photocarriers rearward into the target during ablation is believed to leave the plasma with an overall positive charge. Particulate matter ejected from the target during ablation carries a corresponding negative charge.

The results of a short programme of ZnSe thin film deposition from the laser plasmas are presented in chapter 7.

The deposition programme has demonstrated that ZnSe is an ideal material for deposition by pulsed laser ablation of a solid target. The congruent vapourisation properties greatly simplified the experiments. The 1:1 transfer of material from target to substrate allows target stoichiometry to be reproduced at the layer and the reproducible ablation characteristics allow ablation to take place at a fixed point at the target surface. This minimises the transfer of any target surface contamination to the substrate as clean material is immediately exposed. The crystallinity of the layer grown at 280°C on (100) GaAs was equal to MOCVD material and the fact that this was achieved in a conventional vacuum system with high levels of interfacial contamination was particularly encouraging. The non-stoichiometric target material may also have prevented optimum quality material from being deposited, although it was useful in demonstrating that the target composition is reproduced faithfully at the substrate.

The use of laser ablation as a means of depositing high quality ZnSe depends ultimately on the availability of high purity stoichiometric targets. If targets of sufficient purity and composition are not available then high purity elemental sources will have to be used to deposit very high quality material. The use of separate elemental targets, whilst complicating the experimental setup somewhat, would allow the effects of varying Zn and Se flux ratios to be determined.

The suppression of particulate incorporation by substrate biasing has been demonstrated. However several drawbacks to this technique have been identified. Biasing the substrate results in preferred orientation on polar planes which may have deleterious effects. The deposition of insulators under a negative bias results in the layer acquiring an overall positive charge that eventually suppresses the effects of the bias. The stoichiometry of ionic material may also be affected. For these reasons work was begun on a particle repulsion system that was not dependent on substrate biasing.

This consisted of a biased high transmissivity mesh situated between target and substrate. Under experimental tests this was found to have the opposite effect to that intended, as large particles were formed from small particulates trapped electrostatically between target and mesh.

A further development to this system is proposed and is shown schematically in figure 8.1. A positively charged plate is incorporated to attract negatively charged particles repelled by the

mesh. Although the ZnSe plasmas produced by 193 nm radiation displayed an overall positive charge due to electron deficiency, a neutral laser plasma would also become positively charged due to repulsion of electrons and this may also result in some of the problems outlined above. Layer and substrate electrical neutrality are maintained by incorporation of an electron flood gun which neutralises the layer surface and prevents charging.

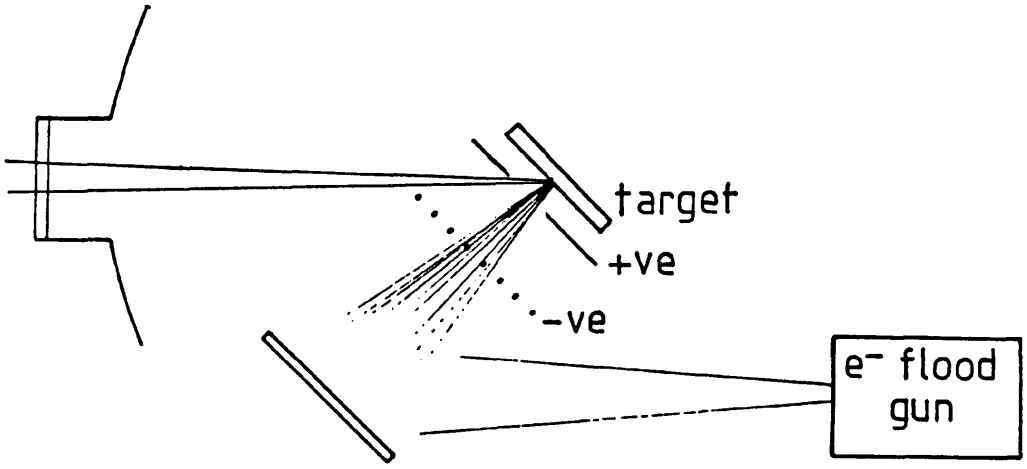

Figure 8.1 Schematic of proposed experimental system to repel negative charged particulates from depositing species whilst maintaining electrical neutrality at the layer surface.

The ablation characteristics of ZnSe over a range of laser wavelengths should be studied. In particular below-band gap wavelengths such as 1.06μm (Nd-YAG) or 10.6 μm (CO_2) may be more useful in generating species of hyperthermal energies. The relationship between epitaxial growth temperature and depositing species energy should be studied, as higher energy species than obtained in this study may be more useful in achieving reductions in deposition temperature. The use of a conducting ZnSe target would also allow drain currents to be measured to quantify photoelectron diffusion into the target in the case of UV irradiation.

Aspects of both the photochemical deposition and the plasma deposition studies could also be combined; a study of the effects of UV irradiation in a situation where the radiation was not directly contributing to the flux of depositing species, e.g. substrate illumination during MBE or laser ablation epitaxy, would be very interesting to determine the fundamental effects of radiation on growth processes and the resulting material quality. A wavelength dependent study of preferred orientation (if any is exhibited) in this situation would be interesting to determine whether energetic surfaces (due to the presence of photocarriers) created by UV irradiation can affect growth processes such as nucleation and adatom mobility and result in an improvement in material quality.